Improved Drug Delivery of next-generation Antibody-Drug Conjugates by utilizing tumor-associated proteases

TECHNISCHE UNIVERSITÄT DARMSTADT

Vom Fachbereich Chemie
der Technischen Universität Darmstadt

zur Erlangung des akademischen Grades eines
Doctor rerum naturalium (Dr. rer. nat.)

vorgelegte Dissertation
von
Janis Mario Roßkopf
aus Dieburg

Referent: Prof. Dr. Harald Kolmar
Korreferent: Prof. Dr. Siegfried Neumann

Tag der Einreichung: 16. Oktober 2019
Tag der mündlichen Prüfung: 02. Dezember 2019

Darmstadt 2019

Die vorliegende Arbeit wurde unter der Leitung von Herrn Prof. Dr. Harald Kolmar am Clemens-Schöpf-Institut für Organische Chemie und Biochemie der Technischen Universität Darmstadt sowie bei Merck KGaA in Darmstadt von November 2016 bis Oktober 2019 angefertigt.

Publications or patents derived from the presented work

Parts of this work have been published or are currently under review.

Contributions to conferences

Shan M., Passafaro M., Becker S., Deutsch C., **Rosskopf J.**, Schroeter C., Gajewski J. (February 1st, 2018): Two Ways to Kill Tumors: Magic Missile & Smart Bomb. *Poster at Innospire Marketplace Darmstadt, Merck, Darmstadt, Germany.*

Publications to related projects

Jäger S., Krah S., Könning D., **Rosskopf J.**, Kolmar H., Hecht S., Schröter C. (2019): Isolation of Anti-Hapten Antibodies by Fluorescence-Activated Cell Sorting of Yeast-Displayed B-cell receptor gene repertoires. Chapter in *Genotype Phenotype Coupling, Methods and Protocols.* Springer Verlag.

Table of contents

1. Abstract

1.1. Zusammenfassung

Die zielgerichtete Therapie mit tumor-spezifischen Antikörpern hat sich im Laufe der Zeit in der klinischen Onkologie etabliert, was durch die Vielzahl an zugelassenen Medikamenten belegt ist. Dennoch gibt es Limitationen bei Antikörpern, die Zelloberflächenantigene adressieren. Onkologische Therapeutika müssen im Rahmen der Tumortherapie in der Lage sein, alle Krebszellen zu erreichen. Wenn unbehandelte Regionen nicht therapiert werden, können diese zu einem Tumor-Rezidiv führen. Die verringerte Tumorpenetration und Wirkstoffabgabe von herkömmlichen Antikörper-basierten Medikamenten stellen eine große Herausforderung für die effektive Behandlung von soliden Tumoren dar. Im Rahmen von Antikörper-Wirkstoff Konjugaten (ADCs), fokussierten sich die größten Forschungsaktivitäten auf neuartige Linker Strukturen, Optimierungen von zytotoxischen Arzneistoffen und Technologien für Positions-spezifische Konjugationen. Weniger Beachtung erhielt die Modifikation des Antikörpergrundgerüsts oder Antikörperalternativen für die Optimierung des Arzneistofftransports. In diesem Kontext spielt die Molekülgröße des ADC Transportvehikels eine essenzielle Rolle für den Transport des zytotoxischen Wirkstoffs zu den Tumorzellen.

In der vorliegenden Studie wurde die Auswirkung des Molekulargewichts und der Valenz auf die Tumorpenetration und die Wirksamkeit untersucht. In diesem Zuge wurde ein neuartiges ADC Design ausgearbeitet und dessen Funktionalität experimentell bestätigt. In einen ADC im IgG Format wurde eine Protease-Schnittstelle in die IgG1 Hingeregion eingefügt, welche von überexprimierten Enzymen des umliegenden Tumorgewebes gespalten werden kann. Die Spaltung resultiert in 2 Fab Fragmente und einen Fc Anteil.

Der Hinge spaltbare ADC wurde hinsichtlich der Tumorpenetration und der Wirksamkeit von Fab-Wirkstoff Konjugaten (FDCs) evaluiert, die mittels enzymatischer Spaltung durch Tumorproteasen lokal freigesetzt werden können. Im Gegensatz zu der kurzen Halbwertszeit der im Tumorgewebe lokal freigesetzten Fabs, behält der ADC im ungespaltenen Zustand in systemischer Zirkulation die für ADCs typischerweise längere Halbwertszeit. ADCs und FDCs mit den zytotoxischen Wirkstoffen MMAE und MMAF wurden durch Positions-spezifische Konjugation mittels Sortase A an die leichte Kette der Antikörper und Antikörper Fragmente hergestellt. Proteolytische Spaltungsreaktionen und Enzymkinetiken offenbarten eine schnelle sowie effiziente Freisetzung der jeweiligen FDCs vom Volllängen ADC durch die Tumorproteasen urokinase-type plasminogen activator (uPA) und matriptase (MT-SP1). Die hergestellten anti-HER2 ADCs und FDCs behielten ihre Antigen Bindeeigenschaften, waren im Mausserum stabil und zeigten vergleichbare *in vitro* Potenz und Aktivität gegenüber einem nicht spaltbaren Kontrollkonstrukt auf HER2-überexprimierenden Tumorzellen. Um eine bessere Tumorlokalisation beurteilen zu können, wurden Antikörper-Fluorophor Konjugate mit Alexa Fluor 488 hergestellt. Im Vergleich zu Volllängen IgG Antikörper zeigen enzymatisch hergestellte Fab-Fluorophor Konjugate eine gleichmäßige Penetration und Verteilung in Tumor Spheroid Modellen. Hierbei korrelierte eine tiefere Penetration und homogenere Verteilung im Spheroid mit der geringeren Molekülgröße des Transportvehikels.

Diese Arbeit zeigt vielversprechende Ergebnisse der *in situ* generierten FDCs aus den Hinge spaltbaren IgG-ADCs, die einen potenziellen Benefit gegen solide Tumore im Hinblick auf Tumorpenetration und -lokalisation bringen könnten. Darüber hinaus ist ein verbessertes Tumor zu Blut Verhältnis von FDCs zu erwarten, dass in einem verringertem Auftreten von Nebenwirkungen resultieren könnte.

Ob sich die *in vitro* gezeigte verbesserte Tumorpenetration auch *in vivo* translatieren lässt, kann abschließend nur durch ein Tiermodell belegt werden. Die Einblicke einer *in vivo* Studie kann Aufschlüsse darüber geben, die Balance zwischen der optimalen Tumorpenetration und –akkumulation, dem Molekulargewicht des Transportvehikels und der Pharmakokinetik zu optimieren.

1.2. Abstract

Targeted therapy with tumor-specific antibodies established in clinical oncology over the past decades with a variety of approved drugs. However, antibodies targeting cell surface antigens also suffer from limitations. Therapeutic agents must reach all tumor cells in cancer therapy, as untreated regions can lead to tumor recurrence. Poor penetration and drug delivery of conventional antibody-based drugs remain a major challenge for effective treatment of solid tumors. In the context of antibody-drug conjugates (ADCs), many research efforts focused on new linker chemistry, optimization of cytotoxic drugs and site-specific conjugation technologies. Less attention was drawn to the underexplored targeting scaffold of the antibody portion or antibody alternatives for optimizing drug delivery. Especially, the molecular size of the ADC pharmacodelivery vehicle plays a key role to deliver the cytotoxic payload to tumor cells.

In the presented study, the effect of molecular weight and valency on tumor penetration and efficacy was investigated, introducing a novel ADC design. In this novel design an additional protease cleavage site was engineered into the IgG1 hinge region. This protease site is sensitive to enzymes commonly active in the tumor microenvironment, resulting in the release of 2 Fab-drug conjugates from the original ADC.
The hinge cleavable ADC was evaluated for the tumor penetration ability and efficacy of Fab-drug conjugates (FDCs) that are generated locally by extracellular tumor proteases while retaining the half-life of the full-length antibody in systemic circulation. Homogeneous ADCs and FDCs with cytotoxic payloads MMAE and MMAF were generated by site-specific conjugation to the light chains of antibodies or antibody fragments using sortase A. Proteolytic cleavage reactions and enzyme kinetics displayed a fast and efficient release of FDCs from the full-length ADC by tumor-associated proteases urokinase-type plasminogen activator (uPA) and matriptase (MT-SP1). The designed anti-HER2 Trastuzumab ADCs and FDCs retained antigen binding properties, were stable in mouse serum and demonstrated high *in vitro* potency and cancer cell killing ability in HER2-overexpressing cell lines. For assessment of a better tumor localization, preparation as antibody-fluorophore conjugates for imaging analysis was achieved with Alexa Fluor 488. Enzymatically generated Fab-fluorophore fragments were able to penetrate and distribute more evenly within tumor spheroids compared to full-length IgG antibodies. A correlation was observed between reduced molecular size of the pharmacodelivery vehicle and tumor penetration and distribution ability. *In vitro* imaging analysis of tumor spheroids demonstrated increased molecular size and increased cellular binding resulted in decreased tumor penetration.

Hence, the presented work showed promising results for the *in situ* generation of FDCs from IgG-ADCs that might have a potential benefit against solid tumors in terms of tumor penetration and localization. Moreover, an improved tumor to blood ratio with FDCs can be expected that could also result in reduced adverse effects. Further *in vivo* evaluation is necessary to optimize the balance between optimum tumor penetration and accumulation, molecular size of the targeting scaffold and pharmacokinetic properties.

2. Introduction

2.1. Cancer etiology, incidence and mortality

Cancer represents a devastating disease and is characterized by uncontrolled proliferation and spread of neoplastic cells. To fulfill different physiological functions, various types of cells grow and divide. Normally, in case that cells grow old or become damaged by a noxe, apoptosis is activated and new cells replace the old and dead cells to restore homeostasis.[1] However, when multiple cells in a part of the body divide without regulation mechanisms, the excess tissue that is formed is called a tumor or neoplasm. The tumor can be classified as malignant or benign by applying distinct criteria.[2] On the one hand, a benign tumor is characterized by a slow proliferation rate with expansive growth without the presence of metastasis. Besides that, the structure of benign tumors have a sharp spatial zoning and histological differences compared to the original tissues are small. On the other hand, malignant tumors exhibit high proliferation rates, invasive growth and metastasize in distant tissues.[2] Several types of cancer evolve by a two-step process. First, a single mutation or a series of mutations occur that are potentially responsible for carcinogenesis. Followed by the promotion of this genetic damage, a recognizable tumor is the result.[3,4] In clinical oncology tumors are classified according to their stage in order to better estimate tumor progression and prognosis. The 'TNM Classification of Malignant Tumors' System arose from the observation that survival rates of patients were higher for cases in which the tumor was localized than for those in which the tumor has spread. With the underlying principles of the TNM system, three major criteria are assessed to describe the extent of a tumor, which are summarized in **Table 1**.[5]

Table 1: Staging and grading according to the TNM classification system.

The three components with corresponding descriptors used for describing a tumor (T), the presence of regional node (N) and presence of metastasis (M) are listed. The extent of malignant disease is indicated by increasing numbers with the respective criteria. Table adapted from Sobin et al.[5]

Criteria	Description	Stage
T	Extent of primary tumor	T0, T1, T2, T3, T4
N	Absence/presence and extent of regional lymph node metastasis	N0, N1, N2, N3
M	Absence/presence of distant metastasis	M0, M1

Clinicians evaluate cancer growth and spread according to the three listed criteria: size/extent of the primary tumor (T), absence/presence of regional lymph nodes that are involved (N), and absence/presence of distant metastasis (M). Each criteria is indicated by a specific number to further characterize the stage of the diseae. In general, the different categories demonstrate that with increasing numbers a more advanced stage and a poor prognosis can be assumed, where effective treatment is limited. Therefore, for T1-T4 an increasing size of the primary tumor is evident, for N1-N3 multiple lymph nodes are involved, and M1 reveals distant metastasis.[5]
During decades of intensive research, cancer etiology revealed that many factors are related to an increased occurrence of a malignant tumor.[3,4] Today, a lot of cancer risk factors are known. These risk factors comprise

genetic predisposition and non-genetic factors like lifestyle and environmental risk factors, but also viruses and other infections. For example, alcohol abuse and addictive substances like tobacco are related to an increasing risk for lung cancer, colorectal cancer, esophageal cancer and stomach cancer, as well as liver cancer and breast cancer, respectively. In case of tobacco-induced cancer one of the primary prevention strategies is reduction of frequent smoking. Aside from tobacco use, obesity and physical inactivity can cause cancer mainly in parts of the gastrointestinal tract, potentially leading to colorectal cancer, kidney cancer, but also to breast cancer and prostate cancer. Environmental risks like urban air pollution or indoor smoke from household use of solid fuels are attributed to lung cancer, but also workplace exposure with carcinogenic substances like benzene or polycyclic aromatic hydrocarbons are attributed to different tumors. Other chemical carcinogens include tobacco-specific nitrosamines (*N*-nitroso derivatives of nicotine and its metabolites), which are also frequently used in cosmetic and rubber products. Another substance is Aflatoxin B_1, one of the most potent carcinogens derived from the pathogenic fungus *Aspergillus flavus*. A clear relationship exists between the occurrence of cervical cancer in women caused by persistent human papillomavirus (HPV) infection, as well as viral infections of hepatitis B and hepatitis C leading to the promotion of hepatocellular carcinoma (HCC).[3,4] Broad evidence shows that for prevention of HPV and hepatitis B infections, vaccination is the most effective way against these viruses and reduce significantly the occurrence of the related cancer. Unfortunately, until now there is no hepatitis C vaccine available against this virus infection, which could potentially prevent liver cancer caused by such a chronic disease.[6] Also a bacterial infection with the gram-negative *Helicobacter pylori* is associated with a higher number of cases of gastric cancer. However, more recent studies exhibited that eradication of *Helicobacter pylori* does not result in complete prevention of all gastric cancers, but leads to a retardation of the precancerous process of the disease.[7] Besides that, usage of pharmacological agents as oral contraceptives (especially hormones like estrogen or progesterone) are known to be an evidence-based cancer cause for breast cancer, especially for younger and post-menopausal women.[8] Also antineoplastic agents like busulfan, melphalan, chlorambucil and cyclophosphamide that are commonly used in cancer therapy are associated with an increasing risk for developing second cancers. This ability is related to the fact that these substances mainly act by alkylation of purine bases in DNA (mostly guanine residues at N7 position) and evolve their genotoxic activity.[9]

Although major improvements in cancer therapy are evident over the last decades, cancer is still the second leading cause of death in the United States (following cardiovascular diseases like ischaemic heart disease and stroke).[10,11] Comprehensive data on cancer incidence (new cases) and mortality exhibit that in 2018, an overall estimate of 1.74 million new cancer cases and 610 thousand cancer-related deaths are projected in the US.[12] Most common cases and cancer-related deaths (both sexes) are depicted in **Figure 1**. According to these numbers, lung cancer, colorectal cancer and prostate cancer represent the most common cases and deaths in men. Prostate cancer accounts for nearly 20% of new diagnoses of cancer in men. Among women, predominantly diagnosed are breast cancer and lung cancer as well as colorectal cancer, indicating also a high mortality rate for these cancer types. Overall, 30% of all new diagnosed cancer in women account to breast cancer alone. The 4 most common cancer in men and women (lung cancer, breast cancer, colorectal cancer and prostate cancer) constitute for nearly 45% of the majority of cancer deaths, led by lung cancer with 25%.[12]

For a distinct prognosis of a diagnosed cancer, five-year survival rates are estimated. The tumor is characterized as localized, regional or distant at the stage of diagnosis. Relative survival rates with a good prognosis are high for prostate cancer (99%), melanoma (92%) and breast cancer in women (90%). A poor prognosis with a low relative survival rate is attributed to pancreas cancer (8%), lung cancer (18%) and liver cancer (18%).[12] Nowadays, the most promising way to treat cancer comprises an early detection and screening system combined with effective treatment. For example, primary prevention of colorectal cancer is pursued with colonoscopy as the predominant screening test, and if necessary, surgical removal to eliminate detected premalignant lesions.

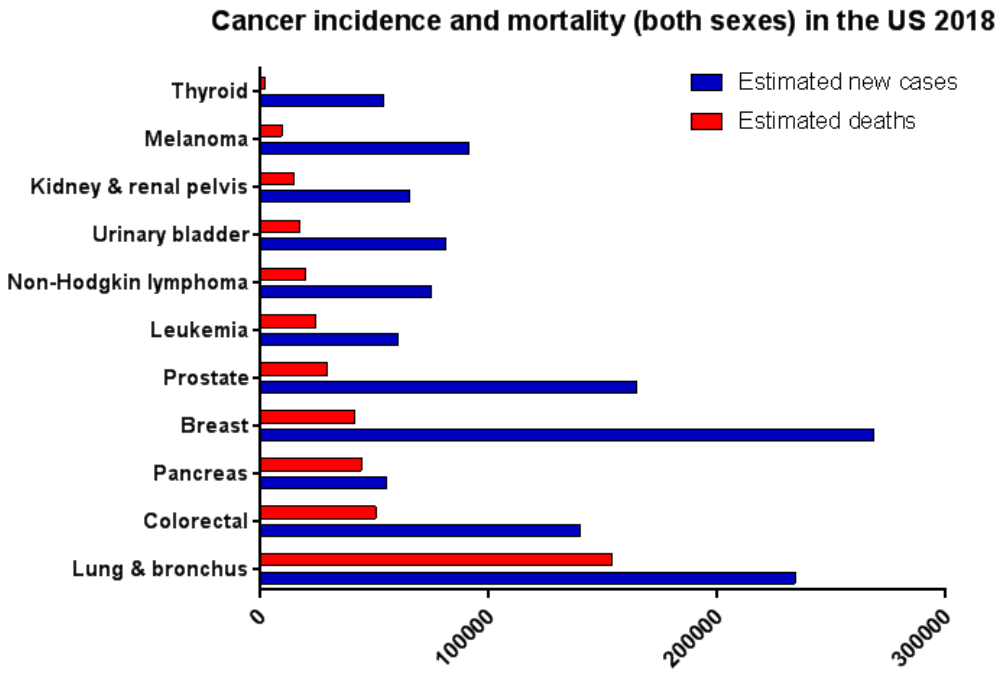

Figure 1: Estimated new cancer cases and deaths (both sexes) in the United States in 2018.

Most common cancers that occurred in the US in 2018 are represented with new cases (illustrated with blue bars) and deaths (illustrated with red bars). Decreasing order of cancer sites affected is arranged from highest mortality rates (lung & bronchus) to lowest mortality rates (thyroid). Figure is adapted from Siegel et al.[12]

Hematological malignancies (40 - 50% account for leukemias and lymphomas), often termed as childhood cancer, occur frequently within the first 15 years in life. Associations between the occurrence of hematological cancers and the exposure to ionizing radiation (extremely low-frequency electromagnetic rays) are evidence-based risk factors.[13] Taken together, many types of cancer with high incidence and mortality rates exhibit preventable risk factors and for an efficient treatment of cancer, an interplay between detection at early stages as well as appropriate medication is crucial. The following part will be focused on major characteristics of cancer biology and the difference between hematological malignancies and solid tumors. Most of the common cancers form solid tumors, which are abnormal masses of tissue. In solid tumors no liquid areas or cysts are present. As described in this chapter, the majority of most common diagnosed cancers and cancer related deaths are attributed to solid tumors, making a high relevance for therapeutic treatment of these cancers inevitable.

Particularly, most cases are associated with lung cancer, breast cancer, colorectal cancer and prostate cancer. Apart from that, hematological cancers (cancers of the blood), like leukemias, normally do not form solid tumors. Leukemia is a cancer that is mainly affecting the bone marrow and blood. The classification into 4 major groups is based on the cell type and tumor growth. Leukemia can be subdivided into 4 different groups, namely acute lymphoblastic leukemia (ALL), acute myeloid leukemia (AML), chronic lymphoblastic leukemia (CLL) and chronic myeloid leukemia (CML).[14] Regarding hematological malignancies, the 2 common blood cancers leukemia and non-hodgkin lymphoma are surpassed significantly with incidence and mortality rates by solid tumors, ranging only in the middle position of the new cancer cases.

2.1.1. Hallmarks of cancer

In the context of multistep tumorigenesis, several key features of cancer cells related to formation of a microscopic and macroscopic tumor with subsequent development were intensively investigated during last decades. These key features – termed as hallmarks of cancer – are of major importance to understand the complexity of neoplastic diseases. The well-established hallmarks of cancer were postulated by Hanahan and Weinberg and initially included the following 6 attributes: sustaining proliferative signaling, evading growth suppressors, resisting cell death, enabling replicative immortality, inducing angiogenesis, and activating invasion and metastasis (depicted in **Figure 2**).[15]

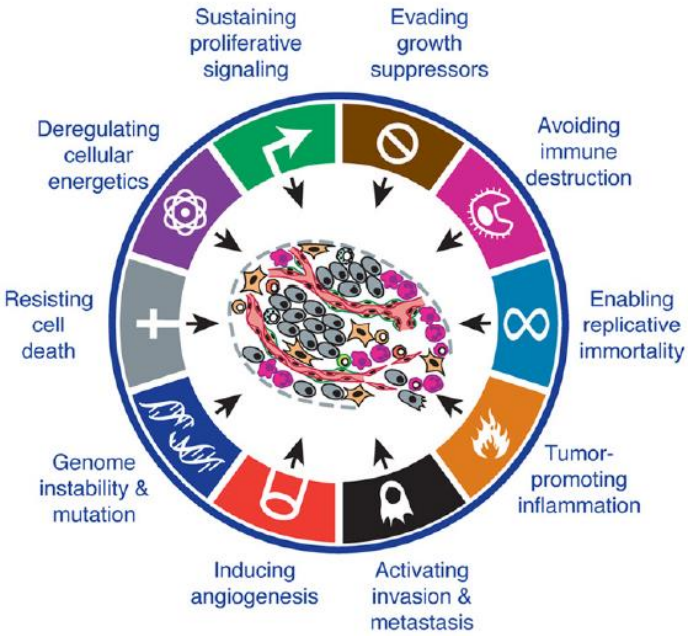

Figure 2: The classical hallmarks of cancer with emerging hallmarks and enabling characteristics.

Illustrated are the key hallmarks of cancer with deregulating cellular energetics and avoiding immune destruction as emerging hallmarks. Genomic instability and tumor-promoting inflammation are associated with enabling characteristics and facilitate the development of the key hallmarks and emerging hallmarks. Figure is modified from Hanahan and Weinberg.[15]

As one predominant attribute of cancers cells, sustaining proliferative signaling enforces uncontrolled, chronic proliferation. In healthy tissues the growth-and-division cycle is usually regulated by production and release of mitogenic factors, ensuring that a sufficient amount of mitogenic factors are delivered to cells in order to obtain

a physiological cell function and homeostasis. Many important growth-promoting signals are associated with well investigated growth factors and corresponding enzyme-coupled receptors, namely receptor tyrosine kinases (RTKs) as key regulators in cell proliferation and differentiation. All RTKs are highly conserved in humans and have a similar molecular structure (illustrated in **Figure 3**).[15,16]

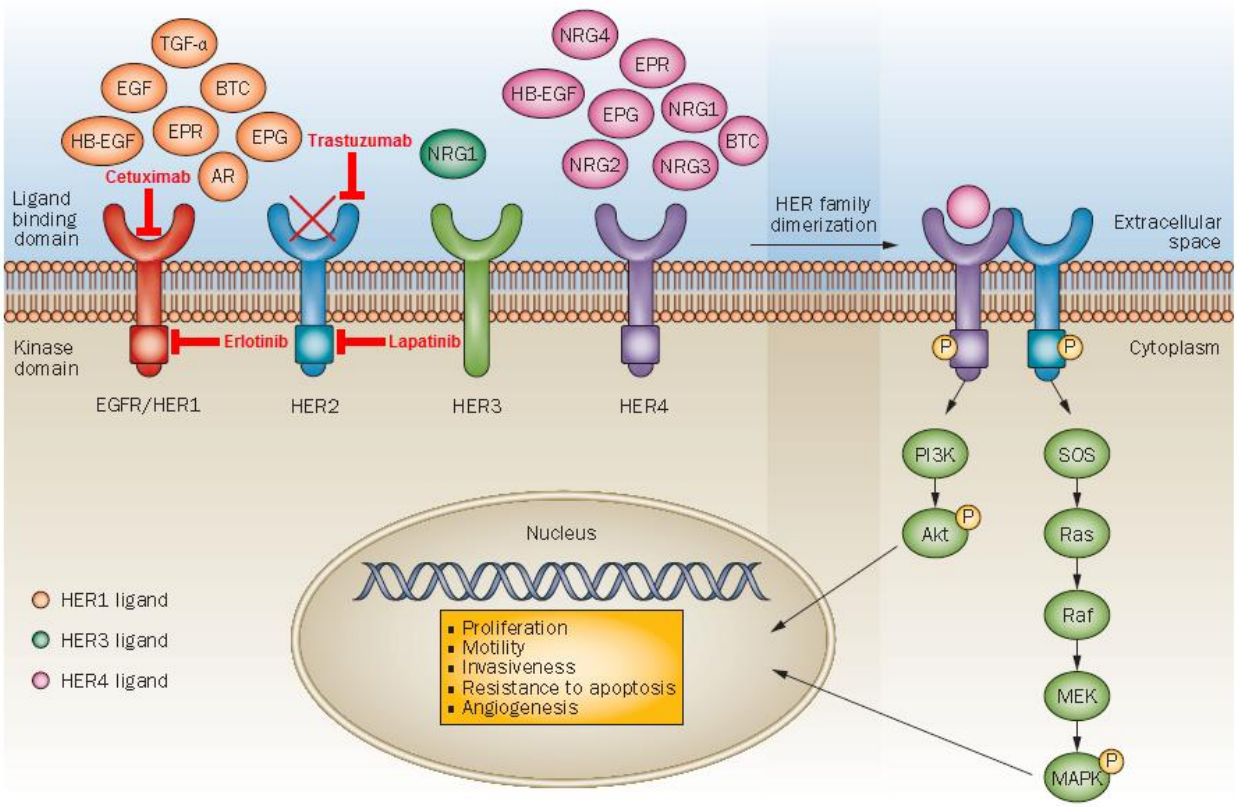

Figure 3: Signaling pathways, various growth factors and receptor formation of members of the HER family.

Depicted are EGFR/HER1, HER2, HER3 and HER4 as the four RTKs of the HER family. Each member consists of a transmembrane receptor with tyrosine kinase domain, except for HER3 which has no tyrosine kinase activity. Growth factor ligands for the different receptors that mediate receptor dimerization and activation are shown. No identified ligand exists for HER2, but the constant active conformation of HER2 facilitates dimerization with other ligand-activated receptors. In the activated state, autophosphorylation (indicated by yellow circle P) of the respective kinase domains with subsequent signal transduction of the PI3K/Akt and Ras/Raf/MEK/MAPK pathway, leads to pro-oncogenic signaling and angiogenesis (resulting from VEGF transcription). Approved therapeutic interventions are highlighted in red. The chimeric monoclonal antibody Cetuximab targets EGFR and the humanized monoclonal antibody Trastuzumab is used for the treatment of HER2-positive cancers. Both act by binding to the extracellular domain of the receptor and thus inhibit receptor dimerization, initiating apoptosis and mediate ADCC. Small molecule tyrosine kinase inhibitors (TKIs) like Erlotinib, which inhibits phosphorylation in the kinase domains of EGFR, and Lapatinib that also blocks cytosolic tyrosine kinase activity in HER2 (and also EGFR), are in clinical use. Figure is modified from Arteaga et al.[17]
AR = Amphiregulin, BTC = Betacellulin, EPG = Epigen, EPR = Epiregulin, HB-EGF = Heparin-binding EGF-like ligand, MAPK = Mitogen-activated protein kinase, NRG = Neuregulin, PI3K = Phosphatidylinositol 3-kinase, Raf = Rat fibrosarcoma, Ras = Rat sarcoma, TGF-a = Transforming growth factor-a

Upon ligand binding of growth factors to extracellular domains of these cell surface receptors, typically receptor dimerization is induced and intracellular tyrosine kinase domains amplify downstream signaling leading to tremendous and malignant cell growth. This process is driven by the activated, ligand-induced dimeric form of the RTK, where one receptor phosphorylates one or multiple tyrosines in an adjacent RTK and other intracellular signaling proteins can be phosphorylated. Cancer cells may produce growth-promoting molecules by themselves and by expression of corresponding receptors, where they function in an autocrine signaling

fashion to potentiate and support tumor formation.[16,18,17] Alternatively, fibroblasts and the tumor-associated stroma may also produce and supply cancer cells with a source of paracrine growth factors promoting cancer progression.[19] Moreover, deregulated receptor signaling by increased levels of cell surface receptors on cancer cells as well as modifications in the receptor structure leading to ligand-independent signaling, affect cells to be more sensitive to normally limiting amounts of growth factor mediators.[15]

Additionally to persistent growth stimuli, another major role is related to the evasion of growth suppressors. Many tumor suppressor genes limit cell growth and proliferation and are part of large cell cycle regulation networks. The prototype of this class is p53, which has central control functions within the growth-and-division cycle. p53 navigates cell proliferation or activates senescence (irreversible cell cycle arrest) and apoptotic cell death to prevent significant cell damage. Approximately, more than half of all human cancers bearing mutations of p53, which leads to inactivation of its crucial protection function. p53 registers within the cell circuit noxe like DNA damage, oncogene activation, stress and other abnormal cell functions. In the event of enormous genotoxic damage or insufficient supply of nucleotides, growth stimuli, glucose or oxygen, p53 can halt the growth-and-division cycle until the damage has been resolved and homeostasis can be restored. If irreparable damage is registered by sensors of the p53 system, p53 can act as a nuclear transcription factor and induce apoptosis by transactivation of a variety of genes to inhibit potential harmful conditions.[20,21]

Resisting cell death belongs also to the core hallmarks and is characterized by an imbalance of proapoptotic proteins and antiapoptotic proteins. As mentioned before, programmed cell death by apoptosis is induced in response to several cellular stresses and damages. On the one hand, extracellular signals are received and processed by a sensor network. On the other hand, intracellular signals are registered by another regulator system. Both converge to the activation of a proteolytic cascade that is related to the intracellular cysteine proteases caspase 8 and 9, leading eventually to apoptosis and consumption of the damaged cell. The interplay between pro- and antiapoptotic proteins regulate programmed cell death. Bcl-2 is the most prominent inhibitor of apoptosis and upon binding to proapoptotic proteins like Bax and Bak, their action is suppressed. If not blocked by antiapoptotic proteins, Bax and Bak can disrupt the membrane of mitochondria and release the important proapoptotic protein cytochrome c.[22] Finally, cytochrome c is able to trigger proteolytic actions of caspases and activating the apoptotic pathway. In addition, tumor cells may have a higher expression of the antiapoptotic factor Bcl-2, and also a decreased expression of proapoptotic signals like Bax and Bak, so that cells can resist cell death in order to promote tumor progression.

Enabling replicative immortality is for the formation of a macroscopic tumor required. It is widely acknowledged, that telomere length and telomerase activity play a central role in the context of carcinogenesis, where cancer cells acquire the ability for uncontrolled proliferation. Telomeres form with their hexanucleotide sequences and associated proteins the end of chromosomes, in order to protect such ends and genetic material efficiently from degradation.[23] The corresponding enzyme telomerase, is a DNA polymerase and elongates telomeres continuously during several growth-and-division cycles. Telomerase is not present in normal, healthy tissues, but upregulated in various types of cancer, indicating that telomerase activity plays a cancer-promoting role. Subcritical shortening of telomeric structures can have significant impact. In the case that an abnormal length is reached, instabilities in chromosomal structures occur, leading to loss of cell viability and eventually

to cell arrest or apoptosis. Therefore, progressive telomere shortening during cell division determines the lifetime of healthy, nonimmortalized cells. Cancer cells need to circumvent the limited replication process in order to be become immortalized with unlimited replication ability.[24]

Yet another key hallmark is the ability of cancer cells to induce angiogenesis to deliver an adequate amount of nutrients and oxygen, and to eliminate metabolic waste products. Angiogenesis is characterized by the multistep formation of new blood vessels from pre-existing vasculature and is triggered by large-scale growth of tumors (~ 2 mm^3) that ultimately require blood supply.[25,26] Proangiogenic proteins initiate and antiangiogenic proteins abolish the process of angiogenesis leading to a tightly controlled system. These angiogenesis regulators act by binding to corresponding cell surface receptors to fulfill their mode of action. In many tumors the balance between proangiogenic and antiangiogenic signals is perturbed, in favor of proangiogenic mediators (**Figure 4**).

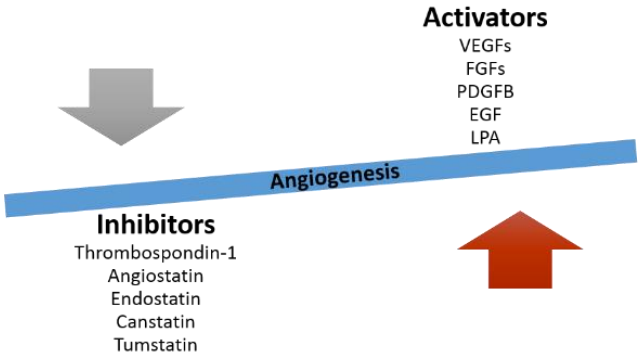

Figure 4: Important pro- (Activators) and antiangiogenic (Inhibitors) signals in the context of angiogenesis.

The angiogenic balance between various Activators and Inhibitors regulates the formation of new blood vessels, and angiogenesis is one of several distinct steps that is observed in cancer progression. Figure is adapted from Bergers et al.[25] FGF = Fibroblast growth factor, LPA = Lysophosphatic acid, PDGF = Platelet-derived growth factor, VEGF = Vascular endothelial growth factor

Among the five VEGF ligands, the protoype of proangiogenic factors is VEGF-A, which is upregulated by several growth factors and also by hypoxia (via HIF-1a). Once secreted from malignant or stromal cells, VEGF-A acts by binding to one of the RTKs VEGFR-1-3 on endothelial cells. This interaction between activated endothelial cells with tumor cells initiates the secretion of matrix-degrading enzymes like matrix metalloproteinases (MMPs) by macrophages. The degradation process of the extracellular matrix by MMPs facilitates migration of activated endothelial cells towards the tumor and enables the formation of new blood vessels. The main endogenous, inhibitory counterpart of VEGF-A is Thrombospondin-1, which suppresses stimuli for angiogenesis.[26,27] Furthermore the majority of angiogenesis inhibitors are generated by cleavage of structural proteins.[28]

The last core hallmark in tumor development is attributed to the activation of invasion and metastasis, and is characterized by the spreading of cancer cells from the primary tumor to other, distant sites and organs within the body. Many reports suggest that the more local invasion and distant metastasis occur in a cancer disease, the more advanced stage is established. One prominent example is the dysregulation and frequent loss of E-cadherin in several epithelial tumors, which normally functions as an important mediator for cell-to-cell

adhesion.[29] Elevated levels of E-cadherin are known to counteract invasion and metastasis, making this adhesion molecule a key regulator of this multistage invasion-metastasis cascade. Cancer metastasis can be regarded as an interrelated and sequential process that starts with the local invasion of the surrounding tissue by tumor cells. Following this starting point, detachment and emboli formation of tumor cells with subsequent circulation of such tumor emboli in the lymphatic and vascular system occurs. Finally, the extravasation and proliferation of the tumor embolus in distant organs takes place and after establishing its vascularized system, a micrometastasis has formed.[30,31,32] As metastases account for almost 90% of cancer-related deaths rather than the primary tumor itself, the huge impact of this key hallmark is undeniable.[33]

As two emerging hallmarks, the deregulated cellular energetics as well as avoidance of immune destruction have a considerable influence on tumor cells and hence are of major importance. To adjust a high proliferation and growth rate of cancer cells to new conditions within a tumor microenvironment (TME), cellular energy metabolism is reprogrammed and altered. Normally, healthy cells convert glucose under aerobic conditions to pyruvate by glycolysis and eventually to carbon dioxide in the mitochondria. In turn, anaerobic circumstances typically favor the formation of lactate from pyruvate resulting in lower energy efficiency. Even if oxygen is present, cancer cells preferentially produce their energy largely by glycolysis over mitochondrial oxidative phosphorylation, leading to a higher glucose consumption than in normal cells. The needed glucose is delivered by elevated levels of GLUT1 transporters, a common phenomenon observed in cancer cells.[34,35]

The variety of activities by immune cells to antagonize, but also to promote cancer progression, is a complex interplay that reflects disparate roles of the immune system on carcinogenesis. Incipient cancer cells are continuously controlled, recognized and eliminated by various immune cells like T lymphocytes, especially $CD8^+$ cytotoxic T lymphocytes or $CD4^+$ T_H1 helper cells. But the ability of some cancer cells to actively evade such elimination systems show, that a lower tumoricidal activity of immune cells is achieved. This led to the assumption that tumors can shut down antitumor activity of immune cells by a molecular switch mechanism. Such immune checkpoints represent inhibitory pathways, and inhibitory ligands or receptors are overexpressed on tumor cells to regulate T cell activation, therefore limiting antitumor activity. Exemplarily, CTLA4 and PD-1 are the prototypic receptors of these pathways and are exclusively expressed on T cells. PD-L1 as an inhibitory ligand is expressed on tumor cells and blocks antitumor response by interaction with its corresponding receptor PD-1 on T cells. Hence, tumor cells evolved escape mechanisms by which cytotoxic activity of T cells is limited.[36,37]

Besides the mentioned core and emerging hallmark capabilities, two enabling characteristics support the development of several of these hallmarks in most cancers. The first characteristic is genomic instability, which results from mutations in genes of DNA repair and occurs mainly in hereditary cancers. One well-known example is BRCA1, a germline mutation that is associated with an increasing risk of breast cancer.[38] The second characteristic is attributed to tumor-promoting inflammation and indicates that chronic, proinflammatory signals as well as conditions in selected organs facilitate tumorigenesis. In most neoplastic areas, the surrounding TME delivers several proinflammatory cytokines like TNF-a, IL-1, IL-6 and other factors that contribute to tumor development and trigger survival and proliferation of cancer cells. Many of such cytokines exhibit growth-promoting and antiapoptotic properties, making inflammatory responses highly relevant in the

context of tumor development.[39] Moreover, tumors comprise a plethora of distinct cell types of recruited, ostensibly normal cells that potentially foster most hallmarks by creating the TME, establishing another layer of complexity. The tumor microenvironment and related tumor proteases with their function, main characteristics and interactions will be elucidated in detail in chapter 2.4.

Many therapeutic approaches arose by targeting specific elements at different stages of these pathways during cancer development, establishing a well-suited, personalized cancer treatment that improves life expectancy and quality of life. In the following section, a brief insight into the history of cancer therapy will be given.

2.1.2. History of cancer therapy development: Landmark achievements

Many treatment options for cancer evolved over decades and tremendous efforts in cancer drug development led to effective therapies. The main types of cancer treatment can be subdivided into surgery, radiation therapy, chemotherapy, immunotherapy, targeted therapy, hormone therapy and stem cell transplant.

Surgery remains a very effective treatment for localized primary tumors and can be regarded as classic cancer therapy, likewise radiation therapy and hormone therapy.[40] More than a century ago, the American surgeon William Halsted published his radical mastectomy based on operations to remove breast cancer tissues that were performed from 1889 – 1894.[41] Only a few years later in 1903, Goldberg and London claimed the first use of radiation therapy leading to a cure of a patient with basal cell carcinoma.[42] Radiation therapy alone or combined with surgery or systemic chemotherapy is of major importance for effective treatment, depending on the specific cancer disease. Radiation therapy is also used prior surgery (neoadjuvant setting) to reduce tumor size, but also after surgical removal (adjuvant/postoperative) to ensure that undetectable micrometastases or oligometastases are not leading to sudden tumor recurrence.[43] These therapeutic settings offer the great capabilities to improve locoregional control of the tumor as well as overall patient survival in certain cancers. Surgery and radiation therapy dominated the area of cancer treatment until the 1960s. However, they were not able to achieve eradication of metastatic cancer.[44] Hormone therapy for therapeutic approaches against hormone-dependent breast cancer consist of reversible aromatase inhibitors like anastrozole and letrozole as well as the prominent SERM tamoxifen, which was approved in 1977.[40]

The early beginning of chemotherapy can be regarded as dye therapy, because many principles derived from histological staining techniques. Paul Ehrlich, the founder of chemotherapy, observed differential staining schemes of dye molecules for certain biological structures. Moreover, his important immunological achievements like the "side-chain theory of immunity", which was rewarded in 1908 with the Nobel Prize for Physiology or Medicine, paved the way for the "magic bullet" concept. Ehrlich imagined that this "magic bullet", a specific drug, can bind only to the intended cell-structural targets in a highly specific fashion, leaving the healthy cells unharmed and thus reducing adverse effects in patients.[45]

However, huge efforts were required, until such specific targeting drugs were established. First efforts in modern chemotherapy came up accidentally by usage of the chemical warfare nitrogen mustard, a nonspecific DNA alkylating agent. Surprisingly, investigations clearly showed that a profound lymphoid hypoplasia and myelosuppression in humans who were exposed to nitrogen mustard during World War II, occurred more frequently. The two pharmacologists Goodman and Gilman at Yale University investigated anticancer effects

of mustine in 1946. They treated patients suffering from non-hodgkin lymphoma with mustine and observed a significant tumor regression. Based on this observation Goodman and Gilman established the basic principle, that a systemic administration of drugs are able to induce tumor regression.[46] Various approaches in the 1950s based on the assumption that cancer cells divide more rapidly than normal cells, a quite revolutionary idea at that time. Further efforts that led to the elucidation of the DNA structure by Watson and Crick in 1953, inspired researchers to develop DNA analogues like 5-fluorouracil, 8-azaguanine as well as additional DNA alkylating drugs like the natural compounds bleomycin and mitomycin C.[47–49] In 1948 Sidney Farber introduced the principle of antimetabolites with the folic acid derivatives methotrexate and aminopterin, both inducing a robust antitumor effect in patients with ALL. Methotrexate specifically inhibits the folate requiring enzymes DHFR and thymidylate-synthase, leading eventually to inhibition of DNA synthesis.[50] With the purine analogon 6-mercaptopurine George Hitchings established the antimetabolite therapy for DNA bases, where a false substrate is introduced to DNA synthesis.[51] Subsequently, early observations by Rosenberg in 1965 identified that platinum compounds and derivatives are able to inhibit cell division in *E. coli*, creating interest for a possible use as a cytotoxic agent. Further investigations resulted in the FDA approval of cisplatin in 1978, a DNA alkylating agent that cross-links purine bases (binding mainly N7 residues) on DNA and finally causing DNA damage as well as triggering apoptosis. Until now, cisplatin is well established in the standard treatment of different types of cancer. However, it is also associated with many toxic and adverse effects like nephrotoxicity, hepatotoxicity, ototoxicity and cardiotoxicity, caused by its unspecific damage to rapidly dividing cells.[52,53]

The era of targeted therapy began with the introduction of targeted small molecules, namely TKIs and therapeutic monoclonal antibodies. A key landmark in cancer drug development was achieved with the first targeted small molecule drug imatinib for the treatment of CML as well as GIST that was approved by the FDA in 2001. Imatinib is an ATP-competitive, RTK-inhibitor that specifically blocks the action of BCR-ABL, a fusion protein that is formed by chromosomal translocation between tyrosine kinase ABL from chromosome 9 and chromosome 22 (BCR).[54,55] The clinical success of imatinib initiated a wave of several TKIs like erlotinib targeting EGFR for the treatment of NSCLC, gefitinib also targeting EGFR against NSCLC as well as the anti-EGFR/HER2 agent lapatinib against breast cancer. Besides that, various multi TKIs as sunitinib and sorafenib for the treatment of RCC are approved.[56]

Large molecule therapeutics like antibodies have advantages over small molecule drugs like high specificity and a better safety profile with reduced adverse events.[45] The long-half life of antibodies allows infrequent dosing. Antibodies will be discussed in detail in the following chapter. Ehrlich's vision of a "magic bullet" is virtually accomplished by the development of monoclonal antibodies and antibody-drug conjugates that recognize their targets with high specificity without harming healthy cells. The production of monoclonal antibodies (mAbs) by using the hybridoma technology was enabled by Köhler and Milstein in 1975.[57] Further development made chimeric and humanized mAbs suitable for therapeutic approaches that resulted in the approval of rituximab and Trastuzumab. With introduction of the chimeric mouse-human antibody rituximab in 1997, the first therapeutically use of a mAb for the treatment of cancer was achieved. Rituximab is directed against the B-cell specific antigen CD20 and is applied for the treatment of non-Hodgkin lymphoma.[58,59] In 1998 Trastuzumab was approved as the first targeted therapy against solid tumors. The anti-HER2 antibody showed remarkable

results in the treatment of HER2-positive metastatic breast cancer.[60] Cetuximab is a chimeric mAb that binds to EGFR and was granted approval by the FDA in 2004 for the treatment of metastatic colorectal cancer.[61] The anti-VEGF mAb bevacizumab was also approved in 2004 for the treatment of colorectal cancer and realized a new targeting strategy by neutralizing the ability of the ligand VEGF to bind to VEGFR and therefore inhibiting tumor angiogenesis.[62,63]

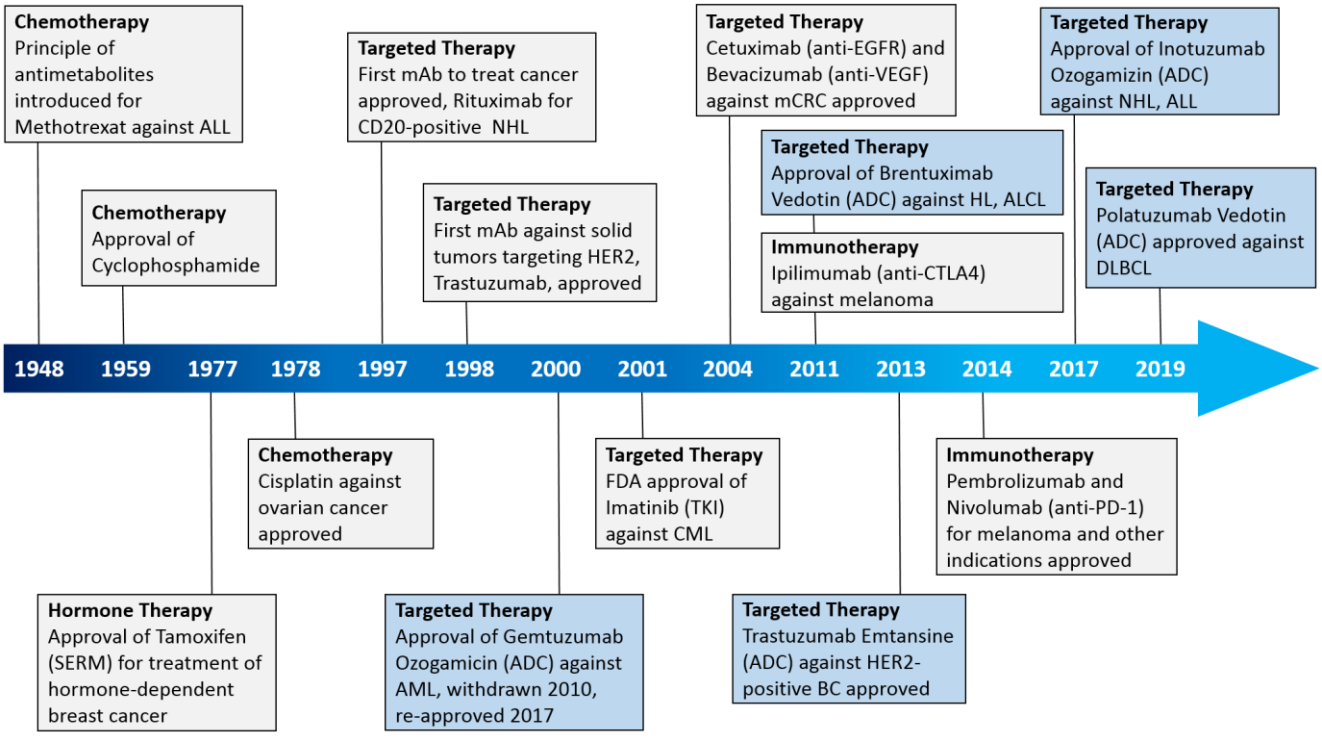

Figure 5: Timeline with selected milestones of cancer drug development.

The illustrated timeline that shows major milestones and findings of historical achievements in cancer treatment. Blue boxes indicate approvals of ADC-based therapies. Abbreviations can be found in the abbreviations section. Figure is adapted from Strebhardt, Chabner, Sievers, Wei et al.[45,50,64,65]

Furthermore, another therapeutic option for cancer treatment that is discussed in this chapter is immunotherapy, which emerged in recent years as a powerful tool against multiple types of cancer. In general, elimination of inhibitory signals mediated through the immune checkpoint blockade by antibodies, restores T cell activation and antitumor activity. Remarkable responses in the field of immunotherapy were observed by the anti-CTLA4 mAb ipilimumab, which was granted FDA approval in 2011 and paved the way for a wave of several analog compounds. Ipilimumab is used for the treatment of metastatic melanoma. Targeting the PD-1/PD-L1 axis was achieved by the 2014 approved anti-PD-1 antibodies pembrolizumab and nivolumab, both immune checkpoint inhibitors are used for the treatment of melanoma and other indications.[65,66]

By attaching toxins to highly specific antibodies and thus generating antibody-drug conjugates (ADCs), the efficacy of antibody-based therapy and the clinical response can be increased. The principles of ADCs will be further explained in subsequent chapters. The first ADC gemtuzumab ozogamicin received marketing authorization in 2000 and is directed against the CD33 antigen on AML tumor cells. Despite its initial FDA approval, further studies showed no clinical benefit of gemtuzumab ozogamicin and addition of the ADC showed

a lack of improvement in response rate as well as patient overall survival. Such uncertainties and safety concerns impelled Pfizer to voluntarily withdraw gemtuzumab ozogamicin from the market in 2010. Based on subsequent trials, that re-investigated the efficacy of gemtuzumab ozogamicin at lower doses in CD33-positive AML patients, the ADC was re-approved in 2017. In 2011, the anti-CD30 ADC brentuximab vedotin was approved by the FDA for the treatment of HL and ALCL, introducing the now well established cytotoxic drug MMAE and a protease-cleavable linker.[67,68] With the approval of Trastuzumab emtansine (T-DM1) in 2013, the first and only ADC against solid tumors that targets HER2 was introduced to the market. Inotuzumab ozogamicin gained FDA approval in 2017 and binds to the antigen CD22. Inotuzumab ozogamicin is used for the treatment of NHL and ALL.[64,69] Since very recently, polatuzumab vedotin for the treatment of DLBCL was granted approval in 2019 and targets the antigen CD79b on B cells.[70,71]

In summary, it can be stated that a broad range of different molecules to treat cancer diseases evolved over decades and resulted in more specific agents. Approaches in the field of targeted therapy remain of high interest for patients, industry as well as for academia. Within the scope of this work, investigations about antibody-drug conjugates with special focus on drug delivery will be pursued and in the following chapter antibodies are introduced in more detail.

2.2. Antibodies as powerful therapeutic proteins

The immune system comprises two substantial components divided in the innate and adaptive immune system. Both immune responses detect and eliminate potential harmful pathogens like bacteria, viruses, fungi or parasites, thereby providing an effective protection system. The innate immune system serves as an initial defense mechanism against pathogens and is characterized by a non-specific and immediate immune response that recognizes conserved pathogen-associated molecular patterns (PAMPs) through toll-like receptors (TLRs). Typical recognized pathogenic structures are proteins, glycoproteins and polysaccharides. TLRs are expressed on the cell surface of phagocytes like macrophages and neutrophils, and upon activation initiate a production of proinflammatory cytokines.[72,73] In contrast, the adaptive immune system is composed of T and B lymphocytes and is characterized by a highly antigen specific and delayed immune response, which is also supported by immunological memory.[74] On the surface of T and B lymphocytes, T-cell receptors (TCRs) and B-cell receptors (BCRs) act as antigen specific receptors and the antigen specific response is established by antibodies or immunoglobulins that represent the soluble form of the BCRs. The BCR on the B cell surface detects antigens by membrane-bound immunoglobulins. After antigen binds to a BCR, lymphocytes differentiate first into short-lived plasmablasts and then develop to antibody-secreting plasma cells, that have the capacity to secrete large amounts of antibodies with the identical antigen specificity.[75] The therapeutic potential of antibodies against cancer was realized since the mid-1990s and they can virtually be generated against every target substance.[76] Such substances are known as antigens, because they stimulate *anti*body *gen*eration.

Antibodies are Y-shaped biomolecules that are used therapeutically against a variety of life-threatening diseases ranging from cancer, inflammatory diseases, infectious diseases, transplantation and cardiovascular diseases. Generally, antibodies are often referred to as monoclonal antibodies (mAbs), which means that a mAb is produced from a single B lymphocyte and represents an identical copy.[77,78] Five main immunoglobulin classes

exist, each with a unique heavy chain and therefore a different isotype: IgG, IgA, IgD, IgE and IgM. In humans, IgG and IgA are divided in further subclasses, namely IgG1, IgG2, IgG3, IgG4 and IgA1, IgA2.

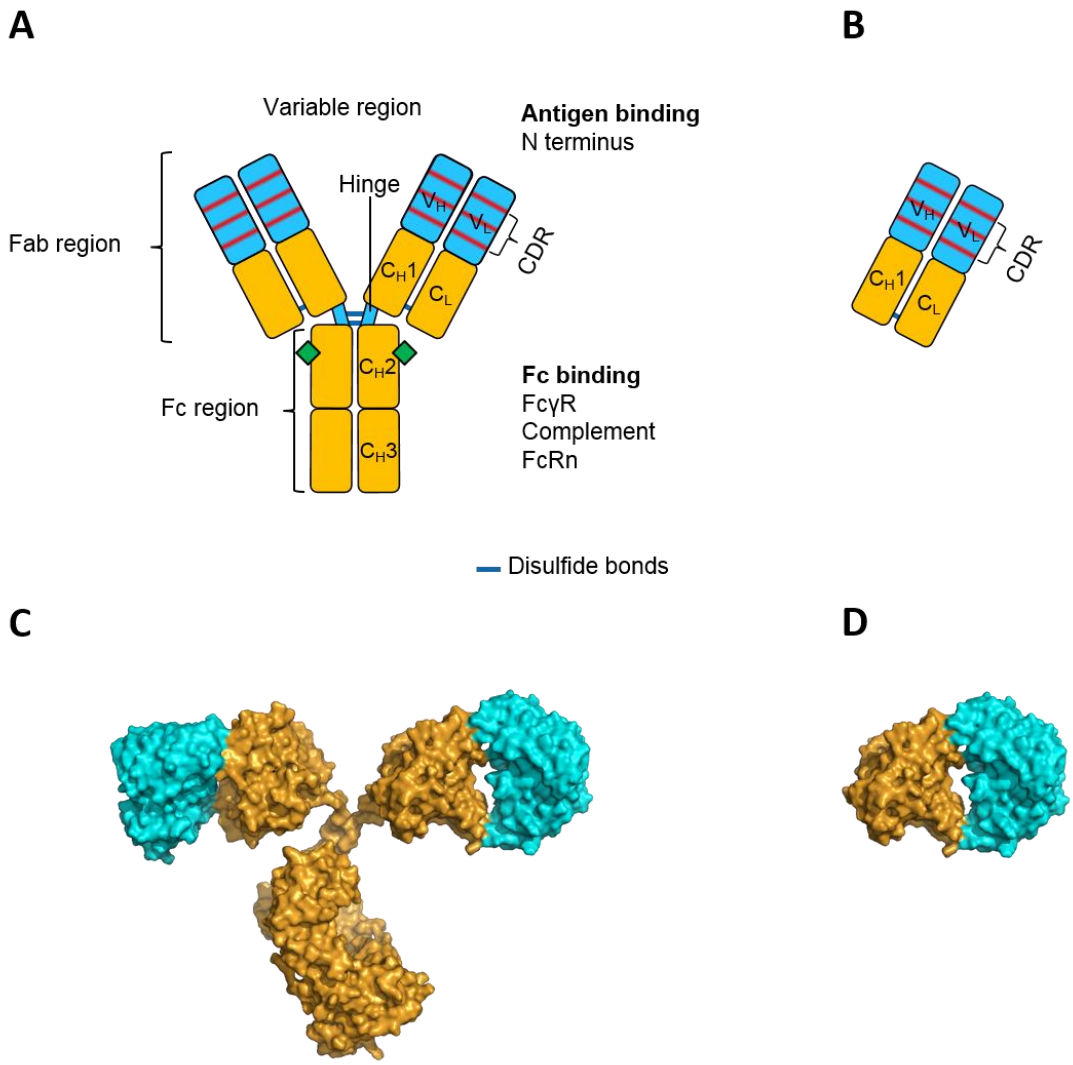

Figure 6: General structural features of an antibody illustrated by an IgG molecule and a Fab fragment.

Schematic representation of an IgG1 (**A**) molecule and a Fab fragment (**B**), both with the variable domains of heavy chain (V_H) and light chain (V_L) in cyan. Constant domains of light chain (C_L) and heavy chain (C_H1, C_H2, C_H3) are depicted in orange. Both Fab arms in an IgG1 (**A**) are linked by the hinge region to the Fc part, allowing structural flexibility. Glycosylation in the C_H2 domain of the heavy chain is located at Asn297 (illustrated by green squares) and is responsible for FcR binding as well as complement binding. CDRs in the variable domains are represented by red lines, comprising six hypervariable loops for each Fab fragment. Heavy chain constant domains are numbered from the amino-terminal part to the carboxy-terminal end. For simplicity, only interchain disulfide bonds are depicted. The monovalent Fab fragment (**B**) binds one antigen with its variable region, but lacks the Fc part and therefore has no effector functions and no interaction with FcRn. The crystal structure of IgG1 (**C**) and Fab fragment (**D**) shown in a cartoon surface model (generated by PyMOL ver. 0.99, PDB: 1IGT).

The majority of therapeutic antibodies consist of the IgG class and IgG1 is the most abundant antibody in serum.[79] Antibodies are composed as heterodimeric proteins with a molecular weight of 150 kDa, consisting of two light chains and two heavy chains connected through disulfide bonds and a hinge region (**Figure 6**).

The polypeptide structure of an antibody can be further distinguished into one amino-terminal part represented by the Fab (Fragment antigen binding) arms as the variable region and a carboxy-terminal end known as the Fc (Fragment crystallizable) part. The variable domains consisting of V_H (H = heavy chain) and V_L (L = light chain) bind the epitope on the antigen and determines the high specificity of the antibody, whereas the constant region with the Fc part mediates effector functions by interaction with different immune cells.[80] Six hypervariable loops within the variable region, termed complementarity-determining regions (CDRs), are crucial for antigen recognition and are situated between 4 constant framework regions. 3 CDRs of the heavy chain in association with 3 CDRs from the light chain are responsible for formation of the antigen-binding site on the antibody, known as the paratope.[81,82] The hinge region with a length of 15 amino acids in IgG1, is located between the first (C_H1) and second (C_H2) domain and allows high flexibility of the Fab arms to bind the antigen. Reduction of the disulfide bonds results in a separated heavy chain with 4 immunoglobulin domains and a light chain with 2 domains, showing a molecular weight of 50 kDa and 25 kDa, respectively. Besides that, intrachain disulfide bonds exist within each domain.[83,84]

Enzymatic fragmentation of antibodies with the proteases papain and pepsin facilitated structural elucidation and functional analysis. Papain is a cysteine protease that cleaves the IgG molecule at the amino-terminal side of the upper hinge region, releasing 2 Fab fragments each with 50 kDa and the corresponding Fc part also with 50 kDa. Besides that, the aspartic protease pepsin cuts the antibody at the carboxy-terminal lower hinge region, yielding one dimeric and bivalent F(ab')2 fragment as well as smaller fragments of the remaining heavy chain (truncated Fc). The F(ab')2 fragment has the same valency as the antibody, but is lacking the Fc part.

The most direct mechanism in which antibodies act, is by binding the target structure like a growth factor receptor or soluble factor and thus blocking its action and signaling pathways. Such mode of action is referred to as receptor blockade or neutralization. Besides that, immune-mediated cell killing mechanisms like antibody-dependent cellular cytotoxicity (ADCC) and complement-dependent cytotoxicity (CDC) are related to Fc binding of the immunoglobulin. Important effector functions are defined by the heavy chain and mediate the interaction of the Fc part with immune cells or the complement system, contributing to therapeutic efficacy. One substantial mechanism termed ADCC, is mediated by binding of the Fc portion of the antibody to immune cells bearing Fc receptors (FcRs). As a consequence, antibody-bound targets are destroyed by macrophages, neutrophils and dendritic cells through phagocytosis, because of FcR binding.[85] The family of FcγRs that bind IgG molecules comprise 3 different FcγRs in humans, with FcγRII (CD32) and FcγRIII (CD16) exhibiting low affinity, and FcγRI (CD64) binding with the highest affinity to the Fc part of IgG.[86,87,88] NK cells as well as basophils and mast cells release mediator molecules upon FcR binding. Most importantly, the activating FcγRIII (CD16) expressed on NK cells and macrophages has the capability to bind the Fc portion of IgG1 and IgG3 antibodies and by this activation, NK cells and macrophages release granzyme and perforin from their intracellular granules, inducing killing mechanisms.[89,90] Another significant effector function is CDC, which is a result of activation of the complement system. Initiation of the classical complement cascade by several proteolytic cleavage reactions is based on Fc binding to C1q complement protein and activates several phagocytic cells which destroy the antigen.[91]

A crucial role regarding the Fc-mediated interaction with immune effector cells depends largely on the conserved N-glycosylation of IgG located at asparagine 297 (N297) in the C_H2 domain. The core of this glycosylation consists of a heptasaccharide with N-acetylglucosamine and mannose. Modifications of glycan structure in the Fc region can modulate Fc binding to various FcRs. The elimination of a core fucose in the glycan composition results in afucosylated antibodies which exhibit significant enhancement in ADCC activity by 50-fold increased affinity to FcγRIII and thus are more efficacious. Completely aglycosylated Fc regions generated by mutations in the C_H2 domains or by deglycosylation, show complete loss of binding to all FcγRs, except FcγRI.[92,93] By contrast, the interaction of deglycosylated IgG with the neonatal Fc receptor (FcRn) is not affected, indicating that FcRn binding is associated to a different region in the Fc part. To maintain the long half-life that is generally observed for antibodies in serum, binding of FcRn to the interface of the C_H2-C_H3 domains of the antibody Fc part is essential. After internalization into cells, IgG-Fc binds to FcRn in the acidic endosome (pH 6.0 – 6.5) with high affinity, protecting IgG from degradation in lysosomes. Afterwards, IgG is recycled to the cell surface and released back in circulation, due to dissociation of IgG from FcRn by a pH change at physiological pH (pH 7.4). FcRn is expressed in the gut and liver as well as on endothelial cells. Typically, IgG molecules exhibit a half-life in the range of 21 days. In contrast to that, single domain antibodies or scFvs that are smaller antibody fragments without FcRn binding are characterized by several minutes.[94,95,96]

In general, the majority of approved antibodies are humanized or completely human. Human antibodies can be derived from transgenic mice and therefore are well tolerated concerning immunogenicity and safety.[97] Modulation of biological activity and pharmacokinetics depend largely on the antibody format (scFv, Fab or IgG) and most therapeutic antibodies comprise the full-length IgG format like Rituximab, Adalimumab, Cetuximab, Trastuzumab, Bevacizumab and many others.[98] Instead of using antibodies in the IgG format, antibody fragments exhibit efficient penetration in tumors as well as better tumor-to-non-tumor binding ratios, which might offer improvements in certain settings.[99] Further potential advantages of smaller formats might be a faster clearance from the body leading to a less whole-body exposure to antibody with modified pharmacokinetic properties. However, using unmodified antibody fragments significantly reduces the half-life from several weeks to a few hours or less, making frequent administration necessary.[99]

Approved non-IgG Fab fragments include the chimeric Abciximab targeting gp IIb/IIIa receptor used for prevention of clot formation during angioplasty and anti-VEGF Ranibizumab for the treatment of wet AMD. To improve the short half-life of Fab fragments polyethylene glycol (PEG) chains can be attached to the fragments in order to increase their hydrodynamic radius. Such a PEGylation strategy was realized in the PEGylated Fab Certolizumab pegol targeting TNF-a, which shows a prolonged half-life of 14 days and is comparable with half-life of IgG.[100,101] Idarucizumab is a Fab fragment that is used as an antidote against the anticoagulant dabigatran, in case of severe bleedings.[102]

Pharmacokinetics of full-length mAbs are attributed to the large size of 150 kDa and are characterized by a slow clearance by the liver as well as non-specific accumulation. For therapeutic applications, antibody fragments show restrictions like rapid renal clearance from the body with a short half-life due to the missing Fc-FcRn interaction. This rapid clearance of smaller fragments is achieved by a size selective barrier in the kidneys, that excretes formats with sizes below renal filtration threshold of 60 kDa (**Figure 7**).[103]

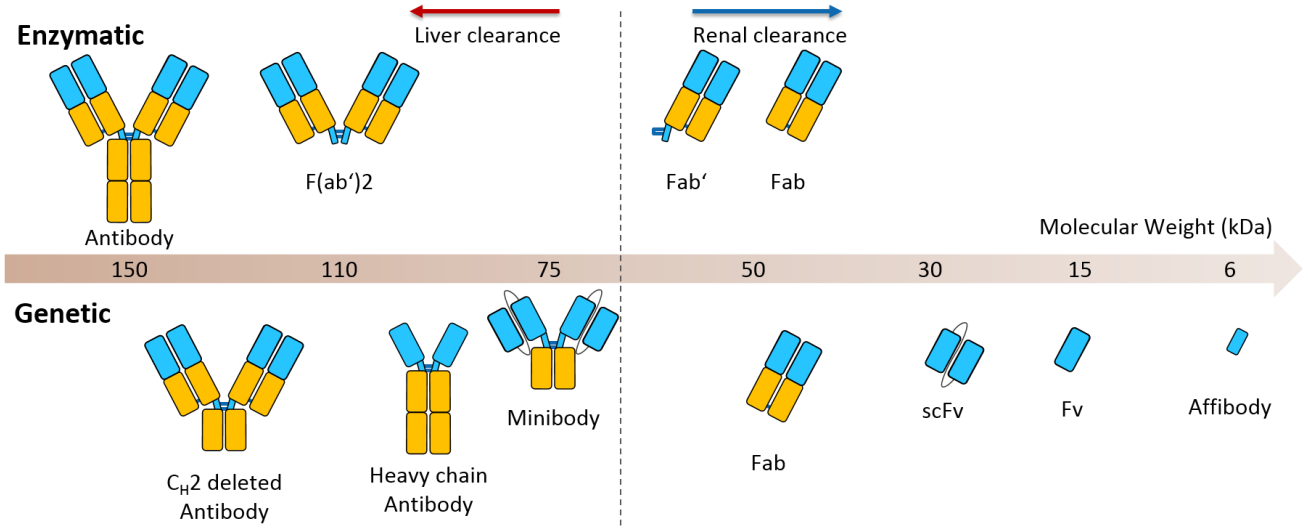

Figure 7: Smaller antibody derivatives generated by enzymatic or genetic approaches with respective clearance routes.

Various formats of antibody fragments can be either generated enzymatically (upper row) or genetically (lower row). Molecules are arranged in order to size. Two main elimination mechanisms are relevant for therapeutic proteins, renal and liver clearance. Clearance routes are mainly size-dependent, and for molecules that are smaller than 60 kDa, excretion through the kidneys is achieved. For high molecular weight species, generally elimination through the liver takes place. Figure is modified from Kobayashi et al.[103]

A plethora of marketed antibodies are utilized with their high specificity and favorable pharmacokinetic properties for the treatment of various diseases. Despite clinical success, many unmodified antibodies exhibit limited activity in the treatment of cancer compared to conventional chemotherapeutic agents. For this reason, antibody-drug conjugates (ADCs) are designed to deliver highly potent agents to tumor cells.

2.2.1. Antibody-drug conjugates (ADCs)

ADCs are emerging as a novel class of oncology therapeutics that combine the antitumor efficacy of highly potent small molecule cytotoxic drugs (300 – 1000 Da) with the favorable pharmacokinetic profile and targeting ability of antibodies. ADCs consist of a mAb as a vehicle that binds with high specificity to a tumor surface antigen. The mAb is linked covalently to a small molecule drug via chemical linkers (**Figure 8**).[104] By combining these components into a single new molecular entity, targeted delivery of normally intolerable small molecule compounds selectively to diseased tissues can be achieved, thereby increasing efficacy while decreasing potential toxicity of the payload compared to traditional chemotherapeutic drugs.[105,106,107] To exploit the benefits of armed antibodies, target antigens should be overexpressed on tumor cells or show nearly no expression in healthy tissue. This would lead to reduced off-target toxicity and an increased therapeutic index (maximum tolerated dose/minimum efficacious dose). Moreover, proteomic approaches indicate that in hematological malignancies target expression in organ tissues is lower compared to cell populations from the whole blood, while most of solid tumor targets are expressed relative broadly in organ tissues.[108]

The mechanism of action of ADCs depends on multiple processes, each of these steps are crucial for efficient delivery of the cytotoxic payload (**Figure 8**). At the beginning, it is necessary that sufficient amount of ADC is able to enter tumor tissue from vasculature.

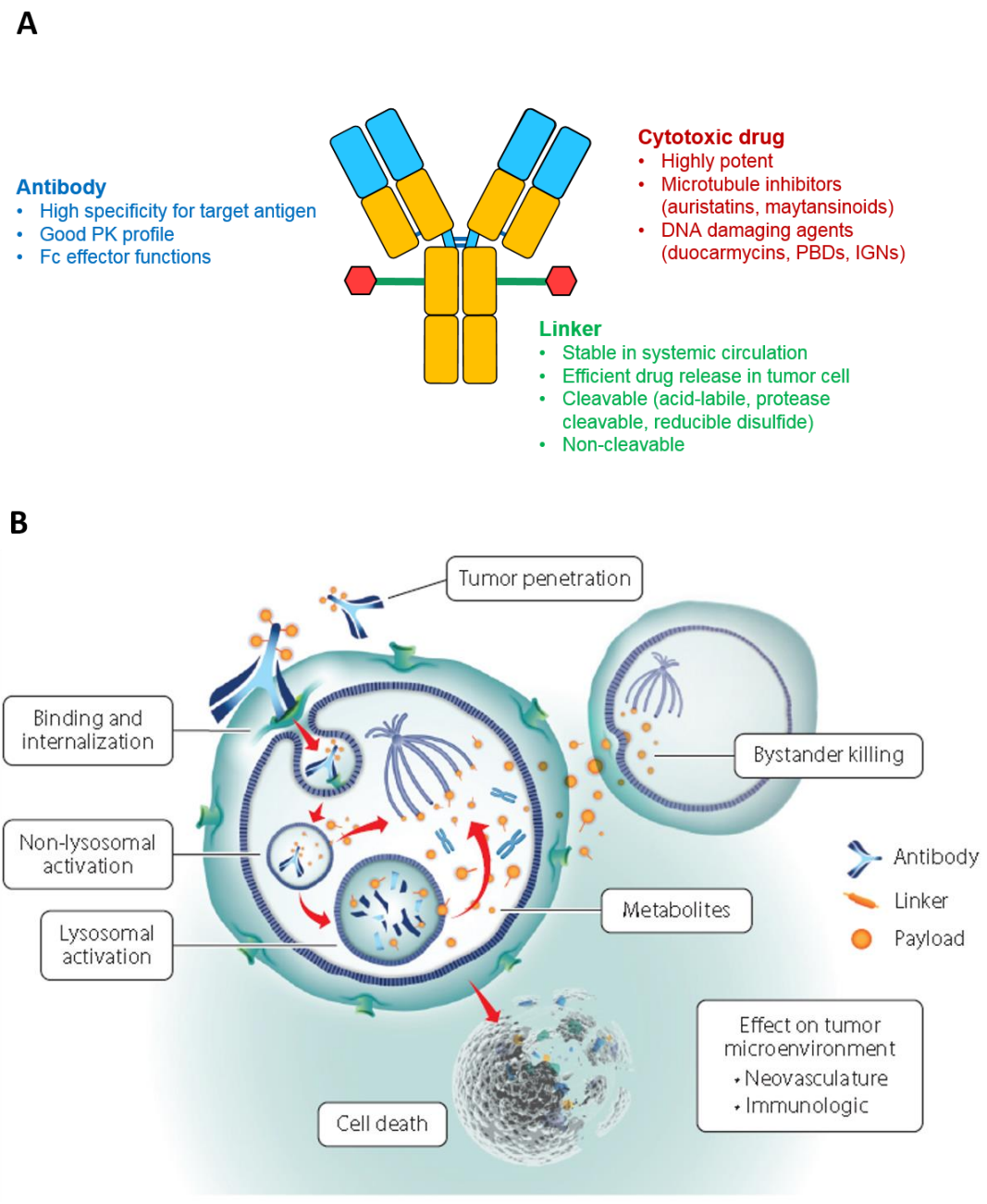

Figure 8: Schematic structure of an ADC and mechanism of action.

Depicted is the structure of an ADC (**A**), with key features represented through the antibody moiety (blue/orange), linker (green) and payload (red). Main characteristics of each component are included, but various alternatives exist. In this scheme, two payloads are conjugated to the mAb. The assumed mechanism of action (**B**) of ADCs on tumor cells is illustrated. After entering the tumor tissue, the ADC binds to its respective tumor antigen on the cell surface and is internalized into tumor cells. After internalization, the ADC is trafficked inside the cell into endosomes and subsequently into lysosomes, where linker cleavage or antibody degradation takes place and cytotoxic drugs are released. Afterwards, payloads can fulfill their cytotoxic activity either by disrupting microtubules or damaging DNA, leading to cell death. In this case, microtubule inhibiting agents and their binding to microtubules is depicted. Depending on payload properties, bystander killing is enabled by diffusion of cell permeable payloads into adjacent cells. Figure is adapted from Lambert and Berkenblit.[109]

Upon binding of the antibody moiety to the target antigen on tumor cell surface, internalization of the whole ADC-antigen complex through receptor-mediated endocytosis is achieved. During intracellular trafficking,

endocytic vesicles fusion leads to formation of early endosomes, subsequently late endosome and eventually lysosomes.[110] Inside lysosomes, linker cleavage or lysosomal degradation of the ADC takes place and the toxic payload is released in the cell, leading to cell death by either microtubule inhibition (e.g. auristatins, maytansinoids) or DNA damage (e.g. duocarmycins, PBDs).[109]

Current approved ADCs as well as more than 60 ADCs in clinical trials, predominantly target hematological malignancies.[104,109,111]

At the beginning of ADC development, first attempts with anti-KS1/4 methotrexate conjugate and anti-KS1/4 vinblastine-based conjugate were tested for NSCLC. In 1993 the anti-Lewis Y BR96-doxorubicin conjugate for breast cancer encountered difficulties and demonstrated only a minor therapeutic benefit. Different factors like poor target selection as well as immunogenic chimeric and murine antibodies, but also the utilization of payloads with lower potency, contributed to clinical failure of such early first-generation ADCs.[112–115] A few decades of optimization and development were necessary, until the current 5 ADCs received market authorization. In 2000 the first ADC, gemtuzumab ozogamicin, was approved by the FDA. Gemtuzumab ozogamicin consists of an IgG4 anti-CD33 mAb that is linked to the DNA damager calicheamicin via randomly lysine conjugated cleavable hydrazone linker.

Table 2: Overview of approved ADCs.

Main features of approved ADCs like antibodies, linkers, payloads as well as target antigens and indications are listed. Table is modified from Hoffmann et al.[111]

ADC	Developer	Indication	Target Antigen	Antibody type/mutations	Linker	Cytotoxin	Year of approval
Gemtuzumab ozogamicin (Mylotarg®)	Pfizer	Acute myeloid leukemia	CD33	Humanized IgG4 κ antibody hP67.6	Acid-lablie hydrazone bifunctional linker	Calicheamicin	FDA approved in 2000, withdrawn 2010, re-approved 2017
Brentuximab vedotin (Adcetris®)	Seattle Genetics	Relapsed Hodgkin lymphoma and systemic ALCL	CD30	Chimeric IgG cAC10	Cathepsin B cleavable ValCit	MMAE DAR 4	FDA approved 2011
Trastuzumab emtansine (Kadcyla®)	Roche	HER2+ metastatic breast cancer	HER2	Humainzed IgG1	Non-cleavable thioether linker	DM1 DAR 3.5	FDA approved in 2013
Inotuzumab ozogamicin (Besponsa®)	Pfizer	NHL, ALL	CD22	Recombinant humanized IgG4	Acid-labile hydrazone	Calicheamicin, CM1	FDA approved in 2017
Polatuzumab vedotin (Polivy®)	Roche	DLBCL	CD79b	Engineered cysteines (THIOMAB)	Cathepsin B cleavable ValCit	MMAE	FDA approved in 2019

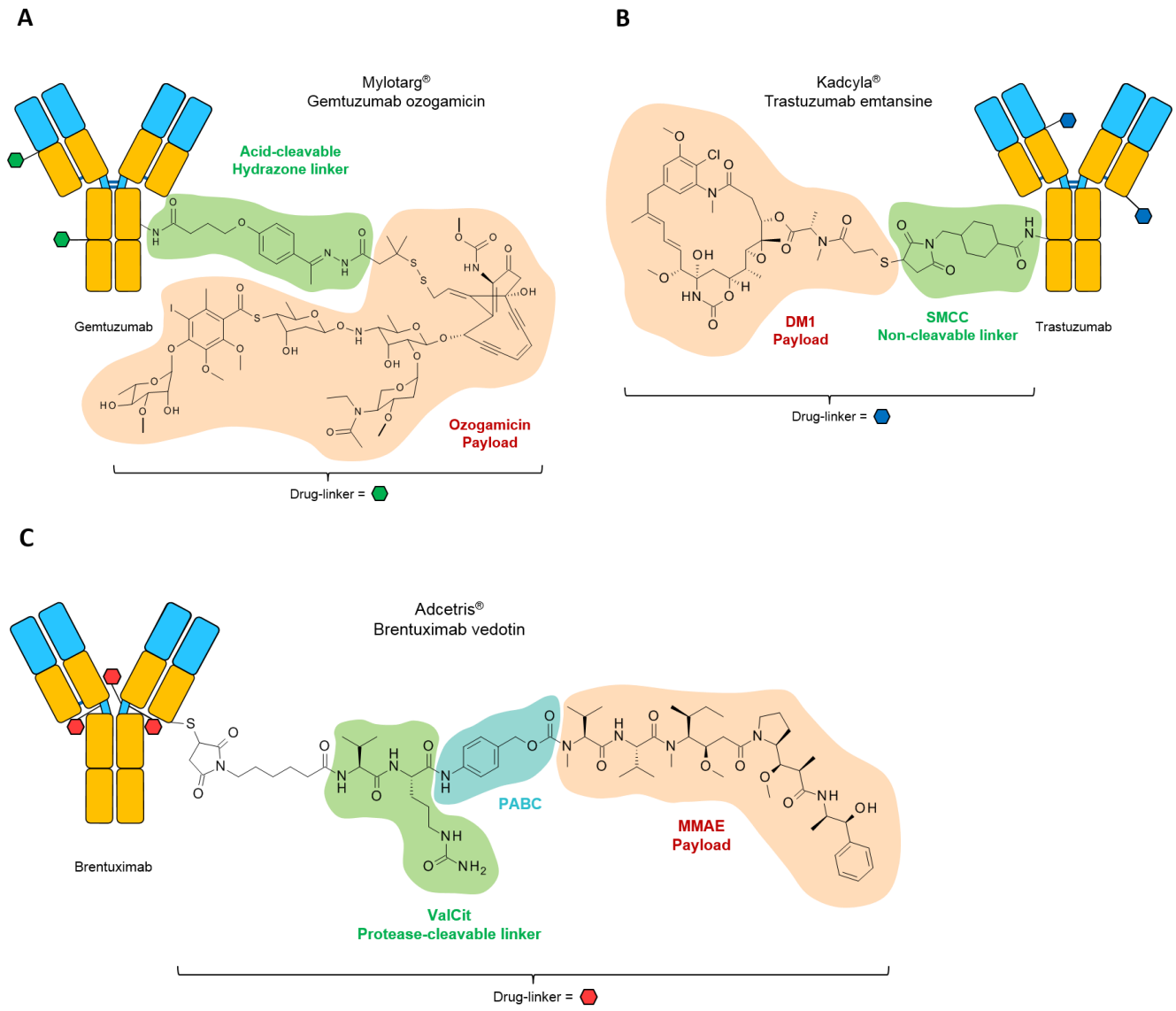

Figure 9: Selected approved first- and second-generation ADCs.

Illustration of approved first-generation ADC gemtuzumab ozogamicin (**A**), and second-generation ADCs Trastuzumab emtansine (**B**) and brentuximab vedotin (**C**). Drug-linker structures and schematic attachments on the antibodies are depicted. Figure is modified from Beck et al.[104]

Gemtuzumab ozogamicin is indicated for the treatment of patients with CD33-positive AML, who are 60 years of age or older and are not considered for further cytotoxic chemotherapy. As already mentioned in chapter 2.1.2, the first-generation ADC gemtuzumab ozogamicin was withdrawn in 2010 and re-approved in 2017. Several reports indicate that gemtuzumab ozogamicin is a heterogeneous mixture of 50% of different drug-to-antibody ratio (DAR) species of conjugated ADC and of approximately 50% unconjugated mAb.[116,117] Moreover, the acid-labile hydrazone linker in gemtuzumab ozogamicin was unstable, releasing 50% of conjugated payload in 48h.[105] In 2011, brentuximab vedotin with the chimeric IgG1 antibody against CD30 established a payload class that is widely used in the ADC field. Brentuximab vedotin utilizes MMAE as a cytotoxic drug that is attached to the cysteines of the hinge region of the mAb via a valine-citrulline protease cleavable linker. Another important approval was achieved with Trastuzumab emtansine (T-DM1) in 2013. T-DM1 consists of the

anti-HER2 mAb Trastuzumab that is conjugated to random lysines via a thioether non-cleavable SMCC linker with DM1. Trastuzumab emtansine is used for the treatment of HER2-positive metastatic breast cancer patients, who previously were treated with Trastuzumab and a taxane (separately or in combination therapy). Besides that, T-DM1 shows tumor growth inhibition against cell lines, that are lapatinib-resistant, which is a TKI of HER2 and EGFR.[118,119]

Furthermore, two other ADCs received FDA approval and an overview of approved ADCs, comprising several data like antibodies, linkers and payloads is given in **Table 2**. Structures of selected approved ADCs are illustrated in **Figure 9**.

Predominantly, two main categories of cytotoxic warheads are optimized and used for ADCs. Compounds that either target DNA (exploiting activity on proliferating and nonproliferating cells) or microtubules (acting on proliferating cells). The majority of payloads used in ADCs which are currently in clinical trials consist of the microtubule inhibitors auristatins and maytansinoids, both originating from natural sources like marine organisms or botanical species.[120]

Auristatins belong to a group of powerful microtubule inhibitors and represent the largest group of ADC payloads used in clinical trials.[121] Auristatins confer their antitumor activity by disrupting microtubules, which are crucial cytoskeletal proteins and play a key role in cell proliferation. The two most common auristatin payloads, MMAE and MMAF, are synthetic analogues of the pentapeptide dolastatin 10 (**Figure 10**) that is extracted from the sea hare *Dolabella auricularia*. Due to the fact, that such derivatives exhibit significant toxicity for systemic application as a single agent, conjugation of such compounds to carrier molecules is inevitable. MMAE and MMAF have been selected among a plethora of potential candidates, because they exhibit advantageous properties like high potency, aqueous solubility and stability under physiological conditions, but also a suitable attachment site for a chemical linker.[122–124]

One major difference between these two auristatins is that MMAF possesses a negatively charged carboxy-terminal phenylalanine group and after lysosomal cleavage the released metabolite is therefore much less cell permeable. By contrast, the uncharged and nonpolar counterpart MMAE is able to cross biomembranes as a neutral molecule, conferring also toxicity to cells in vicinity of tumor cells, irrespective of target expression. This phenomenon is referred to as the bystander effect and is facilitated for hydrophobic, cell permeable cytotoxic metabolites and bystander potency depends on the charge of linker-drug derivatives. MMAE exerts toxicity by bystander activity and is also able to diffuse into target-negative cells. For MMAF, no bystander effect is achieved because of its charged properties. Bystander killing may be preferred in solid tumors, where targets are heterogeneously expressed and eradication of such tumors is less effective when only antigen-positive cells are targeted.[125–128]

The second largest class of ADC payloads are based on the antimitotic agents maytansinoids with the prototype maytansine (**Figure 10**). Maytansinoids belong to a class of natural macrolide antibiotics that were first isolated from the bark of the African shrub *Maytenus ovatus*.[129,130] The most frequently used maytansinoids in ADC development are DM1 and DM4. Just like dolastatins and vinca alkaloids, maytansinoids bind to the same site on tubulin.[120]

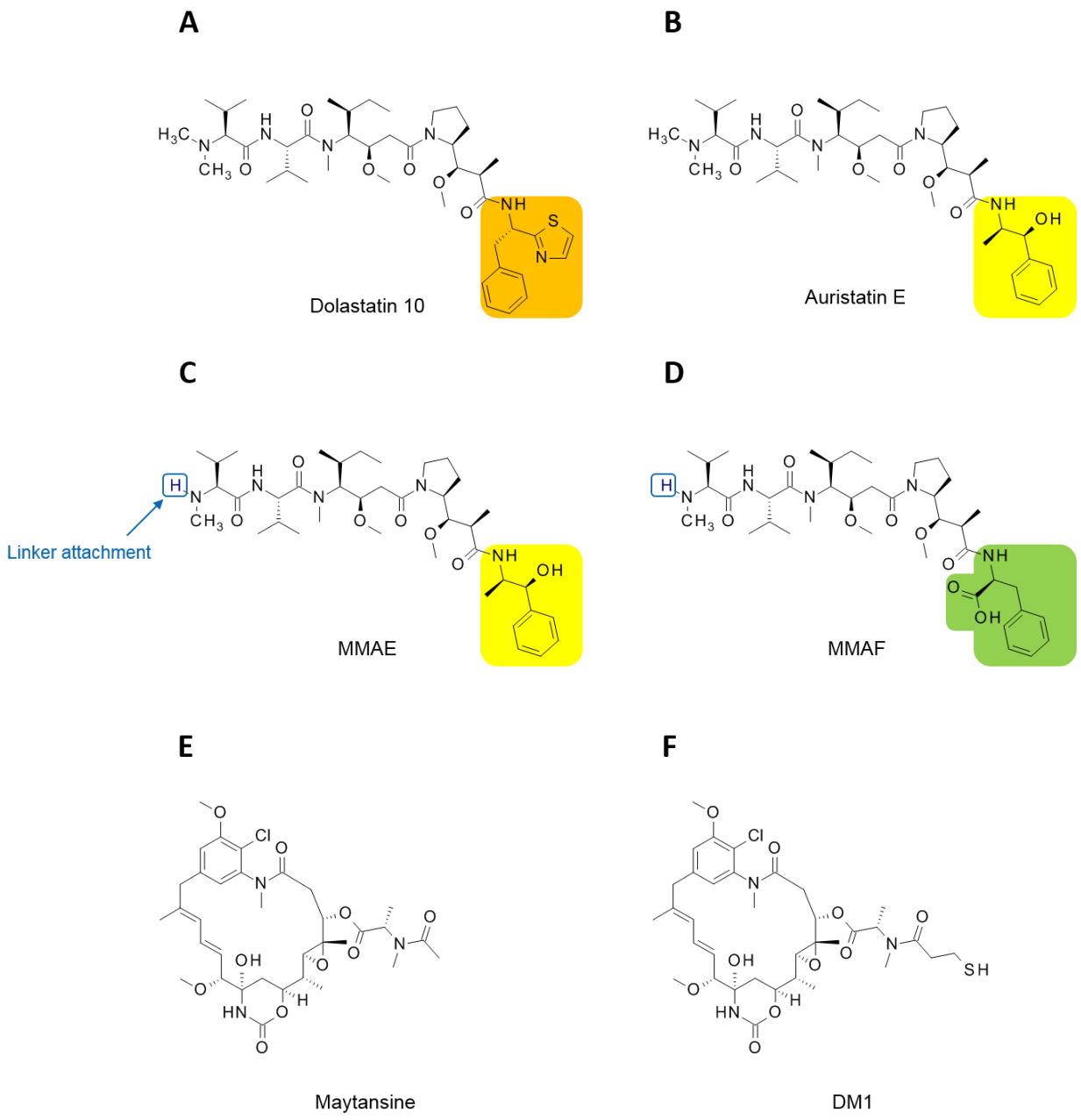

Figure 10: Structures of selected microtubule inhibitors of the auristatin and maytansinoid class.

Illustrated are the chemical structures of auristatin analogues dolastatin 10 (**A**), auristatin E (**B**), MMAE (**C**) and MMAF (**D**). The different C-termini of the auristatines are highlighted with different colors. Dolaphenine (orange), (+)-norephedrine (yellow) and phenylalanine (green). N-terminal linker attachment sites in MMAE and MMAF are indicated by blue boxes. Maytansine (**E**) and DM1 (**F**) are derivatives of the maytansinoids class. All compounds belong to microtubule inhibiting agents. Figure is adapted from Maderna et al.[123,124]

Apart from microtubule inhibitors, several DNA damaging agents are widely used as a class of ADC payloads. Calicheamicin is a DNA minor groove binder and exerts its cytotoxic activity through inducing double-strand breaks, leading subsequent to cell death. Calicheamicin represents a highly potent enediyene antitumor antibiotic that was isolated from actinomycete *Micromonospora echinospora* and despite four monosaccharide units, the hydrophobicity of this compound remains a major challenge for conjugation.[131,132]

Likewise DNA damaging agents and minor groove binders, duocarmycins belong to a drug class of highly potent cytotoxic drugs composed of a DNA-binding and a DNA-alkylating unit (**Figure 11**). DNA-binding is preferential in AT-rich regions and subsequently adenine residues are irreversible alkylated at the N3 position, leading to disruption of nucleic acid architecture and eventually apoptosis. Most of duocarmycins contain a reactive cyclopropyl moiety or a promoiety that is converted into an active form, and has a significant impact on antitumor effects. One of the first discovered duocarmycin derivatives is CC-1065 and was isolated from *Streptomyces sp.* The Trastuzumab duocarmycin (DUBA) based ADC SYD985 developed by Synthon Biopharmaceuticals is conjugated to interchain cysteines via a cleavable valine-citrulline linker. SYD985 is currently in phase III clinical evaluation for the treatment of HER2-positive metastatic breast cancer.[133–135]

Pyrrolobenzodiazepines (PBDs) represent another powerful DNA damaging agents with potencies in the picomolar range. They were developed by Spirogen and are originally derived from the natural product anthramycin, which was isolated from *Streptomyces refuineus*. PBDs bind also in the minor groove of DNA and depending on the PBD unit composition, symmetrical and non-symmetrical PBD dimers (**Figure 11**) can be distinguished. PBDs are able to either cross-link DNA strands by alkylating N2 of guanine through two imine functionalities or with only one PBD monomer, monoalkylating agents can be utilized that also form covalent PBD-DNA adducts. Several studies revealed that PBD dimers generated by the incorporation of an odd-numbered linker length between the PBD monomers show a dramatically increased cytotoxic activity. In contrast, when using an even-numbered linker length, a decreased PBD dimer activity is observed. One advanced PBD dimer-based ADC is rovalpituzumab tesirine (Rova-T) developed by Stemcentrx. Rova-T targets DLL3 and is conjugated via a cathepsin B cleavable valine-alanine linker to hinge cysteines. Rovalpituzumab tesirine is tested in phase III clinical trials against SCLC.[136–138]

To further improve cytotoxicity of PBDs, ImmunoGen developed derivatives termed indolinobenzodiazepine (IGNs), which contain a pseudodimer backbone that exerts slightly stronger cytotoxic activity as original PBDs. The DNA-crosslinking diimine form of IGNs is associated with several off-target toxicities and was therefore converted into an even potent DNA monoalkylating monoimine form which simultaneously attenuates off-target toxicities (**Figure 11**). DGN462 is such an IGN derivative with a single reactive imine group and is used in the ADC IMGN779, which is an anti-CD33 ADC currently in clinical phase I against AML and is designed to balance efficacy and tolerability.[139,140] In addition to microtubule inhibitors and DNA damaging agents, there are several other payloads in ADC development also with different mechanisms of action like the topoisomerase I inhibitors SN38 and exatecan, the RNA polymerase II inhibitor a-amanitin or tubulysins. However, these payloads are less frequently used in ADC generation.[106]

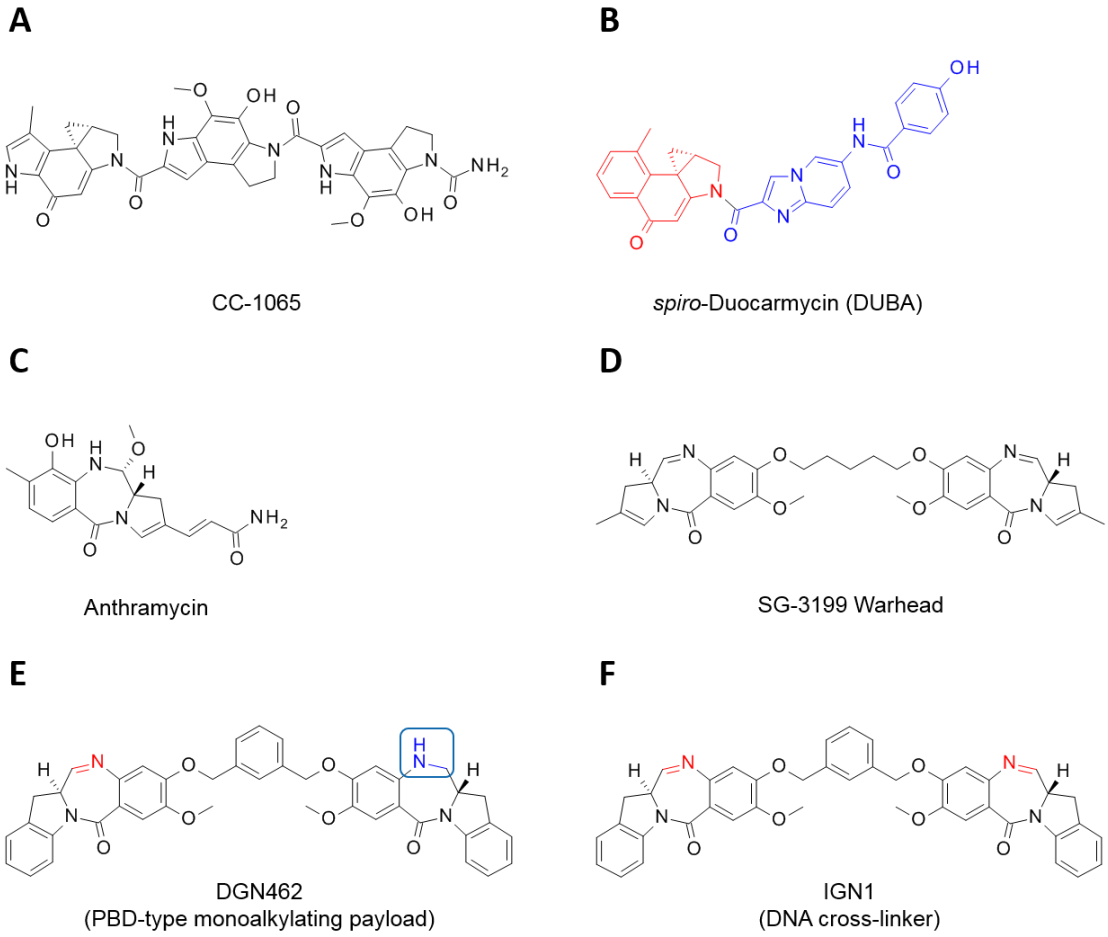

Figure 11: Structures of DNA damaging agents and derivatives used in ADC development.

Structures of selected DNA damaging agents are depicted. CC-1065 (**A**) and DUBA (**B**) belong to the duocarmycin family and DUBA is the payload utilized in SYD985, which is in phase III clinical trials. In the DUBA structure the DNA alkylating unit is highlighted in red and the DNA binding unit in blue. Anthramycin (**C**) and SG-3199 (**D**) are derivatives of the PBD class and the PBD dimer SG-3199 is used in the ADC rovalpituzumab tesirine. DGN462 (**E**) and IGN1 (**F**) belong to the IGN class. DGN462 has a monoalkylating functionality with one single reactive imine group whereas IGN1 represents a DNA cross-linker because of the diimine moiety. Imine functionalities in DGN462 and IGN1 are illustrated in red and amino moiety that only binds to DNA is indicated by a blue box. DGN462 is incorporated as a payload in the ADC IMGN779. Figure is adapted from Elgersma, Mantaj, Miller et al.[134,137,139]

Premature release of the payload often leads to off-target toxicities. Therefore, good stability of the linker is of crucial importance while the ADC is present in the bloodstream. However, also a fast and efficient release inside the tumor cell is necessary. For attachment of the cytotoxic payload to the antibody, two categories of linker technologies can be distinguished: cleavable and non-cleavable linkers.

Cleavable linkers represent a prominent linker type in ADCs and are differentiated in terms of their distinct release mechanism (acid-labile, protease cleavable linker, disulfide linkers). In the case of acid-labile linkers, hydrazone structures are utilized that remain stable at physiological pH 7.4, but are hydrolyzed and release the payload at acidic pH in the lysosomal compartments. The most common linker format used in ADCs, are the protease cleavable linkers that are designed to release the payload upon enzymatic cleavage by lysosomal proteases. Activity and overexpression of specific lysosomal proteases was confirmed and these proteases cleave a unique dipeptide sequence like valine-citrulline or valine-alanine (**Figure 12**). Cathepsin B was identified as a

key enzyme, responsible for such linker cleavage of valine-citrulline motifs with subsequently 1,6-fragmentation across an aryl spacer achieving subsequent drug release. New approaches exploit the presence of ß-glucuronidase that also exists within lysosomes and recognizes and cleaves hydrophilic glucuronide linkers (developed by Seattle Genetics).[141] Besides that, disulfide-linker structures are cleaved upon reduction and make use of the different concentration levels of the thiol-containing tripeptide glutathione, which exhibits intracellularly concentrations in the millimolar range whereas extracellularly micromolar concentrations are present. To increase the stability of disulfide linkers, steric hindrance of the disulfide structure by adjacent methyl groups has been reported. Within the category of cleavable linkers, protease cleavable linker provide higher stability in systemic circulation compared to hydrazone- and disulfide-linked structures.[142–144]

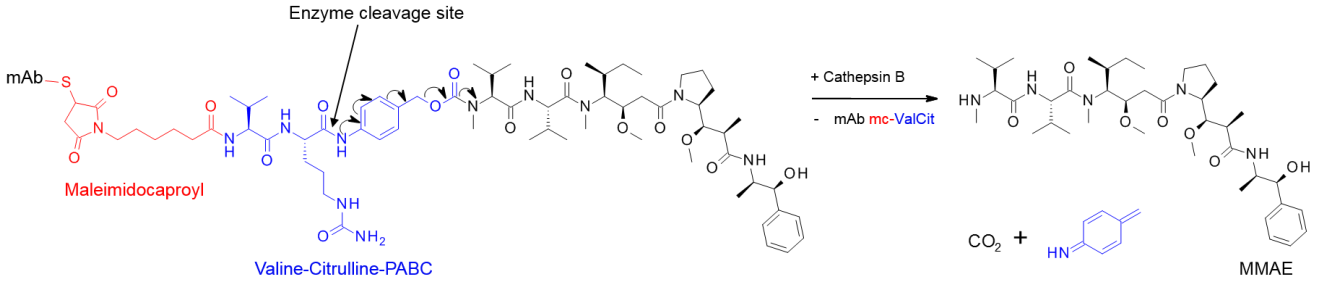

Figure 12: Cathepsin B cleavage of ValCit-based ADC and release of payload.

Schematic cleavage reaction of the ADC brentuximab vedotin by cathepsin B. Lysosomal cathepsin B recognizes and cleaves the ValCit motif between citrulline and PABC. The resulting intermediate is unstable and subsequently undergoes 1,6-fragmentation of the self-immolative PABC spacer that also undergoes decarboxylation leads to iminoquinone and carbon dioxide as byproducts. MMAE as a product is released without any further groups and is able to fulfill its cytotoxic mechanism. Figure is adapted from Burke et al.[141]

The class of non-cleavable linkers provides high stability, but has no specific release mechanism. Within the cell and inside the lysosome, complete proteolytic degradation of the antibody is required and linker-drug with subsequent free drug is released. Unspecific cleavage in acidic lysosomes relies mainly on hydrolysis of acid-labile bonds or cleavage of amide and ester bonds by proteases and esterases.[145] Generally, ADCs bearing non-cleavable linkers often provide a better safety profile, but are less efficacious compared to ADCs containing cleavable linkers.[138]

For construction of ADCs, suitable conjugation methods are necessary that attach the drug-linker to the antibody (**Figure 13**). Traditional conjugation technologies are chemical conjugations based either on lysine amide coupling or cysteine coupling. Generated products differ in the conjugation site as well as in number of linker-drugs per antibody molecule. Lysine coupling is utilized to link the payload to solvent accessible lysine residues on the antibody using linkers with activated groups like NHS ester. Although an IgG1 antibody has approximately 90 lysine residues, generally only 8-10 lysine residues are accessible for conjugation, resulting in a heterogeneous mixture of different DAR species. Such heterogeneity is typically undesired as it has significant impact on the pharmacokinetics, stability, safety and efficacy profile of an ADC.[146,147] Cysteine conjugation generates ADCs with a higher degree of homogeneity and controlled DAR, because fewer potential conjugation sites are available compared to lysine conjugation. IgG1 molecules consist of 4 interchain disulfide bonds and 12 intrachain disulfide bonds. Selective reduction of the accessible interchain disulfides (usually achieved with TCEP) results in up to 8 free reactive thiols whereas the intrachain disulfides remain unaffected. No substantial

structural changes are observed. However, for higher amounts of free thiols a lower thermal stability of the mAb is observed.[148–150]

For cysteine-based conjugation, free cysteine residues on the antibody are connected to a thiol-reactive functional group like maleimides through a Michael addition. The use of maleimide affords a thio-succinimide group, which is known to undergo side reactions like retro-Michael reaction involving the free thiol group (C34) of human serum albumin or gluthathione and thus, potentially leading to premature release of the cytotoxic drug.

Site-specific conjugation technologies have been developed for the generation of homogeneous ADCs and result in a controlled DAR, improving the pharmacological properties of ADCs. Cysteine residues can be genetically engineered (THIOMAB) into specific sites on the antibody heavy or light chain to provide regioselectivity. S239C mutation (developed by Seattle Genetics) or A114C and V205C mutations (developed by Genentech) resulted in homogeneous ADCs without interfering native cysteine functionality.

Additionally, enzyme-assisted ligation is also used for site-specific conjugation of either native or genetically engineered antibodies. Originally derived from *Staphylococcus aureus*, sortase A possesses transpeptidation activity and is utilized for site-specific conjugations yielding homogeneous ADCs with controlled DARs. The biological function of sortase A is related to anchoring proteins like virulence factors to the cell wall of gram-positive bacteria. Sortase A recognizes specifically a LPXTG motif (X = any amino acid) and cleaves the threonine-glycine bond within this pentapeptide, subsequently connecting an oligo-glycine payload. Beerli et al. from NBE Therapeutics introduced the recognition sequence LPETG for sortase A to the C-termini on both the heavy and light chain of an antibody and demonstrated the generation of potent anthracycline-based ADCs.[151,152,153]

An alternative enzymatic conjugation that also catalyzes a site-specific transpeptidation reaction is achieved by transglutaminase. Microbial transglutaminase (mTG) was initially discovered for food industry applications and was isolated from *Streptomyces mobaraensis*. mTG attaches calcium-independently a primary amine substrate (like lysines) to a glutamine (Q295) on the antibody to form an isopeptide bond. It is known that mTG tolerates a broad spectrum of amine substrates. Other natural glutamine residues in the Fc region are not recognized by transglutaminase. The biological function of mammalian transglutaminase relies on its ability to cross-link proteins like factor XIIIa or extracellular matrix proteins. In general, prior to mTG conjugation for ADC generation, deglycosylation of the antibody or mutation of the N297 to alanine are necessary for exposure of native Q295, which lead to successful conjugation yielding a DAR of 2. N297Q mutation results in 4 reaction sites that are addressable, typically leading to a DAR of 4. Furthermore, Pfizer added a LLQG tag into the antibody to the C-terminus of heavy or light chains that is also recognized by an engineered transglutaminase.[154,155]

Besides that, other conjugation technologies that are used in the ADC field comprise the incorporation of unnatural amino acids, click chemistry, enzymatic reaction with formylglycine-generating enzyme (FGE) as well as glyco-engineering with glycosyltransferases.[156]

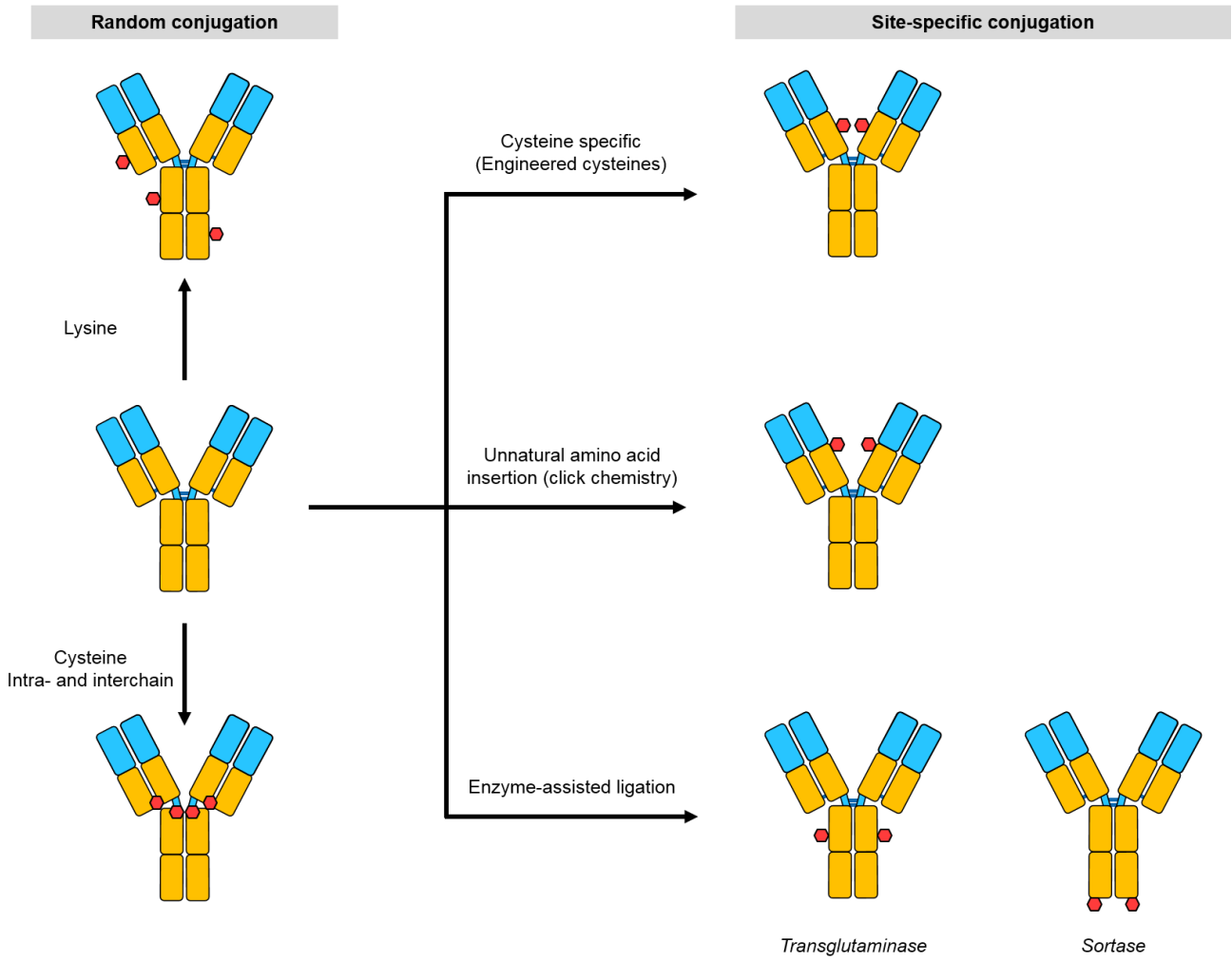

Figure 13: Conjugation technologies for ADC generation.

Illustrated are commonly used ADC conjugation methods like lysine or cysteine conjugation that result in heterogeneous mixtures. Site-specific conjugations can be achieved by engineering cysteine residues into the antibody, inserting unnatural amino acids or using tagged or modified antibodies for enzymatic conjugations with transglutaminase or sortase. Figure is adapted from Perez et al.[106]

Clinical success of ADCs is attributed to rational design of new payloads, improvements of chemical linker properties and site-specific conjugation technologies. Less attention was payed on the antibody moiety as a pharmacodelivery vehicle with alternative formats that may have advantageous properties regarding the biodistribution and tumor penetration of ADCs. Such new approaches need to compromise the beneficial PK profile of antibodies in the IgG format with its impaired solid tumor penetration, and the potentially improved tumor accumulation of smaller fragments, which exhibit by contrast a short half-life.

The following chapter focuses on aspects of tumor penetration and biodistribution of small molecules and large molecules.

2.3. Solid tumor penetration of small molecule and large molecule therapeutics

Despite advances of emerging therapeutics like ADCs, inefficient treatment and poor penetration of solid tumors due to its multi-dimensional complexity remains a formidable challenge for antibody-based therapeutics. In

contrast, hematological malignancies appear to be more accessible to antibodies than solid tumors, because vascularity is directly accessible by intravenous administration. In hematological cancers, besides the lack of requirement for ADCs to penetrate into solid tumor tissue, also low levels of target expression in healthy tissue organs and higher drug exposure in the blood are advantageous.[108] Multiple factors contribute to the uneven distribution of ADCs that are more related to antibody characteristics, antigen properties or features associated to the tumor microenvironment. Paradoxically, delivery of drugs is hampered by tumor physiology and as angiogenesis is achieved within tumors, new formed blood vessels appear to be leakier and disordered than normal blood vessels. This leakiness and heterogeneity of tumor vasculature allows macromolecules to escape easily out of the blood vessels and should be ideal for delivery of large molecules. However, unstructured and hastily formed blood vessels generate a dense extracellular matrix and an elevated interstitial fluid pressure within tumors that opposes convectional flow and limit the diffusion of macromolecules from tumor vasculature to tumors.[157,158,159] Traditionally, tumor targeting focused on the use of full-length IgG antibodies due to high affinity and selectivity to the antigen as well as favorable pharmacokinetic profile. But larger molecules are more restricted to penetrate within the tumor than small molecules, due to dependency on convectional flow.[160] Properties of *in vivo* biodistribution as well as slow penetration rate of conventional full-length antibodies into tissues relative to that of small molecules, limit efficacy of antibody therapy.[161] Taking into account that small molecule agents such as those conjugated to ADCs, distribute extensively in the body but are also rapidly cleared, the molecular size is thought to contribute significantly to tumor penetration. Indeed, antibodies only reach perivascular tumor cells and are mainly located in the plasma and extracellular fluids. Therefore biodistribution properties of small molecules are altered fundamentally when generating an ADC, retaining PK characteristics of the mAb.[162,163] It was reported that only a small amount of presumably 1% or less of administered ADC and antibody reach their final target.[158,164,165]

Inefficient drug delivery due to the limited tumor penetration by the full-length antibody component is a tremendous challenge for an effective and curative treatment of solid tumors. Various tumor targeting agents ranging in size are under development and as tumor accessibility remains a critical issue for ADC delivery, the rise of antibody fragments and even smaller protein scaffolds for ADC construction may potentially be a suitable solution to enhance the efficacy of ADCs by improving the tumor penetration. Owing to the smaller size of Fab fragments and diabodies than IgGs (50 kDa versus 150 kDa), improved extravasation and tumor penetration abilities were demonstrated for smaller antibody fragments with higher diffusion coefficients in several approaches.[166] Dennis and colleagues investigated an albumin-binding Fab fragment (AB.Fab4D5) targeting HER2 and showed that a better tumor penetration and localization was achieved with AB.Fab4D5 than with full-length IgG Trastuzumab. Furthermore, Trastuzumab showed a slow tumor accumulation, slow clearance rate from healthy tissues as well as a heterogeneous tumor distribution resulting in many unreached tumor cell regions. AB.Fab4D5 with its unique properties exhibited low normal tissue exposure and superior tumor to blood ratios compared to the conventional format.[167]

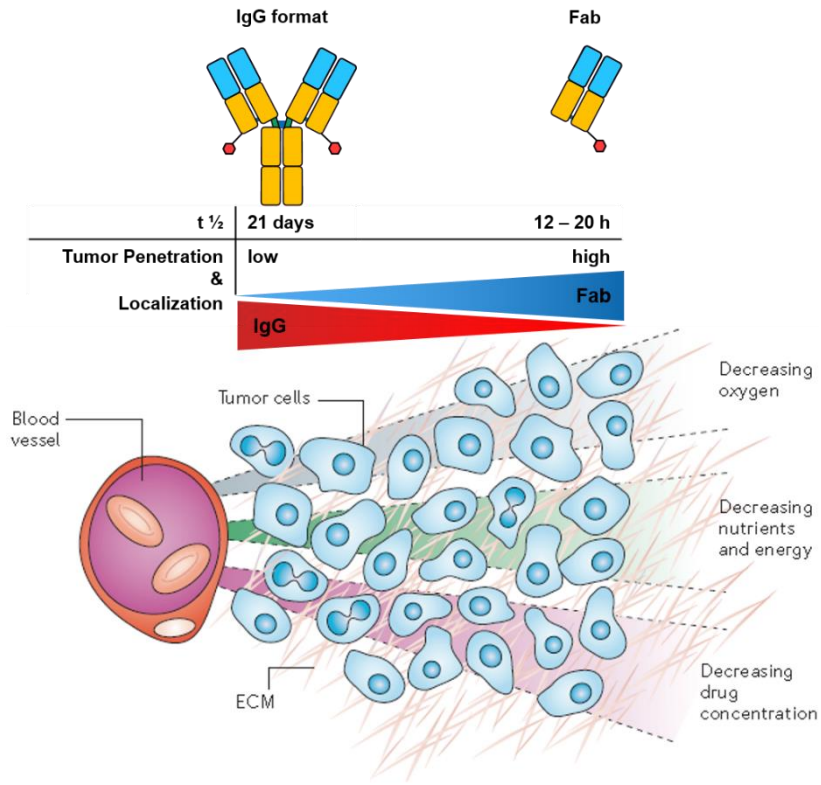

Figure 14: Comparison of tumor penetration of antibody-based therapy.

Illustrated are exemplarily the half-life (t ½) of an ADC in the IgG format and of a Fab fragment. Also the tumor penetration and localization is schematically shown. Tumor penetration for the IgG format (red triangle) is decreased significantly with increasing distance from the blood vessel. For the Fab fragment (blue triangle) the penetration is more evenly within the tumor mass, reaching also distant tumor cells. Gradients in oxygen, nutrients and drug concentration that are present in cells distant from blood vessels are listed. These properties are commonly observed in sold tumors. Figure is modified from Minchinton et al.[159]

Compared to IgG molecules, antibody fragments lack the Fc part that interacts with FcRn, which results in a short half-life and makes frequent administrations necessary. A relationship model between the molecular size of the pharmacodelivery vehicle and tumor uptake was investigated in detail and minimum tumor uptake was predicted for intermediate-sized targeting proteins like monovalent binding scFvs (25 kDa), which also exhibit poor tumor retention. Smaller or larger agents exhibit higher tumor uptake levels and show better tumor accumulation. Molecules that are larger than the kidney filtration cut off undergo sustained circulation in the plasma, leading to an increased probability to extravasate into tumor tissuse. Prediction of high tumor accumulation for IgG antibodies is mainly associated with the slow clearance rate due to FcRn-mediated recycling from lysosomes.[168,169]

Ackerman et al. established a model used for the prediction of the maximum penetration distance R (**Eq. 1**) in solid tumors. A lot of variables in the equation are related to antibody properties like the antibody dose [Ab], void fraction (ε), and diffusivity (D). The remaining variables are antigen properties like antigen expression [Ag] as well as turnover rate (k_e) and are intrinsic regarding penetration limitations. Moreover, the equation indicates that improved tumor penetration can be achieved with higher diffusivity of the targeting agent, higher antibody doses and slower internalization rates. Moreover, the large antibody size reduces tumor penetration due to the low diffusivity and permeability. According Graff et al. values of diffusivity for an IgG molecule and scFv can be assumed to be D = 80 µm²/s (for scFv) and D = 14 µm²/s (for IgG). As the parameter diffusivity D

is a function of antibody size and is inversely proportional to molecular weight, it can be assumed that in a model the scFv distributes about six times faster compared to full-length IgG.[157,161,166]

$$R \approx \sqrt{\frac{D[\mathrm{Ab}]_{\mathrm{surface}}}{k_e([\mathrm{Ag}]_{\mathrm{tumor}}/\varepsilon)}} \qquad \text{Eq. 1}$$

Impressive data in a comparative evaluation of small molecule-drug conjugates (SMDCs) targeting carbonic anhydrase IX (CAIX) confirmed that by using a smaller targeting scaffold a homogenous and complete penetration within solid tumors is achieved, whereas full-length ADC is limited to perivascular tumor cells and fails to localize in deeper structures within the neoplastic mass. Analogous to ADCs, SMDCs utilize a small targeting ligand for the delivery of cyotoxic drugs. So far, small targeting ligands for SMDCs are limited to a very few targets comprising folate receptor, prostate-specific membrane antigen, somatostatin receptors and CAIX. Unfavorable tumor/blood distribution ratios were obtained for radiolabeled preparations of the anti-CAIX antibody after 48 h with tumor uptake of 4 % ID/g, whereas SMDC derivatives exhibited exceptional tumor/blood distribution ratios of 100:1 with 40 % ID/g tumor uptake after 6 h, indicating preferential delivery of the SMDC.[170–173]

Moreover, small format-drug conjugates with higher diffusion rates are under investigation for improved tumor penetration, particularly for solid tumors, where ADCs were not beneficial. For example, BT1718 with a conjugate size of just 2 kDa, is a so called bicycle-drug conjugate employing DM1 and targets MMP-14 that is currently in phase I. Also PEN-221 uses DM1 and is directed against the somatostatin receptor. PEN-221 has a molecular weight of 5 kDa and is in phase II clinical evaluation.

Regardless of size, the degree of solid tumor penetration and accumulation is particularly affected by antibody binding affinity, especially in larger tumors. Many studies showed that high affinity antibody-based molecules (fast on-rate/slow off-rate) represent an obstacle for tumor accumulation and distribution within the entire solid tumor mass, hence they localize predominantly in perivascular regions of the tumor and would limit therapeutic efficacy in clinical studies. Rudnick and colleagues tested different affinity variants and demonstrated with radiolabeled high affinity antibodies that only the first encountered tumor antigens are addressed, before further penetration occurs. A stronger binding of antibody and its antigen results in a reduced tumor penetration due to a lower amount of free, diffusible antibody that is avaible for tumor penetration. These observations indicate that increasing antibody affinity leads to a low tumor accumulation, which is not beneficial, while decreasing binding affinity increases localization and achieves a more uniform distribution in tumor tissues.[99,174,175,176] This phenomenon is known as the "binding site barrier" and suggest that three main factors are responsible for creating this barrier, namely (A) greater antigen density, (B) higher antibody affinity, and (C) faster antibody internalization and metabolism.[167]

Ackerman et al. investigated anti-CEA antibodies with different internalization rates and showed that a slower internalizing antibody penetrated much deeper into tumor spheroids whereas the rapid internalizing antibody was not able to reach distant regions in the tumor spheroid. Furthermore, low antigen density is associated with a greater extent of tumor penetration, but is in contradiction to choose high target expression on tumor cells

for drug discovery and development. Hence, selection of target antigens with a slow internalization rate and low expression level might be beneficial for homogeneous and improved tumor penetration, although both represent intrinsic properties. Concerning ADC mechanism and efficacy, slow internalization rates are inappropriate, because payload delivery depends on efficient and often fast internalization.[157]

To overcome impaired tumor penetration due to the binding site barrier, administered dose of the antibody can be simply increased. With increasing amount of available antibody, more antibodies are able to extravasate, binding the proximal antigens, whereas additional unbound antibodies can reach tumor cells distant (> 100 µm) from blood vessels leading to improved tumor penetration.[159] But increasing the administered dose is not suitable for all therapeutic modalities, particularly for ADCs, because the toxin associated with the antibody drastically decreases the MTD and an increased number of toxic effects is expected.[177,178] Many ADCs are dosed at MTD and frequent dose-limiting toxicities to the bone marrow and other healthy tissues limit the administered dose. Furthermore, some reports showed that coadministration of unconjugated antibody with ADC saturates immediate antigen binding sites, allowing deeper tumor penetration of the ADC from vasculature.[179,180]

As the size of the targeting scaffold is of major importance for the tumor biodistribution and penetration, the following chapter discusses proteases that are overexpressed in the tumor microenvironment and are able to cleave off fragments from modified, full-length antibodies.

2.4. Tumor-associated proteases: uPA and Matriptase

The tumor microenvironment (TME) is composed of the cellular and biochemical composition of different populations of cancer cells as well as non-cancer cells, soluble proteins, blood vessels and an extracellular matrix that also represents a physical barrier for cell movement. Inflammatory cells and cancer-associated fibrolasts secrete a variety of proteins and proinvasive matrix-degrading enzymes like MMPs, cathepsins and serine proteases that facilitate cell migration by extracellular matrix proteolysis.[181,182] Additionally, several other cancer-associated enzymes are known like the serine proteases elastase, cathepsin G but also gelatinases, collagenases and matrilysins, belonging to MMPs.[183]

One well known extracellular tumor protease, the serine protease urokinase-type plasminogen activator (uPA), is overexpressed in several types of cancer and is a central component within a larger network.[183] The uPA system consists of uPA, its corresponding cell surface receptor uPAR and two endogenous inhibitors plasminogen activator inhibitor 1 (PAI-1) and 2 (PAI-2) that negatively regulate uPA activity. uPA has 411 amino acid residues and represents a 53 kDa multidomain glycoprotein with a glycosylation at N302. uPA is produced as an inactive protein known as pro-uPA (or single-chain uPA) and is released in the extracellular environment, where it is activated through a proteolytic event by other proteases. Plasmin, cathepsin B and L, kallikrein, trypsin and also matriptase are able to cleave pro-uPA into the active two-chain uPA form. The structural arrangement of uPA is composed of three functional regions. These regions are a carboxyl-terminal serine protease domain, a kringle domain and an amino-terminal fragment (ATF) containing an EGF-like domain that is responsible for binding to uPAR. The catalytic triade is composed of His57, Asp102 and Ser195 (**Figure 15**).[184]

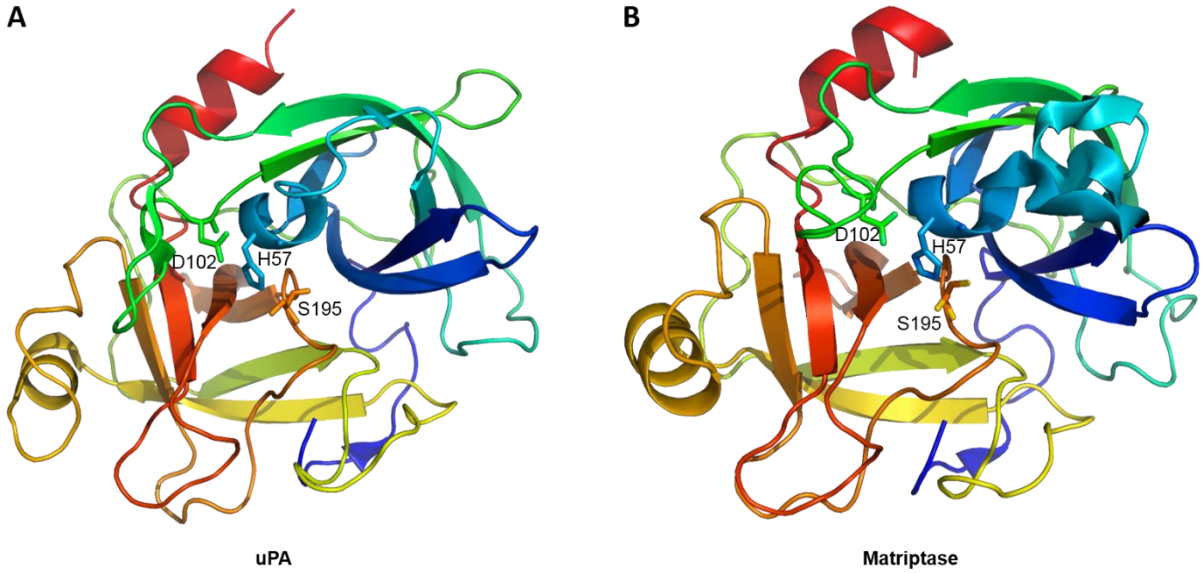

Figure 15: uPA and matriptase structures.

Cartoon ribbon representation of uPA (**A**) and matriptase (**B**) structures, colored according to the spectrum from N-terminus (dark blue) to C-terminus (red). In both serine proteases the catalytic triade (sticks) comprising His57, Asp102, Ser195 are highlighted (generated by PyMOL ver 0.99, PDB: 1W12 and 1EAX).

The main substrate of activated uPA is the inactive zymogen plasminogen, where uPA converts the proenzyme into its active form plasmin. Plasmin has a central role in the degradation and clearance of fibrin blood clots as well as other extracellular matrix constituents and is inhibited by a_2-antiplasmin. Many studies indicated that the involvement of the uPA system has pleiotropic effects in pathophysiological processes like remodelling of extracellular matrix in the context of clot lysis, wound healing, tissue regeneration, angiogenesis, tumor cell proliferation and metastasis.[185,186] Furthermore, uPA is used as an independent prognostic factor for breast cancer and overexpression of one component of the uPA system is associated with poor prognosis. Tissue-tpye plasminogen activator (tPA) plays a key role in the blood clotting cascade and is a homologous enzyme to uPA.[187,188] uPA (Rheothromb®) is used in clinical settings as an anti-fibrinolytic agent in the context of thrombosis, e.g. myocardial infarction or pulmonary embolism.[189]

Another important tumor protease is the type II transmembrane serine protease matriptase (MT-SP1), which is also upregulated in multiple malignant diseases (breast cancer, lung cancer, prostate cancer and colorectal cancer).[190] Main functions of matriptase are associated with extracellular matrix re-modelling as well as tumor growth and metastasis. A fundamental role of matriptase relies on activation of numerous pro-oncogenic and pro-metastatic factors such as pro-uPA, pro-HGF, protease-activated receptor 2 (PAR-2), and various reports indicate that matriptase co-localizes with pro-uPA (**Figure 16**).[191,192,193] The structural composition of the 95 kDa matriptase features a carboxy-terminal extracellular trypsin-like S1 pocket, a small hydrophobic S2 subsite and a negatively charged S4 region, responsible for binding of basic residues. Mature matriptase is a zymogen and proteolytic cleavage is necessary to fulfill its biological function that is generally achieved by auto-activation.[190] The active site of matriptase (**Figure 15**) is also composed of a catalytic triade with His57, Asp102, Ser195 and the arrangement is exactly as in trypsin and chymotrypsin.[194] But substrate specificity of matriptase

differs substantially from that of trypsin, as matriptase cleaves not randomly basic substrates with arginine and lysine residues. The requirement of further surrounding amino acids in close proximity to the cleavage site, enables matriptase to be a very specific protease.[195] The physiological inhibitor of matriptase is hepatocyte growth factor activator inhibitor 1 (HAI-1) and regulates matriptase activity. A strong correlation between matriptase inhibition and reduced tumor growth was investigated with several agents like the potent protease inhibitor ecotin as well as the small molecule inhibitor CVS-3983 and showed a significant reduction in tumor size.[190,196]

As uPA and matriptase are known to be overexpressed in a variety of cancers, extracellular cleavage of specific sequences that are sensitive to these tumor proteases were investigated for different purposes.[197] In an excellent approach, Desnoyers et al. demonstrated the *in vivo* tumor-specific activation of an anti-EGFR probody that is cleaved locally in the tumor microenvironment and binds to the antigen, whereas in systemic circulation the probody remains inactive. Therefore, this probody approach aimed to reduce target-mediated toxicity commonly observed for cetuximab-based therapy due to high levels of EGFR in healthy skin. In their study reduced cutaneous toxicity was observed, leading to an improved safety profile. The probody design was based on an IgG1 sequence with an amino-terminal extension at the light chain containing a masking peptide and a cleavable linker sequence. Based on the sensitivity to tumor proteases, the cleavable substrate motif comprised the 8 amino acids LSGRSDNH.[198]

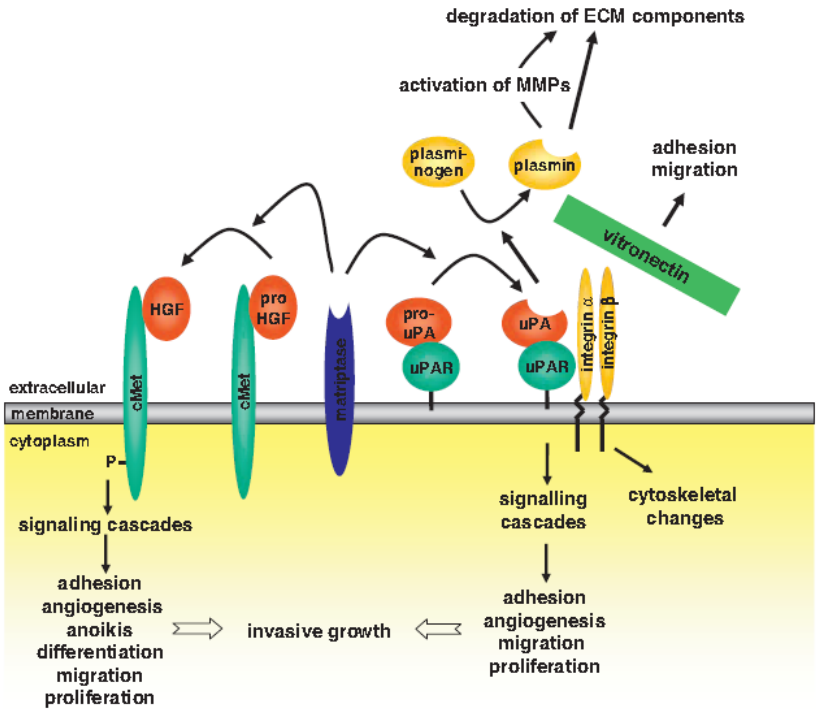

Figure 16: Activity of matriptase on several factors.

Illustration shows activation of pro-oncogenic and pro-metastatic components like pro-uPA and pro-HGF by matriptase. Different signaling pathways promote tumor growth and metastasis. Figure is adapted from Uhland.[190]

2.5. Aim of the study

ADCs emerged as novel therapeutics with clinical success mainly for the treatment of hematological malignancies, but still considerable challenges exist against solid tumors. Impaired tumor penetration and distribution by large therapeutic molecules are a common observation in solid tumors and to overcome this issue, antibody fragments are used to corroborate a potential benefit for the preferential delivery of anticancer drugs. The aim of this work is to evaluate the improved tumor penetration ability and ADC efficacy of smaller-drug conjugates that are generated locally by extracellular proteases in the tumor microenvironment while retaining the long half-life of the IgG format in systemic circulation by a novel ADC design (**Figure 17**). The full-length IgG-ADC is able to bind to FcRn, resulting in a prolonged half-life. For this purpose, a tumor protease cleavage site is genetically engineered into the hinge region of an IgG-ADC, resulting in the release of two 50 kDa Fab-drug conjugates upon proteolytic cleavage. The smaller size of the Fab-drug conjugates accomplish an add-on effect to achieve a better localization and penetration within the tumor. As a model construct, Trastuzumab and Cetuximab are tested and overexpression of tumor proteases in several tumor cell lines was confirmed. For assessment of efficient and selective cleavage as well as accessibility within the hinge region, a cleavable construct containing the specific protease site as well as control constructs were generated and investigated for different characteristics like antigen and cellular binding, stability, enzyme kinetics, potency and *in vitro* spheroid penetration. Efficacy was tested with toxin-based molecules in several cell lines that overexpress HER2 and EGFR and for spheroid penetration studies antibody-fluorophore conjugates were generated. As the size of the ADC delivery vehicle is of major importance for efficient drug delivery, the investigations of this novel ADC design might showcase a potential benefit for the balance between optimum tumor penetration by the released fragments and the maintained pharmacokinetic properties of the IgG format. The more efficient tumor killing by such novel ADC design could lead to higher ADC success rates to improve patient lifes.

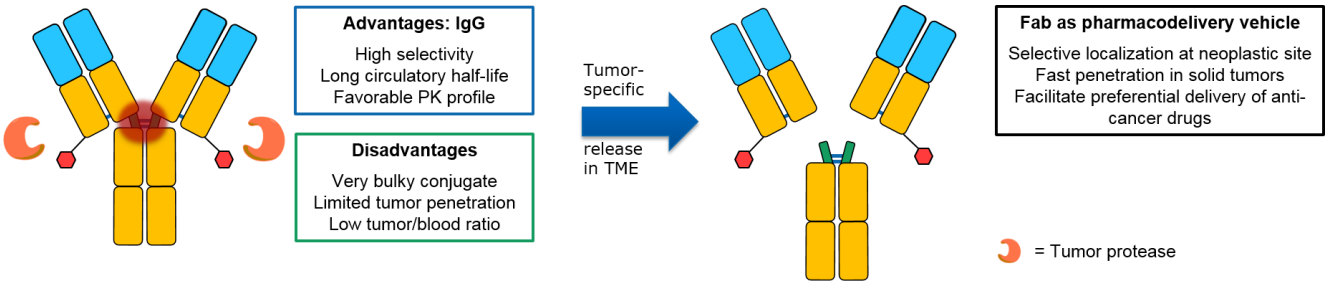

Figure 17: Strategy for improving tumor penetration by released smaller-drug conjugates while retaining safety and half-life.

ADC design with protease site in hinge region (highlighted in red) that is recognized and cleaved by tumor proteases uPA and matriptase. In systemic circulation the listed advantages of the IgG format are dominating wheres disadvantages in solid tumors of the IgG format at the tumor site are mitigated by the benefit from Fab fragments as a vehicle.

3. Material

3.1. Human cell lines and bacterial strains

Mammalian cell lines

Cultivation of mammalian cell lines was performed at 37°C, 5% CO_2. Cancer cell lines were purchased from the American Type Culture Collection (ATCC®, Manassas, VA, USA) or companies as listed below.

Table 3: List of mammalian cell lines used in this work.

Cell type and cell origin are listed for each cell line.

Cell line	Cell type	Origin
A-431	human epidermoid carcinoma	ATCC® CRL-1555™
BT-474	human ductal carcinoma (mammary gland)	ATCC® HTB-20™
CHO-S	Chinese hamster ovary	Life Technologies, Darmstadt, Germany (R80007)
Expi293F™	human embryonic kidney	Life Technologies, Darmstadt, Germany (A14527)
HCC1954	human ductal carcinoma (mammary gland)	ATCC® CRL-2338™
MCF-7	human breast adenocarcinoma (mammary gland)	ATCC® HTB-22™
MDA-MB-361	human breast adenocarcinoma (mammary gland)	ATCC® HTB-27™
MDA-MB-453	human breast metastatic carcinoma (mammary gland)	ATCC® HTB-131™
MDA-MB-468	human breast adenocarcinoma (mammary gland)	ATCC® HTB 132™
NHEK.f-c.	normal human primary keratinocytes	PromoCell, Heidelberg, Germany
NCI-N87	human gastric carcinoma	ATCC® CRL-5822™
SK-OV-3	human ovary adenocarcinoma	ATCC® HTB-77™
SK-BR-3	human breast adenocarcinoma (mammary gland)	ATCC® HTB-30™

Bacterial strains

One Shot™ TOP10 Chemically Competent *E. coli* (#C4040-10, Life Technologies, Karlsruhe, Germany); Genotype: F- *mcr*A Δ (*mrr-hsd*RMS-*mcr*BC) φ80*lac*ZΔ M15 Δ *lac*X74 *rec*A1 *ara*D139 Δ(*ara-leu*) 7697 *gal*U *gal*K *rps*L (StrR) *end*A1 *nup*G

3.2. Antibody sequences

Amino acid sequences (primary structure) of used anti-HER2 antibodies or antibody fragments based on commercial Herceptin (Trastuzumab), where genetic modifications are highlighted with bold font. In general, antibody light chains carry always a sortase recognition tag for conjugation and are not listed each time. DNA sequences of light chain and heavy chain were codon-optimized for mammalian expression and procured from GeneArt (Life Technologies).

Trastuzumab CL (cleavable), LC Srt Tag

Heavy chain with cleavable linker in hinge region:

EVQLVESGGGLVQPGGSLRLSCAASGFNIKDTYIHWVRQAPGKGLEWVARIYPTNGYTRYADSVKG
RFTISADTSKNTAYLQMNSLRAEDTAVYYCSRWGGDGFYAMDYWGQGTLVTVSSASTKGPSVFPL
APSSKSTSGGTAALGCLVKDYFPEPVTVSWNSGALTSGVHTFPAVLQSSGLYSLSSVVTVPSSSLGTQ
TYICNVNHKPSNTKVDKKVEPPKSCDKTHT**LSGRSDNH**CPPCPAPELLGGPSVFLFPPKPKDTLMISR
TPEVTCVVVDVSHEDPEVKFNWYVDGVEVHNAKTKPREEQYNSTYRVVSVLTVLHQDWLNGKEY
KCKVSNKALPAPIEKTISKAKGQPREPQVYTLPPSRDELTKNQVSLTCLVKGFYPSDIAVEWESNGQP
ENNYKTTPPVLDSDGSFFLYSKLTVDKSRWQQGNVFSCSVMHEALHNHYTQKSLSLSPGK

Light chain with sortase recognition motif:

DIQMTQSPSSLSASVGDRVTITCRASQDVNTAVAWYQQKPGKAPKLLIYSASFLYSGVPSRFSGSRSG
TDFTLTISSLQPEDFATYYCQQHYTTPPTFGQGTKVEIKRTVAAPSVFIFPPSDEQLKSGTASVVCLL
NNFYPREAKVQWKVDNALQSGNSQESVTEQDSKDSTYSLSSTLTLSKADYEKHKVYACEVTHQGLSS
PVTKSFNRGEC**GGGGSGGGGSGGGGSLPETGS**

Trastuzumab nCL (noncleavable), LC Srt Tag

Heavy chain with noncleavable linker in hinge region:

EVQLVESGGGLVQPGGSLRLSCAASGFNIKDTYIHWVRQAPGKGLEWVARIYPTNGYTRYADSVKG
RFTISADTSKNTAYLQMNSLRAEDTAVYYCSRWGGDGFYAMDYWGQGTLVTVSSASTKGPSVFPL
APSSKSTSGGTAALGCLVKDYFPEPVTVSWNSGALTSGVHTFPAVLQSSGLYSLSSVVTVPSSSLGTQ
TYICNVNHKPSNTKVDKKVEPPKSCDKTHT**GGSGGSGG**CPPCPAPELLGGPSVFLFPPKPKDTLMIS
RTPEVTCVVVDVSHEDPEVKFNWYVDGVEVHNAKTKPREEQYNSTYRVVSVLTVLHQDWLNGKE
YKCKVSNKALPAPIEKTISKAKGQPREPQVYTLPPSRDELTKNQVSLTCLVKGFYPSDIAVEWESNGQ
PENNYKTTPPVLDSDGSFFLYSKLTVDKSRWQQGNVFSCSVMHEALHNHYTQKSLSLSPGK

Trastuzumab natural, LC Srt Tag

Heavy chain:

EVQLVESGGGLVQPGGSLRLSCAASGFNIKDTYIHWVRQAPGKGLEWVARIYPTNGYTRYADSVKG
RFTISADTSKNTAYLQMNSLRAEDTAVYYCSRWGGDGFYAMDYWGQGTLVTVSSASTKGPSVFPL
APSSKSTSGGTAALGCLVKDYFPEPVTVSWNSGALTSGVHTFPAVLQSSGLYSLSSVVTVPSSSLGTQ
TYICNVNHKPSNTKVDKKVEPPKSCDKTHTCPPCPAPELLGGPSVFLFPPKPKDTLMISRTPEVTCVV
VDVSHEDPEVKFNWYVDGVEVHNAKTKPREEQYNSTYRVVSVLTVLHQDWLNGKEYKCKVSNKAL
PAPIEKTISKAKGQPREPQVYTLPPSRDELTKNQVSLTCLVKGFYPSDIAVEWESNGQPENNYKTTPP
VLDSDGSFFLYSKLTVDKSRWQQGNVFSCSVMHEALHNHYTQKSLSLSPGK

Trastuzumab Fab His, LC Srt Tag

Heavy chain with hexahistidine tag:

EVQLVESGGGLVQPGGSLRLSCAASGFNIKDTYIHWVRQAPGKGLEWVARIYPTNGYTRYADSVKG
RFTISADTSKNTAYLQMNSLRAEDTAVYYCSRWGGDGFYAMDYWGQGTLVTVSSASTKGPSVFPL
APSSKSTSGGTAALGCLVKDYFPEPVTVSWNSGALTSGVHTFPAVLQSSGLYSLSSVVTVPSSSLGTQ
TYICNVNHKPSNTKVDKKVEPPKSCDKTHT**GGGGSHHHHHH**

Trastuzumab oa SEED AG HC His, LC Srt Tag

Heavy chain SEED AG with hexahistidine tag:

EVQLVESGGGLVQPGGSLRLSCAASGFNIKDTYIHWVRQAPGKGLEWVARIYPTNGYTRYADSVKG
RFTISADTSKNTAYLQMNSLRAEDTAVYYCSRWGGDGFYAMDYWGQGTLVTVSSASTKGPSVFPL
APSSKSTSGGTAALGCLVKDYFPEPVTVSWNSGALTSGVHTFPAVLQSSGLYSLSSVVTVPSSSLGTQ
TYICNVNHKPSNTKVDKRVEPKSCDKTHTCPPCPAPELLGGPSVFLFPPKPKDTLMISRTPEVTCVVV
DVSHEDPEVKFNWYVDGVEVHNAKTKPREEQYNSTYRVVSVLTVLHQDWLNGKEYKCKVSNKALP
APIEKTISKAKGQPFRPEVHLLPPSREEMTKNQVSLTCLARGFYPKDIAVEWESNGQPENNYKTTPS
RQEPSQGTTTFAVTSKLTVDKSRWQQGNVFSCSVMHEALHNHYTQKTISLSPGK**HHHHHH**

Heavy chain SEED GA:

MKLPVRLLVLMFWIPASLSEPKSSDKTHTCPPCPAPELLGGPSVFLFPPKPKDTLMISRTPEVTCVVV
DVSHEDPEVKFNWYVDGVEVHNAKTKPREEQYNSTYRVVSVLTVLHQDWLNGKEYKCKVSNKALP
APIEKTISKAKGQPREPQVYTLPPPSEELALNELVTLTCLVKGFYPSDIAVEWLQGSQELPREKYLTW
APVLDSDGSFFLYSILRVAAEDWKKGDTFSCSVMHEALHNHYTQKSLDRSPGK

Trastuzumab natural, HC and LC Srt Tag

Heavy chain with sortase recognition motif:

EVQLVESGGGLVQPGGSLRLSCAASGFNIKDTYIHWVRQAPGKGLEWVARIYPTNGYTRYADSVKG
RFTISADTSKNTAYLQMNSLRAEDTAVYYCSRWGGDGFYAMDYWGQGTLVTVSSASTKGPSVFPL
APSSKSTSGGTAALGCLVKDYFPEPVTVSWNSGALTSGVHTFPAVLQSSGLYSLSSVVTVPSSSLGTQ
TYICNVNHKPSNTKVDKKVEPPKSCDKTHTCPPCPAPELLGGPSVFLFPPKPKDTLMISRTPEVTCVV
VDVSHEDPEVKFNWYVDGVEVHNAKTKPREEQYNSTYRVVSVLTVLHQDWLNGKEYKCKVSNKAL
PAPIEKTISKAKGQPREPQVYTLPPSRDELTKNQVSLTCLVKGFYPSDIAVEWESNGQPENNYKTTPP
VLDSDGSFFLYSKLTVDKSRWQQGNVFSCSVMHEALHNHYTQKSLSLSPG**LPETGS**

Trastuzumab CL, LC Srt Tag, HC N297A

Heavy chain with cleavable linker in hinge region and N297A mutation:

EVQLVESGGGLVQPGGSLRLSCAASGFNIKDTYIHWVRQAPGKGLEWVARIYPTNGYTRYADSVKG
RFTISADTSKNTAYLQMNSLRAEDTAVYYCSRWGGDGFYAMDYWGQGTLVTVSSASTKGPSVFPL
APSSKSTSGGTAALGCLVKDYFPEPVTVSWNSGALTSGVHTFPAVLQSSGLYSLSSVVTVPSSSLGTQ
TYICNVNHKPSNTKVDKKVEPPKSCDKTHT**LSGRSDNH**CPPCPAPELLGGPSVFLFPPKPKDTLMISR
TPEVTCVVVDVSHEDPEVKFNWYVDGVEVHNAKTKPREEQY**A**STYRVVSVLTVLHQDWLNGKEY
KCKVSNKALPAPIEKTISKAKGQPREPQVYTLPPSRDELTKNQVSLTCLVKGFYPSDIAVEWESNGQP
ENNYKTTPPVLDSDGSFFLYSKLTVDKSRWQQGNVFSCSVMHEALHNHYTQKSLSLSPGK

Trastuzumab nCL, LC Srt Tag, HC N297A

Heavy chain with noncleavable linker in hinge region and N297A mutation:

EVQLVESGGGLVQPGGSLRLSCAASGFNIKDTYIHWVRQAPGKGLEWVARIYPTNGYTRYADSVKG
RFTISADTSKNTAYLQMNSLRAEDTAVYYCSRWGGDGFYAMDYWGQGTLVTVSSASTKGPSVFPL
APSSKSTSGGTAALGCLVKDYFPEPVTVSWNSGALTSGVHTFPAVLQSSGLYSLSSVVTVPSSSLGTQ
TYICNVNHKPSNTKVDKKVEPPKSCDKTHT**GGSGGSGG**CPPCPAPELLGGPSVFLFPPKPKDTLMIS
RTPEVTCVVVDVSHEDPEVKFNWYVDGVEVHNAKTKPREEQY**A**STYRVVSVLTVLHQDWLNGKE
YKCKVSNKALPAPIEKTISKAKGQPREPQVYTLPPSRDELTKNQVSLTCLVKGFYPSDIAVEWESNGQ
PENNYKTTPPVLDSDGSFFLYSKLTVDKSRWQQGNVFSCSVMHEALHNHYTQKSLSLSPGK

Trastuzumab natural, LC Srt Tag, HC N297A

Heavy chain with N297A mutation:

EVQLVESGGGLVQPGGSLRLSCAASGFNIKDTYIHWVRQAPGKGLEWVARIYPTNGYTRYADSVKG
RFTISADTSKNTAYLQMNSLRAEDTAVYYCSRWGGDGFYAMDYWGQGTLVTVSSASTKGPSVFPL
APSSKSTSGGTAALGCLVKDYFPEPVTVSWNSGALTSGVHTFPAVLQSSGLYSLSSVVTVPSSSLGTQ
TYICNVNHKPSNTKVDKKVEPPKSCDKTHTCPPCPAPELLGGPSVFLFPPKPKDTLMISRTPEVTCVV
VDVSHEDPEVKFNWYVDGVEVHNAKTKPREEQY**A**STYRVVSVLTVLHQDWLNGKEYKCKVSNKAL
PAPIEKTISKAKGQPREPQVYTLPPSRDELTKNQVSLTCLVKGFYPSDIAVEWESNGQPENNYKTTPP
VLDSDGSFFLYSKLTVDKSRWQQGNVFSCSVMHEALHNHYTQKSLSLSPGK

Trastuzumab oa SEED, LC Srt Tag, AG HC N297A RF

Heavy chain SEED AG with N297A mutation:

EVQLVESGGGLVQPGGSLRLSCAASGFNIKDTYIHWVRQAPGKGLEWVARIYPTNGYTRYADSVKG
RFTISADTSKNTAYLQMNSLRAEDTAVYYCSRWGGDGFYAMDYWGQGTLVTVSSASTKGPSVFPL
APSSKSTSGGTAALGCLVKDYFPEPVTVSWNSGALTSGVHTFPAVLQSSGLYSLSSVVTVPSSSLGTQ
TYICNVNHKPSNTKVDKRVEPKSCDKTHTCPPCPAPELLGGPSVFLFPPKPKDTLMISRTPEVTCVVV
DVSHEDPEVKFNWYVDGVEVHNAKTKPREEQY**A**STYRVVSVLTVLHQDWLNGKEYKCKVSNKALP
APIEKTISKAKGQPFRPEVHLLPPSREEMTKNQVSLTCLARGFYPKDIAVEWESNGQPENNYKTTPS
RQEPSQGTTTFAVTSKLTVDKSRWQQGNVFSCSVMHEALHNHYTQKTISLSPGK

Heavy chain SEED GA with RF mutation:

EPKSSDKTHTCPPCPAPELLGGPSVFLFPPKPKDTLMISRTPEVTCVVVDVSHEDPEVKFNWYVDGV
EVHNAKTKPREEQYNSTYRVVSVLTVLHQDWLNGKEYKCKVSNKALPAPIEKTISKAKGQPREPQVY
TLPPPSEELALNELVTLTCLVKGFYPSDIAVEWLQGSQELPREKYLTWAPVLDSDGSFFLYSILRVAA
EDWKKGDTFSCSVMHEALHN**RF**TQKSLDRSPGK

Amino acid sequences (primary structure) of used anti-EGFR antibodies or antibody fragments based on commercial Erbitux (Cetuximab) are presented, where genetic modifications are highlighted with bold font.

Cetuximab CL, LC Srt Tag

Heavy chain with cleavable linker in hinge region:

QVQLKQSGPGLVQPSQSLSITCTVSGFSLTNYGVHWVRQSPGKGLEWLGVIWSGGNTDYNTPFTSR
LSINKDNSKSQVFFKMNSLQSNDTAIYYCARALTYYDYEFAYWGQGTLVTVSAASTKGPSVFPLAPS
SKSTSGGTAALGCLVKDYFPEPVTVSWNSGALTSGVHTFPAVLQSSGLYSLSSVVTVPSSSLGTQTYI
CNVNHKPSNTKVDKRVEPKSCDKTHT**LSGRSDNH**CPPCPAPELLGGPSVFLFPPKPKDTLMISRTPE
VTCVVVDVSHEDPEVKFNWYVDGVEVHNAKTKPREEQYNSTYRVVSVLTVLHQDWLNGKEYKCK
VSNKALPAPIEKTISKAKGQPREPQVYTLPPSREEMTKNQVSLTCLVKGFYPSDIAVEWESNGQPENN
YKTTPPVLDSDGSFFLYSKLTVDKSRWQQGNVFSCSVMHEALHNHYTQKSLSLSPGK

Light chain with sortase recognition motif:

DILLTQSPVILSVSPGERVSFSCRASQSIGTNIHWYQQRTNGSPRLLIKYASESISGIPSRFSGSGSGTDF
TLSINSVESEDIADYYCQQNNNWPTTFGAGTKLELKRTVAAPSVFIFPPSDEQLKSGTASVVCLLNNF
YPREAKVQWKVDNALQSGNSQESVTEQDSKDSTYSLSSTLTLSKADYEKHKVYACEVTHQGLSSPVT
KSFNRGEC**GGGGSGGGGSGGGGSLPETGS**

Cetuximab nCL, LC Srt Tag

Heavy chain with noncleavable linker in hinge region:

QVQLKQSGPGLVQPSQSLSITCTVSGFSLTNYGVHWVRQSPGKGLEWLGVIWSGGNTDYNTPFTSR
LSINKDNSKSQVFFKMNSLQSNDTAIYYCARALTYYDYEFAYWGQGTLVTVSAASTKGPSVFPLAPS
SKSTSGGTAALGCLVKDYFPEPVTVSWNSGALTSGVHTFPAVLQSSGLYSLSSVVTVPSSSLGTQTYI
CNVNHKPSNTKVDKRVEPKSCDKTHT**GGSGGSGG**CPPCPAPELLGGPSVFLFPPKPKDTLMISRTPE
VTCVVVDVSHEDPEVKFNWYVDGVEVHNAKTKPREEQYNSTYRVVSVLTVLHQDWLNGKEYKCK
VSNKALPAPIEKTISKAKGQPREPQVYTLPPSREEMTKNQVSLTCLVKGFYPSDIAVEWESNGQPENN
YKTTPPVLDSDGSFFLYSKLTVDKSRWQQGNVFSCSVMHEALHNHYTQKSLSLSPGK

Cetuximab natural, LC Srt Tag

Heavy chain:

QVQLKQSGPGLVQPSQSLSITCTVSGFSLTNYGVHWVRQSPGKGLEWLGVIWSGGNTDYNTPFTSR
LSINKDNSKSQVFFKMNSLQSNDTAIYYCARALTYYDYEFAYWGQGTLVTVSAASTKGPSVFPLAPS
SKSTSGGTAALGCLVKDYFPEPVTVSWNSGALTSGVHTFPAVLQSSGLYSLSSVVTVPSSSLGTQTYI
CNVNHKPSNTKVDKRVEPKSCDKTHTCPPCPAPELLGGPSVFLFPPKPKDTLMISRTPEVTCVVVDV
SHEDPEVKFNWYVDGVEVHNAKTKPREEQYNSTYRVVSVLTVLHQDWLNGKEYKCKVSNKALPAP
IEKTISKAKGQPREPQVYTLPPSREEMTKNQVSLTCLVKGFYPSDIAVEWESNGQPENNYKTTPPVL
DSDGSFFLYSKLTVDKSRWQQGNVFSCSVMHEALHNHYTQKSLSLSPGK

Cetuximab Fab His, LC Srt Tag

Heavy chain with hexahistidine tag:

QVQLKQSGPGLVQPSQSLSITCTVSGFSLTNYGVHWVRQSPGKGLEWLGVIWSGGNTDYNTPFTSR
LSINKDNSKSQVFFKMNSLQSNDTAIYYCARALTYYDYEFAYWGQGTLVTVSAASTKGPSVFPLAPS
SKSTSGGTAALGCLVKDYFPEPVTVSWNSGALTSGVHTFPAVLQSSGLYSLSSVVTVPSSSLGTQTYI
CNVNHKPSNTKVDKRVEPKSCDKTHT**GGGGSHHHHHH**

Cetuximab oa SEED AG HC His, LC Srt Tag

Heavy chain SEED AG with hexahistidine tag:

QVQLKQSGPGLVQPSQSLSITCTVSGFSLTNYGVHWVRQSPGKGLEWLGVIWSGGNTDYNTPFTSR
LSINKDNSKSQVFFKMNSLQSNDTAIYYCARALTYYDYEFAYWGQGTLVTVSAASTKGPSVFPLAPS
SKSTSGGTAALGCLVKDYFPEPVTVSWNSGALTSGVHTFPAVLQSSGLYSLSSVVTVPSSSLGTQTYI
CNVNHKPSNTKVDKRVEPKSCDKTHTCPPCPAPELLGGPSVFLFPPKPKDTLMISRTPEVTCVVVDV
SHEDPEVKFNWYVDGVEVHNAKTKPREEQYNSTYRVVSVLTVLHQDWLNGKEYKCKVSNKALPAP
IEKTISKAKGQPFRPEVHLLPPSREEMTKNQVSLTCLARGFYPKDIAVEWESNGQPENNYKTTPSRQ
EPSQGTTTFAVTSKLTVDKSRWQQGNVFSCSVMHEALHNHYTQKTISLSPGK**HHHHHH**

Heavy chain SEED GA:

EPKSSDKTHTCPPCPAPELLGGPSVFLFPPKPKDTLMISRTPEVTCVVVDVSHEDPEVKFNWYVDGV
EVHNAKTKPREEQYNSTYRVVSVLTVLHQDWLNGKEYKCKVSNKALPAPIEKTISKAKGQPREPQVY
TLPPPSEELALNELVTLTCLVKGFYPSDIAVEWLQGSQELPREKYLTWAPVLDSDGSFFLYSILRVAA
EDWKKGDTFSCSVMHEALHNHYTQKSLDRSPGK

3.3. Enzymes and proteins

ADAM10	R&D Systems, Minneapolis, MN, USA
Antarctic phosphatase, calf intestinal (CIP)	New England Biolabs, Beverly, USA
Benzonase	Novagen, Nottingham, GB
Bovine serum albumin (BSA), fraction V	Merck, Darmstadt, Germany
BSA standard solution (2 mg/ml)	Thermo Scientific, Schwerte, Germany
CD40 Avi His	Acro Biosystems, Newark, USA
Ecotin	Merck, Darmstadt, Germany
EGF (236-EG/CF), Recombinant Human	R&D Systems, Minneapolis, MN, USA
EGFR (1-618)-His, Recombinant Human	Merck, Darmstadt, Germany
Furin, Recombinant Human (#1503-SE)	R&D Systems, Minneapolis, MN, USA
HAI-1, Recombinant Human (#1048-PI)	R&D Systems, Minneapolis, MN, USA
HER2, murine Fc-His	Merck, Darmstadt, Germany
ILT5-His	Merck, Darmstadt, Germany
Legumain (#2199-CY)	R&D Systems, Minneapolis, MN, USA
Lysozyme	Roche, Mannheim, Germany
Matriptase/ST14 Catalytic Domain (#3946-SE)	R&D Systems, Minneapolis, MN, USA
MMP-2, Recombinant Human (#902-MPN)	R&D Systems, Minneapolis, MN, USA
MMP-9, Active, Recombinant Human (#PF140)	Merck, Darmstadt, Germany
MMP-14/MT1-MMP, Recombinant Human (#918-MP)	R&D Systems, Minneapolis, MN, USA

Phosphatase Inhibitor Cocktail Set II (#524625)	Merck, Darmstadt, Germany (Calbiochem)
Phusion DNA polymerase	New England BioLabs, Ipswich, MA, USA
Protease Inhibitor Cocktail Set III, EDTA-Free (#539134)	Merck, Darmstadt, Germany (Calbiochem)
Rherbb2 murine Fc	R&D Novoprotein, New Jersey, USA
Recombinant Human ErbB2/Her2 His-tag Protein (#10126-ER)	R&D Systems, Minneapolis, MN, USA
Sortase A, Recombinant	Merck, Darmstadt, Germany
T4 DNA ligase	New England BioLabs, Ipswich, MA, USA
tPA, Recombinant Human (#7449-SE)	R&D Systems, Minneapolis, MN, USA
Trypsin	Sigma Aldrich, Steinheim, Germany
Trypsin-EDTA	Life Technologies, Darmstadt, Germany
Transglutaminase, microbial	Merck, Darmstadt, Germany
u-Plasminogen Activator (uPA)/Urokinase (#1310-SE)	R&D Systems, Minneapolis, MN, USA
uPAR, Recombinant Human (#807-UK)	R&D Systems, Minneapolis, MN, USA

3.3.1. Antibodies

Reference and control antibodies and antibody-drug conjugates

Anti-Dig (Digoxigenin)	Merck, Darmstadt, Germany
Anti-hen egg lysozyme (HEL)	Merck, Darmstadt, Germany
Cetuximab (Erbitux®, C225)	Merck, Darmstadt, Germany
Trastuzumab (Herceptin®)	Roche, Basel, Switzerland
Trastuzumab emtansine (Kadcyla®, T-DM1)	Roche, Basel, Switzerland

All reference antibodies and antibody-drug conjugates were kindly provided by Merck, Darmstadt, Germany.

Primary antibodies for Western Blot

Goat anti-human IgG Antibody, F(ab')2 Fragment specific	Jackson ImmunoResearch, Suffolk, GB
Mouse IgG1 anti-human Matriptase Antibody (#MAB3946)	R&D Systems, Minneapolis, MN, USA
Mouse IgG1 anti-Penta His Antibody (#34660)	Qiagen, Hilden, Germany
Mouse anti-human IgG, F(ab')2 Fragment specific	Jackson ImmunoResearch, Suffolk, GB
Mouse IgG_{2A} anti-human uPA Antibody (#MAB1310)	R&D Systems, Minneapolis, MN, USA

Mouse anti-human uPAR Antibody (#MAB807)	R&D Systems, Minneapolis, MN, USA
Mouse anti-human IgG, Fcg Fragment specific	Jackson ImmunoResearch, Suffolk, GB
Rabbit anti-EGFR mAb, clone D38B1	Cell Signaling Technologies, Cambridge GB

Secondary antibodies for Western Blot

Goat anti-mouse IgG (H+L) x AP conjugate (#115-055-062)	Jackson ImmunoResearch, Suffolk, GB
Goat anti-mouse Fc F(ab')2 FITC conjugate	Jackson ImmunoResearch, Suffolk, GB
Goat anti-rabbit Alexa Fluor® 680 IgG (H+L), A21076	Life Technologies, Darmstadt, Germany
Precision Protein™ StrepTactin-HRP conjugate (#1610381)	Bio-Rad, Munich, Germany
Rabbit anti-goat IgG (H+L) x AP conjugate (#305-056-045)	Jackson ImmunoResearch, Suffolk, GB

Detection antibodies for flow cytometry

Anti-Alexa Fluor® 488 Rabbit IgG Antibody Fraction (Quenching) (#A11094)	Life Technologies, Darmstadt, Germany
Goat Anti-Human IgG (H+L) Fab Fragment, Alexa Fluor® 488 (#109-547-003)	Jackson ImmunoResearch, Suffolk, GB
Goat anti-human IgG, Fc specific, FITC conjugate	Jackson ImmunoResearch, Suffolk, GB

Antibodies for ELISA

Goat anti-mouse IgG (H+L) peroxidase (HRP) conjugate	Jackson ImmunoResearch, Suffolk, GB
Goat anti-human IgG, Fcγ fragment specific peroxidase (HRP) conjugate	Jackson ImmunoResearch, Suffolk, GB
Goat anti-human IgG, F(ab)2-fragment specific (#109-035-006)	Jackson ImmunoResearch, Suffolk, GB
Rabbit anti-goat IgG (H+L) peroxidase (HRP) conjugate	Jackson ImmunoResearch, Suffolk, GB
Rabbit Anti-human IgG, anti-Fc (#Clone RM116)	Merck, Darmstadt, Germany

3.4. Oligonucleotides

Oligonucleotides were obtained from Eurofins MWG Operon, Ebersberg, Germany.

Primers for sequencing:

pTT5_UP	CTGCGCTAAGATTGTCAGT
pTT5_RP	CCATATGTCCTTCCGAGTG

3.5. Chemicals

1-Step™ Ultra TMB-ELISA substrate solution	Thermo Scientific, Schwerte, Germany
Accutase	Merck, Darmstadt, Germany
Acetic acid	Merck, Darmstadt, Germany
Acetonitrile	Merck, Darmstadt, Germany
Agar-agar	Merck, Darmstadt, Germany
Agarose	Life Technologies, Darmstadt, Germany
Albumin fraction V (from bovine serum), BSA	Merck, Darmstadt, Germany
Alexa Fluor 488 Cadaverine (#A30676)	Thermo Scientific, Schwerte, Germany
Alexa Fluor 647 Cadaverine (#A30679)	Thermo Scientific, Schwerte, Germany
Ammonium sulfate	Merck, Darmstadt, Germany
Ampicillin, sodium salt	Life Technologies, Darmstadt, Germany
BHQ-1 Amine	LGC Biosearch Technologies, Petaluma, CA, USA
BHQ-3 Amine	LGC Biosearch Technologies, Petaluma, CA, USA
BHQ-10 Succinimidyl Ester	LGC Biosearch Technologies, Petaluma, CA, USA
Blocking solution for fluorescent Western Blot	Biomol, Hamburg, Germany
Calcium chloride ($CaCl_2$)	Merck, Darmstadt, Germany
Coomassie Plus - Bradford Assay™ Reagent	Thermo Scientific, Schwerte, Germany
1,5-Dansyl-Glu-Gly-Arg Chloromethyl Ketone	Merck, Darmstadt, Germany
Desocyribonucleotide triphosphates (dNTPs)	Novagen, Nottingham, GB
Disodium hydrogen phosphate (Na_2HPO_4*$2H_2O$)	Merck, Darmstadt, Germany
DM1	Merck, Darmstadt, Germany
DMSO	VWR International, Darmstadt, Germany
Eagle Minimal Essential Medium (MEM)	Sigma-Aldrich, Steinheim, Germany
EDTA (ethylenediaminetetraacetic acid)	Sigma Aldrich, Steinheim, Germany
Expi293™ expression medium	Life Technologies, Darmstadt, Germany
Gel filtration standards (#151-1901)	Bio-Rad, Munich, Germany
Gel loading dye (6x)	Novagen, Nottingham, GB
GelRed™	VWR International, Darmstadt, Germany
Gibco® Dulbecco's Modified Eagle Medium (DMEM)	Life Technologies, Darmstadt, Germany

Gibco® Dulbecco's PBS (DPBS, w/o $CaCl_2$, $MgCl_2$); Phosphate Buffered Saline	Life Technologies, Darmstadt, Germany
Gibco® Fetal Calf Serum (FCS), Fetal Bovine Serum	Life Technologies, Darmstadt, Germany
Gibco® L-Glutamine	Life Technologies, Darmstadt, Germany
Gibco® Sodium pyruvate	Life Technologies, Darmstadt, Germany
Gibco® RPMI 1640 medium	Life Technologies, Darmstadt, Germany
Glucose	Sigma-Aldrich, Steinheim, Germany
Guava Instrument Cleaning Fluid (ICF)	Merck, Darmstadt, Germany
Glycine	Merck, Darmstadt, Germany
Hydrochloric acid (HCl)	Merck, Darmstadt, Germany
Isopropyl-β,D-thiogalactopyranosid (IPTG)	Merck, Darmstadt, Germany (Calbiochem)
Imidazole	Merck, Darmstadt, Germany
InstantBlue™ Protein Stain	Expedeon Ltd, San Diego, CA, USA
Insulin	Sigma-Aldrich, Steinheim, Germany
Kanamycin sulfate	Merck, Darmstadt, Germany
Magnesium chloride hexahydrate	Merck, Darmstadt, Germany
Methanol	Merck, Darmstadt, Germany
Monomethyl auristatin E (MMAE)	Merck, Darmstadt, Germany
Monomethyl auristatin F (MMAF)	Merck, Darmstadt, Germany
Monomethyl auristatin E (MMAE) linker-drug (Gly3-ValCit-PABC-MMAE)	Merck, Darmstadt, Germany
Monomethyl auristatin F (MMAF) linker-drug (Gly3-ValCit-PABC-MMAF)	Merck, Darmstadt, Germany
Nickel(II)sulfate hexahydrate	Merck, Darmstadt, Germany
NuPAGE® LDS sample buffer (4x)	Life Technologies, Darmstadt, Germany
NuPAGE® MES SDS running buffer (20x)	Life Technologies, Darmstadt, Germany
NuPAGE® Sample Reducing Agent (10x)	Life Technologies, Darmstadt, Germany
NuPAGE® Tris-acetate running buffer	Life Technologies, Darmstadt, Germany
Formaldehyde 37%	Merck, Darmstadt, Germany
Formic acid	Sigma-Aldrich, Steinheim, Germany
PageRuler™ Plus Prestained Protein Ladder, 10 to 250 kDa (#26620)	Thermo Scientific, Schwerte, Germany
Peptone	Merck, Darmstadt, Germany
Perfect DNA™ markers, 0.1 – 12 kbp	Merck, Darmstadt, Germany
Phusion HF buffer (5x)	New England Biolabs, Ipswich, MA, USA
Polyethylene glycol 8000	Sigma-Aldrich, Steinheim, Germany
Potassium chloride (KCl)	Merck, Darmstadt, Germany
Potassium di-hydrogen phosphate (KH_2PO_4)	Merck, Darmstadt, Germany

Precision Plus Protein™ Unstained Protein Standards (#1610363)	Bio-Rad, Munich, Germany
ProCHO5 medium	Lonza, Basel, Switzerland
Propidium iodide (PI)	Life Technologies, Darmstadt, Germany
Protein standard HiMark™ pre-stained	Life Technologies, Darmstadt, Germany
Restriction enzyme buffers CutSmart or NEB1-4	New England Biolabs, Ipswich, MA, USA
RIPA cell lysis buffer (10x, #9806)	Cell Signaling Technologies, Cambridge GB
Sucrose	Merck, Darmstadt, Germany
S.O.C. medium	Life Technologies, Darmstadt, Germany
SeeBlue® Plus2 Pre-Stained Protein Standard	Life Technologies, Darmstadt, Germany
Skim milk powder	Merck, Darmstadt, Germany
Sodium azide	Merck, Darmstadt, Germany
Sodium chloride (NaCl)	Merck, Darmstadt, Germany
Sodium hydroxide solution (NaOH)	Merck, Darmstadt, Germany
Sodium perchlorate monohydrate ($NaClO_4$*H_2O)	Merck, Darmstadt, Germany
Sulfo-Cyanin-5-amin	Lumiprobe, Hannover, Germany
Sulfuric acid (H_2SO_4)	Bernd Kraft, Duisburg, Germany
SYPRO Orange	Life Technologies, Darmstadt, Germany
T4 DNA Ligation Buffer (10x)	New England BioLabs, Ipswich, MA, USA
TAE buffer	Life Technologies, Darmstadt, Germany
Tetracycline	VWR International, Darmstadt, Germany
Trifluoroacetic acid (TFA)	Life Technologies, Darmstadt, Germany
Tris(hydroxymethyl)aminomethane (Tris)	Carl Roth, Karlsruhe, Germany
Tris-hydrochloride (Tris-HCl)	Sigma-Aldrich, Steinheim, Germany
Tween®20 (Polysorbate 20)	Merck, Darmstadt, Germany
Yeast extract	Becton Dickinson, Heidelberg, Germany

3.6. Cell culture media

A-431, HEK293 adherent, MCF-7, MDA-MB-361, MDA-MB-453, SK-BR.3, SKOV-3	DMEM, 10% (v/v) FCS, 1 mM sodium pyruvate
MDA-MB-468, HCC1954, NCI-N87	RPMI 1640, 10% (v/v) FCS, 2 mM L-glutamine, 1 mM sodium pyruvate
BT-474	DMEM, 10% (v/v) FCS, 2 mM L-glutamine, 1 mM sodium pyruvate, 10 µg/ml insulin
CHO-S	ProCHO5, 4 mM L-glutamine
Expi293F™	Expi293™ expression medium

3.7. Solutions, media and buffer

2xTY medium	16 g/l peptone, 10 g/l yeast extract, 5 g/l NaCl, pH 7.0
5xTY medium	10 g/l peptone, 50 g/l yeast extract, pH 7.0
Analytical Size Exclusion Chromatography (SEC) mobile phase	PBS, pH 7.4 or 50 mM sodium phosphate (NaH_2PO_4, Na_2HPO_4), 0.4 M sodium perchlorate, pH 6.35
BCIP/NBT Reagent, Blue/purple, AP substrate	Merck, Darmstadt, Germany
EDTA solution	0.5 M EDTA, pH 8.0
FACS binding buffer	1% (w/v) BSA in DPBS
Hydrophobic Interaction Chromatography buffer	A: 1.5 M Ammonium sulfate, 25 mM Tris, pH 7.5 B: 20 % Isopropanol, 25 mM Tris, pH 7.5
Imidazole buffer	2 M Imidazole, pH 7.5
Kinetics buffer (KB) for BLI	0.1% (w/v) BSA, 0.02% (v/v) Tween®20 in PBS
LB medium	10 g/l peptone, 5 g/l yeast extract, 10 g/l NaCl
LB-A medium	LB, 0.1 mg/l ampicillin
LB-A agar	LB-A, 15 g/l agar-agar
Legumain activation buffer	50 mM Sodium Acetate, 100 mM NaCl, pH 4.0
MMP-14/MT1-MMP activation buffer	50 mM Tris, 1 mM CaCl2, 0.5% (w/v) Brij-35, pH 9.0
Nickel(II)sulfate solution	0.5 M Nickel(II)sulfate
Opti-MEM, Reduced Serum Media	Life Technologies, Darmstadt, Germany
Phosphate buffered saline (10x PBS)	1.5 M NaCl, 84 mM Na_2HPO_4 x $2H_2O$, 16 mM KH_2PO_4, pH 7.4
Phosphate buffer (8x)	4 M NaCl, 199.5 mM Na_2HPO_4 x $2H_2O$, 201.5 mM NaH_2PO_4 x H_2O, pH 7.4
Polyethylenelgycol (PEG)/NaCl	200 g/l PEG6000, 2.5M NaCl ad dH_2O
Preparative SEC mobile phase	PBS, pH 7.4
ProSepA binding buffer A	1.5 M Glycine/NaOH, 3 M NaCl, pH 9.0
ProSepA elution buffer B2	0.2 M Glycine/HCl, pH 2.5
ProSepA neutralization buffer C	1 M Tris/HCl, pH 9.0
Protein A Chromatography binding buffer	PBS, pH 6.8 – pH 7.0 or 10 mM Na_2HPO_4, 10 mM NaH_2PO_4, 500 mM NaCl, pH 7.0
Protein A Chromatography elution buffer	0.1 M sodium citrate, pH 3.0 or 20 mM acetic acid, pH 3.2

Protein A Chromatography neutralization buffer	3 M Tris/HCl, pH 8.5 or 1 M Tris/HCl, pH 9.0
Sortase conjugation buffer	150 mM NaCl, 50 mM Tris-HCl, pH 7.5
Transglutaminase conjugation buffer	150 mM NaCl, 25 mM Tris-HCl, pH 8.0
Tris/HCl	3 M Tris, pH 8.0
Wash solution/PBS-Tween®20	0.05% (v/v) Tween®20 in 1x PBS pH 7.4

3.8. Kits and consumable materials

AirPore™ Tape Sheets, sealing foil	Qiagen, Hilden, Germany
Amicon® Ultra-15 and 0.5 ml centrifugal filter devices, 10K and 30K	Merck, Darmstadt, Germany
BCA Protein Assay Kit	Thermo Scientific, Schwerte, Germany
Cell culture flasks T25, T75, T175	Greiner Bio-One, Kremsmuenster, Austria
Cell culture flat and round bottom Nucleon™ delta surface 96 well plates	Thermo Scientific, Schwerte, Germany
Cell culture 24 well plates Costar®	Thermo Scientific, Schwerte, Germany
Cell culture microplate 384 well, white, clear	Greiner Bio-One, Kremsmuenster, Austria
CellTiter-Glo® Luminescent Cell Viability Assay	Promega, Mannheim, Germany
Chromolith Performance RP-18e 100-3mm	Merck, Darmstadt, Germany
Corning 384 well Spheroid microplates, black/clear bottom round, ULA (#3830)	Sigma-Aldrich, Steinheim, Germany
GenElute™ HP Plasmid Midiprep, Maxiprep Kit	Sigma-Aldrich, Steinheim, Germany
ExpiFectamine™ 293 transfection kit	Life Technologies, Darmstadt, Germany
Falcon® tubes, 15 ml and 50 ml	VWR International, Darmstadt, Germany
FortéBio tips (AHC, FAB2G, ProteinA)	Pall ForteBio LLC, Menlo Park, CA, USA
Gel and PCR clean-up kit NucleoSpin®	Macherey-Nagel, Dueren, Germany
Glas autosampler vials	VWR International, Darmstadt, Germany
Glas autosampler insert micro vials, 100 µl	VWR International, Darmstadt, Germany
HiPrep 26/10 Desalting	GE Healthcare, Munich, Germany
HiLoad Superdex 200 pg 26/60 columns	GE Healthcare, Munich, Germany
HiTrap MabSelect SuRe columns, 1 ml and 5 ml	GE Healthcare, Munich, Germany
His Buffer Kit	GE Healthcare, Munich, Germany
His GraviTrap	GE Healthcare, Munich, Germany
HisTrap™ HP, 1 ml and 5 ml	GE Healthcare, Munich, Germany
Human Serum HIV tested (#S4200)	BioWest, Nuaillé, France
iBind™ Solution Kit (#SLF1020)	Life Technologies, Darmstadt, Germany
iBlot™ Transfer Stack, Nitrocellulose, mini	Life Technologies, Darmstadt, Germany
iBlot™ Transfer Stack, PVDF, mini	Life Technologies, Darmstadt, Germany

Limulus amebocyte lysate Endosafe®-PTS™ cartriges, PTS2001F, FDA-licensed, 1-0.01 EU/ml	Charles River Laboratories, Wilmington, MA, USA
MAB PAK Butyl 5 µm 4.6 mm ID x 100 mm	Thermo Scientific, Schwerte, Germany
MaxiSorp®f flat-bottom 96 well micotiter plates	Sigma-Aldrich, Steinheim, Germany
Mini-Sub® Cell GT cell gel chambers	Bio-Rad, Munich, Germany
Montage PROSEP-A spin columns (#P36486)	Merck, Darmstadt, Germany
Mouse Serum (#S2160)	BioWest, Nuaillé, France
NuPAGE® 3-8% Tris-Acetate gels	Life Technologies, Darmstadt, Germany
NuPAGE® 4-12% Bis-Tris gels	Life Technologies, Darmstadt, Germany
Pellicon® 3 Cassette with Ultracel® 10 kDa Membrane, D screen, 88 cm^2	Merck, Darmstadt, Germany
Pierce™ Coomassie Plus (Bradford) Assay Kit	Thermo Scientific, Schwerte, Germany
Pierce™ Fab Preparation Kit	Thermo Scientific, Schwerte, Germany
Pierce™ $F(ab')_2$ Preparation Kit	Thermo Scientific, Schwerte, Germany
Polypropylene microtiter plates, black	Greiner Bio-one, Frickenhausen, Germany
Polypropylene microtiter plates, clear	Greiner Bio-one, Frickenhausen, Germany
Polystyrene round bottom 96 well microtiter plates	Greiner Bio-one, Frickenhausen, Germany
PLRP-S 5 µm, 50 x 2,1 mm, 4000A	Agilent Technologies, Waldbronn, Germany
Pur-A-Lyzer™ Maxi Dialysis Kit	Sigma-Aldrich, Steinheim, Germany
PureLink™ Quick Plasmid Miniprep Kit	Life Technologies, Darmstadt, Germany
Qiaprep® Spin Miniprep kit	Qiagen, Hilden, Germany
Quick Ligation Kit	New England BioLabs, Ipswich, MA, USA
Safe-lock tubes 0.2, 1.5, 2.0, 5.0 ml	Eppendorf, Hamburg, Germany
Standard Capillary Chips	NanoTemper Technologies, Munich, Germany
Steriflip® filter device 0.22 µm	Merck, Darmstadt, Germany
Steritop™ bottle top filter 0.22 µm	Merck, Darmstadt, Germany
The Blocking Solution	Candor Bioscience, Wangen, Germany
Tissue culture 24 well plates	Greiner Bio-one, Frickenhausen, Germany
TMB peroxidase substrate solution	Vector Laboratories, Burlingame, CA, USA
TSKgel SuperSW3000 column, 4.6 x 300 mm	Tosoh Bioscience, Darmstadt, Germany
Ultrafree® Centrifugal filter units	Merck, Darmstadt, Germany
ViaFlow pipette 16 channel	Integra, Biebertal, Germany
Wizard® SV Gel and PCR Clean-Up System	Promega, Mannheim, Germany
Zeba Spin desalting PD-10 columns	Life Technologies, Darmstadt, Germany

3.9. Equipment

Analytical balance New Classic MF MS3002S	Mettler Toledo, Giessen, Germany
Cell counter Vi-CELL® XR	Beckmann Coulter, Brea, CA, USA
Chromatography systems ÄKTAxpress, ÄTKAexplorer 100, ÄKTApure	GE Healthcare, Munich, Germany
Cogent® µScale TFF System	Merck, Darmstadt, Germany
Electrophoresis chambers	Bio-Rad, Munich, Germany
Endosafe®-PTS™ reader, PTS100	Charles River, Wilmington, MA, USA
EnVision 2104	Perkin Elmer, Boston, MA, USA
EVOS FL Auto 2 Imaging System	Life Technologies, Darmstadt, Germany
Flow cytometer Guava easyCyte HT 2L	Merck, Darmstadt, Germany
Fluoresence reader Odyssey® CLx	LI-COR Biosciences, Bad Homburg, Germany
FortéBio Octet RED	Pall ForteBio LLC, Menlo Park, CA, USA
Gel imaging system GBOX	Syngene, Cambridge, GB
HeraSafe® Clean Bench	Thermo Scientific, Schwerte, Germany
Hot plate magnetic stirrer IKA® RCT basic	Sigma-Aldrich, Steinheim, Germany
HPLC Agilent Technologies 1260 Infinity, ChemStation LC 3D	Agilent Technologies, Waldbronn, Germany
iBind™ Western System	Life Technologies, Darmstadt, Germany
iBlot® Dry Blotting System	Life Technologies, Darmstadt, Germany
Incubation shaker Minitron	Infors HT, Bottmingen, Switzerland
Incubator Heracell 150	Thermo Scientific, Schwerte, Germany
IncuCyte® S3 Live-Cell Analysis System	Sartorius, Göttingen, Germany
Megafuge 1.0R, rotor BS4402/A	Thermo Scientific, Schwerte, Germany
Microplate washer, ELx405™	BioTeK, Bad Friedrichshall, Germany
Microtiter plate reader BioTeK Synergy™ 4	BioTeK, Bad Friedrichshall, Germany
Microtiter plate reader SpectraMax® Paradigm®	Molecular Devices, Wals, Austria
Multifuge 3 S-R	Heraeus, Hanau, Germany
Nanodrop ND-1000 Spectrophotometer	Thermo Scientific, Schwerte, Germany
Nanodrop One Spectrophotometer	Thermo Scientific, Schwerte, Germany
pH meter 744	Metrohm, Filderstadt, Germany
Power supply EC 250-90	Thermo Scientific, Schwerte, Germany
PowerPac™ basic power supply	Bio-Rad, Munich, Germany
Prometheus NT.PLEX nanoDSF	NanoTemper Technologies, Munich, Germany
Table centrifuge 5415D	Eppendorf, Hamburg, Germany
Tecan D300e Digital Dispenser	Tecan, Maennedorf, Switzerland
ThermoMixer®	Eppendorf, Hamburg, Germany

Ultracentrifuge Beckmann OptimaTM LE-80K, SW41 TI rotor	Global Medical Instrumentation, Ramsey, MN, USA
Synapt-G2 mass spectrometer	Waters, Milford, MA, USA
XCell SureLock™ gel electrophoresis device	Life Technologies, Darmstadt, Germany

Further basic laboratory equipment and instrumentation that are commonly used were also utilized.

3.10. Software

Accelrys Draw 4.2	Biovia, San Diego, CA, USA
ÄKTA UNICORN software ver. 5.31 (Build 407)	GE Healthcare, Munich, Germany
ChemBioDraw Ultra 13.0	Perkin Elmer, Boston, MA, USA
Endosafe®-PTS™ Data logging utility ver. 1.0	Charles River Laboratories, Wilmington, MA, USA
FortéBio Octet Data Acquisition ver. 8.0	Pall ForteBio LLC, Menlo Park, CA, USA
FortéBio Octet Data Analysis ver. 8.0	Pall ForteBio LLC, Menlo Park, CA, USA
Gen5™ microplate reader Software ver. 1.11.5	BioTeK Instruments, Bad Friedrichshall, Germany
GraphPad Prism ver. 7.00	GraphPad Software, La Jolla, CA, USA
GuavaSoft ver 2.7	Merck, Darmstadt, Germany
HPLC Software ChemStation	Agilent Technologies, Waldbronn, Germany
Image Studio™ Software ver. 2.1	LI-COR Biosciences, Bad Homburg, Germany
Incucyte S3 2018A	Sartorius, Göttingen, Germany
Lasergene ver. 14	DNA Star Inc., Wisconsin, WI, USA
Mendeley Desktop ver. 1.19.4	Elsevier, New York, NY, USA
Microsoft Office 2013	Microsoft Corp., Redmond, WA, USA
Paradigm™ Software SoftMaxPro ver. 6.3	Molecular Devices, Wals, Austria
Protein Thermal Shift™ Software ver. 1.0	Life Technologies, Darmstadt, Germany
PyMOL ver. 0.99	Schrodinger LLC, San Diego, CA, USA
Reference Manager ver. 12	Thomson Reuters, FFM, Germany
SnapGene® Viewer ver. 2.6.2	GSL Biotech LLC, Chicago, IL, USA
Tecan D300e Software	Tecan, Maennedorf, Switzerland
PR.Thermo Control	NanoTemper Technologies, Munich, Germany
Vi-CELL® XR ver. 2.04	Beckmann Coulter, Brea, CA, USA
Wallac Envision Manager	Perkin Elmer, Boston, MA, USA

4. Methods

4.1. Molecular biological and microbiological methods

4.1.1. Determination of DNA concentration

The concentration of nucleic acids in aqueous solutions was measured by UV spectrophotometer Nanodrop ND-1000 or Nanodrop One applying 1.5 or 2.0 µl of sample on the pedestal. As blank measurements the nucleic acid formulation buffer was used. The law of Lambert-Beer is the fundamental physical principle as well as the absorption of aromatic nucleobases within the DNA at the wavelength 260 nm. The ratios of absorbance A_{260}/A_{280} and A_{260}/A_{230} can be used as quality criteria for the purity of the DNA and should be in the range 1.8 and 2.0-2.2, respectively. Lower values indicate a contamination with undesired products (typically proteins).

4.1.2. Purification of DNA

DNA fragments were purified after PCR reactions using the Wizard® SV Gel and PCR Clean-Up System according to the manufacturer's protocol. Elution of DNA was carried out in 10-50 µl elution buffer from the kit or dH_2O. DNA concentration was measured by a UV spectrophotometric analysis.

4.1.3. Agarose gel electrophoresis

Agarose gel electrophoresis was used for size-dependent separation of linear DNA fragments in an electric field. Generally, 1-2% (w/v) agarose gels were prepared in TAE buffer supplemented with GelRed™ solution (1:10,000). Samples of 10 µl DNA together with 2 µl 6x loading dye buffer were loaded on gels along with 10 µl Perfect DNA™ marker (0.1-12 kbp) for determination of size and quantity of separated DNA fragments. Gels were run for 50 min at 110 V and after the run, DNA bands were visualized under UV light using the gel imaging system GBOX.

4.1.4. DNA sequencing

Sequence analysis of isolated plasmid DNA samples (15 µl with 50-100 ng/µl) or transformed *E. coli* glycerol stocks in 96 well plates was carried out at Eurofins MWG Operon (Ebersberg, Germany) by using pTT5_UP and pTT5_RP primers.

4.1.5. Transformation in *E. coli*

For plasmid amplification, heat shock transformation of One Shot™ TOP10 Chemically Competent *E. coli* cells with plasmid DNA was performed. Briefly, 50 µl Chemically Competent *E. coli* cells were thawed on ice for 5-10 min, subsequently adding 1 µl plasmid DNA and incubating for 30 min on ice. Heat shock was carried out at 42 °C in a water bath for 45 sec without shaking. After heat shock, vials were incubated on ice for 2 min, transformed cells were immediately mixed with 250 µl pre-warmed S.O.C. medium and incubated at 37 °C and 450 rpm for 1 h. Afterwards, cell suspensions were plated on pre-warmed LB-Ampicillin selective agar plates and incubated overnight at 37 °C.

4.1.6. Plasmid preparation

Single *E. coli* colonies were picked from the agar plate and inoculated overnight at 37 °C, 250 rpm in *E. coli* cultures in LB-medium. Plasmid preparation was performed according to the manufacturer's instruction. Plasmid DNA was isolated from 5 ml *E. coli* cultures using the GenElute™ HP Plasmid Miniprep Kit or from 100-200 ml *E. coli* cultures applying the GenElute™ HP Plasmid Midiprep Kit or GenElute™ HP Plasmid Maxiprep Kit, respectively. DNA elution was carried out with 100-3000 µl dH_2O depending on the size of the *E. coli* culture.

4.2. Biochemical methods

4.2.1. Determination of protein concentration

Determination of protein concentration was performed by measuring absorbance at 280 nm (A_{280}) according to the law of Lambert-Beer by Bradford assay using the Pierce™ Coomassie Plus (Bradford) Assay Kit, BCA Protein Assay Kit or applying 1.5 or 2.0 µl of sample on the pedestal of UV spectrophotometer Nanodrop ND-1000 or Nanodrop One. As blank measurements the respective protein formulation buffer was used. Concentration was determined with the parameters molecular weight (in kDa) and molar extinction coefficient (M^{-1} cm^{-1}; BRAIN, Genedata; Protean Software, Lasergene DNASTAR) of the protein. For the Bradford assay, a standard curve with serial dilutions of BSA (0.1-1 mg/ml) were prepared for protein quantitation. Samples were diluted (1:2 to 1:40 depending on the concentration), 5 µl of each sample or standard dilution were added in duplicates to a microtiter plate well together with 150 µl Bradford reagent. After shaking and incubation for 30 min in the dark, absorbance is measured at 595 nm with an ELISA reader. Protein concentration of samples are calculated by using the calibration curve. For the BCA assay also BSA standard solutions are prepared. 25 µl of each sample or BSA standard are added into a microplate well. Afterwards, 200 µl working reagent (containing BCA) are added to each well and mixed on a plate shaker for 30 sec. Microplate is incubated for 30 min at 37 °C and plate is cooled to RT before measuring absorbance at 562 nm.

4.2.2. Protein A affinity chromatography

For IgG antibody purification from cell free Expi293 supernatants of small scale productions (25-50 ml), purification was carried out with PROSEP® A centrifugal Protein A columns. Due to the fact that Protein A has a high affinity for the Fc part of an IgG antibody, established purification procedures are used. For this approach, recommended buffers binding buffer A, elution buffer B2 and neutralization buffer C were used, following antibody purification protocol. In brief, before loading on PROSEP® A columns, samples were clarified by filtration through Steriflip® filter device 0.22 µm to remove any debris. Filtered samples were diluted with binding buffer A in a ratio of 1:1 (v/v) and were applied on the columns, centrifuged with 150 xg for 20 min and followed by two washing steps (500 xg for 2 min) à 10 ml binding buffer A. Elution of bound antibodies was achieved by addition of 10 ml elution buffer B2 in tubes containing 1.3 ml neutralization buffer C. Eluates containing antibodies were concentrated with Amicon® Ultra-15 centrifugal filter device (with 10,000 molecular weight cut-off MWCO; 3000 xg, 15 min) and subsequently buffer exchanged to PBS pH 7.4 using PD-10 desalting columns or Pur-A-Lyzer™ Dialysis Kit.

Purification of antibodies from cell free Expi293 supernatants of large scale productions (200 ml) was performed by using affinity chromatography with a 1 ml or 5 ml HiTrap MabSelect SuRe column on an ÄKTAxpress or ÄKTApure system. Column equilibration was achieved with 5 column volumes (CV) binding buffer PBS pH 7.4 at a flow rate of 2.5 ml/min, subsequently sample was loaded (2.5 ml/min) on MabSelect column using active air sensor and wash out with 5 CV binding buffer. Isocratic elution was carried out with 5 CV using 20 mM acetic acid, pH 3.2. Eluate is buffered through HiPrep 26/10 Desalting column with PBS ph 7.4. 1 ml fractions were collected in 96 deep well plates and fractions from the target protein peak were pooled and checked for purity with SDS PAGE and analytical SEC. Samples were concentrated with Amicon® Ultra-15 centrifugal filter device with 10,000 MWCO (3000 xg, 15 min) and subjected to preparative size exclusion chromatography, if necessary.

4.2.3. Immobilized metal ion affinity chromatography (IMAC)

Purification of antibody fragments from cell free Expi293 supernatants of small scale productions (25-50 ml) was achieved with single-use columns His GraviTrap and His Buffer Kit based on immobilized metal ion affinity chromatography (IMAC) according to the manufacturer's protocol. Before purification the supernatants were dialyzed using Pur-A-Lyzer™ Maxi Dialysis Kit to exchange buffer to PBS pH 7.4. The gravity-flow purification was carried out by equilibration of the column using 10 ml binding buffer 20 mM sodium phosphate, 500 mM NaCl, pH 7.4, sample application, washing step and elution of the sample with 3 ml elution buffer containing 500 mM imidazole.

Prior to purification, cell free Expi293 supernatants of large scale productions (200 ml) were diafiltrated and concentrated using the Cogent® µScale Tangential Flow Filtration (TFF) System with three Pellicon® 3 88 cm^2 cassettes and a MWCO of 10 kDa. The retentate was buffer exchanged to PBS pH 7.4. To facilitate purification of histidine-tagged antibody fragments, IMAC was designed to capture the protein with hexahistidine tag based on high selective affinity for Ni^{2+} (in Ni sepharose medium). Buffer-exchanged and concentrated supernatants were loaded on a HisTrap™ HP, 1 ml or 5 ml column using an ÄKTAexplorer or ÄKTApure system. Column equilibration was achieved with 5 column volumes (CV) 1x phosphate buffer pH 7.4 at a flow rate of 5.0 ml/min, subsequently sample was loaded (5.0 ml/min) on HisTrap column using active air sensor and wash out with 5 CV binding buffer. Stepwise elution was carried out with a gradient 10 CV using 20 mM, 50 mM, 100 mM, 200 mM, 300 mM, 500 mM imidazole, pH 7.4 and 1x phosphate buffer (5.0 ml/min). 1 ml fractions were collected in 96 deep well plates and fractions from target protein peaks were pooled and checked for purity with SDS PAGE and analytical SEC. Samples were concentrated with Amicon® Ultra-15 centrifugal filter device with 10,000 MWCO (3000 xg, 15 min) and subjected to preparative size exclusion chromatography.

4.2.4. Preparative size exclusion chromatography (SEC)

Antibodies and antibody fragments were purified using chromatography techniques that separate them according to differences in size, hence obtaining pure antibody monomer separating from high molecular weight protein aggregates. Preparative size exclusion chromatography (SEC) was carried out using HiLoad 26/60 Superdex 200 pg with PBS pH 7.4 or other desired buffer as mobile phase. Columns were equilibrated with 5 CV

buffer at 10.0 ml/min, before 2 ml concentrated protein solution was loaded with a sample loop. 1 ml fractions were collected in a 96 deep well plate and selected fractions were pooled (2.5 ml/min). Antibody samples were concentrated with Amicon® Ultra-15 centrifugal filter device (10 kDa MWCO) resulting in final concentrations of 6-7 mg/ml protein. Determination of protein concentrations and purity was achieved by A_{280} spectroscopy, gel electrophoreses and analytical SEC. Endotoxin levels were assessed for final protein samples by Limulus amebocyte lysate (LAL) Endosafe® PTS cartridges and Endosafe® PTS reader according to the manufacturer's instructions.

4.2.5. Analytical size exclusion chromatography

Evaluation of protein purity, molecular size and relative amount of high molecular weight protein aggregates was performed by using analytical size exclusion high performance liquid chromatography (SE-HPLC) with TSK Super SW3000 column and HPLC Agilent 1260 (ChemStation LC 3D). Briefly, columns were equilibrated with mobile phase buffer at 0.35 ml/min until obtaining stable baseline (~45 min). The gel filtration standard (Bio-Rad) that was used contains a mixture of 5 molecular weight markers. 10 µg of protein samples (typically 10 µl of a solution with a concentration of 1.0 mg/ml) in PBS was applied per run. The following sequence was injected: mobile phase, gel filtration standard, protein samples, gel filtration standard, mobile phase. Chromatograms recorded with UV detection at 214 nm (or alternatively 254 and 280 nm) and were analyzed by the ChemStation software by peak area integration and target purity as well as other species were determined.

4.2.6. SDS-PAGE

Sodium dodecyl sulfate polyacrylamide gel electrophoresis (SDS-PAGE) represents an established method for analysis of protein purity of samples and cell lysates. The intrinsic charge of proteins is masked by addition of the anionic detergent SDS or lithium dodecyl sulfate (LDS) that denatures the protein and creates a relatively uniform negative charge distribution. SDS-PAGE separates proteins primarily according to molecular weight (sieving effect), migrating to the anode in an electric field. For this purpose, protein samples or cell lysates were mixed with 4x LDS sample buffer and 10x sample reducing agent (optional, if reduction of disulfide bonds was necessary), followed by incubation in a ThermoMixer for 10 min at 70°C for protein denaturation. Samples were centrifuged shortly and subjected to NuPAGE® Bis-Tris gels (4-12%), installed in a gel electrophoreses chamber. Generally, an amount of 2 µg/lane for Coomassie staining or 1 µg/lane for Western blotting was loaded on the gel. As molecular weight markers for antibody samples, SeeBlue® Plus2 Pre-Stained Protein Standard or Precision Plus Protein™ Unstained Protein Standards and for cell lysates PageRuler™ Plus Prestained Protein Ladder were used. Bis-Tris gels were run for 40 min at 200 V. Afterwards, gels were rinsed with deionized water and analyzed with Coomassie staining or Western blotting.

4.2.7. Coomassie staining

Coomassie staining was performed for detection of proteins that were previously separated by SDS-PAGE using InstantBlue™ Protein Stain. Gels were stained for at least 10-30 min on an orbital shaker, the staining solution

was discarded and the gels were rinsed 3 times with deionized water, according to the manufacturer's instructions.

4.2.8. Western blotting

Detection of proteins through Western blotting was carried out by detection antibodies conjugated to enzymes (e.g. AP, Alkaline phosphatase; HRP, horseradish peroxidase). Blotting was performed with the iBlot® Dry Blotting System according to the manufacturer's instructions. Briefly, proteins from SDS-PAGE gels were electro-transferred to polyvinylidene difluoride (PVDF) membranes (program 3, 7 min, 20 V) and immobilized proteins were detected with labeled antibodies.

4.2.9. Labeled antibodies

After transfer of proteins or ADCs to PVDF membrane, western blot workflow was achieved with the iBind™ Western System. This platform is based on sequential lateral flow technology and offers the advantage that simply all reagents like primary antibody, secondary antibody and wash solution are added sequentially to the system. Briefly, blotted membrane was immersed in 1X iBind™ Solution, primary and secondary antibodies were diluted in 1X iBind™ Solution. Afterwards, the iBind™ Card was prepared and the membrane was applied with the protein-side down. Finally, all solutions were added to the wells and the system was incubated for at least 2.5 h or overnight. After incubation, membrane was rinsed with deionized water and immunodetection protocol was performed by addition of BCIP/NBT Alkaline Phosphatase Substrate following the manufacturer's instructions.

4.2.10. Enzyme cleavage reactions and kinetics

For enzymatic hinge cleavage, cleavable antibodies and ADCs were incubated with respective enzymes recombinant human uPA and matriptase (R&D Systems). Protease cleavage was performed by adding antibody solutions at 500 nM to protease samples uPA (50 nM) or matriptase (20 nM), and incubation of the mixture at 37°C for 24 h in DPBS pH 7.4 under nonreduced conditions. The cleavage of antibody was analyzed by SDS-PAGE and ESI-MS. For enzyme kinetics, modified ADCs where incubated with uPA and matriptase at a ratio 25:1 (ADC:enzyme) and samples were taken at different time points. To stop the reaction, the irreversible inhibitor 1,5-Dansyl-Glu-Gly-Arg Chloromethyl Ketone was added at 10 µM and samples were stored at -80°C until analysis. Time points were analyzed by RP-HPLC using an Agilent PLRP-S 5 µm, 50 x 2,1 mm, 4000A column with water/0,1% TFA and acetonitrile/0,1% TFA as mobile phase (1.0 ml/min), where pre-assignment of fragments was achieved by RP coupled to MS in a previous run.

4.2.11. Total antibody enzyme-linked immunosorbent assay (ELISA) for serum stability

Prior to analysis, antibody or ADC samples were incubated at 0.5 mg/ml in human or mouse serum for 96 h at 37°C, 5% CO_2. Sampling at different time points was achieved and samples were frozen at - 80°C. Determination of antibody concentrations in complex matrices like human or mouse serum was achieved by enzyme-linked immunosorbent assay (ELISA). Prior to the main assay, antibodies were titrated for determining the linear

range for the concentration dependent reduction in ELISA signal in order to prevent signal saturation for the assay antibody concentration. Calibration standards and serum samples were diluted in The Blocking Solution. 96 well MaxiSorp® polystyrene microtiter plates were coated with 100 µl/well HER2, murine Fc-His at 2 µg/ml overnight at 4°C. Additionally, ILT5-His was included as an unrelated antigen to detect possible non-specific binding. After incubation and washing steps with 300 µl/well 1x DPBS/0.5 % Tween®20 using microplate washer ELx405™, calibration standards or analytes were added with 100 µl/well for 1 h at RT. Then, after washing steps 100 µl/well goat-anti human F(ab')2 x POD antibody was added and plate was washed again. The peroxidase was detected by addition of 100 µl 1 step Ultra TMB ELISA substrate solution and the reaction was stopped with 100 µl 2 N sulfuric acid. Absorbance was measured at 450 nm using the BioTek Synergy4 reader and respective software. The initial concentration time point at the beginning served for each antibody as 100% control and based on this, reduction in protein functionality was determined. In addition to total antibody concentration, free payload analysis of serum samples was measured with LC-MS.

4.2.12. Sortase-mediated toxin conjugation

Several conjugation technologies are established for site-specific conjugation of antibodies with linker payloads. Sortase-mediated antibody conjugation technology was performed with triple-glycine modified linker payloads to tagged light chains of the antibody or antibody fragment, resulting in a homogeneous and site-specific product. Triple-glycine modified linker payloads and sortase A were kindly provided by Merck KGaA. Antibodies were diluted to a concentration of 5 mg/ml in sortase conjugation buffer (150 mM NaCl, 50 mM Tris-HCl, pH 7.5). Briefly, tagged antibodies carrying a sortase recognition motif LPETGS with a (Gly_4-Ser_3)-spacer C-terminally on light chains were generated and purified by affinity chromatography. Afterwards, the reaction was carried out by using one equivalent of antibody construct and incubated with 10 equivalents of Gly_3-ValCit-PABC-MMAE substrate per sortase conjugation site, in the presence of 5 µM (0.37 eq) sortase and 5 mM $CaCl_2$ for 90 min at 25°C. Other used linker-payloads comprised Gly_3-ValCit-PABC-MMAF, as well as Gly_3-C_5-Alexa Fluor 488. The reaction was stopped by addition of 10 mM EDTA as calcium ion chelator, removing calcium ions and the resulting ADC reaction mix was purified by SEC with HiLoad Superdex 200 pg increase as described before. Purified ADC was concentrated with Amicon® Ultra-15 centrifugal filter device with 10,000 MWCO (3000 xg, 15 min) and analyzed by HIC and ESI-MS.

4.2.13. Transglutaminase conjugation

For conjugation of N297A mutated, deglycosylated antibodies, transglutaminase conjugation was achieved for site-specific modification of Q295. For this purpose, antibodies were diluted at 5 mg/ml in transglutaminase conjugation buffer (150 mM NaCl, 25 mM Tris-HCl, pH 8.0) and antibody-fluorophore conjugates were generated by attaching the quencher Gly_3-C_3-BHQ-10 to Q295 of the antibody. In this case, as described above, sortase conjugation was used to attach the fluorophore Gly_3-C_5-Alexa Fluor 488 to the light chain. To the antibody solution 10 equivalents linker quencher per transglutaminase site were added and incubated with transglutaminase (75 U/ml) at 37°C for 16 h. After incubation the reaction was cooled down to 10°C and resulting conjugates were purified by SEC as described before.

4.2.14. Intact mass analysis

ESI-MS analysis was performed using a Dionex U3000 HPLC system coupled to a Synapt-G2 mass spectrometer. 10 µg of protein solution was applied on a Proteomix RP-1000 4.6 mm x 100 mm (Sepax) column with mobile phase water/0.1% formic acid (0.5 ml/min). Detection at 214 nm was achieved for protein fragments and identification was done by the online coupled mass spectrometer.

4.3. Cell biological methods

4.3.1. Thawing of mammalian cells

Cells provided as cryovials at -180 °C were thawed rapidly in a water bath at 37 °C until the ice was dissolved. Resuspension of cells with 10 ml of pre-warmed medium was achieved and transferred into a 50 ml falcon tube. Cells were centrifuged for 10 min, 250 xg at RT. The supernatant was removed and the pellet was resuspended in 10 ml cell culture medium and seeded in a cell culture flask, incubating 3-4 days at 37°C, 5% CO_2, 180 rpm .

4.3.2. Cultivation of mammalian cells

Mammalian cell lines were cultured in cell culture flasks of appropriate sizes (T25-T175 for adherent cells or alternatively Erlenmeyer flask) using the recommended media formulations in an incubator with sterile conditions at 37°C, 5% CO_2 under humidified atmosphere. Cells were passaged usually every 3-4 days and cells were certified mycoplasma-free and never exceeded passage 20. Adherent cells were detached by 0,05% trypsin-EDTA (1 ml) or accutase for 3-5 min at 37°C after washing with pre-warmed DPBS to remove residual serum components. Trypsin activity was stopped by addition of FCS-containing medium and cell number as well as viability of detached adherent cells or suspension cells were measured by Vi-CELL® XR device by calculating the average of 20 images of trypan blue treated cells. Depending on cell growth and density, a sufficient amount of cells was re-seeded in a new cell culture flask with fresh medium. For further experiments, cells with a viability > 95% were pelleted (250 xg, 10 min, RT), supernatants were discarded and cells were diluted in pre-warmed medium yielding appropriate cell numbers (dependent on cell line).

4.3.3. Transfection of mammalian cells and antibody expression

Antibody expression was performed through transient transfection of antibody chains in Expi293F™ cells using the corresponding ExpiFectamine™ 293 transfection kit and media according to the manufacturer's instruction. Briefly, Expi293F™ cells were cultivated in 200 ml in Erlenmeyer flasks at 37°C, 5% CO_2 and 90 rpm orbital shaking. For passaging, cells were counted and diluted with fresh medium resulting in final cell number of 0.5 x 10^6 viable cells per ml. Two days before expression, Expi293F cells were diluted to a concentration of 1.3 x 10^6 viable cells per ml. On the day of transfection, cells with a viability > 96% were seeded with a final density of 2.9 x 10^6 viable cells per ml in pre-warmed Expi293™ Expression Medium.

For small scale expression (25 ml), 25 µg plasmid DNA (plasmid ratio: 1:1 HC:LC for mAbs and Fab fragments or 3:3:1 AG:LC:GA for one-armed SEED molecules) and 67.5 µl ExpiFectamine™293 Reagent were preincubated each in 1.25 ml OptiMEM® Reduced Serum Medium and subsequently mixed and incubated for 5 min. Afterwards, the diluted DNA solution was added to the ExpiFectamine™ 293 Reagent solution. After

20-30 min incubation, the DNA-transfection mix was added to 22 ml cells. 16-18 h post transfection, 150 µl of Enhancer 1 and 1.5 ml of Enhancer 2 were added. Supernatants were harvested 120 h post transfection by centrifugation (3500 xg, 15 min) and supernatants were clarified by sterile filtration through 0.22 µm Steriflip devices. For mid scale expression, the transfection volume was adjusted to 200 ml and the transfection mix was scaled up proportionately adjusting the amounts of the reagents used to 200 µg DNA and 540 µl ExpiFectamine™293. The overall procedure was analog to the description above. Supernatants were harvested by centrifugation (3500 xg, 15 min) and sterile filtration using Stericup devices.

4.3.4. Flow cytometry binding analysis

Flow cytometric analysis for antibody cellular binding to HER2-positive and EGFR-positive cell lines was carried out with a Guava easyCyte HT cytometer using corresponding software Guava ExpressPro. FACS binding buffer 1x PBS-1% BSA was prepared freshly and stored at 2-8°C. All washing and sample incubation steps were performed in FACS binding buffer. All incubation steps were performed darkened on ice during the whole experiment. Adherent cell lines were detached with trypsin-EDTA and cells were counted with the Vi-CELL®. Cells were centrifuged at 250 xg, 4°C for 10 min. The volume used for incubation and washing steps was 100 µl/well, final volume for flow cytometry measurement was 200 µl/well. Antibody binding to cellular targets by flow cytometry analysis was achieved by seeding $1x10^5$ vc/100 µl in a 96 microtiter plate and incubate with dilution of respective antibody and antibody fragments for 1 h (10 µg/ml). After washing with FACS binding buffer (3 times), antibody binding through incubation with polyclonal detection antibody goat anti-human IgG (H+L) Fab Fragment, Alexa Fluor® 488 was carried out at 20 µg/ml, 100 µl/well and incubated for 1 h. Fixation of the cells was achieved with 4% formaldehyde solution for 20 min (100 µl/well). Finally, microtiterplate was transferred to Guava easyCyte HT cytometer and 5,000 counts/well were measured per sample. Overlays of respective antibodies, positive and negative controls were compared on several cancer cell lines, indicating binding to the target.

4.3.5. Cellular internalization assay

Evaluation of internalization of antibody and antibody fragments was determined by flow cytometry using a quenching anti-Alexa Fluor® 488 Rabbit IgG Antibody to quench the fluorescence outside of the cell and to detect the amount of antibody that was internalized in the cell. The internalization assay has the same preparation and procedure as flow cytometry binding assay with additional internalization and quenching steps. For this approach, $1x10^5$ vc/well were incubated for 1 h with 10 µg/ml of analyte followed by detection with polyclonal antibody goat anti-human IgG (H+L) Fab Fragment, Alexa Fluor® 488 (20 µg/ml, 100 µl/well, 1 h.). After washing steps, cells were incubated at either 37°C, 5% CO_2 for the internalization step or at 4°C as a control preventing internalization for 1 h and 48 h. Afterwards, residual surface binding of analyte was quenched by anti-Alexa Fluor® 488 Rabbit IgG Antibody. Control samples were not quenched. Finally, fixation of cells with 4% formaldehyde solution was performed and subjected to Guava easyCyte HT cytometer. The relative internalization rate was quantified from the x-geometric mean fluorescence based on the following equation:

$$rel.internalization\ [\%] = \frac{(MFI\ 37°C\ quenched) - (MFI\ 4°C\ quenched)}{(MFI\ 37°C\ unquenched)} * 100$$

4.3.6. Preparation of cell lysates

For cell lysis of cultured mammalian cells, RIPA buffer was used to facilitate protein extraction from cytoplasmic, membrane and nuclear proteins and subsequently screen cells for western blotting. Culture medium was removed and cells were washed with ice-cold 1x PBS pH 7.4. Cells were lysed with 1 ml of RIPA buffer supplemented with Phosphatase Inhibitor Cocktail Set II (1:100), Protease Inhibitor Cocktail Set III (1:100), Benzonase (1:1000) and $MgCl_2$. The solution was added to a T75 flask and incubated on ice for 5 min. After incubation, lysate was collected and centrifuged in a tube at 14.000 xg for 15 min to pellet cell debris. Supernatant was transferred to a new tube for further analysis comprising Bradford assay, SDS-PAGE and Western Blot.

4.3.7. Cell Cytotoxicity Assay or Cell Viability Assay

Evaluation of the cytotoxic effect of ADCs on the viability of cancer cell lines was quantified using the ATP-based CellTiter-Glo® Luminescent Cell Viability Assay according to the manufacturer's instructions. ATP present in cell culture represents the metabolically active cells. In brief, cells were detached as described before and seeded (40 µl/well) in an opaque cell culture 384 well microplate to let cells settle down for 24 h at 37°C, 5% CO_2. Cells were seeded (only listed for HER2 cell lines) at the following densities: SKBR-3 (6000 vc/well), HCC1954 (3000 vc/well), MDA-MB-468 (2500 vc/well), BT-474 (7000 vc/well), NCI-N87 (2000 vc/well), SKOV-3 (2000 vc/well). ADCs as well as proteins were diluted at 1 µM in PBS/0.3% Tween®20 and small molecule compounds at 40 µM in DMSO. All samples were added in serial dilution by using Tecan D300e Digital Dispenser. ADC treatment (starting concentration 100 nM) was performed in duplicates in cell line specific medium. After 72 h incubation, viability of cells was detected by adding 30 µl/well of CellTiter-Glo® reagent with subsequent plate shaking for 2 min at 350 rpm and followed by 10 min incubation in the dark at RT. The luminescence was measured with Envision 2104 plate reader and data was processed using Genedata Screener. Luminescence values were normalized to values of untreated cells. Data were plotted as percentage of untreated cell viability versus the logarithm of antibody concentration and fitted using GraphPad Prism 7. At least three independent experiments with duplicates were used to calculate mean IC_{50} ± standard deviation (s.d.).

4.3.8. Tumor spheroid distribution/penetration

Tumor spheroids were grown for tumor penetration analysis by antibodies and antibody fragments in a 3D model. Before spheroid formation, cell culture medium was sterile filtered and cell line development was performed with cancer cell lines by seeding cells (40 µl/well) at different cell densities in 384 well spheroid microplates (Corning). After seeding cells, the plate is centrifuged twice at 1000 xg for 4 min, turning the plate 180 ° after first centrifugation step to make sure cells are centered in the middle of the well. The plate was incubated for at least 48 h at 37°C, 5% CO_2. After incubation, 3D spheroid formation was checked with the IncuCyte® S3 Live-Cell Analysis System using the spheroid scan type. Spheroid treatment was carried out with

6.25 nM of antibody-fluorophore conjugate and imaging of tumor spheroid penetration was carried out with the IncuCyte device over time using green fluorescence detection.

4.4. Biophysical methods

4.4.1. Biolayer interferometry (BLI)

For kinetic characterization of biomolecular interactions of antibodies, biosensor experiments using biolayer interferometry (BLI) were performed on an Octet Red96 platform using Octet Data Acquisition and Analysis software. In BLI experiments, the increase in layer thickness on biosensors tips by association and dissociation of bound molecules is measured, creating a shift in the interference pattern at the detector. In brief, anti-human Fab-CH1 (FAB2G) biosensor tips were pre-equilibrated in DPBS for 10 min before measurement. 200 µl/well of antibody solution at 3 µg/ml in DPBS was added in black 96 well plates and measurement was carried out at 25°C, 1000 rpm orbital sensor agitation. A baseline was established for the biosensors in DPBS for 60 sec and for the loading step, antibodies were immobilized on biosensor tips for 180 sec. Association and dissociation of the rherbb2-Fc analyte diluted in KB buffer was measured for 400 sec and 800 sec, respectively. Binding parameters were analyzed assuming a 1:1 Langmuir binding and model performing global curve fitting with Octet Data Analysis software. As negative controls, unrelated isotype control antibody anti-hen egg lysozyme (anti-HEL) and unrelated antigen CD40 Avi His were implemented to exclude unspecific binding effects.

4.4.2. Nano Differential Scanning Fluorimetry (nanoDSF)

Thermal unfolding analysis and thermal stability of antibodies was measured to determine the melting point and aggregation of proteins using Prometheus NT.PLEX nanoDSF according to the manufacturer's instruction. With nanoDSF technology no fluorescence labeling is required and the system detects the intrinsic fluorescence of tyrosine and tryptophane residues at 330 nm and 350 nm under native conditions. In brief, in a 384 well plate 15 µl of 1 mg/ml protein formulation (1x PBS pH 7.4) was dispensed, in order to fill up Standard Capillary Chips with at least 10 µl of protein sample. Before starting the measurement, an initial discovery scan is necessary to adjust the excitation power that detects the initial fluorescence in the capillaries. Protein unfolding characteristics were analyzed from 20-95°C with excitation power 11% and a temperature gradient 1.0°C/min by monitoring the change of intrinsic protein fluorescence. Data acquisition and analysis was processed with Software PR.Thermo Control (NanoTemper Technologies) and melting points were determined by measuring the maximum of the first derivative curve of F330nm/F350nm ratios.

5. Results

5.1. Design and generation of cleavable antibodies and ADCs

To investigate the specific hinge cleavage by tumor-associated proteases uPA and matriptase, a cleavable linker design was utilized to introduce an additional 8 amino acids protease site in the IgG1 hinge region of Trastuzumab and Cetuximab.[199] The anti-HER2 antibody Trastuzumab and the anti-EGFR antibody Cetuximab were used as model antibodies because both molecules are well characterized in several studies and many development efforts in the field of ADCs are using these antibodies. Cleavable antibodies are denoted Trastuzumab CL (cleavable) and Cetuximab CL, containing the cleavable protease site LSGRSDNH in the hinge region, adjacent to the natural papain cleavage site (**Figure 18**).[198] As negative controls Trastuzumab nCL (noncleavable) and Cetuximab nCL constructs were designed that replace the protease site by a GGSGGSGG linker.

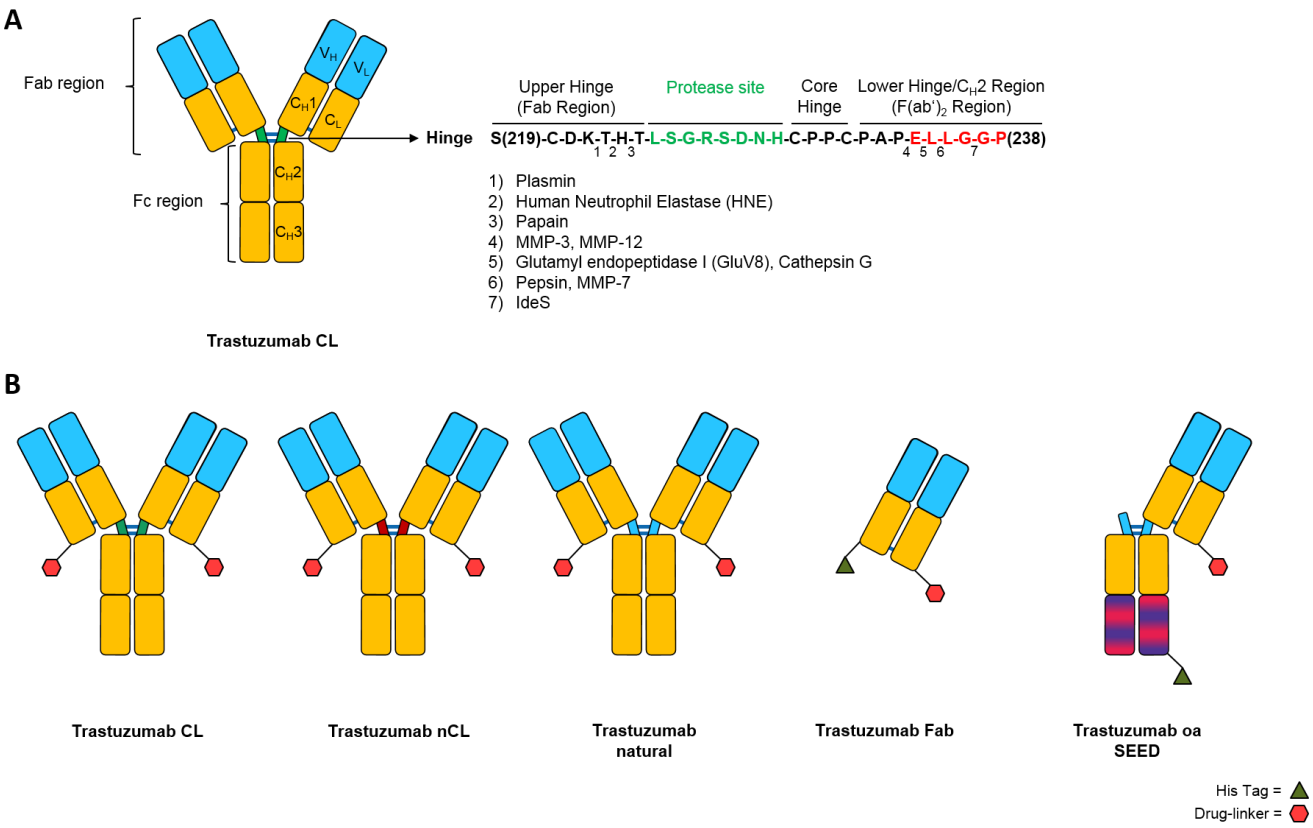

Figure 18: Design of cleavable protease site in hinge region of IgG antibody and Trastuzumab ADC variants.

Depicted are the hinge amino acids with the upper, core and lower hinge region. Additional protease site that is sensitive to tumor proteases is highlighted in green (**A**). Cleavage sites for natural occuring proteases are indicated with numbers below amino acid sequence and responsible amino acids for FcγR binding are highlighted in red. ADC variants (**B**) with Trastuzumab CL (with cleavable hinge region), Trastuzumab nCL (noncleavable hinge), Trastuzumab natural (native antibody), Trastuzumab Fab fragment and Trastuzumab oa SEED. Payloads are attached to the light chains via sortase-mediated antibody conjugation technology. Figure is modified from Brezski et al.[199] CL = cleavable, nCL = noncleavable, oa = one-armed

For comparison of key antibody characteristics, different antibody formats were generated and included in further experiments. In the present study, in addition to the constructs Trasutuzmab CL, Trastuzumab nCL, also Trastuzumab natural (native antibody), Trastuzumab Fab fragment and Trastuzumab oa (one-armed) SEED were used as references (**Figure 18**). By analogy, Cetuximab variants and also Trastuzumab N297A mutated antibodies were utilized with the same design. All constructs carry the sortase A recognition tag LPETGS C-terminally on the light chain that is used for site-specific conjugation of cytotoxic drugs and only the Trastuzumab Fab fragment is lacking the Fc-part. Generally, two routes enable Fab fragment production and purification, namely papain digestion of an IgG antibody and transient mammalian expression. For papain digestion protein A affinity chromatography can be used, whereas for his-tagged Fab fragments IMAC is utilized.[200] Due to insufficient yields with papain digestion of Trastuzumab (data not shown), expression of Trastuzumab Fab was preferred. The different antibody variants were produced by transient expression in Expi293 cells, purified by protein A affinity chromatography and analyzed by SDS-PAGE as well as analytical SEC (**Appendix 1, 2 and 7**). Trastuzumab Fab and Trastuzumab oa SEED were purified using IMAC and anti-penta His Western Blot confirmed present His-Tag (**Appendix 3 and 4**). Besides the Trastuzumab variants, Cetuximab-based antibodies and Trastuzumab N297A mutated constructs were also expressed in Expi293 cells and purified (**Appendix 5 and 6**). The expression yields as well as protein purity by analytical SEC of the generated antibodies are summarized in **Table 4**.

Table 4: Expression yields of different antibody constructs and purity as monomeric protein.

Purified antibody yields after transient expression in Expi293 cells using protein A affinity chromatography for mAbs or IMAC for antibody fragments. Yields are calculated as mg/200ml or mg/l. Protein purity was determined by analytical SEC and is indicated as percentage [%] monomeric product. CL = cleavable, nCL = noncleavable, oa = one-armed

Antibody construct	Yield [mg/200 ml]	Yield [mg/l]	Purity after SEC [%]
Trastuzumab CL	26.9	134.5	97.9
Trastuzumab nCL	37.6	188.0	93.7
Trastuzumab natural	34.0	170.0	100.0
Trastuzumab Fab	32.8	164.0	100.0
Trastuzumab oa SEED	25.1	125.5	100.0
Trastuzumab CL N297A	19.9	99.5	100.0
Trastuzumab nCL N297A	39.5	197.5	97.2
Trastuzumab natural N297A	33.1	165.5	97.4
Trastuzumab oa SEED N297A	16.4	82.0	95.8
Cetuximab CL	20.5	102.5	97.2
Cetuximab nCL	19.8	99.0	99.8
Cetuximab natural	18.9	94.5	99.6
Cetuximab Fab	6.6	33.0	98.5
Cetuximab oa SEED	5.2	26.0	87.4

Separate sterilcontrols of used plasmids were prepared by adding plasmid DNA in Expi293 expression medium alone and incubating at 37°C, 5% CO_2. Expression yields of Trastuzumab variants ranged from 82 to 197 mg/l after purification, whereas for Cetuximab antibodies values from 26 to 102 mg/l were achieved. Generally, expression of Cetuximab constructs showed lower yields compared to Trastuzumab. Especially, monovalent Cetuximab Fab and Cetuximab oa SEED showed low protein amounts after purification. Highest yields were obtained for the Trastuzumab nCL and Trastuzumab natural constructs (also deglycosylated N297A variants), but also Trastuzumab CL showed good expression values. Regarding protein purity, almost all constructs were monomeric and showed purity > 95%, indicating that no high molecular weight species like protein aggregates are present. This is of particular importance for cell based assays because aggregates lead to unexpected results and bias.

5.1.1. Preparation of ADCs

As an initial experiment, the protease cleavage of the designed Trastuzumab CL was assessed by tumor proteases uPA and matriptase, to determine the selective cleavage site within the hinge region. On the assumption that the cleavable sequence is still accessible buried in the hinge region, Trastuzumab CL was incubated with and without uPA and matriptase for 24 h and 37°C, and also with negative controls. As it is obvious, that only the Fab and Fc band occurred for unconjugated Trastuzumab CL with tumor proteases, specific enzymatic cleavage occurred and the accessibility to the cleavage site was demonstrated (**Appendix 8**). Based on the first results, unconjugated antibodies were proceeded to ADC conjugation. The general ADC design is depicted in **Figure 18 B**, and is structural illustrated for MMAE-based constructs in **Figure 19**.

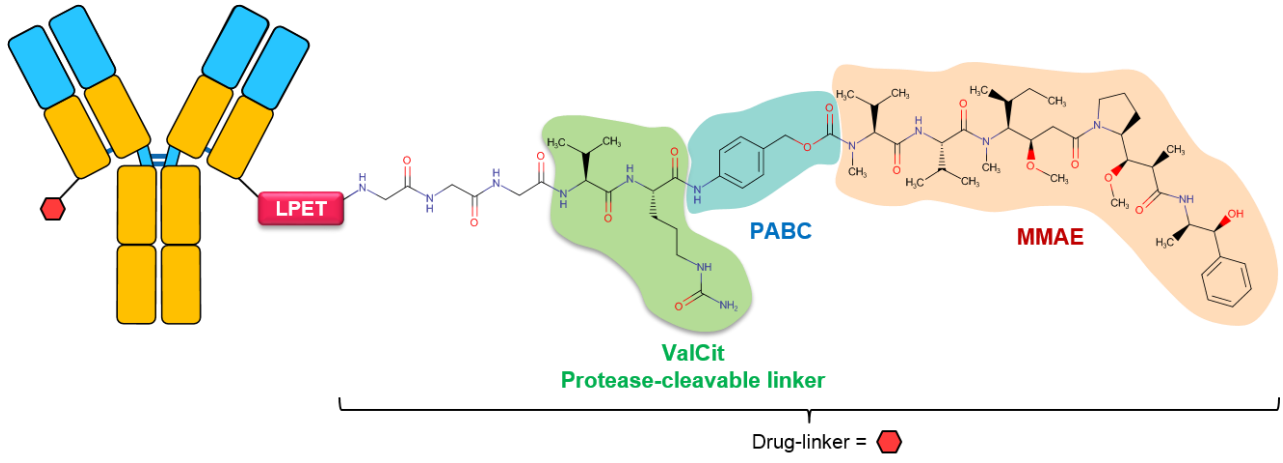

Figure 19: General ADC structure with MMAE as payload.

Illustration shows generic structural composition of generated ADCs (Antibody-Gly_3-ValCit-PABC-MMAE). Site-specific conjugation was achieved by sortase A mediated antibody conjugation technology by attaching triple-glycine drug-linker to sortase A recognition motif LPETGS C-terminally to light chain of the antibody. The drug-linker consists beside the triple-glycine of valine-citrulline, PABC and MMAE as the cytotoxic compound.

ADCs were generated based on the anti-HER2 antibody Trastuzumab and anti-EGFR antibody Cetuximab. In general, in the course of this work, an ADC is denoted by describing the mAb and the conjugated payload as mAb x payload (e.g. Trastuzumab CL x MMAE). Payloads that were used for toxin-based ADCs were mainly

microtubule inhibiting agents like MMAE and MMAF. The basic structure of the linker drugs comprised a valine-citrulline dipeptide motif that is cleaved within the lysosomes by cathepsin B. The dipeptide linker is connected to a self immolative PABC portion that is fragmented upon cleavage and releases efficiently the payload. The triple-glycine motif is utilized for sortase conjugation and is attached to the LPETGS recognition motif on the antibody. An overview of the generated ADCs and monovalent FDCs (Fragment-drug conjugates) used in this work is given in **Table 5**.

Table 5: Overview of ADCs and monovalent FDCs conjugated by sortase A technology.

Generated ADCs and FDCs (Fragment-drug conjugates) with respective DAR after conjugation reaction using sortase A. Listed are the ADC constructs with the used payloads and the linker structure. Protein purity was determined by analytical SEC and is indicated as percentage [%] monomeric product. AF488 = Alexa Fluor 488, BHQ-10 = Black Hole Quencher-10, CL = cleavable, nCL = noncleavable, oa = one-armed, Gly_3-ValCit-PABC = triple-glycine valine-citrulline para-aminobenzyloxycarbonyl, N297A = mutation of asparagine (N) to alanine (A) at position 297

ADC construct	Payload	Linker	DAR	Purity after SEC [%]
Trastuzumab CL x MMAE	MMAE	Gly_3-ValCit-PABC	1.9	98.6
Trastuzumab nCL x MMAE	MMAE	Gly_3-ValCit-PABC	1.8	99.2
Trastuzumab natural x MMAE	MMAE	Gly_3-ValCit-PABC	1.8	99.1
Trastuzumab Fab His x MMAE	MMAE	Gly_3-ValCit-PABC	0.9	99.1
Trastuzumab oa SEED x MMAE	MMAE	Gly_3-ValCit-PABC	0.8	99.0
Trastuzumab CL x MMAF	MMAF	Gly_3-ValCit-PABC	1.7	99.5
Trastuzumab nCL x MMAF	MMAF	Gly_3-ValCit-PABC	1.8	99.3
Trastuzumab natural x MMAF	MMAF	Gly_3-ValCit-PABC	1.9	100.0
Trastuzumab Fab His x MMAF	MMAF	Gly_3-ValCit-PABC	0.7	88.9
Trastuzumab oa SEED x MMAF	MMAF	Gly_3-ValCit-PABC	0.8	98.8
Trastuzumab CL N297A x AF488 x BHQ-10	AF488	Gly_3-C_5, Gly_3-C_3	3.3	100.0
Trastuzumab nCL N297A x AF488	AF488	Gly_3-C_5	1.6	97.1
Trastuzumab natural N297A x AF488	AF488	Gly_3-C_5	1.6	96.3
Trastuzumab Fab His x AF488	AF488	Gly_3-C_5	0.8	98.8
Cetuximab CL x MMAE	MMAE	Gly_3-ValCit-PABC	1.1	99.4
Cetuximab nCL x MMAE	MMAE	Gly_3-ValCit-PABC	1.3	99.4
Cetuximab natural x MMAE	MMAE	Gly_3-ValCit-PABC	1.1	99.5
Cetuximab Fab His x MMAE	MMAE	Gly_3-ValCit-PABC	0.8	99.5
Cetuximab oa SEED x MMAE	MMAE	Gly_3-ValCit-PABC	0.8	99.4

Conjugation of antibody constructs with $(G_4S)_3$-LPETGS tag C-terminally on the light chain was performed using sortase A technology. After conjugation reaction, the purified ADC formulated in PBS pH 7.4 was analyzed by analytical SEC and HIC as well as ESI-MS to evaluate conjugation reactions. The Drug-to-antibody ratio (DAR) of ADCs is used to describe how many molecules are conjugated to the antibody. As Fab fragments and one-armed (oa) SEED molecules have only one light chain, also only one conjugation site is available, reaching at most a DAR of 1. The DAR of Fab fragments and oa SEEDs ranged from 0.7 to 0.9. For the other

formats, conventional IgGs were used that have two intact light chains present each with a sortase A tag. Therefore a possible DAR of 2 can be reached. The Trastuzumab IgG variants yielded DAR species from 1.6 to 1.9. Cetuximab ADCs exhibited a poor conjugation efficiency, reaching a DAR of approximately 1.1 to 1.3. Therefore, the conjugation reaction with Cetuximab ADCs was incomplete. Regarding protein purity, almost all constructs exhibited a monomeric content of > 95%. Successful conjugation was confirmed by ESI-MS and HIC indicating attached toxin to the light chains (**Appendix 9**). The general structure of MMAF-based ADCs is displayed in **Appendix 10** and SEC chromatograms are depicted in **Appendix 11**. In the following, investigations regarding the protease cleavage of the hinge region, the exact cleavage site and the selectivity of the protease site were pursued.

5.1.2. Characterization of hinge cleavable ADCs and determination of cleavage site

In the context of ADC generation, it was tested if tumor proteases uPA and matriptase are still able to cleave the modified hinge region, when a drug-linker is attached to the antibody. For this purpose, Trastuzumab CL x MMAE, Trastuzumab nCL x MMAE and Trastuzumab natural x MMAE were incubated with catalytic amounts of uPA, tPA and matriptase at 37°C for 24 h. The same ADC samples were also incubated without respective enzymes. Semi-quantitative evaluation was carried out with SDS-PAGE analysis and demonstrated specific protease cleavage within the hinge region. Only Trastuzumab CL x MMAE incubated with uPA showed a Fab band at approximately 50 kDa as well as a Fc band at 53 kDa, whereas incubation of the ADC sample with matriptase exhibited a much faster and quantitative reaction compared to the sample with uPA because no intact ADC band is observed at 150 kDa (**Figure 20**). Trastuzuman nCL x MMAE and Trastuzumab natural x MMAE were unaffected by enzyme activity.

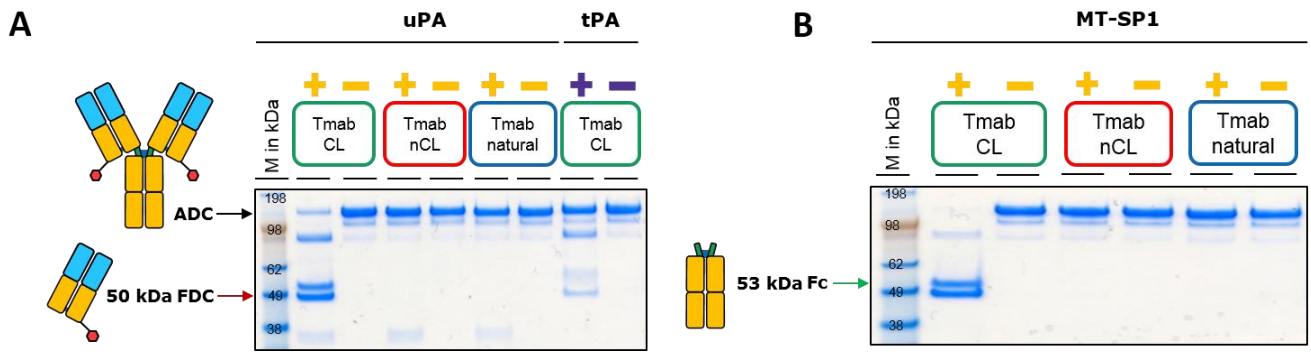

Figure 20: SDS-PAGE analysis of Trastuzumab x MMAE ADCs incubated with tumor proteases uPA and matriptase.

Protease cleavage of ADC variants with MMAE by uPA (**A**) and matriptase (MT-SP1) (**B**). Incubation of tPA, a homologous enzyme to uPA was also tested. Samples Tmab CL x MMAE, Tmab nCL x MMAE and Tmab natural x MMAE were incubated with (+) or without (-) enzyme at 37°C for 24 h and were non-reduced. After SDS-PAGE run, InstantBlue stain was performed at least for 30 min. Tmab = Trastuzumab, + = with enzyme, - = without enzyme

Hence, specific hinge cleavage of Trastuzumab CL x MMAE by extracellular tumor proteases corroborated that smaller fragment-drug conjugates were released. Incubation with tPA, a homologous enzyme to uPA, displayed a slightly, unspecific cleavage of Trastuzumab CL x MMAE that is only observed to a minor extent. To

determine whether protease cleavage could be transferred to different antibodies as well as other linker-payload structures, Trastuzumab x MMAF ADCs, deglycosylated Trastuzumab x AF488 conjugates and Cetuximab x MMAE ADCs were tested. As observed with Trastuzumab x MMAE constructs, the same pattern for other cleavable antibodies based on Cetuximab or N297A mutated Trastuzumab variants was obtained as well as for different linker-payloads (**Appendix 12**). Therefore, independent of the antibody as well as for various linker-payloads, no sterical hindrance is assumed for the protease site. For evaluation whether the selectivity of the linker cleavage is solely related to uPA and matriptase, a broader panel of proteases including proteases not restricted to the tumor microenvironment (like MMPs) were tested for enzymatic cleavage. These proteases comprised prominent matrix metalloproteinases MMP-9, MMP-14, but also ADAM-10, Legumain and Kallikrein. These experiments indicated that none of the proteases was capable to cleave the protease site LSGRSDNH in Trastuzumab CL x MMAE, therefore suggesting a high selectivity for this sequence. In order to verify the observed bands from the cleavage reactions and to determine the exact cleavage site within the hinge region, ESI-MS analysis was utilized. Analysis of cleavage site was carried out with intact protein analysis by using non-reduced samples. As with the SDS-PAGE samples, Trastuzumab CL x MMAE and Trastuzumab CL x MMAF were incubated with uPA or matriptase at 37°C for 24 h and mass fragments were determined. For the cleavable ADC the most important fragments are the FDC and Fc fragments, because this will give valuable information about the exact cleavage site within the engineered hinge region. As the MS spectra illustrate, the selective cleavage site of the proteases is between arginine and serine within the 8 amino acid sequence (**Figure 21**). The expected mass from the FDC and Fc part match perfectly with the observed mass that was measured by ESI-MS. The released FDC of Trastuzumab CL x MMAE was found to have a mass of 50.91 kDa whereas the Fc part shows a mass of 53.64 kDa. The higher molecular weight of the Fc portion can be attributed to the N-glycosylation that is represented by N-glycan type G0F, which accounts for 1445.3 Da and consists of a core structure with 4 N-acetylglucosamine (2 terminal), 3 mannose and 1 fucose residue.
Moreover, another crucial information extracted from ESI-MS analysis is that the Fab fragment is still intact and the linker-drug is attached to it. Therefore, the tumor proteases have no impact on the linker-drug structure. Besides tested MMAE-based constructs, Trastuzumab CL x MMAF as well as Cetuximab CL x MMAE were analyzed by ESI-MS for protease cleavage and obtained results indicate that in accordance with Trastuzumab CL x MMAE, expected mass of fragments could be verified (**Appendix 13, 14 and 15**). In the case of Cetuximab-based ADCs, different glycoform species are present that comprise various sugar derivatives and thus make this ADC a more heterogeneous product. To summarize the cleavage experiments, it was proved that the modification of the hinge region including a protease site can be successfully used to generate a FDC originating from an ADC upon incubation with tumor proteases. This FDC should be capable to deliver the cytotoxic compound and induce a pronounced cytotoxic activity as the payload is conjugated to the fragment.

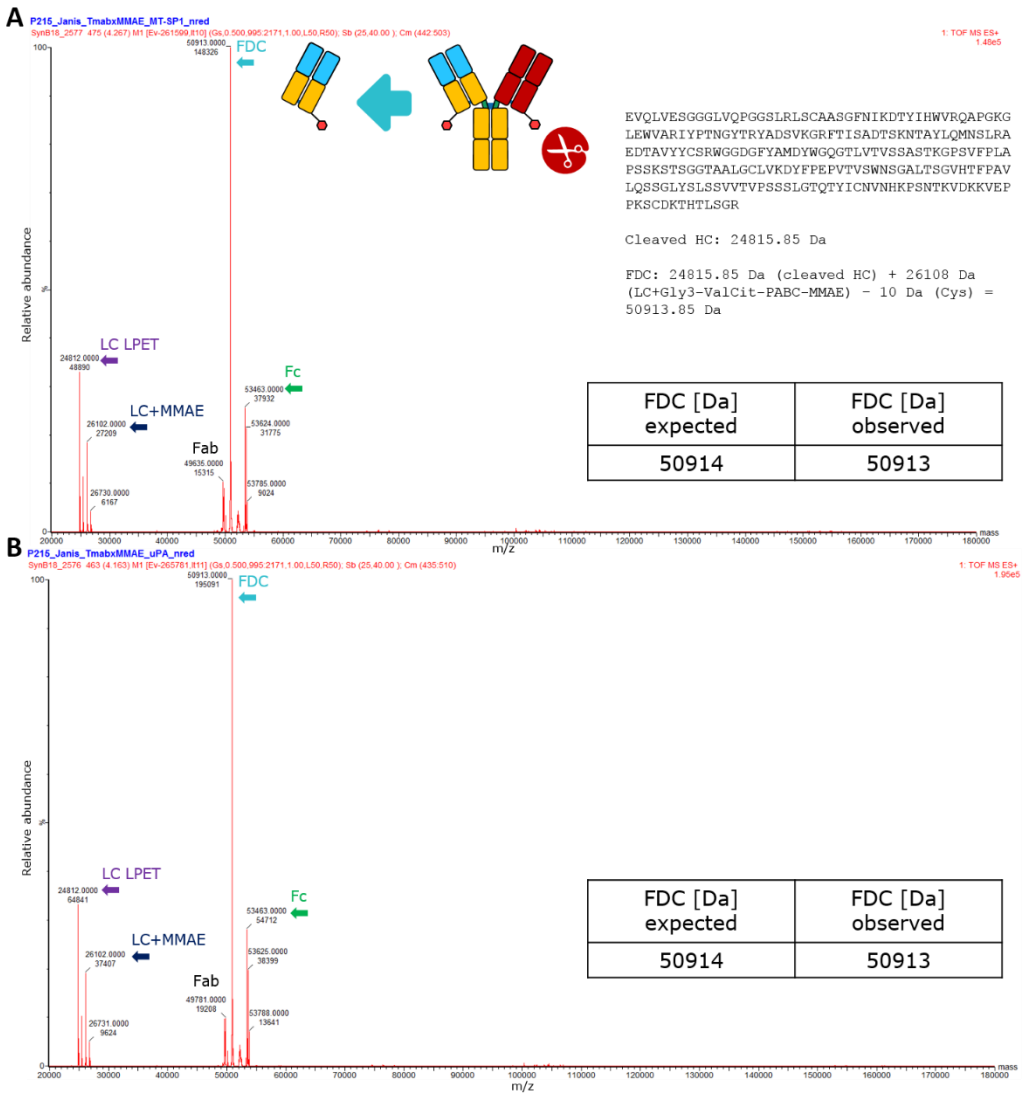

Figure 21: Mass confirmation of FDC and verification of uPA/MT-SP1 cleavage site by ESI-MS.

MS spectra of Trastuzumab CL x MMAE that was incubated with MT-SP1 (**A**) and uPA (**B**) and cleaved fragments were analyzed by ESI-MS. In accordance with the expected mass, hinge cleavage releases FDC fragment that correlates with observed mass.

As it was observed by SDS-PAGE analysis that the two tumor proteases seem to have different cleavage rates, enzyme kinetic studies will be achieved. In the following chapter, experiments regarding the fast cleavage reaction by the two tumor proteases will be investigated.

5.1.3. Enzyme kinetics and release of FDC

For quantification of released FDCs over time, Trastuzumab CL x MMAE was incubated with uPA and matriptase at 37°C for 24 h and samples were taken at different time points. Prior to analysis, experiments with enzyme inhibitors revealed that enzyme activity is abrogated by addition of Ecotin, HAI-1 and 1,5-Dansyl-Glu-Gly-Arg Chloromethyl Ketone. As the reaction was stopped most efficiently with the irreversible inhibitor 1,5-Dansyl-Glu-Gly-Arg Chloromethyl Ketone (**Appendix 16**), this small molecule was used at 10 µM to stop the reaction of uPA and matriptase at 10 different time points and samples were analyzed by RP-HPLC (**Appendix 17**). Assignment of fragment peaks was achieved in a previous run by RP coupled to MS, where the

first peak was attributed to the Fc part, the second unconjugated Fab and the third peak was the FDC carrying the payload (**Appendix 16**). After cleavage reaction with uPA and matriptase the resulting DAR was determined and was 0.8, hence indicating intact FDC with payload. Besides Trastuzumab CL x MMAE cleavage, this peak pattern was also obtained by Trastuzumab CL x MMAF with tumor proteases (data not shown).

Enzyme kinetic studies exhibited a high conversion of the cleavable substrate Trastuzumab CL x MMAE. uPA showed a slower cleavage reaction compared to matriptase, because the catalytic reaction of uPA reaches its plateau at approximately 4 h after incubation, whereas matriptase converts all substrate completely after 1 h (**Figure 22**).

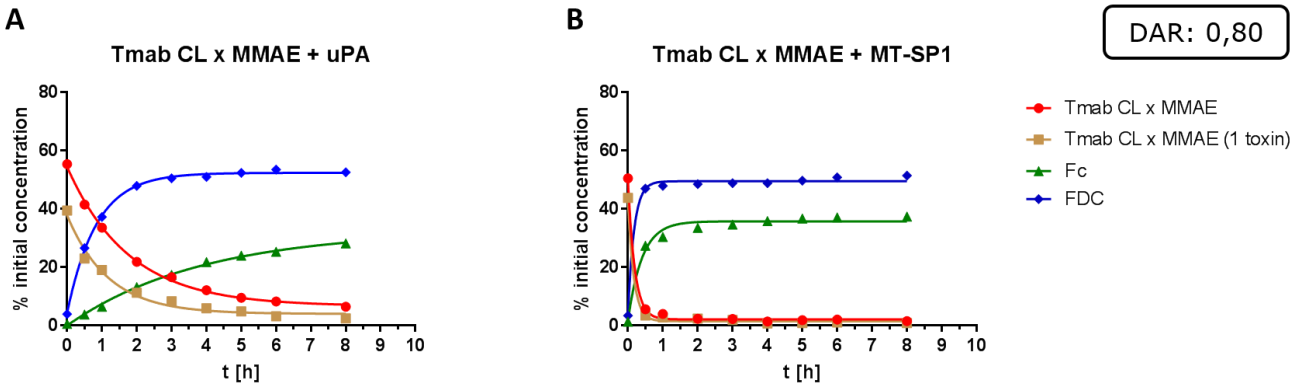

Figure 22: Enzyme kinetics of uPA and matriptase incubated with Trastuzumab CL x MMAE.

Enzyme kinetic studies of uPA (**A**) and matriptase (MT-SP1) (**B**) exhibited high conversion of substrate Trastuzumab CL x MMAE. Quantification of cleaved fragments was achieved by using RP-HPLC with respective peak assignment. Plotted are the percentage [%] of initial concentration of different species against the time points. Curves are depicted of Trastuzumab CL x MMAE (red), Trastuzumab CL x MMAE with DAR 1 (brown), Fc part (green) and FDC (blue). Each time point was measured in duplicates. For simplicity reasons, the 24 h time point was excluded. Tmab = Trastuzumab

In both cases, the reactions show a proportional decrease of substrate as well as an increase of respective products that was also confirmed by SDS-PAGE analysis (**Appendix 18**). For the uPA reaction after 24 h, 2.4% of the Trastuzumab CL x MMAE construct and 1.3% for Trastuzumab CL x MMAE (1 toxin) are remaining, whereas 31.6% of the Fc part and 53.5% of the FDC are released. Matriptase conversion resulted in 1.9% remaining Trastuzumab CL x MMAE and 0.8% Trastuzumab CL x MMAE (1 toxin) after 24 h. Released Fc portion accounts for 38.3% and 53.2% FDC is released.

Consequently, the high turnover rate of the catalytic reactions indicate that the sequence of the protease site in the hinge region is well suited for a fast and efficient release of FDCs. To investigate whether the modified hinge region affects antibody binding and internalization properties, molecular interactions with the target as well as cellular binding and internalization of the antibodies are tested.

5.2. Characterization of antibody binding affinity and internalization

To assess the influence of the engineered hinge region on antibody function and binding, kinetic parameters of conventional IgG antibodies and antibody fragments were evaluated by biolayer interferometry (BLI). For this biophysical method, antibodies were immobilized on anti-human Fab-CH1 (FAB2G) biosensor tips and association and dissociation of the antigen HER2 is analyzed. Kinetic parameters of unconjugated antibodies

and antibody fragments are summarized in **Table 6** and association and dissociation graphs are exemplarily shown in **Figure 23**. BLI experiments showed that no significant alteration in functional binding of modified antibodies to the antigen is observed and monovalent fragments maintained nanomolar affinity values in the same range like IgG antibodies. The commercial product Herceptin was included for the experiments as the benchmark molecule and had an affinity of 0.51 nM, likewise for the Trastuzumab CL construct a binding affinity to recombinant HER2 was in the subnanomolar range with 0.46 nM. Trastuzumab nCL exhibited K_D values of 0.70 nM. For Trastuzumab Fab His, a binding affinity of 0.27 nM was determined and for Trastuzumab natural the affinity was 0.06 nM.

Table 6: Overview of kinetic parameters for engineered antibodies and monovalent fragments determined by BLI.

Affinities are shown as equilibrium dissociation constant (K_D), association (k_a) and dissociation rates (k_d) were measured by BLI. Antibodies were immobilized on FAB2G biosensor tips followed by association and dissociation of the antigen HER2. For each measurement, six analyte concentrations were measured ranging from 1.56 nM to 50 nM. Trastuzumab CL, Trastuzumab nCL, Trastuzumab natural and commercial Herceptin are bivalent IgGs and Trastuzumab Fab His represents a monovalent binder.

Antibody construct	Analyte	K_D [M]	k_a [$M^{-1}s^{-1}$]	k_d [s^{-1}]
Herceptin	HER2	5,13E-10	1,35E+05	6,94E-05
Trastuzumab CL	HER2	4,63E-10	1,24E+05	5,74E-05
Trastuzumab nCL	HER2	7,01E-10	1,38E+05	9,64E-05
Trastuzumab natural	HER2	5,60E-11	1,38E+05	7,70E-06
Trastuzumab Fab His	HER2	2,70E-10	1,39E+05	3,76E-05

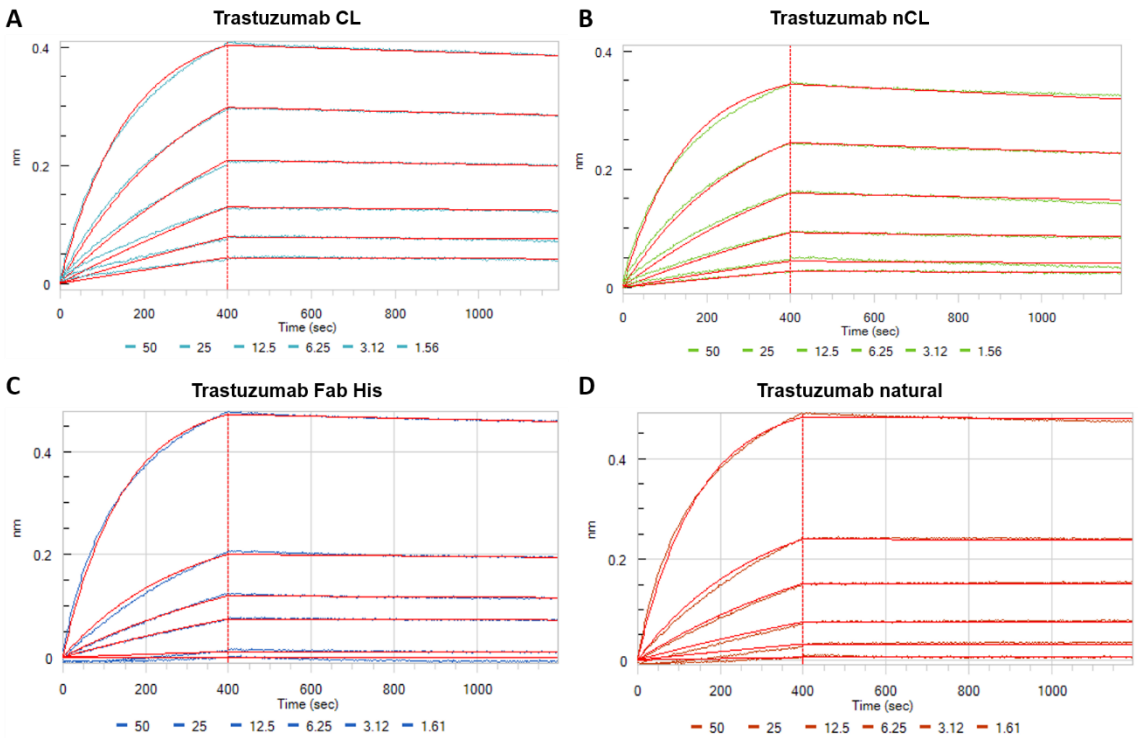

Figure 23: Comparison of affinity and kinetic analysis of produced antibodies and antibody fragments determined by BLI.

Bivalent Trastuzumab CL (**A**), Trastuzumab nCL (**B**) and Trastuzumab natural (**D**) and monovalent Trastuzumab Fab His (**C**) were analyzed with anti-human Fab-CH1 (FAB2G) biosensors. For K_D values the association and dissociation were monitored for 400 sec and 800 sec, respectively. Interference pattern shift [nm] is monitored with varying concentrations of analyte over the time [sec].

Anti-HEL antibody was used as an isotype control and CD40 Avi His as an unrelated antigen to test unspecific binding behavior (**Appendix 19**). In both cases, no binding was detected. Taken together, molecular interactions of antibodies to its cognate antigen was verified, exhibiting high affinity for all produced constructs and to test antibodies in a more appropriate setting, cellular binding was investigated.

5.2.1. Flow cytometry binding analysis of antibodies and antibody fragments

As antibodies and antibody fragments displayed suitable kinetic parameters with high affinities in the subnanomolar range to HER2, as a following step cellular binding to target expressing cells was determined. In a FACS binding assay, it was tested if the modified hinge region is affecting cellular binding of the antibodies. For this purpose, antibodies at a concentration of 10 µg/ml were incubated with cancer cell lines and detected by goat anti-human IgG (H+L) Fab Fragment, Alexa Fluor 488 conjugate. HER2-expressing cancer cell lines with different receptor expression levels were selected for FACS binding analysis. According to Li et al., for the HER2-negative cell line MDA-MB-468 no detectable HER2 level is achieved. Whereas for MCF-7, low HER2 expression levels are known to be 3.646 relative HER2 density on a cell. SKBR-3 was used as a high expressing HER2-positive cell line that expresses 1.517.135 relative HER2 molecules on a cell.[201] Different receptor expression of used cell lines was also confirmed in previous studies (personal communication, Merck, Darmstadt, Germany).

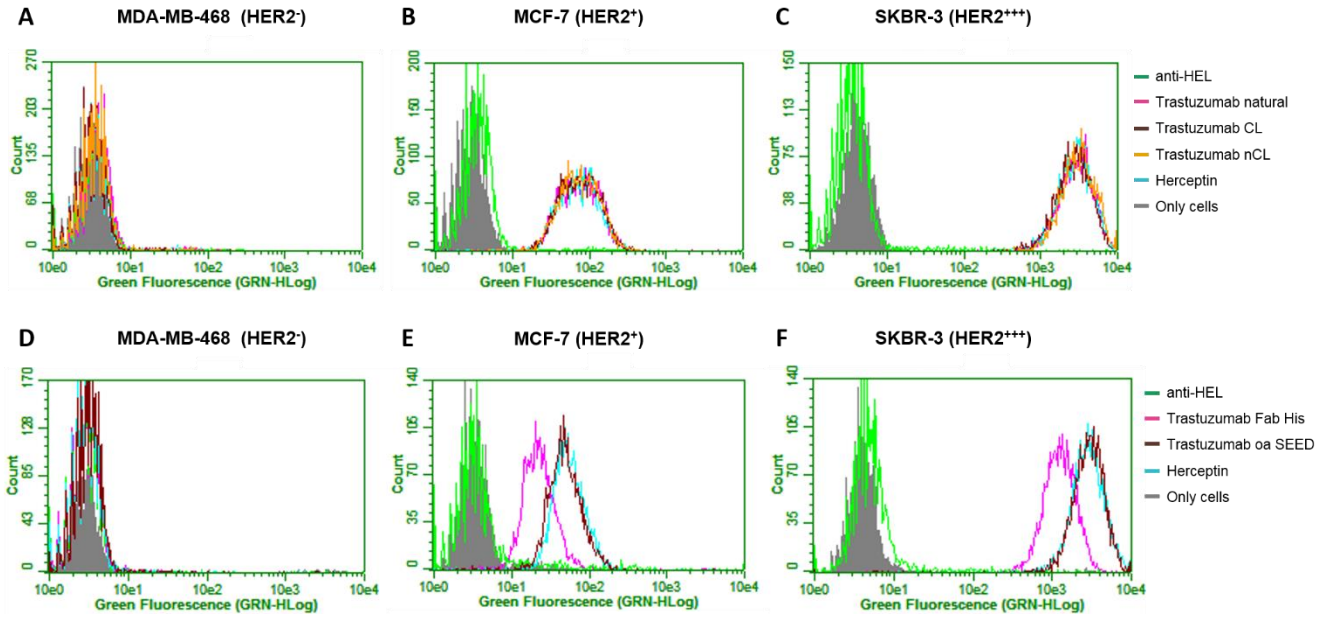

Figure 24: Cellular binding of designed antibodies and antibody fragments to several cancer cell lines.

Cells were seeded with 1 x 10^5 vc/well, incubated with antibodies at 10 µg/ml and detected with goat anti-human IgG (H+L) Fab Fragment, Alexa Fluor 488 conjugate via flow cytometry. Antibodies and antibody fragments displayed no binding to HER2-negative MDA-MB-468 cells for bivalent (**A**) and monovalent antibodies (**D**). On the low-expressing HER2 cell line MCF-7, binding of all antibodies is increased (**B**), whereas monovalent Trastuzumab Fab His shows a slightly weaker binding compared to IgG antibodies (**E**). For SKBR-3 cells a strong binding effect is obtained for conventional antibody format (**C**) and antibody fragments (**F**). In all cases, binding is comparable to commercial Herceptin. Measurement was carried out with Guava easyCyte HT cytometer using the green fluorescence channel. FSC (forward scatter) and SSC (side scatter) were adjusted, samples were measured in duplicates.

Also for flow cytometry, anti-HEL was utilized as isotype control and other controls comprised unstained cancer cells or cells incubated with goat anti-human IgG (H+L) Fab Fragment, Alexa Fluor® 488 conjugate. Overlay of histograms for relative fluorescence intensities of produced Trastuzumab-based antibodies are exemplarily shown in **Figure 24**. The results exhibited a slight binding of antibodies to low-expressed HER2 on MCF-7 cells, whereas a strong cellular binding was observed on HER2-overexpressing cell line SKBR-3, indicated by the pronounced shift. As a reference antibody Herceptin was also tested and overlays of produced antibodies are identical with this control, suggesting similar binding properties on the cell surface. Trastuzumab Fab His shows a slightly weaker binding compared to IgG antibodies. Moreover, on HER2-negative cells MDA-MB-468 no unspecific binding of IgG antibodies and antibody fragments was detected and also with the anti-HEL antibody no target-dependent binding to HER2-positive and HER2-negative cells was observed. For Cetuximab-based constructs (**Appendix 20)** and for deglycosylated Trastuzumab N297A mutated variants (data not shown) FACS binding results reveal also similar binding to benchmark antibody Erbitux or Herceptin, respectively. To summarize cellular binding experiments, binding properties are similar to commercial Herceptin or Erbitux on target positive and negative cells and antibodies with hinge modification exhibit similar binding to cancer cell lines.

5.2.2. Cellular internalization assay

As antibodies bind to cell surface targets on cancer cells, subsequent internalization should be sufficient and is a critical parameter particularly in the context of ADC delivery and trafficking. Therefore, investigations regarding internalization rates of the different antibody formats were carried out. Generally, upon binding to HER2, receptor mediated endocytosis is induced and vesicle formation from the cell surface is achieved. Afterwards, transport to endosomes proceeds at which point the receptor can be recycled back to the cell surface or alternatively, receptor is trafficked to lysosomes and degradation is achieved. For the cellular internalization assay, fluorescence of each internalized antibody was measured by flow cytometry after quenching with anti-Alexa Fluor® 488 Rabbit IgG Antibody cell surface bound Alexa Fluor 488-labeled antibodies. The percentage of internalization of antibodies and antibody fragments was calculated by the difference of quenched samples at 37°C and 4°C and normalized by unquenched samples as indicated by the equation in the Methods chapter. Percentage of internalization of the different formats were determined in time for 1 h and 48 h using flow-cytometric analysis in cell lines with different HER2 expression: MDA-MB-468 (negative), MCF-7 (low), and SKBR-3 (high).

Internalization experiments displayed sufficient rates for all antibody formats after 48 h. Internalization results are consistent for the different antibody formats and are comparable with previous internalization experiments based on Herceptin (personal communication, Merck, Darmstadt Germany). After 1 h incubation, the internalization rates on MCF-7 cells range from 9 to 17 % for the constructs, whereas on SKBR-3 cells less internalization is observed with values from 0 to 5 % relative internalization. Apart from that, after 48 h on MCF-7 about 34 to 39 % of the antibodies are internalized and on SKBR-3 even 38 to 52 % are achieved. Furthermore, as a control no internalization was observed with HER2-negative MDA-MB-468 cells.

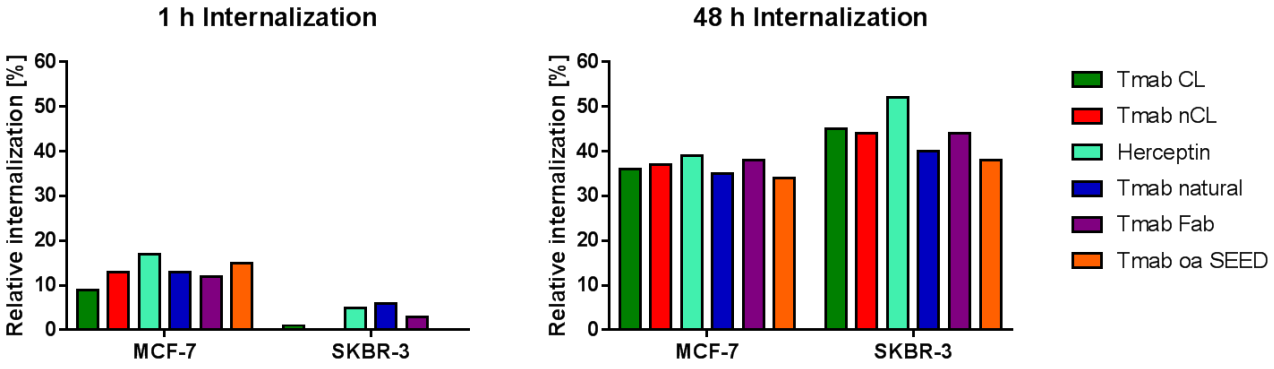

Figure 25: Comparison of relative internalization of produced antibodies and antibody fragments measured by flow cytometry.

Cellular internalization assay using flow cytometry analysis was carried out by incubation of cancer cell lines MDA-MB-468, MCF-7 and SKBR-3 with antibodies at 10 µg/ml. After incubation, secondary antibody goat anti-human IgG (H+L) Fab Fragment, Alexa Fluor 488 was added and cells were either incubated for 1 h and 48 h at 37°C allowing internalization or at 4°C preventing internalization. Cell surface bound Alexa Fluor 488-labeled antibodies was quenched with an anti-Alexa Fluor® 488 Rabbit IgG Antibody. Percentage of internalization was calculated by comparing MFI of cells incubated at 37°C and those at 4°C. Tmab = Trastuzumab

Table 7: Overview of internalization rates in percentage [%] after 1 h and 48 h incubation.

Different antibody formats were analyzed for internalization rates by flow cytometry. Cancer cell lines MCF-7, SKBR-3 and MDA-MB-468 (HER2-negative) were tested and MDA-MB-468 is not listed due to no internalization.

		MCF-7		SKBR-3	
Antibody construct	**Target**	**1 h**	**48 h**	**1 h**	**48 h**
Herceptin	HER2	17	39	5	52
Trastuzumab CL	HER2	9	36	1	45
Trastuzumab nCL	HER2	13	37	0	44
Trastuzumab natural	HER2	13	35	6	40
Trastuzumab Fab His	HER2	12	38	3	44
Trastuzumab oa SEED	HER2	15	34	0	38

5.3. Antibody and ADC thermal stability analysis

To analyze the influence of the modified cleavable hinge region in the IgG format, nano Differential Scanning Fluorimetry (nanoDSF) was performed. NanoDSF was used for thermal stability analysis and investigates parameters that contribute to forced degradation of therapeutic proteins and might indicate long-term stability during storage of biologics. For this purpose, unconjugated antibodies, deglycosylated antibodies and ADCs were tested. In the course of thermal denaturation of proteins, the change of intrinsic protein fluorescence (mainly based on tyrosine and tryptophane residues) is monitored and the melting point is determined. Raw data of the measurements are shown in **Appendix 21**. Melting temperature (T_m) of produced glycosylated antibodies ranged from 65.5°C to 71.2°C for the CH2 domain, whereas results for the Fab domain were consistent for all constructs ranging from 79.5 to 81.7°C (**Figure 26**). In contrast to that, deglycosylated N297A antibodies were thermally less stable with melting temperatures from 61.3 to 63.3°C for the CH2 domain, making them more susceptible to unfolding.

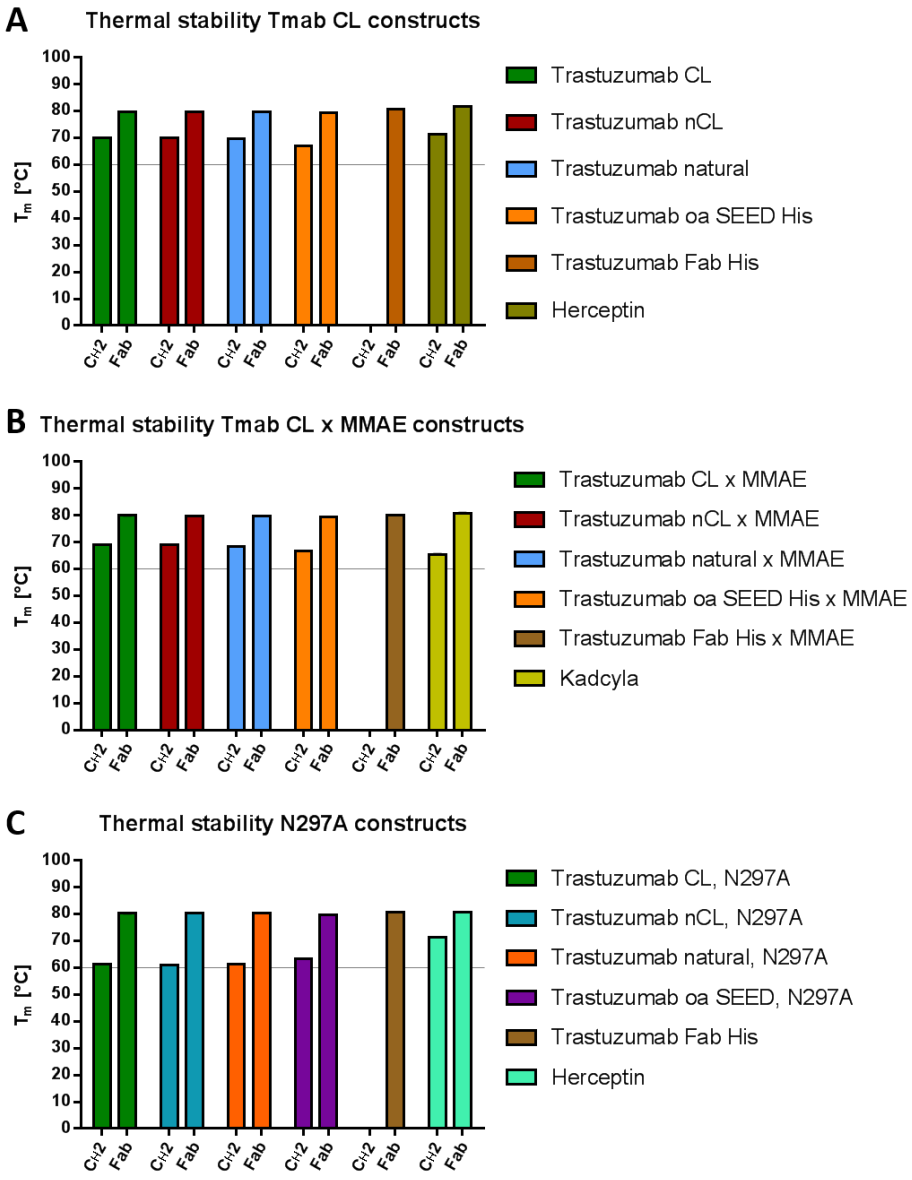

Figure 26: Thermal stability of Trastuzumab-based antibody variants and ADCs measured by nanoDSF.

Melting temperatures (T_m) in °C of Trastuzumab glycosylated antibodies (**A**), ADCs (**B**) and deglycosylated antibodies (**C**) were measured with nanoDSF for thermal unfolding using 15 µl of protein solution per capillary. Values were calculated as means and samples were measured in duplicates.

Values of deglycosylated antibodies are approximately 10°C lower compared to glycosylated IgGs and 60°C is considered as critical T_m for therapeutic antibodies. An overview of the melting temperatures of tested constructs is given in **Table 8**.

In conclusion, thermal unfolding experiments exhibited no alteration of thermal stability of antibodies as well as ADCs due to modified hinge region. Antibodies with N297A mutation bearing no glycosylation show uniform results with melting temperature 10°C lower than conventional glycosylated antibodies Moreover, sortase toxin-conjugation has also no impact on biophysical properties of ADCs.

Table 8: Overview of melting temperatures (T_m) of antibodies and ADCs.

Listed are melting temperature values of the CH2 domain (first derivate) and Fab domain of unconjugated and deglycosylated antibodies as well as ADCs.

Antibody	T_m [°C] (CH2 domain)	T_m [°C] (Fab domain)
Herceptin	71,2	81,7
Trastuzumab CL	69,9	79,5
Trastuzumab nCL	70,1	79,8
Trastuzumab natural	69,7	79,5
Trastuzumab oa SEED	67,2	79,5
Trastuzumab Fab His	-	80,7
Trastuzumab CL x MMAE	69,0	79,9
Trastuzumab nCL x MMAE	68,9	79,7
Trastuzumab natural x MMAE	68,6	79,7
Trastuzumab Fab His x MMAE	-	80,2
Trastuzumab oa SEED x MMAE	66,7	79,6
Kadcyla	65,5	80,9
Trastuzumab CL HC N297A	61,3	80,2
Trastuzumab nCL HC N297A	61,1	80,3
Trastuzumab natural HC N297A	61,4	80,4
Trastuzumab oa SEED HC N297A RF	63,3	79,7

As a next step, the stability of ADC constructs in mouse and human serum will be evaluated.

5.3.1. *In vitro* mouse and human serum stability of ADCs

Trastuzumab x MMAE constructs were incubated in mouse or human serum at 37°C, 5% CO_2 for 96 h to evaluate stability in these matrices due to concerns regarding the stability of the hinge region. Thus, investigations of the ADC constructs in serum from species that are relevant for preclinical testing was achieved. Sampling time points were 0 h, 2 h, 4 h, 6 h, 24 h, 48 h, 72 h and 96 h. The concentration of ADCs used for incubation was 0.5 mg/ml. The stability of the total antibody was analyzed by ELISA by coating HER2 murine Fc-His and detection with goat-anti human F(ab')2 x POD.

As a reference value the first time point at 0 h was used and set as 100% at the beginning. Illustrated are the serum stability time curves of the different ADCs as percentage of concentration remaining (**Figure 27**). The concentration profiles of Trastuzumab CL x MMAE and Trastuzumab nCL x MMAE remained almost constant for the duration of the experiment and show similar results. Therefore, the stability of the ADCs in mouse and human serum indicate that no hinge cleavage is expected.

For mouse serum analysis, nearly all constructs exhibited high stability and stable concentration profiles ranged from 90 to 100 % at 96 h. Apart from that, human serum stability revealed slightly less concentration for IgG-based Trastuzumab CL x MMAE, Trastuzumab nCL x MMAE and Trastuzuman oa SEED x MMAE with values from 78 to 95%, whereas Trastuzumab Fab His x MMAE exhibited a more pronounced decrease in concentration of 54% only in human serum.

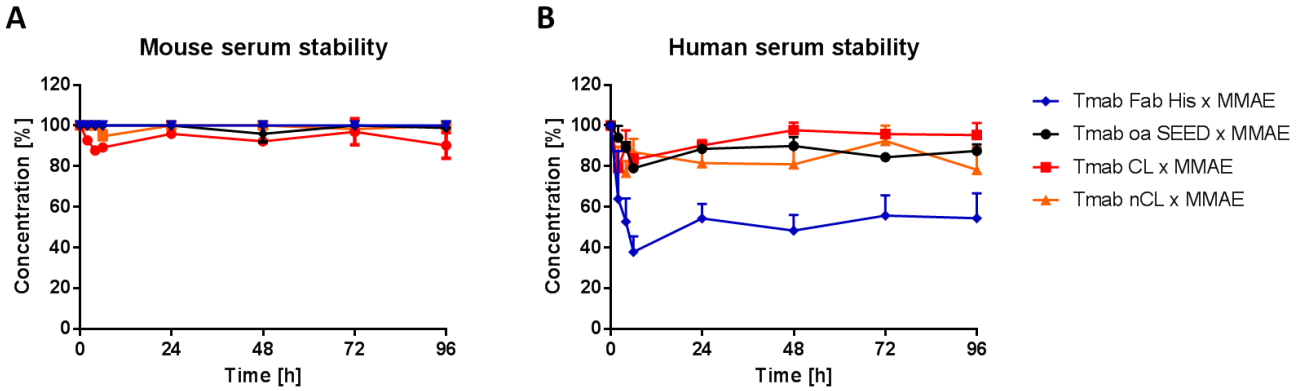

Figure 27: Mouse and human serum stability analysis of Trastuzumab x MMAE ADCs.

Samples were incubated in mouse serum (**A**) or human serum (**B**) at 37°C, 5% CO_2 for 96 h. HER2, murine Fc-His was coated in microtiter plates and detection was achieved with goat-anti human F(ab')2 x POD antibody. Aliquots were removed at different time points and concentration analysis was performed by ELISA. Depicted are total antibody concentration profiles as triplicates over time.

An overview of the remaining total antibody concentration in percentage of the tested constructs at 96 h is shown in **Table 9** and terminal drug load as well as time curves of MMAE for mouse and human serum are shown in **Appendix 22 and 23**. For drug load experiments, all constructs (except Trastuzumab Fab His x MMAE) remained unchanged in human serum over time and payload loss was not detected by LC-MS. Unlike mouse serum stability, all constructs display MMAE toxin release that is contributed to the well known activity of carboxylesterase 1c, exclusively present in rodent species.

Table 9: Overview of percentage of total antibody concentration in percentage of Trastuzumab MMAE ADCs.

Samples were incubated in mouse or human serum and remaining total antibody concentrations at 96 h are listed.

ADC	[%] remaining at 96 h in mouse serum	[%] remaining at 96 h in human serum
Trastuzumab CL x MMAE	90	95
Trastuzumab nCL x MMAE	100	78
Trastuzumab Fab His x MMAE	100	54
Trastuzumab oa SEED x MMAE	99	88

Taken together, Trastuzumab Fab His x MMAE tended to be less stable in human serum, but stability in mouse serum was similar to all other constructs for total antibody analysis. IgG-based ADCs showed high total antibody concentrations in mouse and human serum, indicating appropriate stability of these constructs that is necessary for exploiting long half-life of antibody molecules.

5.4. Matriptase expression in multiple solid tumor cell lines

Surface expression of matriptase is evident in a variety of solid tumors, including breast cancer, gastric cancer, colorectal cancer and lung cancer. To identify suitable cell lines that express matriptase as it is necessary for hinge cleavage of the ADC, western blot analysis was performed with tumor cell lysates. Oberst et al. detected matriptase in various cancer cell lines, mainly by using northern blotting and western blotting was performed with tumor samples from patients.[202] As the model ADC is based on Trastuzumab, different HER2-positive and HER2-negative cell lines were selected. Tumor cell lines that were used for matriptase detection comprised MDA-MB-468, MCF-7, SKBR-3, HCC1954, BT-474, SKOV-3, adherent HEK293. In brief, cultivated cells were lysed using RIPA buffer to facilitate protein extraction and tumor cell lysates were separated by SDS-PAGE applying a protein amount of 20-40 µg protein. Detection of matriptase was carried out by using as a primary antibody mouse IgG1 anti-human Matriptase Antibody with the recommended concentration 1 µg/ml that detects human matriptase/ST14 catalytic domain. As a secondary antibody goat anti-mouse IgG (H+L) x AP conjugate (1:1000) was used. Western blot results of cell lysates are shown in **Figure 28**.

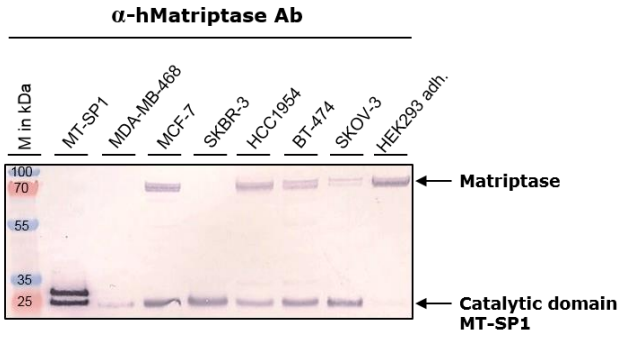

Figure 28: Western blot analysis of tumor cell lysates with detection of human matriptase.

Different cancer cell lines were cultivated and cell lysates were subjected to SDS-PAGE and Western blotting. Detection was achieved with anti-human matriptase antibody directed at matriptase/ST14 catalytic domain and adding goat anti-mouse IgG (H+L) x AP. For Immunodetection, BCIP/NBT was added.

Expression of matriptase in several tumor cell lines was verified and as a reference control recombinant matriptase/catalytic domain (MT-SP1) was utilized. The results reveal that mature matriptase displays a molecular weight of 95 kDa and in all cancer cell lines the catalytic domain of matriptase was dectected. Hence, these cell lines are suitable for further cell experiments. In another attempt, detection of the other tumor protease uPA with mouse IgG2A anti-human uPA Antibody could not be detected in cell lysate samples. No detection of uPAR using mouse anti-human uPAR Antibody was observed.

5.4.1. Detection of cleaved Fab fragment on tumor cells

For evaluation of hinge cleavage by tumor proteases uPA and matriptase present on tumor cells, cancer cell lines MDA-MB-468, HCC1954 and SKBR-3 were used. These cell lines were incubated with Trastuzumab CL,

Trastuzumab nCL, Trastuzumab CL + MT-SP1 and Trastuzumab Fab His at 37°C, 5% CO_2 for 72 h.

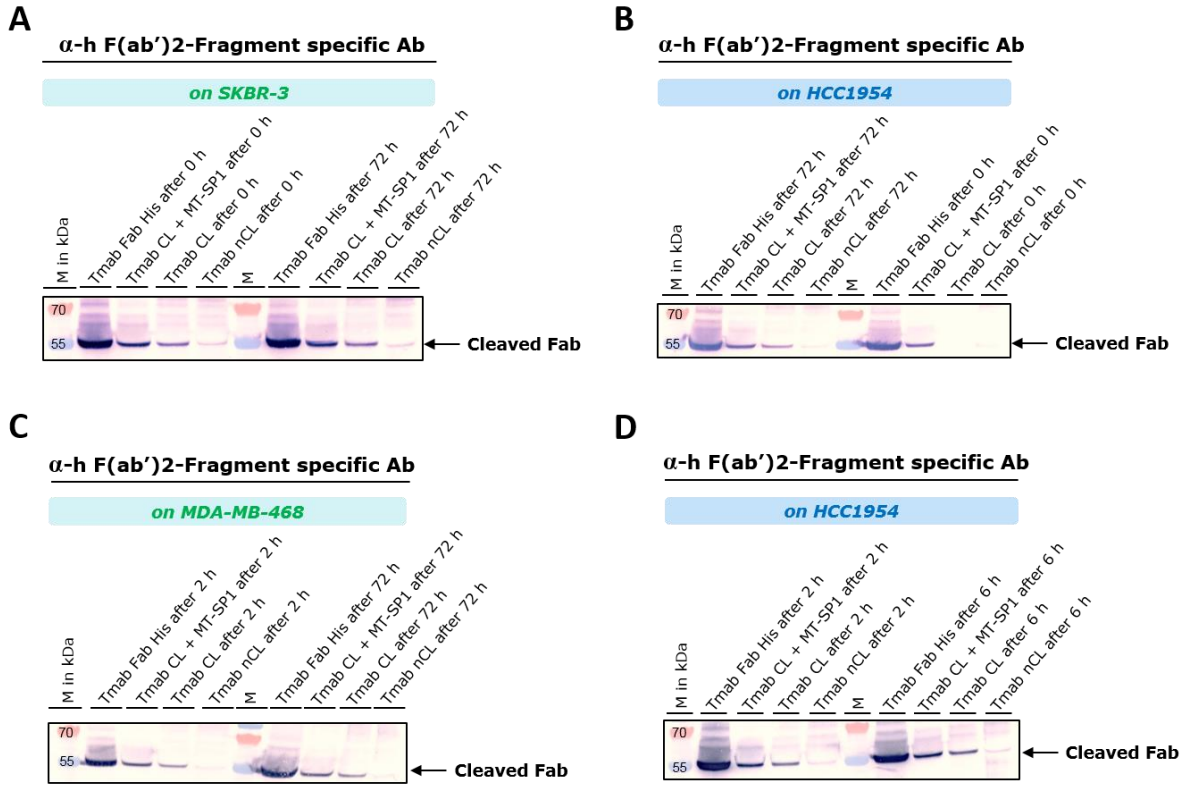

Figure 29: Western Blot analysis of trastuzumab-based antibodies incubated with cancer cell lines.

Detection of cleaved Fab fragments was carried out with goat anti-human IgG Antibody, F(ab')2 specific. Samples and controls comprised Tmab Fab His, Tmab CL + MT-SP1, Tmab CL and Tmab nCL and were incubated with SKBR-3 (**A**), HCC1954 (**B, D**) and MDA-MB-468 cells (**C**) at 37°C for 72 h. Western Blots of different time points are depicted and Tmab CL + MT-SP1 was preincubated with supplmented MT-SP1. For Immunodetection, BCIP/NBT was added. Tmab = Trastuzumab

Trastuzumab CL + MT-SP1 was preincubated 24 h to ensure that a quantitative cleavage by supplemented matriptase is attained. Protein samples were resolved by SDS-PAGE and anti-F(ab')2-Fragment specific Western Blot was performed to detect the cleaved Fab fragment. As a primary antibody goat anti-human IgG Antibody, F(ab')2 specific (1:1000) and as a secondary antibody rabbit anti-goat IgG, (H+L)-Alk. Phos (1:1000) were used. Samples were removed at different time points and stored at -80°C until analysis.

As the results reveal, detection of antibodies with Fab bands was achieved and proteolytic cleavage on tumor cell surface was evident (**Figure 29 and Appendix 24**). Cleavage was observed on HER2-positive cell lines HCC1954 and SKBR-3 and indicate that longer incubation times only slightly increased the amount of cleaved Fab fragment at 50 kDa.

As positive controls Trastuzumab Fab His and preincubated Trastuzumab CL + MT-SP1 were used and in comparison to Trastuzumab CL + MT-SP1, similar amounts of protein were detected by the solely incubated Trastuzumab CL. For the negative control Trastuzumab nCL, no (only unspecific in the case of SKBR-3) specific

detection at 50 kDa was observed, displaying that intact IgG antibody without a cleavable sequence remains unchanged. On HER2-negative cell line MDA-MB-468 also Fab fragment detection was achieved, suggesting that matriptase is also present as observed in a previous experiment.

Therefore, *in situ* Fab fragment generation by the tumor cells that express matriptase could be confirmed for the hinge cleavable Trastuzumab CL construct. In order to test that released toxin-conjugated Fab fragments still exert sufficient cytotoxic activity, cell based cytotoxicity assays were performed with several cancer cell lines.

5.5. Cytotoxic activity of hinge cleavable ADCs and FDCs *in vitro*

The confirmed specific hinge cleavage and efficient release of FDCs by tumor proteases, as well as maintained stability and cellular binding and internalization properties of the intact ADC, are essential criteria that pave the way for cytotoxic assessment related to the potency of these constructs.

In a first attempt, ADCs based on the highly potent cytotoxic compound MMAE were tested in cytotoxicity assays on HER2-overexpressing cell lines, measuring the cell viability.

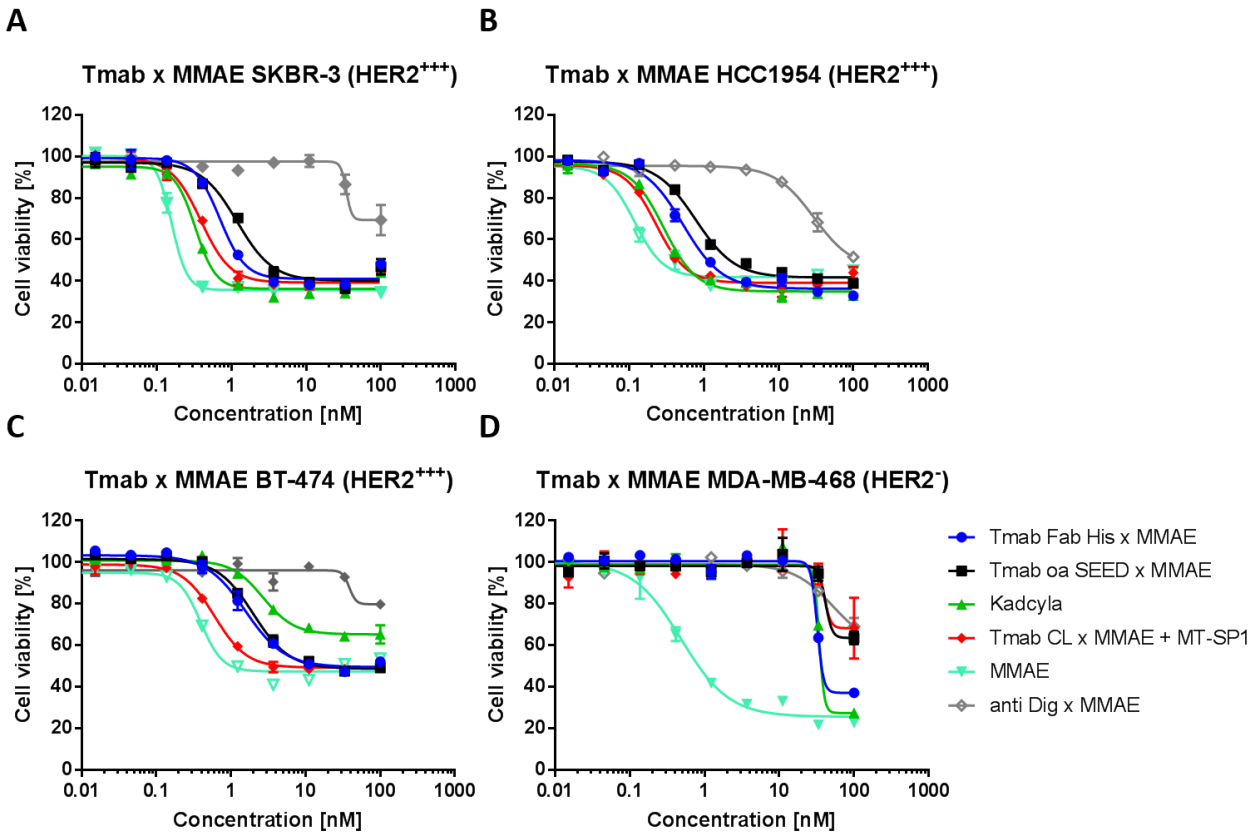

Figure 30: Cytotoxicity of Trastuzumab x MMAE ADCs on cancer cell lines.

Trastuzumab antibodies and antibody fragments generated by enzyme-assisted, site-specific conjugation of cleavable ValCit-PABC-MMAE to light chains were incubated on HER2-overexpressing SKBR-3 (**A**), HCC1954 (**B**) and BT-474 cells (**C**) as well as on HER-2 negative cells MDA-MB-468 (**D**) for 72 h. Cell viability was analyzed by measurement of ATP-levels using the CellTiter-Glo assay. High cytotoxic activity was observed on HER2-overexpressing cells with subnanomolar potencies (IC_{50} values), whereas cell killing by Trastuzumab ADCs only at high concentrations could be detected on HER2-negative cells. Illustrated are exemplary cell viability graphs with data points of two replicates from at least three independent experiments.

The HER2-overexpressing cell lines used comprised HCC1954, SKBR-3, BT-474, NCI-N87 as positive cell lines and as HER2-negative cell line MDA-MB-468. MMAE was selected as a well established and characterized microtubule inhibiting agent that targets mainly fast dividing cells.

MMAE is connected to the linker dipeptide valine-citrulline-PABC, which ensures predominantly intracellular toxin release by lysosomal enzymes like cathepsin B. As reference constructs, the approved ADC Kadcyla (Trastuzumab emtansine, T-DM1) was used and as an isotype control anti-Dig x MMAE that was also conjugated by sortase A. For evaluation of the activity of MMAE-based ADCs, serial dilutions of the samples were added to the respective cancer cell lines and incubated at 37°C, 5% CO_2 for 72 h. Tmab CL x MMAE + MT-SP1 was preincubated with matriptase for 24 h, resulting in cleaved products. Exemplarily illustrated are the cell viability curves of the constructs on HER2-positive cells SKBR-3, HCC1954, BT-474 and on HER2-negative cells MDA-MB-468 (**Figure 30**). Trastuzumab nCL x MMAE and Trastuzumab natural x MMAE as well as Kadcyla and other controls are shown in **Appendix 25**.

Cytotoxicity of MMAE-conjugated constructs showed on SKBR-3, HCC1954 and BT-474 cells a strong cell killing in the nanomolar to subnanomolar range that was comparable to the benchmark Kadcyla (**Table 10**). In **Appendix 26** cytotoxicity of Trastuzumab MMAE ADCs on NCI-N87 cell line is listed. The strongest activity was observed on HCC1954 with Trastuzumab CL x MMAE + MT-SP1 having an IC_{50} of 0.19 nM that was comparable to full-length MMAE ADCs (0.24 to 0.34 nM).

ADCs with a DAR of approximately 2 exhibit consistent IC_{50} values in the subnanomolar range on SKBR-3 and HCC1954. Also Trastuzumab CL x MMAE + MT-SP1 and Trastuzumab Fab His x MMAE, which both have a DAR of nearly 1 exert similar cytotoxicity. As a general trend, Trastuzumab oa SEED x MMAE always displayed less cyototoxic activity than Trastuzumab Fab His x MMAE, except on BT-474.

Table 10: Overview of cytotoxicity of Trastuzumab MMAE ADCs.

Depicted are cellular potencies of MMAE ADCs in different formats on several HER2 cancer cell lines. ADCs in the IgG format have a DAR of nearly 2 (Kadcyla has a DAR of 3.5), whereas antibody fragments and cleaved ADC with matriptase displays a DAR of 1. Used control ADCs comprised Kadcyla and anti-Dig x MMAE. Mean IC_{50} in nM from at least three independent experiments were used.

Construct	DAR	HCC1954	SKBR-3	BT-474	MDA-MB-468
Tmab CL x MMAE	1.9	0,24 ± 0,15	0,30 ± 0,14	0,23 ± 0,07	> 100
Tmab nCL x MMAE	1.8	0,22 ± 0,10	0,38 ± 0,19	0,48 ± 0,15	> 100
Tmab natural x MMAE	1.8	0,34 ± 0,13	0,50 ± 0,17	0,73 ± 0,01	> 100
Tmab CL x MMAE + MT-SP1	0.8	0,19 ± 0,03	0,31 ± 0,07	0,58 ± 0,01	> 100
Tmab Fab His x MMAE	0.9	0,50 ± 0,24	0,47 ± 0,19	2,31 ± 0,53	50,54 ± 35,53
Tmab oa SEED x MMAE	0.8	0,90 ± 0,33	1,17 ± 0,09	1,91 ± 0,05	> 100
Kadcyla	3.5	0,29 ± 0,26	0,35 ± 0,22	3,06 ± 1,82	42,64 ± 36,18
MMAE	-	0,12 ± 0,04	0,32 ± 0,23	0,43 ± 0,06	0,70 ± 0,45
DM-1	-	0,39 ± 0,13	1,11 ± 0,40	3,82 ± 0,97	0,99 ± 0,32

Cytotoxic activity on BT-474 was slightly decreased for all constructs compared to HCC1954, but Kadcyla was even 13-fold less active than Trastuzumab CL x MMAE on BT-474. On HER2-negative cell line MDA-MB-468 only at higher concentrations Trastuzumab Fab His x MMAE showed at 50.54 nM cell killing, but that was similar to Kadcyla with an IC_{50} of 42.64 nM. In all tested cell lines, non-related isotype control ADC, anti-Dig x MMAE, did not indicate a significant reduction in cell viability.

For small molecules MMAE and DM-1, cell and target independent cytotoxic effects in the range from 0.12 to 3.82 nM were observed, indicating a free diffusion and cell permeable payload.

To better differentiate *in vitro* between only cell killing that is more related to bystander effect by cell permeable toxin MMAE or real tumor penetration, constructs conjugated with MMAF as a more cell impermeable payload were used. Therefore, comparison of a bystander molecule in the case of MMAE and a non bystander molecule like MMAF was investigated. Generally, all used MMAF constructs displayed increased potencies than MMAE ADCs and as shown in all cell viability graphs the small molecule MMAF is much less active (**Figure 31**).

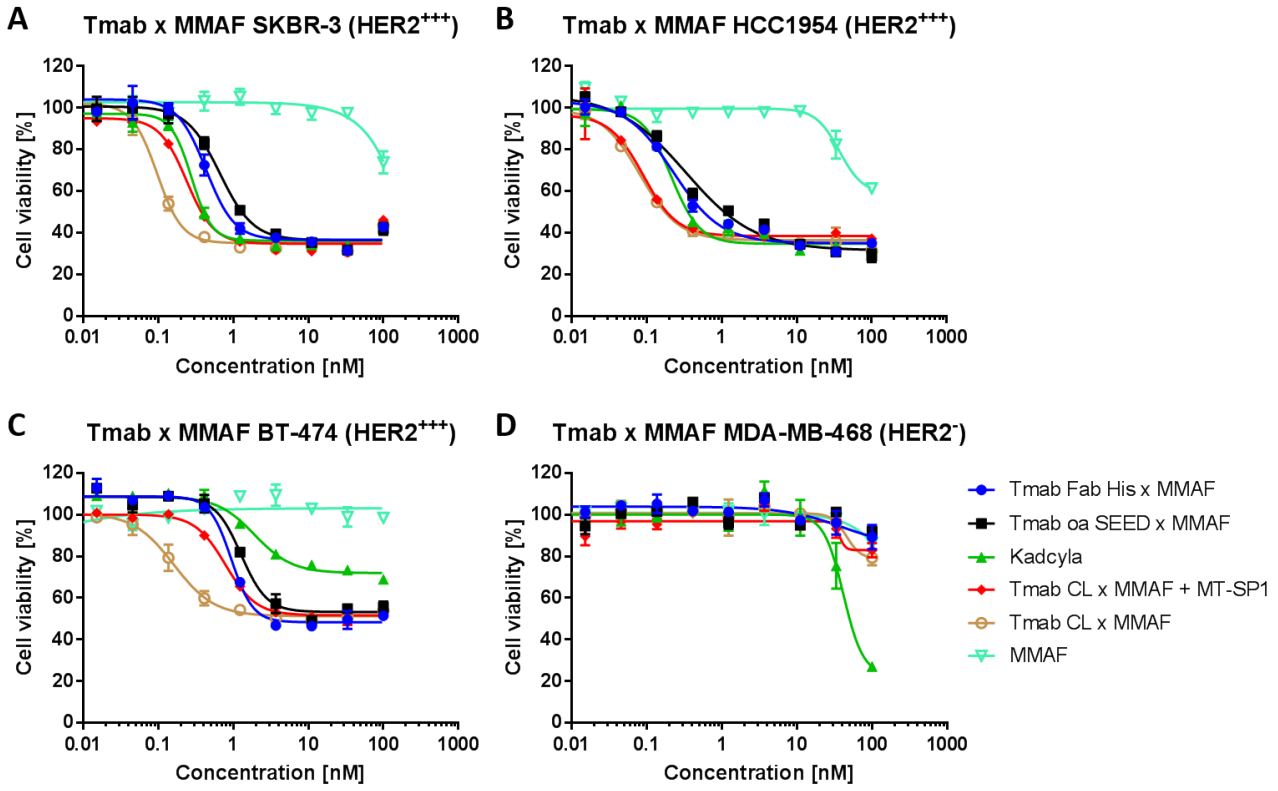

Figure 31: Cytotoxicity of Trastuzumab x MMAF ADCs on cancer cell lines.

Trastuzumab ADCs with cleavable ValCit-PABC-MMAF linker drug conjugated to light chains were incubated on HER2-overexpressing SKBR-3 (**A**), HCC1954 (**B**) and BT-474 cells (**C**) as well as on HER-2 negative cells MDA-MB-468 (**D**) for 72 h. Cell viability was analyzed by measurement of ATP-levels using the CellTiter-Glo assay. High cytotoxic activity was observed on HER2-overexpressing cells with subnanomolar potencies (IC_{50} values), whereas cell killing by Kadcyla only at high concentrations could be detected on HER2-negative cells. Illustrated are exemplary cell viability graphs with data points of two replicates from at least three independent experiments.

Table 11: Overview of cytotoxicity of Trastuzumab MMAF ADCs.

Depicted are cellular potencies of MMAF ADCs in different formats on several HER2 cancer cell lines. ADCs in the IgG format have a DAR of nearly 2, whereas antibody fragments and cleaved ADC with matriptase displays a DAR of approximately 1. Used control ADCs comprised Kadcyla and anti-Dig x MMAE. Mean IC_{50} values in nM from at least three independent experiments were used.

Construct	DAR	HCC1954	SKBR-3	BT-474	MDA-MB-468
Tmab CL x MMAF	1.7	0,13 ± 0,07	0,17 ± 0,13	0,31 ± 0,31	> 100
Tmab nCL x MMAF	1.8	0,12 ± 0,06	0,20 ± 0,17	0,58 ± 0,37	> 100
Tmab natural x MMAF	1.9	0,10 ± 0,05	0,21 ± 0,15	0,32 ± 0,13	> 100
Tmab CL x MMAF + MT-SP1	0.7	0,10 ± 0,03	0,23 ± 0,03	0,46 ± 0,23	> 100
Tmab Fab His x MMAF	0.7	0,28 ± 0,22	0,34 ± 0,14	0,60 ± 0,33	> 100
Tmab oa SEED x MMAF	0.8	0,44 ± 0,27	0,54 ± 0,10	0,78 ± 0,47	> 100
Kadcyla	3.5	0,32 ± 0,22	0,42 ± 0,22	2,45 ± 0,25	36,96 ± 45,34
Tmab natural x MMAF DAR 3.5	3.5	0,12 ± 0,08	0,42 ± 0,23	1,81 ± 0,21	> 100
MMAF	-	-	-	-	-
DM-1	-	0,42 ± 0,13	0,66 ± 0,45	2,51 ± 1,26	1,09 ± 0,34

An overview of the cytotoxicity results is shown in **Table 11**. Trastuzumab CL x MMAF + MT-SP1 and Trastuzumab natural x MMAF ADCs potently killed HCC1954 cells with an IC_{50} of 0.10 nM, and thus were 3-fold more potent than Kadcyla with an IC_{50} of 0.32 nM. On SKBR-3 and BT-474 cells, Trastuzumab CL x MMAF and Trastuzumab natural x MMAF showed the highest potencies ranging from 0.17 to 0.32 nM, surpassing slightly Kadcyla. Another construct termed Trastuzumab natural x MMAF DAR 3.5, was also tested with the MMAF ADCs that bears 4 MMAF payloads and showed a pronounced effect with an IC_{50} of 0.12 nM on HCC1954 and 0.42 nM on SKBR-3 cells. In this case, payloads are conjugated again to light chains by sortase A and also to the heavy chains that carry a LPETGS recognition motif. On HER-2 negative cells MDA-MB-468 of the ADCs only Kadcyla showed at higher concentrations (36.96 nM) cell killing, whereas all MMAF-based ADCs where inactive in the evaluated concentration range and did not show any unspecific cell killing. The cell viability graphs of full-length constructs Trastuzumab CL x MMAF, Trastuzumab nCL x MMAF and Trastuzumab natural x MMAF can be found in **Appendix 27**.

For all cytotoxicity assays, evaluation of the target inhibition on cell viability was investigated using unconjugated antibodies analogously. Antibodies without toxins showed no significant activity on cell viability, but when conjugated with a toxin, strong cytotoxic activity was achieved.

When comparing the DAR with the obtained IC_{50} values of tested anti-HER2 ADCs and FDCs, similar IC_{50} values on HCC1954 of higher DAR and low DAR ADCs in the case of MMAF as a payload were observed. *In vitro* cytotoxicity of the cleaved ADC and FDC are equipotent to higher DAR Trastuzumab natural x MMAF DAR 3.5 and Kadcyla (**Figure 32**).

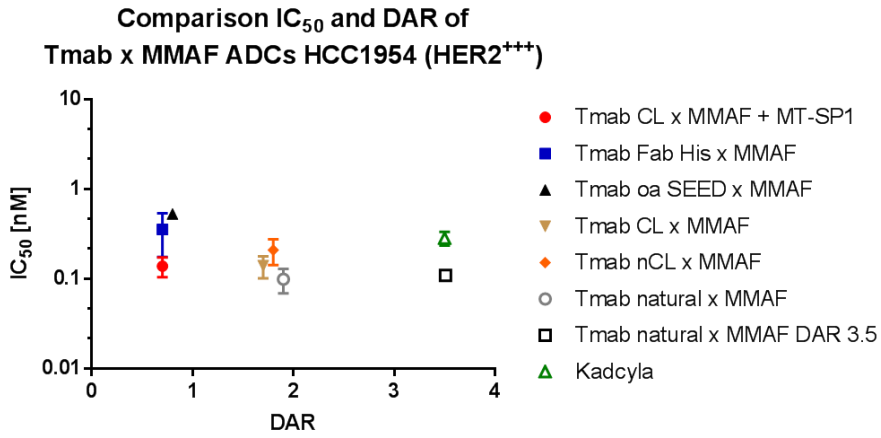

Figure 32: Comparison of IC50 and DAR of Trastuzumab x MMAF ADCs on HCC1954 cell line.

Cytotoxic activity of Trastuzumab ADCs and FDCs conjugated with MMAF on HCC1954. Plotted are the obtained IC_{50} values against the DAR of the respective construct. Strong cytotoxicity is observed by cleaved ADC and FDC despite the low drug load of approximately 1.

Furthermore, analogous to the clevable antibodies and antibody fragments that were based on Trastuzumab, cell viability was also analyzed with Cetuximab-based ADCs conjugated to MMAE on EGFR-overexpressing cell lines. Cetuximab x MMAE ADCs displayed strong cytotoxicity on EGFR-positive A431 and MDA-MB468 cells, whereas no unspecific cell killing was observed on EGFR-negative MCF-7 cell line.

An overview of the IC_{50} values of Cetuximab x MMAE ADCs is shown in **Appendix 28** and cell viability curves are depicted in **Appendix 29**.

As cytotoxicity of generated cleavable ADCs and FDCs is maintained, a suitable approach to investigate tumor distribution and penetration of solid tumors is necessary. For evaluation of tumor localization, antibody-fluorophore conjugates will be used for imaging studies.

5.6. Tumor spheroid distribution and penetration

To investigate tumor distribution and penetration *in vitro*, tumor spheroids were prepared. Spheroids represent spherical clusters of growing, self-adhered cancer cells that mimic the three-dimensional environment and structure of a solid tumor.

Due to the fact that tumor cell killing is not directly related to an improved penetration, the different formats of antibody molecules were prepared as antibody-fluorophore conjugates using Alexa Fluor 488 as a green fluorescent dye. Alexa Fluor 488-conjugates contain a triple-glycine motif and a noncleavable C5-spacer in the linker structure of Alexa Fluor 488. The antibody-fluorophore conjugate Trastuzumab CL N297A x AF488 x BHQ10 was generated by a dual conjugation method.

In the case of Alexa Fluor 488, sortase A conjugation was used to attach the fluorophore to the light chains, whereas dark soluble BHQ-10 is conjugated to Q295 in the heavy chain by transglutaminase reaction (**Figure 33**). In the intact IgG form, the green fluorescence is quenched by BHQ-10, which has a broad quenching range for emission maxima at 516 nm. Upon cleavage in the hinge region fluorescence is activated, because of the

separation of the Fc part with BHQ-10 from Fab-Alexa Fluor 488. All other formats carry the fluorophore on the light chains and an overview of antibody-fluorophore conjugates is shown in **Table 5**.

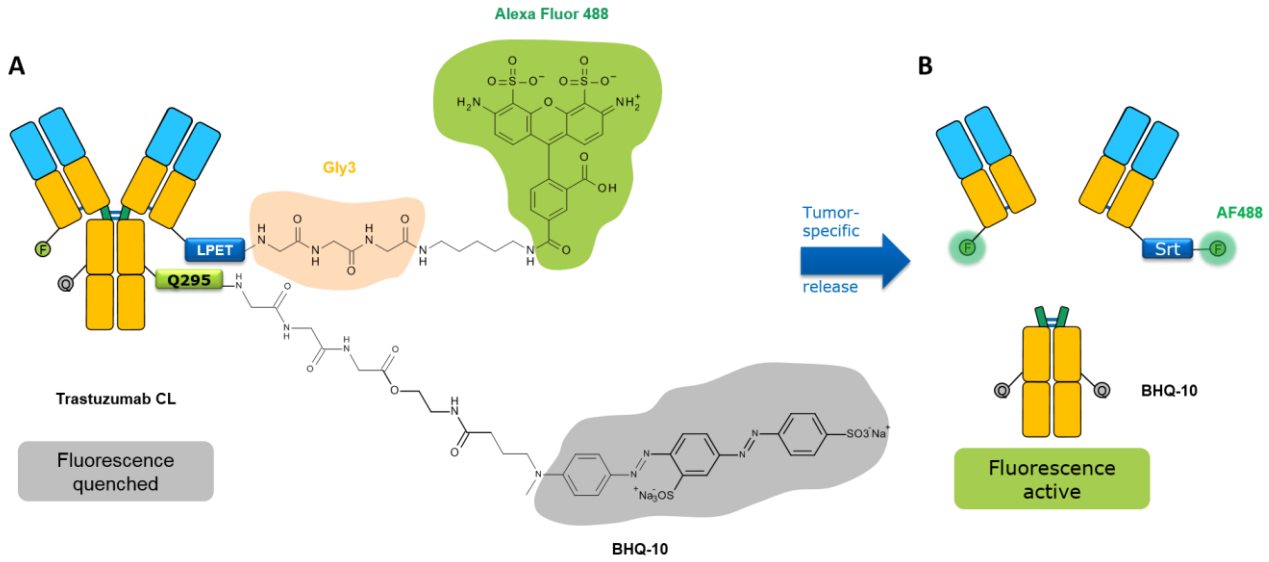

Figure 33: Structure of Trastuzumab CL N297A x AF488 x BHQ-10 using Alexa Fluor 488 as the fluorophore and BHQ-10 as a quencher.

Cleavable antibody-fluorophore conjugate Trastuzumab CL N297A x AF488 x BHQ-10 was generated by sortase A conjugation of Gly_3-C_5-AF488 to the light chains of the antibody. BHQ-10 was conjugated to Q295 by transglutaminase reaction (**A**). The whole intact construct is cleaved in the hinge region, releasing the Fab fragments with the fluorophore attached to it (**B**).

For analysis of efficient fluorescence activation, measurements were performed with Trastuzumab CL x AF488 x BHQ-10 alone, with enzymes uPA and matriptase, as well as control samples. Control samples comprised Trastuzumab CL x BHQ-10 only with quencher conjugated as well as Trastuzumab natural x AF488. Prior to enzyme cleavage experiments, a calibration curve was carried out by measuring solely increasing AF488 concentrations. The obtained correlation coefficient R^2 with 0.9383 was significant enough for analytical evaluation and indicated a proportional increase of the relative fluorescence units (RFU). For the cleavage of Trastuzumab CL x AF488 x BHQ-10 with matriptase a strong increase in RFU was observed from early time points with 320203 RFU to 511733 RFU at 24 h. Compared to the cleavage with matriptase, incubation with uPA resulted in a less increase of fluorescence intensity at 24 h with 382340 RFU (**Figure 34**).

These results displayed that fluorescence of the Trastuzumab CL x AF488 x BHQ-10 construct is increased upon efficient separation of the Fab fragment containing Alexa Fluor 488 from the Fc portion bearing the BHQ-10 quencher. Moreover, control samples Trastuzumab CL x AF488 x BHQ-10 as well as Trastuzumab natural x AF488 remained unchanged in their RFU over time.

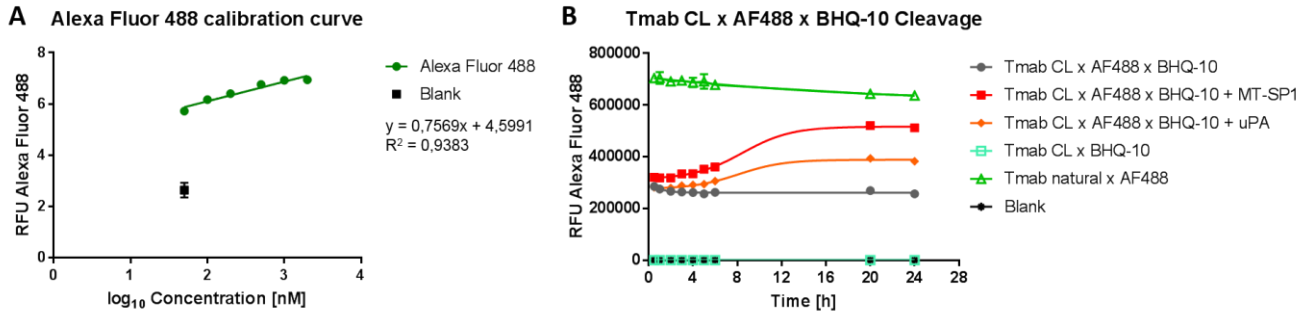

Figure 34: Alexa Fluor 488 calibration and fluorescence intensity over time of different antibody-fluorophore conjugates.

Alexa Fluor 488 was analyzed for an increasing, proportional fluorescence with varying concentrations (**A**). Alexa Fluor 488 was conjugated to Trastuzumab CL N297A antibody with the quencher BHQ-10 and was incubated with tumor proteases uPA and matriptase. Increasing RFU were observed for both samples over time, indicating a sufficient separation of the Fab fragment with the fluorophore from the Fc portion bearing the quencher (**B**). Control samples Trastuzumab CL x AF488 x BHQ-10 (without enzyme), Trastuzumab CL x BHQ-10 (only with quencher) and Trastuzumab natural x AF488 (only with fluorophore) were used. Samples were measured in triplicates with EnVision multiplate reader. RFU = Relative Fluorescence Units, AF488 = Alexa Fluor 488, BHQ-10 = Black Hole Quencher-10

As the basic principle for fluorescence activation was confirmed, imaging experiments were carried out with tumor spheroids. Cancer cell lines HCC1954, SKBR-3 and MDA-MB-468 were used to form spheroids, as these cell lines express matriptase. Spheroid formation was checked with IncuCyte S3 Live-Cell Analysis System and was unfortunately only successful with HCC1954 at a cell density of 3000 cells/well, indicated by the presence of an extracellular matrix (**Appendix 30**). Spheroids had an average diameter size of approximately 300 µm and were grown within 48 h. HCC1954 spheroids were treated for 14 h with antibody-fluorophore conjugates Trastuzumab CL x AF488 x BHQ-10 (with and without matriptase), Trastuzumab nCL x AF488 and Trastuzumab Fab x AF488 to evaluate size-dependent tumor distribution and penetration in an *in vitro* model. Live cell imaging was carried out over the time and green fluorescence was detected.

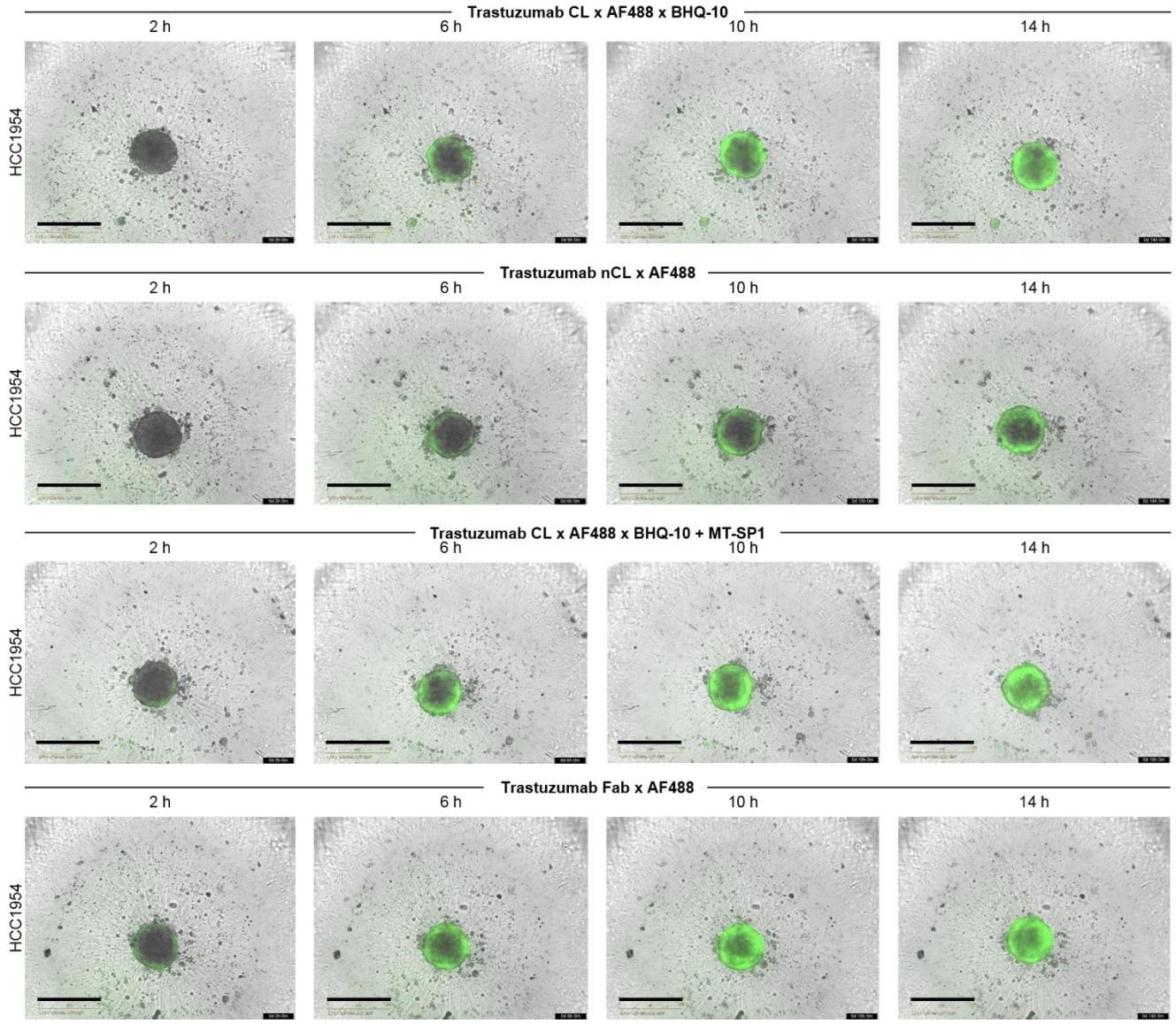

Figure 35: Spheroid distribution and penetration with antibody-fluorophore conjugates.

Depicted are HER2-overexpressing HCC1954 spheroids at a cell density of 3000 cells/well. Antibody-fluorophore conjugates were applied with a concentration of 6.25 nM and cells were imaged over time for 14 h. Trastuzumab CL x AF x BHQ-10 was applied without enzyme to ensure matriptase cleavage is achieved by tumor cells. Control samples that are applied as Fab fragments attached to Alexa Fluor 488 comprised Trastuzumab CL x AF488 x BHQ-10 + MT-SP1 and Trastuzumab Fab x AF488. Trastuzumab nCL x AF488 remains unchanged in the intact IgG form. Scale bar = 400 µm

Imaged time points were 2 h, 6 h, 10 h and 14 h and are illustrated in **Figure 35**. When comparing the results of Trastuzumab CL x AF488 x BHQ-10 (with and without matriptase) and Trastuzumab Fab x AF488, comparable green fluorescence is observed over the spheroid area at 14 h. This indicates that functional Trastuzumab CL x AF488 x BHQ-10 is cleaved by present tumor protease on tumor cell surface and the cleaved Fab-fluorophore conjugate distributes and penetrates evenly into the spheroid core, reaching almost all cancer cells. In contrast to that, Trastuzumab nCL x AF488 predominantly localizes at exterior fractions compared to the other tested constructs and is not able to reach the central region.

In another experiment with the fluorescence microscope EVOS FL Auto 2 Imaging System, the penetration of the conjugates with fluorophore along the z-stack was monitored and reveales that inside the tumor core a stronger fluorescence is observed for Trastuzumab CL x AF488 x BHQ-10 and Trastuzumab Fab x AF488. Exemplarily images are shown in **Appendix 31**.

Taken together, results of cleaved Trastuzumab CL x AF488 x BHQ-10 as well as Trastuzumab Fab x AF488 showed that these constructs significantly better localize across the tumor spheroids and even within the tumor core, leading to an improved tumor distribution and penetration *in vitro*.

6. Discussion

6.1. Protease-cleavable ADCs with prolonged half-life as a novel format

Efficient, site-specific and uniform delivery of antibody-based therapies to solid tumors remains a major challenge. Previous studies have demonstrated a strong correlation between the size and penetration ability of targeting agents and hence a novel ADC design is pursued in this study to address the penetration issue while retaining advantages of the full-length antibody.[157,167]

In the course of this study, smaller-drug conjugates that are released by an ADC through cleavage in the hinge region were utilized to improve the tumor penetration and accumulation while maintaining long-half life by the intact ADC in systemic circulation. Thus, rapid clearance of the Trastuzumab CL compound would be avoided but as the toxin-based fragment is generated, faster penetration but also rapid renal clearance of the fragment would be achieved. Moreover, such rapid clearance could be a potential benefit for reducing toxic exposure to healthy cells.

The purpose of this study was to compare the tumor penetration and localization of hinge cleavable Trastuzumab ADCs with a noncleavable counterpart as well as with Trastuzumab Fab control constructs.

Fab fragments exhibit a typical plasma half-life of 12 - 20 h, which make them more appropriate for diagnostic and imaging applications rather than for therapeutic use.[203] Nomerous strategies are described for prolonging the half-life of therapeutic agents in drug development. The most prominent approaches are the PEGylation of molecules (like Certolizumab pegol with 2 x 40 kDa PEG residues or PEGylated interferon alfa-2a with 2 x 20 kDa PEG) or association of targeting agents with albumin.[204–206] However, for PEGylation a high amount of PEG chains is necessary to achieve an extended half-life, leading to a higher molecular weight and hence an impaired tumor penetration. In the case of albumin, this 67 kDa protein has no targeting ability and only one payload molecule per native albumin can be achieved, resulting in a restricted cargo loading. As albumin already exceeds the molecular weight of a 50 kDa Fab fragment and has to be modified with a targeting molecule, no improved tumor penetration is assumed. PEGylated Fab fragments exhibit potential advantages over IgG antibodies like a lack of any undesirable Fc-mediated effects. Elimination of effector functions is considered in many cases as this leads to reduced side-effects. For example, these immune effects are associated with exaggerated cytokine secretion after antibody therapy or off-target toxicities in the case of ADCs.[207] The long circulatory half-life of antibody-based drugs leads to elevated blood concentration, often resulting in bone marrow toxicity even before therapeutic activity in a solid tumor is reached.[157] In addition to that, Fc-fusion proteins are also an important alternative for prolonging the half-life.[208]

All ADCs and FDCs generated for this work are homogeneous and site-specific by way of their predefined attachment sites for the payload on the C-termini of light chains of antibodies and antibody fragments. Site-specific conjugation is superior compared to chemical conjugation in terms of defined pharmacokinetics, safety, stability and efficacy profile. All Trastuzumab ADC conjugations with sortase A displayed good yields with a DAR of 1.6 to 1.9 and conjugation efficiency was in the range of 60 - 70%. In contrast to that, Cetuximab ADCs achieved a lower DAR of 1.1 to 1.3, leading to the assumption that conjugation is not efficient. This could be due to the heterogeneous mixture of Cetuximab, which is present with different glycoforms that might have a

negative impact on the conjugation reaction. As the same linker-drug structure like for Trastuzumab ADCs was used for the generation of Cetuximab ADCs, no interference of the Gly_3-ValCit-PABC-MMAE substrate with the enzyme's active site is conceivable. Possibly, steric hindrance for sortase A to reach the LPETGS motif on Cetuximab could also lead to an inefficient conjugation reaction.

To improve the tumor penetration and simultaneously make use of the well established conventional IgG format, a protease cleavable site is engineered in the hinge region. Desnoyers and colleagues deployed the protease site when they used its amino acid sequence as a cleavable linker between a masking peptide and the N-terminus of the antigen binding site of an antibody. This approach abolishes binding to the target and the tumor-specific activation of the tested probody by tumor proteases was verified in an *in vivo* study.[198] In such case, the protease site was exposed at the surface of the antibody and no steric hindrance was expected, whereas in this work the protease site was buried within the hinge region. Nevertheless, it could be demonstrated that the hinge region is still accessible to tumor proteases as Fab cleavage was observed upon matriptase and uPA addition. As shown by ESI-MS analysis, the selective cleavage site of the proteases is between arginine and serine within the 8 amino acid sequence. This is in accordance with Yang et al., where the linker sequence was used for another approach.[197] The expression of such enzymes like matriptase in several cancer cell lines was confirmed by Western Blot anaylsis, as also evidenced by other research groups.[202]

These data reveal that the antigen HER2 and matriptase are expressed on selected cancer cell lines, which are both crucial for this concept. Moverover, matriptase overexpression is mainly restricted to malignant cells, whereas in normal cells minor amounts are present for physiological functions. This could lead to a suitable application that is preferentially in tumor tissue and results in more cleaved fragments that accumulate within the tumor. The overexpression compared to cancer cells is more likely, because a greater split in safety could be achieved.

6.2. Evaluation of cleavage reactions, cellular binding and internalization

The hinge region of IgG antibodies with its high flexibility is susceptible to specific cleavage by proteases *in vitro* and various modifications like reductive cleavage of interchain groups, cysteinylation and glutathionylation are known to affect the stability of mAbs. Particularly, the IgG3 subclass with its short half-life of 7 days and its extended hinge region that is prone to cleavage, is not used as a therapeutic.[83] The evaluation of the designed cleavable IgG1 antibodies revealed that the elongated hinge region is not impeding the structural integrity and functionality of the antibody. Cleavage reactions that occur in the upper hinge region can impact epitope binding due to the loss of bivalency, whereas cleavage reactions in the lower hinge region lead to impaired Fc effector function.[199,209]

The time-dependent cleavage results demonstrated that a fast and efficient cleavage reaction in the hinge region of Trastuzumab CL constructs is achieved with tumor proteases uPA and matriptase, whereas matriptase displays a significant faster proteolytic cleavage than uPA. These results are consistent with earlier observations, where kinetic parameters of substrate conversion for matriptase were k_{cat}/K_m 2200 ± 424 M^{-1} s^{-1} and for uPA k_{cat}/K_m 500 ± 79 M^{-1} s^{-1}.[198] A fast cleavage rate is important for this work, because otherwise the full-length ADC can be internalized in a short period of time and thus would not be anymore available for the

extracellular protease cleavage, targeting the tumor only in the IgG-ADC form. As the quantitative and fast cleavage rate of matriptase is obvious, this enzyme was used for all subsequent experiments where preincubated samples are of importance as controls.

Besides that, it is generally assumed that ADC internalization into tumor cells is required in order to exert pronounced therapeutic activity.[64,165] In contrast to that, ADCs against CD20, CD21, CD22 and fibronection exhibited activity even when antibodies and antigens are poorly internalized.[210,211,212] Moreover, such experiments showed that non-internalizing ADCs carrying the cytoxic drug by means of disulfide linkers are cleaved in the tumor microenvironment. Recent investigations by Neri and colleagues also revealed that the non-internalizing F16 antibody is able to release cytotoxic drugs at the extracellular tumor site, resulting in anti-cancer activity in preclinical studies of U87 and A431 xenografted tumors. The human F16 antibody targets the non-internalizing antigen tenascin-C (splice isoform) and was generated as an ADC by conjugation of ValCit-PABC-MMAE to cysteine residues. In these experiments, unexpected extracellular proteolytic cleavage of the ValCit dipeptide linker was observed, leading to the conclusion that such peptide linker is not selectively cleaved by cathepsin B in intracellular compartments.[213,214]

Taken together, previous studies showed that non-internalizing ADCs with a dipeptide linker release efficiently the payload. As efficient drug release of ADCs at the tumor site is not only achieved by reductive conditions, but also by extracellular proteases, this approach can also be used for the protease site used in this work. uPA and matriptase sensitive cleavable linker could be utilized for the design of non-internalizing ADCs to release cytotoxic payloads in the extracellular regions of tumor cells. Such an application expands the ADC target space to non-internalizing cell membrane proteins offering potential therapeutic advantages for the treatment of further antigens. Consistent with previous reports and impaired solid tumor penetration of antibodies that are mainly located in the perivascular region, the release of drugs in the extracellular space enables diffusion and subsequently penetration of the tumor.[167]

In principle, many extracellular proteolytic enzymes that reside in the tumor microenvironment can influence activity and stability of ADCs. Elevated expression levels of many proteases in the tumor microenvironment are evident, especially the activity of several MMPs.[209] In this work, analysis of Western Blots confirmed the selectivity of the protease site to uPA and matriptase due to the fact that no upper or lower hinge cleavage was observed with the Trastuzumab nCL construct upon incubation with cancer cell lines.

As affinity and avidity play a critical role, cellular binding of monovalent and bivalent constructs was tested and showed only slight differences on HER2-overexpressing cells. As monovalent Trastuzumab Fab has no avidity, marginal altered binding interaction to the single antigen might result from loss of bivalency. Binding strength of the tested constructs correlated with expression levels of the antigen on different cancer cell lines. Furthermore, no unspecific binding was detected for bivalent and monovalent constructs for HER2-negative cell line MDA-MB-468.

Parameters that influence the internalization rate are less understood. However, the choice of target antigen, kinetic parameters as association and dissociation rates for the antibody-antigen interaction as well as processing and intracellular events such as recycling to the cell surface rather than lysosomal degradation play a key role.[175] Previous observations with high affinity anti-CEA scFv molecules showed that affinity and avidity had no

dramatic impact on internalization rates and the internalization rate of mAb and antibody fragment is probably largely dependent on recycling of the respective antigen.[157] In this case, an equivalent uptake of monovalent and bivalent scFvs was observed, leading to the assumption that crosslinking of CEA antigens on cell surface displays only a minor effect on trafficking.[215] The internalization results shown here for Trastuzumab antibodies and antibody fragments are in accordance with these observations, displaying that Trastuzumab Fab has comparable internalization rates like commercial Herceptin and bivalent construct Trastuzumab CL. All evaluated antibodies and antibody fragments were internalized in HER2-positive cells with a relative internalization rate of 34 to 39 % after 48 h on MCF-7 cells and on SKBR-3 cells even 38 to 52 % after 48 h. Based on these results, the prerequisite for payload delivery in the context of ADCs is met with a sufficient internalization. As Trastuzumab Fab has no Fc portion and hence is not able to bind FcRn for recycling, probably better processing and trafficking is achieved of this molecule. In contrast to that, other groups demonstrated that Herceptin undergoes a very fast and extensive recycling via early endosomes of about 85 % within 30 min.[216]

Similar investigations of researchers concerning internalization with different mAbs concluded that different properties of the targeting molecule have no effect on internalization and that this process is totally dependent on the antigen of interest.[217]

6.3. *In vitro* serum stability and thermal stability

Due to concerns regarding the hinge stability in serum from different species, *in vitro* serum stability of ADC samples in mouse and human serum were analyzed and displayed mainly unchanged total antibody concentrations. As the stability graphs of Trastuzumab CL x MMAE and Trastuzumab nCL x MMAE display comparable results over time, the stability of the cleavable protease site in the hinge region can be assumed. Only Trastuzumab Fab His x MMAE showed a strong decrease at early time points in human serum that could result from the missing second Fab fragment and Fc portion that contribute to full-length antibody stability. Regarding the drug-linker stability in mouse serum, results showed expected cleavage of the dipeptide linker valine-citrulline that is attributed to murine carboxylesterase 1c and is in accordance with previous studies.[218] This structure related cleavage that leads to release of active toxin can be mitigated by simply using another release mechanism like hydrophilic ß-glucuronide linkers or non-cleavable linkers.[138,141]

Regarding the thermal stability, individual domains of antibodies are susceptible to thermal unfolding. The first transition point represents the CH2 domain and the second one the Fab fragment.[219] Evaluation of glycosylated, unconjugated Trastuzumab constructs as well as ADCs with MMAE, showed that no alteration in the transition temperatures of both CH2 domains and Fab domains were observed. Therefore, both domains were not negatively affected by toxin conjugation with sortase A to the light chains. For further concept evaluation, deglycosylated Trastuzumab N297A constructs were used for the generation of antibody-fluorophore conjugates. N-glycosylation is an important posttranslational modification that not only affects structural properties of the Fc part of antibodies but also plays a key role for effector functions and pharmacokinetics, and therefore also modulates the efficacy and safety of these drugs.[220,221] The conserved N-glycosylation at N297 position in the Fc part stabilizes the CH2 domain of antibodies, as shown by deglycosylated antibodies that are

thermally less stable and more susceptible to thermal induced unfolding. Additionally, deglycosylation makes antibodies less hydrohphilic and prone to aggregation.[222] This derives from the assumption that several hydrophobic amino acid residues are masked by the glycan structure and by removing the glycans, these residues are exposed. Moreover, the removal of the glycan structure from the CH2 domain of antibodies may also increase the protease accessibility to the hinge region.[222] The measured melting temperatures of the CH2 domain of the deglycosylated Trastuzumab N297A constructs appear to be approximately 10°C lower than for glycosylated antibodies, which is in good agreement with previous literature reports.

6.4. Cleavable ADCs and FDCs exhibit high potency *in vitro*

After the comprehensive functional characterization of designed antibodies and ADCs, *in vitro* cytotoxicity was evaluated for all constructs. First, the MMAE-based Trastuzumab ADCs were tested on HER2-overexpressing cell lines. Currently, most of the published ADC formats show an average DAR of 2 to 4. This is mainly based on several observations. Investigations demonstrated that by increasing the DAR of ADCs, the *in vitro* potency increases as well. But higher DAR ADCs are not only associated with advantages as their plasma clearance is also accelerated, resulting in a reduced exposure and poor *in vivo* efficacy. Previous studies by Lyon et al. showed that such accelerated clearance correlates with ADC hydrophobicity, which they demonstrated by using several hydrophilic (PEG and glucuronide) drug-linkers and ADCs with different DARs.[223,224] Moreover, higher drug loading of ADCs often lead to poor tolerability, which is observed by various toxicities.[225]

Aforementioned reasons and characteristics of ADC drug load led to the conclusion, that for the present study conjugates with a DAR of 1 to 2 are sufficient. Hence, when using highly potent payloads, the low DAR should be appropriate to struck the balance between a pronounced cytotoxic activity while preserving tolerability of produced ADCs.

Cytotoxicity of Trastuzumab x MMAE ADCs on high expressing HER2-positive cell lines were tested head-to-head with Kadcyla. The cytotoxic compound MMAE is frequently used as an ADC payload and its beneficial properties like high solubility and remarkable potency resulted in the approved ADC Adcetris. MMAE acts similar like the payload DM1 of Kadcyla as an antimitotic agent by inhibiting microtubule assembly and subsequently preventing mitosis.[124,130] Trastuzumab CL x MMAE and Trastuzumab CL x MMAE + MT-SP1 samples exhibited on all tested cell lines superior potency in comparison to Kadcyla. Moreover, a better safety profile was also obtained with these constructs due to the fact that Kadcyla showed higher off-target toxicity on HER2-negative MDA-MB-468 cell line. These results might be due to several differences that probably will have a stronger influence, at least *in vivo*. Firstly, Kadcyla is a heterogeneous mixture generated by lysine conjugation with different DAR species, which impact all ADC properties like efficacy, safety, pharmacokinetics. For Trastuzumab CL x MMAE ADC a site-specific conjugation with defined DAR species was achieved. Secondly, Kadcyla utilizes a non-cleavable linker with a different release mechanism, which depends on complete degradation of the antibody.[118] Upon degradation the resulting DM1-containing lysine derivative that is released, is cell impermeable. In contrast to that, Trastuzumab CL x MMAE relies upon lysosomal cleavage of the cleavable dipeptide valine-citrulline linker to release the payload in a traceless manner without any amino

acid attached. Once MMAE is released, the cell permeable toxin can diffuse to neighbouring cells.[226] Therefore MMAE is able to induce bystander killing of HER2-positive cells as well as antigen-negative cells.

Despite the low drug load of cleaved Trastuzumab CL x MMAE + MT-SP1 and Trastuzumab Fab x MMAE of 0.8 and 0.9 respectively, remarkable potency was observed. Such cytotoxic activity can be associated with the high receptor densities on HCC1954, SKBR-3 and BT-474. Other reports with single drug conjugated products Fab_{TRA}-bisAlk-vc-MMAE (PolyTherics) targeting HER2 and anti-HER2 ADC SYD985 (Synthon) with duocarmycin as a payload obtained comparable results for *in vitro* potency.[134,227] Furthermore, an increasing interest in the development of small-format drug conjugates by several pharmaceutical and biotechnological companies (e.g. Bicycle Therapeutics and Tarveda) paved the way for first clinical investigations for such new modalities. Most of the molecules are evaluated in preclinical R&D (e.g. Seattle Genetics) and the typical molecular weight of these conjugates range from 1 kDa up to 80 kDa.[173]

When comparing the herein presented design to other small-format drug conjugates in development, most approaches might exploit an improved tumor penetration, but the molecules are still lacking a prolonged half-life. Therefore, the pharmacokinetic properties negatively influence the potential benefit of the small format.[173] The hinge cleavable ADCs used in this work might show the potential benefit for a long half-life in systemic circulation, while achieving a better tumor penetration by released Fab-drug conjugates at the tumor site.

When tested as MMAF-based ADCs, Trastuzumab constructs achieved stronger efficacy and showed slightly greater potency than MMAE counterparts. MMAF was chosen as an additional payload, because it is cell impermeable and hence it is not able to cross biomembranes and can not induce bystander effect, leading to a more precise assessment of tumor penetration *in vitro*. Therefore, only cells that are reached by the delivery vehicle are efficiently killed.

Interestingly, when comparing the IC_{50} values of the higher DAR ADCs with that of lower DAR ADCs, no dramatic change is observed. As ADC exposure-response correlation is not well understood, this suggests that a certain threshold of intratumor payload concentration is needed to exert efficacy. Above this concentration a plateau effect is reached, where excessive levels of payload to tumors are not able to enhance the efficacy even cause toxicity. This is in line with observations by Zhang and colleagues, where DAR changes of a PBD-ADC could not rationalize observed efficacies.[228]

Regarding the deglycosylated Trastuzumab N297A constructs, when tested in the toxin-based format with MMAE, similar values for *in vitro* cytotoxicity compared to glycosylated variants were observed (personal communication Merck KGaA, Darmstadt, Germany). Therefore the lack of glycosylation has probably no influence on cell binding or internalization

In summary, the cytotoxicity results of the presented study show that hinge cleavable ADCs can be generated that are homogeneous, highly efficacious on different cancer cell lines while being stable against unspecific cleavage and degradation.

6.5. Relationship between molecular size and tumor spheroid penetration and distribution

Although full-length antibodies with a long half-life can accumulate in tumor tissues and bind target cells, restricted distribution is common to the tumor cell surface, eventually resulting in poor solid tumor penetration.

On the other hand, antibody fragments with a low half-life could accumulate less efficiently, but tumor penetration is more efficiently compared to antibodies.[94,95,166,167]

Since solid tumors are exposed to various microenvironments as well as to a large concentration gradient, a spheroid model was preferred over a monolayer culture approach. Tumor spheroids reflect many properties of solid tumors. These include beside the concentration gradient, a nutrient gradient, the development of an extracellular matrix and tight junctions between cells.[159] Although limitations like the geometry of drug penetration towards the spheroid centre is not identical to the *in vivo* situation, such a spheroid model can be useful to evaluate the distribution of antibody-based molecules.

The three-dimensional spheroid model provides a useful evaluation to complement *in vitro* experiments for solid tumor penetration and distribution studies of therapeutic antibodies and antibody fragments. In autoradiography experiments, Sutherland and colleagues tested the penetration of ^{125}I-labeled anti-CEA mAb and Fab in spheroid models *in vitro*. In their study, Fab fragments were bound at surface area of tumor spheroids and additionally penetrated about eight to ten cell layers into the spheroid core, whereas intact full-length mAb was localized predominantly at exterior fractions of the spheroid surface.[229] These observations from previous experiments are similar to the used cleavable antibody-fluorophore conjugates in this study, which showed an increased tumor penetration and distribution *in vitro*.

The improved *in vitro* spheroid penetration of the Fab fragment is also in accordance with *in vivo* experiments with Co 112 xenografts in nude mice that revealed a deeper penetration of antibody fragments compared to intact antibodies and resulted in the greatest tumor to normal tissue ratio.[230] Moreover, another study confirmed also a better tumor penetration *in vivo* by antibody fragments in nephrectomized mice to exclude renal clearance related aspects.[231]

This study demonstrated that Trastuzumab CL x AF488 x BHQ-10 and Trastuzumab Fab x AF488 constructs had remarkable differences in tumor penetration and distribution properties *in vitro* compared to full-length antibody Trastuzumab nCL x AF488.

Despite better distribution, toxin-based ADCs Trastuzumab CL x MMAE and Trastuzumab Fab x MMAE exhibited nearly equivalent pharmacological characteristics like cellular binding, internalization efficiency as well as cytotoxicity against HER2-overexpressing cell lines.

Tumor spheroid experiments with HC1954 cells revealed that an improved distribution throughout the entire tumor spheroid was achieved with Trastuzumab CL x AF488 x BHQ-10 and Trastuzumab Fab x AF488 constructs, whereas Trastuzumab nCL x AF488 localized only at exterior fractions on tumor cell surface. The smaller antibody-fluorophore conjugates fill a shell at the surface of the sphere, moving progressively towards the spheroid core.

In summary, the results indicated that hinge cleavable ADCs and FDCs with a lower molecular weight and reduced size can distribute more efficiently within tumor spheroids. Selective localization of hinge cleavable antibodies at the tumor site may offer a potential benefit to target the entire solid tumor. It will be interesting to see how these early *in vitro* imaging data will translate into a biodistribution study *in vivo*.

The hinge cleavable ADC design described here is universally applicable. This work showed that additionally to the auristatins MMAE and MMAF conjugated to glycosylated Trastuzumab formats, also the fluorophore

Alexa Fluor 488 with a triple-glycine tag can be conjugated to the light chains of deglycosylated Trastuzumab N297A variants using sortase A mediated conjugation. Furthermore, the drug-linker Gly_3-ValCit-PABC-MMAE used here can be attached to different mAbs like EGFR-specific Cetuximab constructs also with a hinge cleavable design and consistently delivers highly potent ADCs and FDCs.

6.6. Outlook

Further investigations are needed to confirm the potential benefit against solid tumors in terms of tumor penetration and localization. As it is difficult to establish a relation between tumor shrinkage and tumor penetration, *in vivo* biodistribution studies with antibody-fluorophore conjugates will be performed. The constructs that were already tested with tumor spheroids *in vitro* using Alexa Fluor 488 will be used for imaging analysis. Furthermore, the hinge non-cleavable control will be prepared with the red fluorophore Cy5 for a better differentiation. Conjugates will be applied in HCC1954 xenografted mice. Imaging of cleavable conjugates within a complex, intact tumor microenvironment and with existing vasculature will present valuable insights not only for tumor penetration, but also for pharmacokinetics. One major advantage of this work relies in the maintained half-life, which can only appropriately tested *in vivo*.

The toxin-based ADCs showed remarkable *in vitro* potency results even with a low DAR. Generally, for an *in vivo* cancer model the tumor cells proximal to the blood vessel are proliferating and viable. Hence, targeting with microtubule inhibitors like in the presented study with MMAE and MMAF would be suitable to efficiently eradicate perivascular tumor cells. However, cells distant from the vasculature are often not proliferating and necrotic. For such case, DNA damaging agents like duocarmycins, PBDs or IGNs should be selected as payloads, because these drugs can address also non-dividing tumor cells.[120,133] For future investigations it would be interesting to see, if these hinge cleavable ADCs with DNA damaging agents can address non-proliferating cells properly.

Besides the therapeutic application, three single Fab fragments are used for diagnostic purposes for SPECT (single photon emission computed tomography) imaging. Other approaches were developed for surgical navigation in patients like image-guided surgery. Image-guided surgery has become an essential tool in brain tumor surgery and neurosurgery. For detection of brain tumors it is very important to localize the exact position of the tumor in order to prevent healthy tissue damage and ensure no residual cancer cells left behind. In general, Fab molecules or small molecule ligands are used due to the shorter half-life. The cleavable antibody could thus be utilized in diagnostic applications, where a longer half-life is needed.[100]

7. References

1. Tortora, G. J. & Derrickson, B. *Principles of Anatomy & Physiology*. (John Wiley & Sons, 2014).
2. American Cancer Society. Cancer Facts & Figures 2019. *Atlanta Am. Cancer Soc.* (2019).
3. Danaei, G. *et al.* Causes of cancer in the world : comparative risk assessment of nine behavioural and environmental risk factors. *Lancet* **366**, 1784–93 (2005).
4. Colditz, G. A., Sellers, T. A. & Trapido, E. Epidemiology — identifying the causes and preventability of cancer? *Nat. Rev. Cancer* **6**, 75–83 (2006).
5. Sobin, L. H., Gospodarowicz, M. K. & Wittekind, C. *TNM - Classification of Malignant Tumours*. (John Wiley & Sons, 2009).
6. Strickland, G. T., El-Kamary, S. S., Klenerman, P. & Nicosia, A. Hepatitis C vaccine : supply and demand. *Lancet Infect Dis* **8**, 379–386 (2008).
7. Correa, P. Is gastric cancer preventable ? *Gut* **53**, 1217–1219 (2004).
8. Mørch, L. S. *et al.* Contemporary Hormonal Contraception and the Risk of Breast Cancer. *N. Engl. J. Med.* **377**, 2228–39 (2017).
9. Stewart, B. W. & Wild, C. P. World Cancer Report 2014. *Int. Agency Res. Cancer* (2014).
10. Heron, M. Deaths : Leading Causes for 2013. *Natl. Vital Stat. Reports* **65**, 1–95 (2016).
11. Murphy, S. L., Xu, J., Kochanek, K. D. & Arias, E. Mortality in the United States , 2017. *NCHS Data Brief* 1–8 (2018).
12. Siegel, R. L., Miller, K. D. & Jemal, A. Cancer Statistics , 2018. *Ca Cancer J Clin* **68**, 7–30 (2018).
13. Kaatsch, P. Epidemiology of childhood cancer. *Cancer Treat. Rev.* **36**, 277–285 (2010).
14. NCI. A Snapshot of Leukemia. *Natl. Cancer Inst.* 1–2 (2013).
15. Hanahan, D. & Weinberg, R. A. Hallmarks of Cancer: The Next Generation. *Cell* **144**, 646–674 (2011).
16. Lemmon, M. A. & Schlessinger, J. Cell Signaling by Receptor Tyrosine Kinases. *Cell* **141**, 1117–1134 (2010).
17. Arteaga, C. L. *et al.* Treatment of HER2-positive breast cancer: current status and future perspectives. *Nat. Rev. Clin. Oncol.* **9**, 16–32 (2012).
18. Witsch, E., Sela, M. & Yarden, Y. Roles for Growth Factors in Cancer Progression. *Physiology* **25**, 85–101 (2010).
19. Bhowmick, N. A., Neilson, E. G. & Moses, H. L. Stromal fibroblasts in cancer initiation and progression. *Nature* **432**, (2004).
20. Green, D. R. & Kroemer, G. Cytoplasmic functions of the tumour suppressor p53. *Nature* **458**, 1127–1130 (2009).
21. Vousden, K. H. & Prives, C. Blinded by the Light: The Growing Complexity of p53. *Cell* **137**, 413–431 (2009).
22. Adams, J. M. & Cory, S. The Bcl-2 apoptotic switch in cancer development and therapy. *Oncogene* **26**, 1324–1337 (2007).
23. Blackburn, E. H. Telomeres and Telomerase: The Means to the End (Nobel Lecture). *Angew. Chem. Int. Ed.* **49**, 7405–7421 (2010).
24. Blasco, M. A. Telomeres and human disease: Ageing, cancer and beyond. *Nat. Rev. Genet.* **6**, 611–622 (2005).
25. Bergers, G. & Benjamin, L. E. Tumorigenesis and the angiogenic switch. *Nat. Rev. Cancer* **3**, 401–410 (2003).
26. Cristofanilli, M., Charnsangavej, C. & Hortobagyi, G. N. Angiogenesis modulation in cancer research: novel clinical approaches. *Nat. Rev. Drug Discov.* **1**, 415–426 (2002).
27. Grothey, A. & Galanis, E. Targeting angiogenesis: progress with anti-VEGF treatment with large molecules. *Nat. Rev. Clin. Oncol.* **6**, 507–518 (2009).
28. Nyberg, P., Xie, L. & Kalluri, R. Endogenous Inhibitors of Angiogenesis. *Cancer Res.* **65**, 3967–3980 (2005).
29. Peinado, H., Ballestar, E., Esteller, M. & Cano, A. Snail Mediates E-Cadherin Repression by the Recruitment of the Sin3A/Histone Deacetylase 1 (HDAC1)/HDAC2 Complex. *Mol. Cell. Biol.* **24**, 306–319 (2004).
30. Talmadge, J. E. & Fidler, I. J. AACR Centennial Series : The Biology of Cancer Metastasis: Historical Perspective. *Cancer Res.* **70**, 5649–5670 (2010).
31. Joyce, J. A. & Pollard, J. W. Microenvironmental regulation of metastasis. *Nat. Rev. Cancer* **9**, 239–52

(2009).
32. Berx, G. & Roy, F. Van. Involvement of Members of the Cadherin Superfamily in Cancer. *Cold Spring Harb Perspect Biol* **1**, 1–29 (2009).
33. Lambert, A. W., Pattabiraman, D. R. & Weinberg, R. A. Emerging Biological Principles of Metastasis. *Cell* **168**, 670–691 (2017).
34. DeBerardinis, R. J., Lum, J. J., Hatzivassiliou, G. & Thompson, C. B. The Biology of Cancer: Metabolic Reprogramming Fuels Cell Growth and Proliferation. *Cell Metab.* **7**, 11–20 (2008).
35. Jones, R. G. & Thompson, C. B. Tumor suppressors and cell metabolism: a recipe for cancer growth. *Genes Dev.* **23**, 537–548 (2009).
36. Bindea, G., Mlecnik, B., Fridman, W.-H., Pages, F. & Galon, J. Natural immunity to cancer in humans. *Curr. Opin. Immunol.* **22**, 215–222 (2010).
37. Pardoll, D. M. The blockade of immune checkpoints in cancer immunotherapy. *Nat. Rev. Cancer* **12**, 252–64 (2012).
38. Negrini, S., Gorgoulis, V. G. & Halazonetis, T. D. Genomic instability — an evolving hallmark of cancer. *Nat. Rev. Mol. Cell Biol.* **11**, 220–228 (2010).
39. Colotta, F., Allavena, P., Sica, A., Garlanda, C. & Mantovani, A. Cancer-related inflammation, the seventh hallmark of cancer: links to genetic instability. *Carcinogenesis* **30**, 1073–1081 (2009).
40. Urruticoechea, A. *et al.* Recent Advances in Cancer Therapy: An Overview. *Curr. Pharm. Des.* **16**, 3–10 (2010).
41. Halsted, W. S. The Results of Operations for the Cure of Cancer of the Breast Performed at the Johns Hopkins Hospital from June, 1889, to January, 1894. *Ann Surg* **20**, 497–555 (1894).
42. Mould, R. F. Priority for radium therapy of benign conditions and cancer. *Curr. Oncol.* **14**, 118–122 (2007).
43. Bristow, R. G. *et al.* Combining precision radiotherapy with molecular targeting and immunomodulatory agents: a guideline by the American Society for Radiation Oncology. *Lancet Oncol.* **19**, 240–251 (2018).
44. DeVita, V. T. & Chu, E. A History of Cancer Chemotherapy. *Cancer Res* **68**, 8643–8653 (2008).
45. Strebhardt, K. & Ullrich, A. Paul Ehrlich's magic bullet concept: 100 years of progress. *Nat. Rev. Cancer* **8**, 473–480 (2008).
46. Gilman, A. The Initial Clinical Trial Nitrogen Mustard. *Am. J. Surg.* **105**, 574–578 (1963).
47. Watson, J. D. & Crick, F. H. Molecular structure of nucleic acids; a structure for deoxyribose nucleic acid. *Nature* **171**, 737–738 (1953).
48. Heidelberger, C. *et al.* Fluorinated pyrimidines, a new class of tumour-inhibitory compounds. *Nature* **179**, 663–666 (1957).
49. Chen, J. & Stubbe, J. Bleomycins: Towards better therapeutics. *Nat. Rev. Cancer* **5**, 102–112 (2005).
50. Chabner, B. A. & Roberts, T. G. Chemotherapy and the war on cancer. *Nat. Rev. Cancer* **5**, 65–72 (2005).
51. Skipper, H. E., Thomson, J. R., Elion, G. B. & Hitchings, G. H. Observations on the Anticancer Activity of 6-Mercaptopurine. *Cancer Res* **14**, 294–299 (1954).
52. Dasari, S. & Tchounwou, P. B. Cisplatin in cancer therapy: Molecular mechanisms of action. *Eur. J. Pharmacol.* **740**, 364–378 (2014).
53. Fennell, D. A. *et al.* Cisplatin in the modern era: The backbone of first-line chemotherapy for non-small cell lung cancer. *Cancer Treat. Rev.* **44**, 42–50 (2016).
54. Druker, B. J. *et al.* Effects of a selective inhibitor of the Abl tyrosine kinase on the growth of Bcr-Abl positive cells. *Nat. Med.* **2**, 561–566 (1996).
55. Deininger, M., Buchdunger, E. & Druker, B. J. The development of imatinib as a therapeutic agent for chronic myeloid leukemia. *Blood* **105**, 2640–2654 (2005).
56. Levitzki, A. Tyrosine Kinase Inhibitors: Views of Selectivity, Sensitivity, and Clinical Performance. *Annu. Rev. Pharmacol. Toxicol.* **53**, 161–85 (2013).
57. Köhler, G. & Milstein, C. Continuous cultures of fused cells secreting antibody of predefined specificity. *Nature* **256**, 495–497 (1975).
58. Maloney, D. G. *et al.* IDEC-C2B8 (Rituximab) Anti-CD20 Monoclonal Antibody Therapy in Patients With Relapsed Low-Grade Non-Hodgkin's Lymphoma. *Blood* **90**, 2188–2195 (1997).
59. Gürcan, H. M. *et al.* A review of the current use of rituximab in autoimmune diseases. *Int. Immunopharmacol.* **9**, 10–25 (2009).
60. Nahta, R., Yu, D., Hung, M. C., Hortobagyi, G. N. & Esteva, F. J. Mechanisms of Disease:

understanding resistance to HER2-targeted therapy in human breast cancer. *Nat Clin Pr. Oncol* **3**, 269–280 (2006).
61. Graham, J., Muhsin, M. & Kirkpatrick, P. Cetuximab. *Nat. Rev. Drug Discov.* **3**, 549–550 (2004).
62. Muhsin, M., Graham, J. & Kirkpatrick, P. Bevacizumab. *Nat. Rev. Drug Discov.* **3**, 995–996 (2004).
63. Shih, T. & Lindley, C. Bevacizumab: An Angiogenesis Inhibitor for the Treatment of Solid Malignancies. *Clin. Ther.* **28**, 1779–1802 (2006).
64. Sievers, E. L. & Senter, P. D. Antibody-Drug Conjugates in Cancer Therapy. *Annu. Rev. Med.* **64**, 15–29 (2013).
65. Wei, S. C., Duffy, C. R. & Allison, J. P. Fundamental Mechanisms of Immune Checkpoint Blockade Therapy. *Cancer Discov* **8**, 1069–1086 (2018).
66. Hargadon, K. M., Johnson, C. E. & Williams, C. J. Immune checkpoint blockade therapy for cancer: An overview of FDA-approved immune checkpoint inhibitors. *Int. Immunopharmacol.* **62**, 29–39 (2018).
67. Jen, E. Y. *et al.* FDA Approval: Gemtuzumab Ozogamicin for the Treatment of Adults with Newly Diagnosed CD33-Positive Acute Myeloid Leukemia. *Clin Cancer Res* **24**, 3242–3247 (2018).
68. Senter, P. D. & Sievers, E. L. The discovery and development of brentuximab vedotin for use in relapsed Hodgkin lymphoma and systemic anaplastic large cell lymphoma. *Nat. Biotechnol.* **30**, 631–637 (2012).
69. Kantarjian, H. M. *et al.* Inotuzumab Ozogamicin versus Standard Therapy for Acute Lymphoblastic Leukemia. *N Engl J Med* **375**, 740–753 (2016).
70. Dornan, D. *et al.* Therapeutic potential of an anti-CD79b antibody–drug conjugate, anti–CD79b-vc-MMAE, for the treatment of non-Hodgkin lymphoma. *Blood* **114**, 2721–2730 (2009).
71. F. Hoffmann-La Roche Ltd. Media Release - FDA grants Roche's Polivy accelerated approval for people with previously treated aggressive lymphoma. 1–4 (2019).
72. Murphy, K. *Janeway's Immunobiology*. (Garland Science, 2012).
73. Akira, S. & Hemmi, H. Recognition of pathogen-associated molecular patterns by TLR family. *Immunol. Lett.* **85**, 85–95 (2003).
74. Iwasaki, A. & Medzhitov, R. Regulation of Adaptive Immunity by the Innate Immune System. *Sci. Transl. Med.* 291–296 (2010).
75. Nutt, S. L., Hodgkin, P. D., Tarlinton, D. M. & Corcoran, L. M. The generation of antibody-secreting plasma cells. *Nat. Rev. Immunol.* **15**, 160–171 (2015).
76. Kasamatsu, J. Evolution of innate and adaptive immune systems in jawless vertebrates. *Microbiol Immunol* **57**, 1–12 (2013).
77. Reichert, J. M., Rosensweig, C. J., Faden, L. B. & Dewitz, M. C. Monoclonal antibody successes in the clinic. *Nat. Biotechnol.* **23**, 1073–1078 (2005).
78. Reichert, J. M. Marketed therapeutic antibodies compendium. *MAbs* **4**, 413–415 (2012).
79. Salfeld, J. G. Isotype selection in antibody engineering. *Nat. Biotechnol.* **25**, 1369–1372 (2007).
80. Davies, D. R. & Chacko, S. Antibody Structure. *Acc. Chem. Res.* 421–427 (1993).
81. Schroeder, H. W. & Cavacini, L. Structure and function of immunoglobulins. *J Allergy Clin Immunol* **125**, 41–52 (2010).
82. Sela-Culang, I., Kunik, V. & Ofran, Y. The structural basis of antibody-antigen recognition. *Front. Immunol.* **4**, 1–13 (2013).
83. Moritz, B. & Stracke, J. O. Assessment of disulfide and hinge modifications in monoclonal antibodies. *Electrophoresis* **38**, 769–785 (2017).
84. Correia, I. R. Stability of IgG isotypes in serum. *MAbs* **2**, 221–232 (2010).
85. Hudis, C. A. Trastuzumab — Mechanism of Action and Use in Clinical Practice. *N Engl J Med* **357**, 39–51 (2007).
86. Dijstelbloem, H. M., van de Winkel, J. G. J. & Kallenberg, C. G. M. Inflammation in autoimmunity: receptors for IgG revisited. *TRENDS Immunol.* **22**, 510–516 (2001).
87. Nimmerjahn, F. & Ravetch, J. V. Fcγ Receptors: Old Friends and New Family Members. *Immunity* **24**, 19–28 (2006).
88. Shields, R. L. *et al.* High Resolution Mapping of the Binding Site on Human IgG1 for FcγRI, FcγRII, FcγRIII, and FcRn and Design of IgG1 Variants with Improved Binding to the FcγR. *J. Biol. Chem.* **276**, 6591–6604 (2001).
89. Dall'Ozzo, S. *et al.* Rituximab-Dependent Cytotoxicity by Natural Killer Cells: Influence of FCGR3A Polymorphism on the Concentration-Effect Relationship. *Cancer Res.* **64**, 4664–4669 (2004).
90. Nimmerjahn, F. & Ravetch, J. V. Fcγ receptors as regulators of immune responses. *Nat. Rev. Immunol.*

8, 34–47 (2008).
91. Scott, A. M., Wolchok, J. D. & Old, L. J. Antibody therapy of cancer. *Nat. Rev. Cancer* **12**, 278–287 (2012).
92. Matsumiya, S. *et al.* Structural Comparison of Fucosylated and Nonfucosylated Fc Fragments of Human Immunoglobulin G1. *J. Mol. Biol.* **368**, 767–779 (2007).
93. Pereira, N. A., Chan, K. F., Lin, P. C. & Song, Z. The "less-is-more" in therapeutic antibodies: Afucosylated anti-cancer antibodies with enhanced antibody-dependent cellular cytotoxicity. *MAbs* **10**, 693–711 (2018).
94. Roopenian, D. C. & Akilesh, S. FcRn: the neonatal Fc receptor comes of age. *Nat. Rev. Immunol.* **7**, 715–25 (2007).
95. Petkova, S. B. *et al.* Enhanced half-life of genetically engineered human IgG1 antibodies in a humanized FcRn mouse model: potential application in humorally mediated autoimmune disease. *Int. Immunol.* **18**, 1759–1769 (2006).
96. Chaudhury, C. *et al.* The Major Histocompatibility Complex–related Fc Receptor for IgG (FcRn) Binds Albumin and Prolongs Its Lifespan. *J. Exp. Med.* **197**, 315–322 (2003).
97. Hwang, W. Y. K. & Foote, J. Immunogenicity of engineered antibodies. *Methods* **36**, 3–10 (2005).
98. Fredericks, Z. L. *et al.* Identification of potent human anti-IL-1RI antagonist antibodies. *Protein Eng. Des. Sel.* **17**, 95–106 (2004).
99. Carter, P. J. Potent antibody therapeutics by design. *Nat. Rev. Immunol.* **6**, 343–357 (2006).
100. Chapman, A. P. *et al.* Therapeutic antibody fragments with prolonged in vivo half-lives. *Nat. Biotechnol.* **17**, 780–783 (1999).
101. Choy, E. H. S. *et al.* Efficacy of a novel PEGylated humanized anti-TNF fragment (CDP870) in patients with rheumatoid arthritis: a phase II double-blinded, randomized, dose-escalating trial. *Rheumatology* **41**, 1133–1137 (2002).
102. Sheridan, C. Ablynx's nanobody fragments go places antibodies cannot. *Nat. Biotechnol.* **35**, 1115–1117 (2017).
103. Kobayashi, H., Choyke, P. L. & Ogawa, M. Monoclonal antibody-based optical molecular imaging probes; considerations and caveats in chemistry, biology and pharmacology. *Curr. Opin. Chem. Biol.* **33**, 32–38 (2016).
104. Beck, A., Goetsch, L., Dumontet, C. & Corvaïa, N. Strategies and challenges for the next generation of antibody–drug conjugates. *Nat. Rev. Drug Discov.* **16**, 315–337 (2017).
105. Panowski, S., Bhakta, S., Raab, H., Polakis, P. & Junutula, J. R. Site-specific antibody drug conjugates for cancer therapy. *MAbs* **6**, 34–45 (2014).
106. Perez, H. L. *et al.* Antibody–drug conjugates: current status and future directions. *Drug Discov. Today* **19**, 869–881 (2014).
107. Chari, R. V. J., Miller, M. L. & Widdison, W. C. Antibody–Drug Conjugates: An Emerging Concept in Cancer Therapy. *Angew. Chem. Int. Ed.* **53**, 3796–3827 (2014).
108. Damelin, M., Zhong, W., Myers, J. & Sapra, P. Evolving Strategies for Target Selection for Antibody-Drug Conjugates. *Pharm Res* **32**, 3494–3507 (2015).
109. Lambert, J. M. & Berkenblit, A. Antibody–Drug Conjugates for Cancer Treatment. *Annu. Rev. Med.* **69**, 191–207 (2018).
110. Ritchie, M., Tchistiakova, L. & Scott, N. Implications of receptor-mediated endocytosis and intracellular trafficking dynamics in the development of antibody drug conjugates. *MAbs* **5**, 13–21 (2013).
111. Hoffmann, R. M. *et al.* Antibody structure and engineering considerations for the design and function of Antibody Drug Conjugates (ADCs). *Oncoimmunology* **7**, 1–11 (2018).
112. Starling, J. J. *et al.* In vivo efficacy of monoclonal antibody-drug conjugates of three different subisotypes which bind the human tumor-associated antigen defined by the KS1/4 monoclonal antibody. *Cancer Immunol Immunother* **28**, 171–178 (1989).
113. Trail, P. A. *et al.* Cure of Xenografted Human Carcinomas by BR96-Doxorubicin Immunoconjugates. *Sci. Transl. Med.* **261**, 212–216 (1993).
114. Elias, D. J. *et al.* Phase I Clinical Comparative Study of Monoclonal Antibody KS1/4 and KS1/4-Methotrexate Immunconjugate in Patients with Non-Small Cell Lung Carcinoma. *Cancer Res* **50**, 4154–4159 (1990).
115. Saleh, M. N. *et al.* Phase I Trial of the Anti–Lewis Y Drug Immunoconjugate BR96-Doxorubicin in Patients With Lewis Y–Expressing Epithelial Tumors. *J. Clin. Oncol.* **18**, 2282–2292 (2000).

116. Bross, P. F. *et al.* Approval Summary: Gemtuzumab Ozogamicin in Relapsed Acute Myeloid Leukemia. *Clin. Cancer Res.* **7**, 1490–1496 (2001).
117. Sievers, E. L. Antibody-targeted chemotherapy of acute myeloid leukemia using gemtuzumab ozogamicin (Mylotarg). *Blood Cells, Mol. Dis.* **31**, 7–10 (2003).
118. Lambert, J. M. & Chari, R. V. J. Ado-trastuzumab Emtansine (T-DM1): An Antibody–Drug Conjugate (ADC) for HER2-Positive Breast Cancer. *J. Med. Chem.* **57**, 6949–6964 (2014).
119. Junttila, T. T., Li, G., Parsons, K., Phillips, G. L. & Sliwkowski, M. X. Trastuzumab-DM1 (T-DM1) retains all the mechanisms of action of trastuzumab and efficiently inhibits growth of lapatinib insensitive breast cancer. *Breast Cancer Res Treat* **128**, 347–356 (2011).
120. Dumontet, C. & Jordan, M. A. Microtubule-binding agents: a dynamic field of cancer therapeutics. *Nat. Rev. Drug Discov.* **9**, 790–803 (2010).
121. Chari, R. V. J. Expanding the Reach of Antibody–Drug Conjugates. *ACS Med. Chem. Lett.* **7**, 974–976 (2016).
122. Pettit, G. R. *et al.* The Isolation and Structure of a Remarkable Marine Animal Antineoplastic Constituent: Dolastatin 10. *J. Am. Chem. Soc.* **109**, 6883–6885 (1987).
123. Maderna, A. *et al.* Discovery of Cytotoxic Dolastatin 10 Analogues with N-Terminal Modifications. *J. Med. Chem.* **57**, 10527–10543 (2014).
124. Maderna, A. & Leverett, C. A. Recent Advances in the Development of New Auristatins: Structural Modifications and Application in Antibody Drug Conjugates. *Mol. Pharm.* **12**, 1798–1812 (2015).
125. Okeley, N. M. *et al.* Intracellular Activation of SGN-35, a Potent Anti-CD30 Antibody-Drug Conjugate. *Clin Cancer Res* **16**, 888–897 (2010).
126. Doronina, S. O. *et al.* Enhanced Activity of Monomethylauristatin F through Monoclonal Antibody Delivery: Effects of Linker Technology on Efficacy and Toxicity. *Bioconjugate Chem.* **17**, 114–124 (2006).
127. Widdison, W. C. *et al.* Development of Anilino-Maytansinoid ADCs that Efficiently Release Cytotoxic Metabolites in Cancer Cells and Induce High Levels of Bystander Killing. *Bioconjugate Chem.* **26**, 2261–2278 (2015).
128. Goeij, B. E. C. G. De *et al.* High Turnover of Tissue Factor Enables Efficient Intracellular Delivery of Antibody–Drug Conjugates. *Mol Cancer Ther* **14**, 1130–1141 (2015).
129. Widdison, W. C. *et al.* Semisynthetic Maytansine Analogues for the Targeted Treatment of Cancer. *J. Med. Chem.* **49**, 4392–4408 (2006).
130. Cassady, J. M., Chan, K. K., Floss, H. G. & Leistner, E. Recent Developments in the Maytansinoid Antitumor Agents. *Chem. Pharm. Bull.* **52**, 1—26 (2004).
131. Shor, B., Gerber, H.-P. & Sapra, P. Preclinical and clinical development of inotuzumab-ozogamicin in hematological malignancies. *Mol. Immunol.* **67**, 107–116 (2015).
132. Smith, A. L. & Nicolaou, K. C. The Enediyne Antibiotics. *J. Med. Chem.* **39**, 2103–2117 (1996).
133. Dokter, W. *et al.* Preclinical Profile of the HER2-Targeting ADC SYD983/ SYD985: Introduction of a New Duocarmycin-Based Linker- Drug Platform. *Mol Cancer Ther* **13**, 2618–2630 (2014).
134. Elgersma, R. C. *et al.* Design, Synthesis, and Evaluation of Linker-Duocarmycin Payloads: Toward Selection of HER2-Targeting Antibody–Drug Conjugate SYD985. *Mol. Pharm.* **12**, 1813–1835 (2015).
135. Tietze, L. F., Herzig, T., Fecher, A., Haunert, F. & Schuberth, I. Highly Selective Glycosylated Prodrugs of Cytostatic CC-1065 Analogues for Antibody-Directed Enzyme Tumor Therapy. *Chembiochem* **2**, 758–765 (2001).
136. Saunders, L. R. *et al.* A DLL3-targeted antibody-drug conjugate eradicates high-grade pulmonary neuroendocrine tumor-initiating cells in vivo. *Sci. Transl. Med.* **7**, 1–13 (2015).
137. Mantaj, J., Jackson, P. J. M., Rahman, K. M. & Thurston, D. E. From Anthramycin to Pyrrolobenzodiazepine (PBD)- Containing Antibody–Drug Conjugates (ADCs). *Angew. Chem. Int. Ed.* **56**, 462–488 (2017).
138. Pillow, T. H. *et al.* Modulating Therapeutic Activity and Toxicity of Pyrrolobenzodiazepine Antibody–Drug Conjugates with Self-Immolative Disulfide Linkers. *Mol Cancer Ther* **16**, 871–879 (2017).
139. Miller, M. L. *et al.* A New Class of Antibody–Drug Conjugates with Potent DNA Alkylating Activity. *Mol Cancer Ther* **15**, 1870–1879 (2016).
140. Kovtun, Y. *et al.* IMGN779, a Novel CD33-Targeting Antibody– Drug Conjugate with DNA-Alkylating Activity, Exhibits Potent Antitumor Activity in Models of AML. *Mol Cancer Ther* **17**, 1271–1280 (2018).
141. Burke, P. J. *et al.* Optimization of a PEGylated Glucuronide- Monomethylauristatin E Linker for

Antibody–Drug Conjugates. *Mol Cancer Ther* **16**, 116–123 (2017).
142. Forman, H. J., Zhang, H. & Rinna, A. Glutathione: Overview of its protective roles, measurement, and biosynthesis. *Mol. Aspects Med.* **30**, 1–12 (2009).
143. Tsuchikama, K. & An, Z. Antibody-drug conjugates: recent advances in conjugation and linker chemistries. *Protein Cell* **9**, 33–46 (2018).
144. Senter, P. D. Potent antibody drug conjugates for cancer therapy. *Curr. Opin. Chem. Biol.* **13**, 235–244 (2009).
145. Alley, S. C., Okeley, N. M. & Senter, P. D. Antibody–drug conjugates: targeted drug delivery for cancer. *Curr. Opin. Chem. Biol.* **14**, 529–537 (2010).
146. Hu, X., Lerch, T. F. & Xu, A. Efficient and Selective Bioconjugation Using Surfactants. *Bioconjugate Chem.* **29**, 3667–3676 (2018).
147. Zhou, Q. Site-Specific Antibody Conjugation for ADC and Beyond. *Biomedicines* **5**, 1–15 (2017).
148. Liu, H. & May, K. Disulfide bond structures of IgG molecules. *MAbs* **4**, 17–23 (2012).
149. Jackson, D. Y. Processes for Constructing Homogeneous Antibody Drug Conjugates. *Org. Process Res. Dev.* **20**, 852–866 (2016).
150. Jain, N., Smith, S. W., Ghone, S. & Tomczuk, B. Current ADC Linker Chemistry. *Pharm Res* **32**, 3526–3540 (2015).
151. Stefan, N. *et al.* Highly Potent, Anthracycline-based Antibody–Drug Conjugates Generated by Enzymatic, Site-specific Conjugation. *Mol Cancer Ther* **16**, 879–893 (2017).
152. Popp, M. W.-L. & Ploegh, H. L. Making and Breaking Peptide Bonds: Protein Engineering Using Sortase. *Angew. Chem. Int. Ed.* **50**, 5024 – 5032 (2011).
153. Agarwal, P. & Bertozzi, C. R. Site-Specific Antibody–Drug Conjugates: The Nexus of Bioorthogonal Chemistry, Protein Engineering, and Drug Development. *Bioconjugate Chem.* **26**, 176–192 (2015).
154. Strop, P. Versatility of Microbial Transglutaminase. *Bioconjugate Chem.* **25**, 855–862 (2014).
155. Dennler, P. *et al.* Transglutaminase-Based Chemo-Enzymatic Conjugation Approach Yields Homogeneous Antibody–Drug Conjugates. *Bioconjugate Chem.* **25**, 569–578 (2014).
156. Rashidian, M., Dozier, J. K. & Distefano, M. D. Enzymatic Labeling of Proteins: Techniques and Approaches. *Bioconjugate Chem.* **24**, 1277–1294 (2013).
157. Ackerman, M. E., Pawlowski, D. & Wittrup, K. D. Effect of antigen turnover rate and expression level on antibody penetration into tumor spheroids. *Mol Cancer Ther* **7**, 2233–2241 (2008).
158. Bornstein, G. G. Antibody Drug Conjugates: Preclinical Considerations. *AAPS J.* **17**, 525–534 (2015).
159. Minchinton, A. I. & Tannock, I. F. Drug penetration in solid tumours. *Nat. Rev. Cancer* **6**, 583–592 (2006).
160. Sharkey, R. M. & Goldenberg, D. M. Use of antibodies and immunoconjugates for the therapy of more accessible cancers. *Adv. Drug Deliv. Rev.* **60**, 1407–1420 (2008).
161. Thurber, G. M., Schmidt, M. M. & Wittrup, K. D. Antibody tumor penetration: Transport opposed by systemic and antigen-mediated clearance. *Adv. Drug Deliv. Rev.* **60**, 1421–1434 (2008).
162. Han, T. H. & Zhao, B. Absorption, Distribution, Metabolism, and Excretion Considerations for the Development of Antibody-Drug Conjugates. *Drug Metab Dispos* **42**, 1914–1920 (2014).
163. Peters, C. & Brown, S. Antibody–drug conjugates as novel anti-cancer chemotherapeutics. *Biosci. Rep.* **35**, 1–20 (2015).
164. Epenetos, A. A., Snook, D., Durbin, H., Johnson, P. M. & Taylor-Papadimitriou, J. Limitations of Radiolabeled Monoclonal Antibodies for Localization of Human Neoplasms. *Cancer Res.* **46**, 3183–3191 (1986).
165. Teicher, B. A. & Chari, R. V. J. Antibody Conjugate Therapeutics: Challenges and Potential. *Clin Cancer ResRes* **17**, 6389–97 (2011).
166. Graff, C. P. & Wittrup, K. D. Theoretical Analysis of Antibody Targeting of Tumor Spheroids: Importance of Dosage for Penetration, and Affinity for Retention. *Cancer Res* **63**, 1288–1296 (2003).
167. Dennis, M. S. *et al.* Imaging Tumors with an Albumin-Binding Fab, a Novel Tumor-Targeting Agent. *Cancer Res.* **67**, 254–261 (2007).
168. Singh, S. K., Luisi, D. L. & Pak, R. H. Antibody-Drug Conjugates: Design, Formulation and Physicochemical Stability. *Pharm Res* **32**, 3541–3571 (2015).
169. Schmidt, M. M. & Wittrup, K. D. A modeling analysis of the effects of molecular size and binding affinity on tumor targeting. *Mol Cancer Ther* **8**, 2861–71 (2009).
170. Cazzamalli, S., Corso, A. D., Widmayer, F. & Neri, D. Chemically Defined Antibody– and Small Molecule–Drug Conjugates for in Vivo Tumor Targeting Applications: A Comparative Analysis. *J.*

Am. Chem. Soc. **140**, 1617–1621 (2018).
171. Cazzamalli, S., Corso, A. D. & Neri, D. Targeted Delivery of Cytotoxic Drugs: Challenges, Opportunities and New Developments. *Chimia (Aarau).* **71**, 712–715 (2017).
172. Casi, G. & Neri, D. Antibody–Drug Conjugates and Small Molecule–Drug Conjugates: Opportunities and Challenges for the Development of Selective Anticancer Cytotoxic Agents. *J. Med. Chem.* **58**, 8751–8761 (2015).
173. Deonarain, M. P. Miniaturised 'antibody'-drug conjugates for solid tumours? *Drug Discov. Today Technol.* **30**, 47–53 (2018).
174. Adams, G. P. *et al.* High Affinity Restricts the Localization and Tumor Penetration of Single-Chain Fv Antibody Molecules. *Cancer Res.* **61**, 4750–4755 (2001).
175. Rudnick, S. I. *et al.* Influence of affinity and antigen internalization on the uptake and penetration of anti-HER2 Antibodies in Solid Tumors. *Cancer Res.* **71**, 2250–2259 (2011).
176. Tsumura, R. *et al.* Influence of the dissociation rate constant on the intra-tumor distribution of antibody-drug conjugate against tissue factor. *J. Control. Release* **284**, 49–56 (2018).
177. Blumenthal, R. D. *et al.* The effect of antibody protein dose on the uniformity of tumor distribution of radioantibodies: an autoradiographic study. *Cancer Immunol Immunother* **33**, 351–358 (1991).
178. Sato, N. *et al.* Intratumoral Distribution of Radiolabeled Antibody and Radioimmunotherapy in Experimental Liver Metastases Model of Nude Mouse. *J Nucl Med* **40**, 685–692 (1999).
179. Boerman, O. C. *et al.* Influence of antibody protein dose on therapeutic efficacy of radioiodinated antibodies in nude mice bearing GW-39 human tumor. *Cancer Immunol Immunother* **35**, 127–134 (1992).
180. Cilliers, C., Menezes, B., Nessler, I., Linderman, J. & Thurber, G. M. Improved Tumor Penetration and Single-Cell Targeting of Antibody–Drug Conjugates Increases Anticancer Efficacy and Host Survival. *Cancer Res* **78**, 758–769 (2018).
181. Kessenbrock, K., Plaks, V. & Werb, Z. Matrix Metalloproteinases: Regulators of the Tumor Microenvironment. *Cell* **141**, 52–67 (2010).
182. Qian, B.-Z. & Pollard, J. W. Macrophage Diversity Enhances Tumor Progression and Metastasis. *Cell* **141**, 39–51 (2010).
183. Koblinski, J. E., Ahram, M. & Sloane, B. F. Unraveling the role of proteases in cancer. *Clin. Chim. Acta* **291**, 113–135 (2000).
184. Huai, Q. *et al.* Structure of Human Urokinase Plasminogen Activator in Complex with Its Receptor. *Sci. Transl. Med.* **311**, 656–660 (2006).
185. Ulisse, S., Baldini, E., Sorrenti, S. & D'Armiento, M. The Urokinase Plasminogen Activator System: A Target for Anti-Cancer Therapy. *Curr. Cancer Drug Targets* **9**, 32–71 (2009).
186. Blasi, F. & Carmeliet, P. uPAR: a versatile signalling orchestrator. *Nat. Rev. Mol. Cell Biol.* **3**, 932–943 (2002).
187. Barber, C. G., Dickinson, R. P. & Horne, V. A. Selective Urokinase-Type Plasminogen Activator (uPA) Inhibitors. Part 1: 2-Pyridinylguanidines. *Bioorg. Med. Chem. Lett.* **12**, 181–184 (2002).
188. Smith, H. W. & Marshall, C. J. Regulation of cell signalling by uPAR. *Nat. Rev. Mol. Cell Biol.* **11**, 23–36 (2010).
189. Reiter, W., Ehrensberger, H., Steinbrückner, B. & Keller, F. Parameters of Haemostasis during Acute Venous Thrombosis. *Thromb Haemost* **74**, 596–601 (1995).
190. Uhland, K. Matriptase and its putative role in cancer. *Cell. Mol. Life Sci.* **63**, 2968–2978 (2006).
191. Hammami, M. *et al.* New 3-amidinophenylalanine-derived inhibitors of matriptase. *Med. Chem. Commun.* **3**, 807–813 (2012).
192. Colombo, E. *et al.* Design and Synthesis of Potent, Selective Inhibitors of Matriptase. *ACS Med. Chem. Lett.* **3**, 530–534 (2012).
193. Fittler, H., Avrutina, O., Empting, M. & Kolmar, H. Potent inhibitors of human matriptase-1 based on the scaffold of sunflower trypsin inhibitor. *J. Pept. Sci.* **20**, 415–420 (2014).
194. Friedrich, R. *et al.* Catalytic Domain Structures of MT-SP1/Matriptase, a Matrix-degrading Transmembrane Serine Proteinase. *J. Biol. Chem.* **277**, 2160–2168 (2002).
195. Takeuchi, T. *et al.* Cellular Localization of Membrane-type Serine Protease 1 and Identification of Protease-activated Receptor-2 and Single-chain Urokinase-type Plasminogen Activator as Substrates. *J. Biol. Chem.* **275**, 26333–26342 (2000).
196. Galkin, A. V *et al.* CVS-3983, a Selective Matriptase Inhibitor, Suppresses the Growth of Androgen Independent Prostate Tumor Xenografts. *Prostate* **61**, 228–235 (2004).
197. Yang, Y. *et al.* Generation and characterization of a target-selectively activated antibody against

epidermal growth factor receptor with enhanced anti-tumor potency. *MAbs* **7**, 440–450 (2015).
198. Desnoyers, L. R. *et al.* Tumor-Specific Activation of an EGFR-Targeting Probody Enhances Therapeutic Index. *Sci. Transl. Med.* **5**, 1–10 (2013).
199. Brezski, R. J. & Jordan, R. E. Cleavage of IgGs by proteases associated with invasive diseases. *MAbs* **2**, 212–220 (2010).
200. Zhao, Y. *et al.* Two routes for production and purification of Fab fragments in biopharmaceutical discovery research: Papain digestion of mAb and transient expression in mammalian cells. *Protein Expr. Purif.* **67**, 182–189 (2009).
201. Li, J. Y. *et al.* A Biparatopic HER2-Targeting Antibody-Drug Conjugate Induces Tumor Regression in Primary Models Refractory to or Ineligible for HER2-TargetedTherapy. *Cancer Cell* **29**, 117–129 (2016).
202. Oberst, M. *et al.* Matriptase and HAI-1 Are Expressed by Normal and Malignant Epithelial Cells in Vitro and in Vivo. *Am. J. Pathol.* **158**, 1301–11 (2001).
203. Flanagan, R. J. & Jones, A. L. Fab Antibody Fragments. *Drug Saf.* **27**, 1115–1133 (2004).
204. Knop, K., Hoogenboom, R., Fischer, D. & Schubert, U. S. Poly(ethylene glycol) in Drug Delivery: Pros and Cons as Well as Potential Alternatives. *Angew. Chem. Int. Ed.* **49**, 6288 – 6308 (2010).
205. Turecek, P. L., Bossard, M. J., Schoetens, F. & Ivens, I. A. PEGylation of Biopharmaceuticals: A Review of Chemistry and Nonclinical Safety Information of Approved Drugs. *J. Pharm. Sci.* **105**, 460–475 (2016).
206. Smith, A. A. A. *et al.* Albumin-Polymer-Drug Conjugates: Long Circulating, High Payload Drug Delivery Vehicles. *ACS Macro Lett.* **5**, 1089–1094 (2016).
207. Wang, X., Mathieu, M. & Brezski, R. J. IgG Fc engineering to modulate antibody effector functions. *Protein Cell* **9**, 63–73 (2018).
208. Hirasawa, S. *et al.* Facile and Efficient Chemoenzymatic Semisynthesis of Fc-Fusion Compounds for Half-Life Extension of Pharmaceutical Components. *Bioconjug. Chem.* **30**, 2323–2331 (2019).
209. Fan, X. *et al.* A single proteolytic cleavage within the lower hinge of trastuzumab reduces immune effector function and in vivo efficacy. *Breast Cancer Res.* **14**, 1–13 (2012).
210. Polson, A. G. *et al.* Antibody-Drug Conjugates for the Treatment of Non–Hodgkin's Lymphoma: Target and Linker-Drug Selection. *Cancer Res* **69**, 2358–64 (2009).
211. Perrino, E. *et al.* Curative Properties of Noninternalizing Antibody–Drug Conjugates Based on Maytansinoids. *Cancer Res* **74**, 2569–78 (2014).
212. Gébleux, R., Wulhfard, S., Casi, G. & Neri, D. Antibody Format and Drug Release Rate Determine the Therapeutic Activity of Noninternalizing Antibody–Drug Conjugates. *Mol Cancer Ther* **14**, 2606–2613 (2015).
213. Gébleux, R., Stringhini, M., Casanova, R., Soltermann, A. & Neri, D. Non-internalizing antibody–drug conjugates display potent anti-cancer activity upon proteolytic release of monomethyl auristatin E in the subendothelial extracellular matrix. *Int. J. Cancer* **140**, 1670–1679 (2017).
214. Corso, A. D., Cazzamalli, S., Gébleux, R., Mattarella, M. & Neri, D. Protease-Cleavable Linkers Modulate the Anticancer Activity of Noninternalizing Antibody−Drug Conjugates. *Bioconjugate Chem.* **28**, 1826−1833 (2017).
215. Schmidt, M. M., Thurber, G. M. & Wittrup, K. D. Kinetics of anti-carcinoembryonic antigen antibody internalization: effects of affinity, bivalency, and stability. *Cancer Immunol Immunother* **57**, 1879–1890 (2008).
216. Chalouni, C. & Doll, S. Fate of Antibody-Drug Conjugates in Cancer Cells. *J. Exp. Clin. Cancer Res.* **37**, 1–12 (2018).
217. Rudnick, S. I. & Adams, G. P. Affinity and Avidity in Antibody-Based Tumor Targeting. *Cancer Biother. Radiopharm.* **24**, 155–161 (2009).
218. Ubink, R. *et al.* Unraveling the Interaction between Carboxylesterase 1c and the Antibody–Drug Conjugate SYD985: Improved Translational PK/PD by Using Ces1c Knockout Mice. *Mol Cancer Ther* **17**, 2389–2399 (2018).
219. Spix, B. J. & Veurink, M. Chemical and Thermal Stability Screening of an IgG1-Antibody, Application Note NT-PR-009. *Chem. Therm. Unfolding* 1–6 (2016).
220. Higel, F., Seidl, A., Sörgel, F. & Friess, W. N-glycosylation heterogeneity and the influence on structure, function and pharmacokinetics of monoclonal antibodies and Fc fusion proteins. *Eur. J. Pharm. Biopharm.* **100**, 94–100 (2016).
221. Jefferis, R. Glycosylation as a strategy to improve antibody-based therapeutics. *Nat. Rev. Drug Discov.*

8, 226–234 (2009).
222. Zheng, K., Bantog, C. & Bayer, R. The impact of glycosylation on monoclonal antibody conformation and stability. *MAbs* **3**, 568–576 (2011).
223. Lyon, R. P. *et al.* Reducing hydrophobicity of homogeneous antibody-drug conjugates improves pharmacokinetics and therapeutic index. *Nat. Biotechnol.* **33**, 733–736 (2015).
224. Hamblett, K. J. *et al.* Effects of drug loading on the antitumor activity of a monoclonal antibody drug conjugate. *Clin. Cancer Res.* **10**, 7063–70 (2004).
225. White, J. B. *et al.* Design and characterization of homogenous antibody-drug conjugates with a drug-to- antibody ratio of one prepared using an engineered antibody and a dual-maleimide pyrrolobenzodiazepine dimer. *MAbs* **11**, 500–515 (2019).
226. van der Lee, M. M. C. *et al.* The Preclinical Profile of the Duocarmycin-Based HER2-Targeting ADC SYD985 Predicts for Clinical Benefit in Low HER2-Expressing Breast Cancers. *Mol Cancer Ther* **14**, 692–703 (2015).
227. Badescu, G. *et al.* Bridging Disulfides for Stable and Defined Antibody Drug Conjugates. *Bioconjugate Chem.* **25**, 1124–1136 (2014).
228. Zhang, D. *et al.* Intratumoral Payload Concentration Correlates with the Activity of Antibody–Drug Conjugates. *Mol Cancer Ther* **17**, 677–685 (2018).
229. Sutherland, R., Buchegger, F., Schreyer, M., Vacca, A. & Mach, J. P. Penetration and Binding of Radiolabeled Anti-Carcinoembryonic Antigen Monoclonal Antibodies and Their Antigen Binding Fragments in Human Colon Multicellular Tumor Spheroids. *Cancer Res.* **47**, 1627–1633 (1987).
230. Buchegger, F. *et al.* Radiolabeled fragments of monoclonal antibodies against carcinoembryonic antigen for localization of human colon carcinoma grafted into nude mice. *J. Exp. Med.* **158**, 413–427 (1983).
231. Halpern, S. E., Buchegger, F., Schreyer, M. & Mach, L. J.-P. Effect of size of radiolabeled antibody and fragments on tumor uptake and distribution in nephrectomized mice. *Clin. Nucl. Med.* **9**, 1–3 (1984).

8. Appendix

Appendix 1: Antibody purification of trastuzumab variants using protein A affinity chromatography

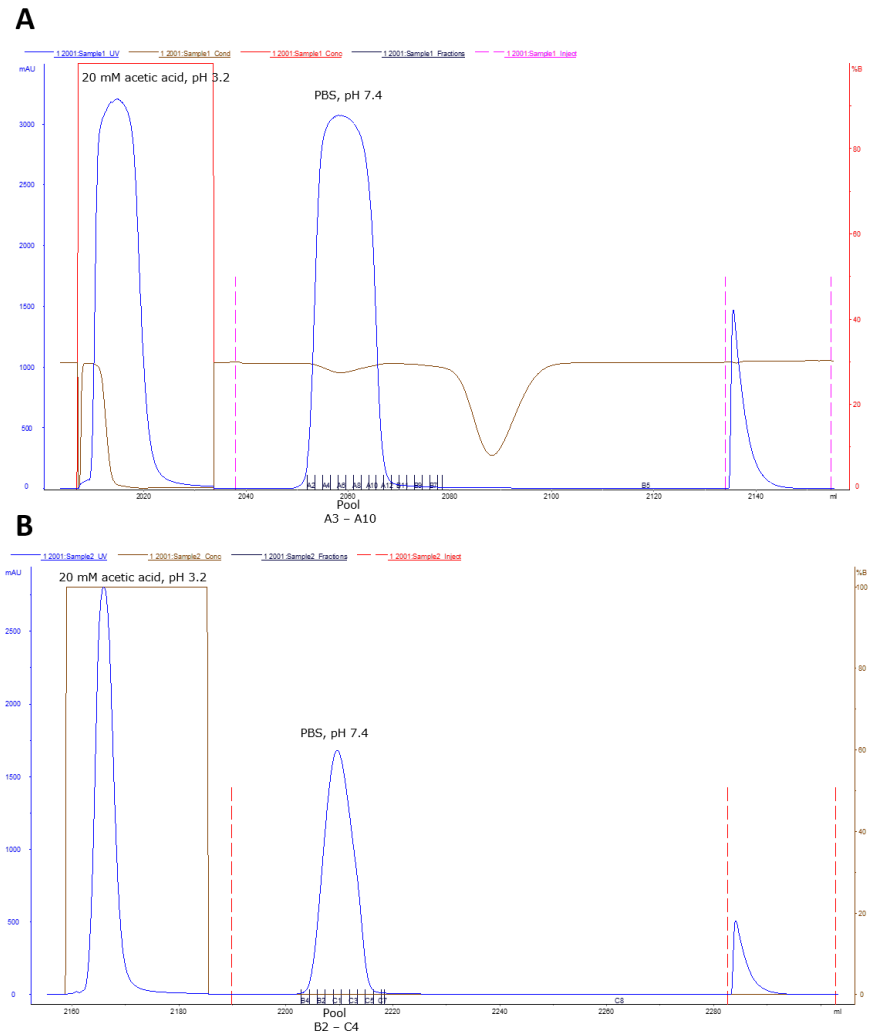

Downstream processing exemplarily depicted for representative mAbs Trastuzmab CL, LC Srt Tag (**A**) and Trastuzumab nCL, LC Srt Tag (**B**) using HiTrap MabSelect SuRe 5 ml column. Blue line represents UV detection of proteins. Isocratic elution was carried out with 20 mM acetic acid, pH 3.2 and subsequently desalting step with PBS, pH 7.4.

Appendix 2: Preparative SEC of Trastuzumab CL, LC Srt Tag

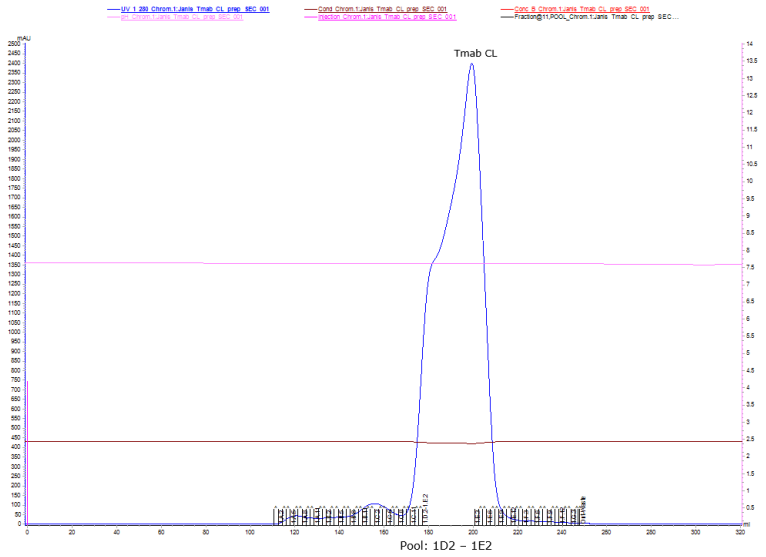

Selected preparative SEC of Trastuzumab CL, LC Srt Tag using HiLoad Superdex 200 pg column with isocratic elution PBS pH 7.4. UV chromatogram (blue) at 280 nm.

Appendix 3: Purification of Trastuzumab antibody fragments using IMAC

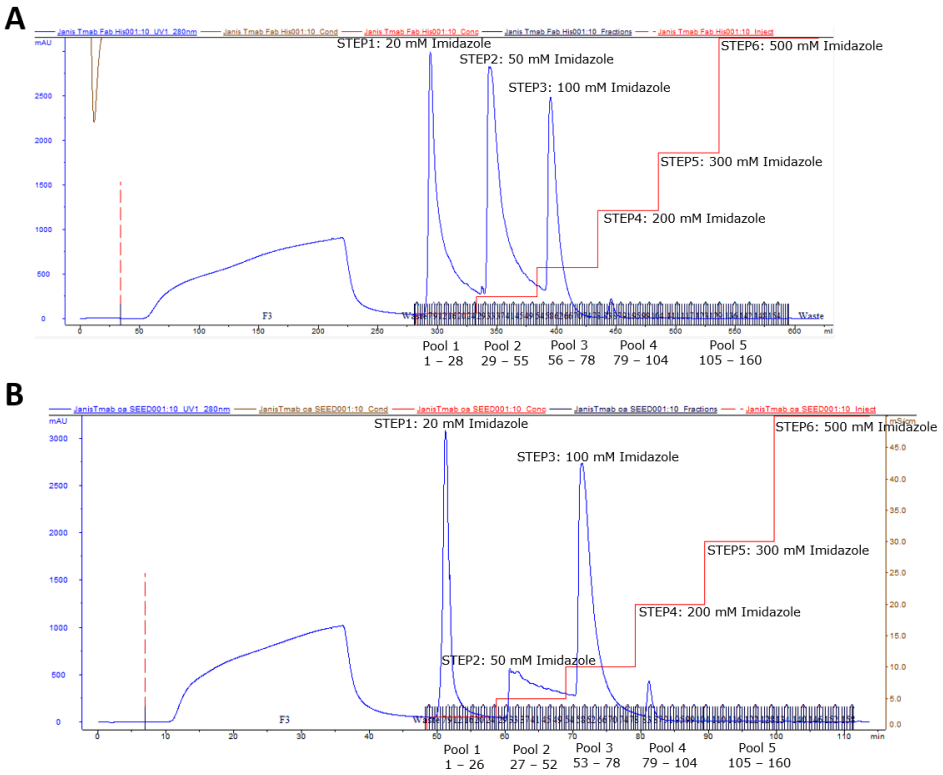

IMAC purification exemplarily depicted for Trastuzumab Fab His, LC Srt Tag (**A**) and Trastuzumab oa SEED AG HC His, LC Srt Tag (**B**) with stepwise elution using HisTrap HP 5 ml column and imidazole as elution buffer. UV chromatogram (blue) at 280 nm.

Appendix 4: Preparative SEC of Trastuzumab antibody fragments and anti-penta His Western Blot

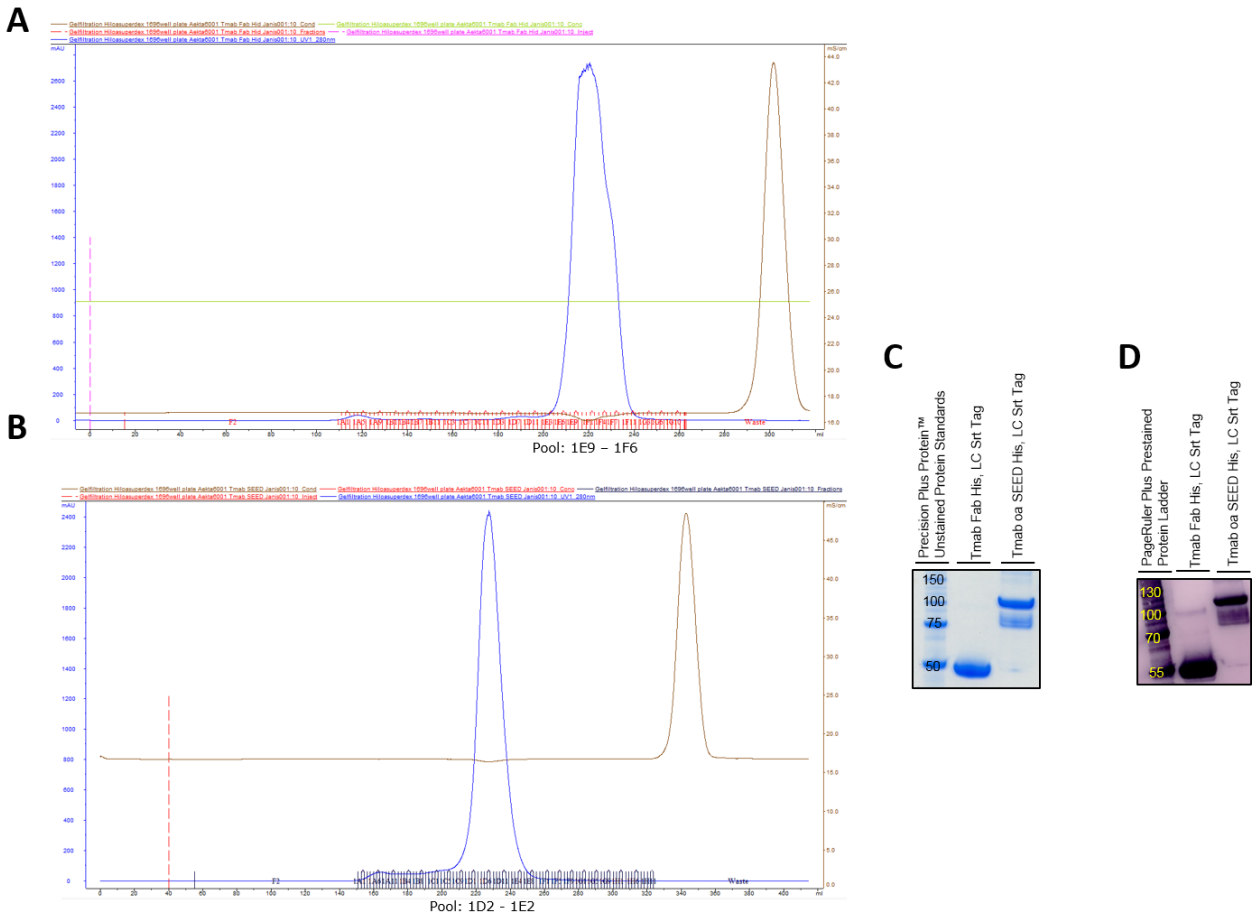

Preparative SEC of Trastuzumab Fab His, LC Srt Tag (**A**) and Trastuzumab oa SEED AG HC His, LC Srt Tag (**B**) with isocratic elution using PBS pH 7.4. Non-reduced SDS-PAGE (**C**) and Western Blot (**D**) of purified Trastuzumab Fab His, LC Srt Tag and Trastuzumab oa SEED AG HC His, LC Srt Tag. SDS-PAGE was stained with InstantBlue and Western Blot was detected with primary mouse IgG1 anti-Penta His Antibody following goat IgG anti-Mouse IgG (H+L)-Alk. Phos. For Immunodetection, BCIP/NBT was added.

Appendix 5: Purification of Cetuximab antibody fragments using IMAC and anti-penta His Western Blot

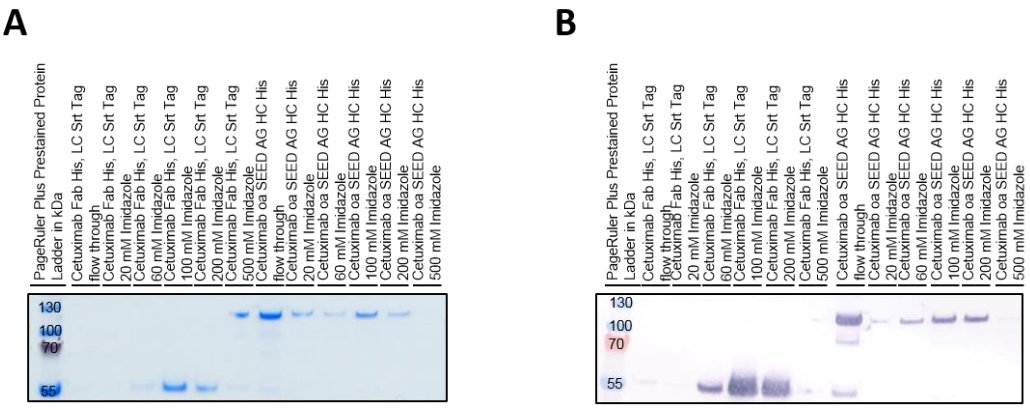

Non-reduced SDS-PAGE (**A**) and Western Blot (**B**) of purified Cetuximab Fab His, LC Srt Tag and Cetuximab oa SEED AG HC His, LC Srt Tag. IMAC Purification was carried out with His GraviTrap columns. SDS-PAGE was stained with InstantBlue and Western Blot was detected with primary mouse IgG1 anti-Penta His Antibody following goat IgG anti-Mouse IgG (H+L)-Alk. Phos. For Immunodetection, BCIP/NBT was added.

Appendix 6: Antibody purification of Cetuximab variants using protein A affinity chromatography

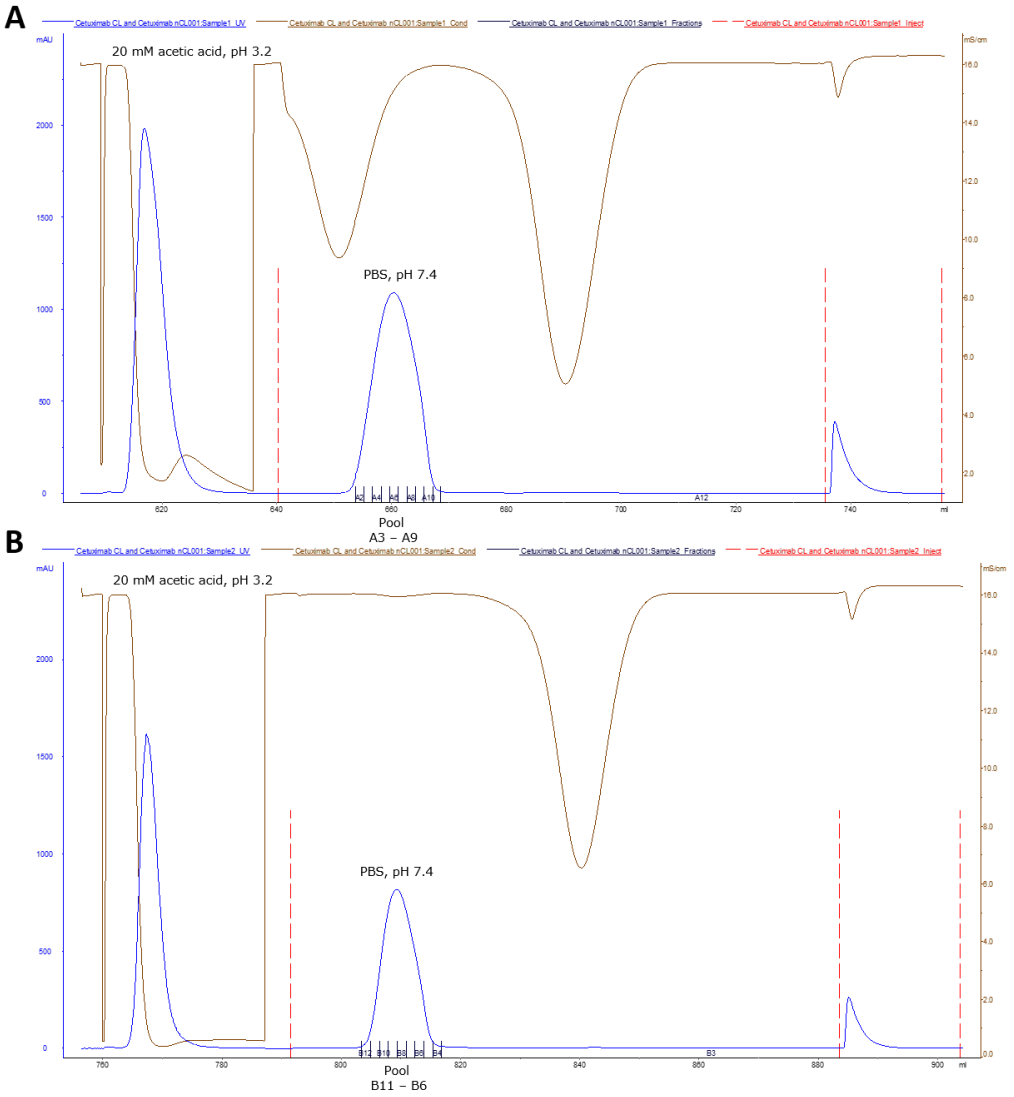

Downstream processing exemplarily depicted for representative mAbs Cetuximab CL, LC Srt Tag (**A**) and Cetuximab nCL, LC Srt Tag (**B**) using HiTrap MabSelect SuRe 5 ml column. Blue line represents UV detection of proteins. Isocratic elution was carried out with 20 mM acetic acid, pH 3.2 and subsequently desalting step with PBS, pH 7.4.

Appendix 7: Analytical SEC for protein purity of antibody constructs

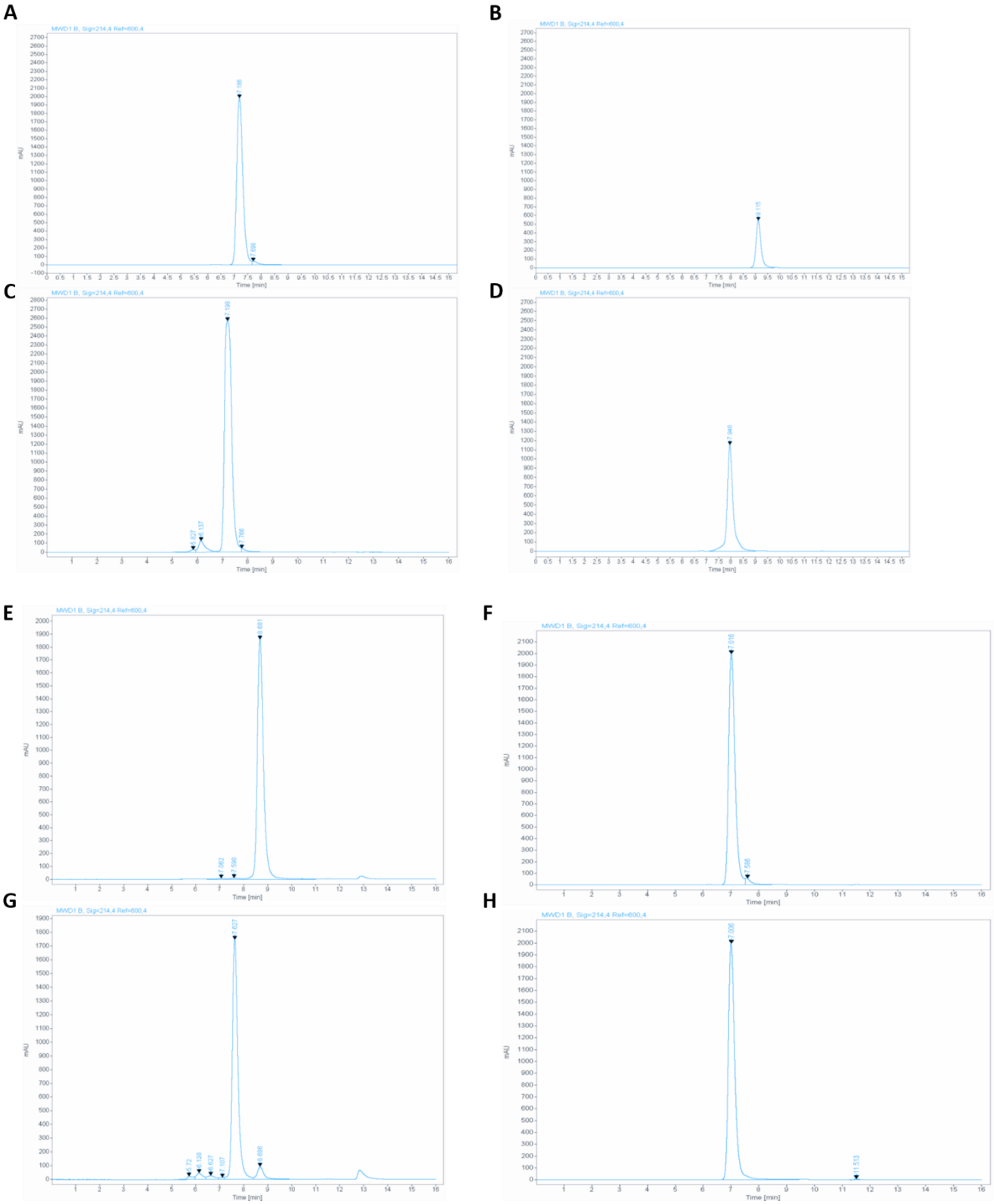

Analytical SEC of Trastuzumab CL, LC Srt Tag (**A**) and Trastuzumab Fab His, LC Srt Tag (**B**), Trastuzumab nCL, LC Srt Tag (**C**), Trastuzumab oa SEED AG His, LC Srt Tag (**D**), Cetuximab Fab His, LC Srt Tag (**E**), Cetuximab CL, LC Srt Tag (**F**), Cetuximab oa SEED AG His, LC Srt Tag (**G**) and Cetuximab nCL, LC Srt Tag (**H**) using TSK Super SW3000 column and HPLC Agilent 1260. Mobile phase was PBS, pH 7.4 or 50 mM sodium phosphate (NaH_2PO_4, Na_2HPO_4), 0.4 M sodium perchlorate, pH 6.35. UV chromatogram at 214 nm.

Appendix 8: Protease cleavage of unconjugated antibody by tumor proteases

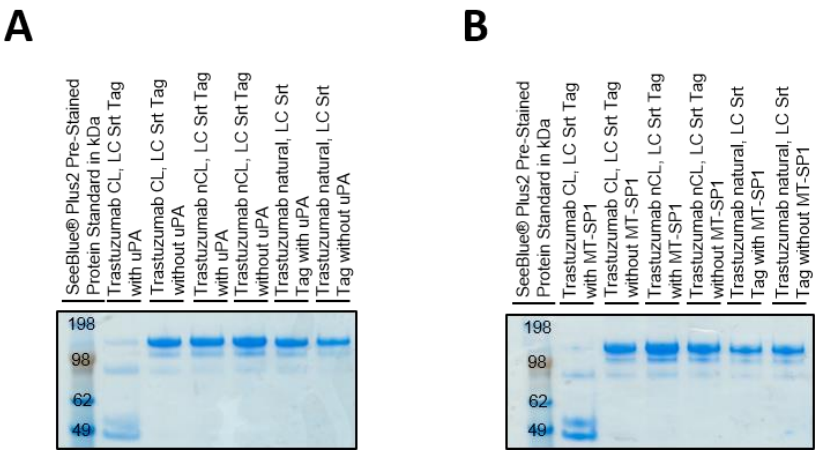

Incubation of unconjugated Trastuzumab CL, Trastuzumab nCL, and Trastuzumab natural with uPA (**A**) or matriptase (**B**) for 24 h at 37°C. Samples were non-reduced and gels were stained with InstantBlue after SDS-PAGE run.

Appendix 9: Mass confirmation by ESI-MS and analytical HIC of selected ADCs

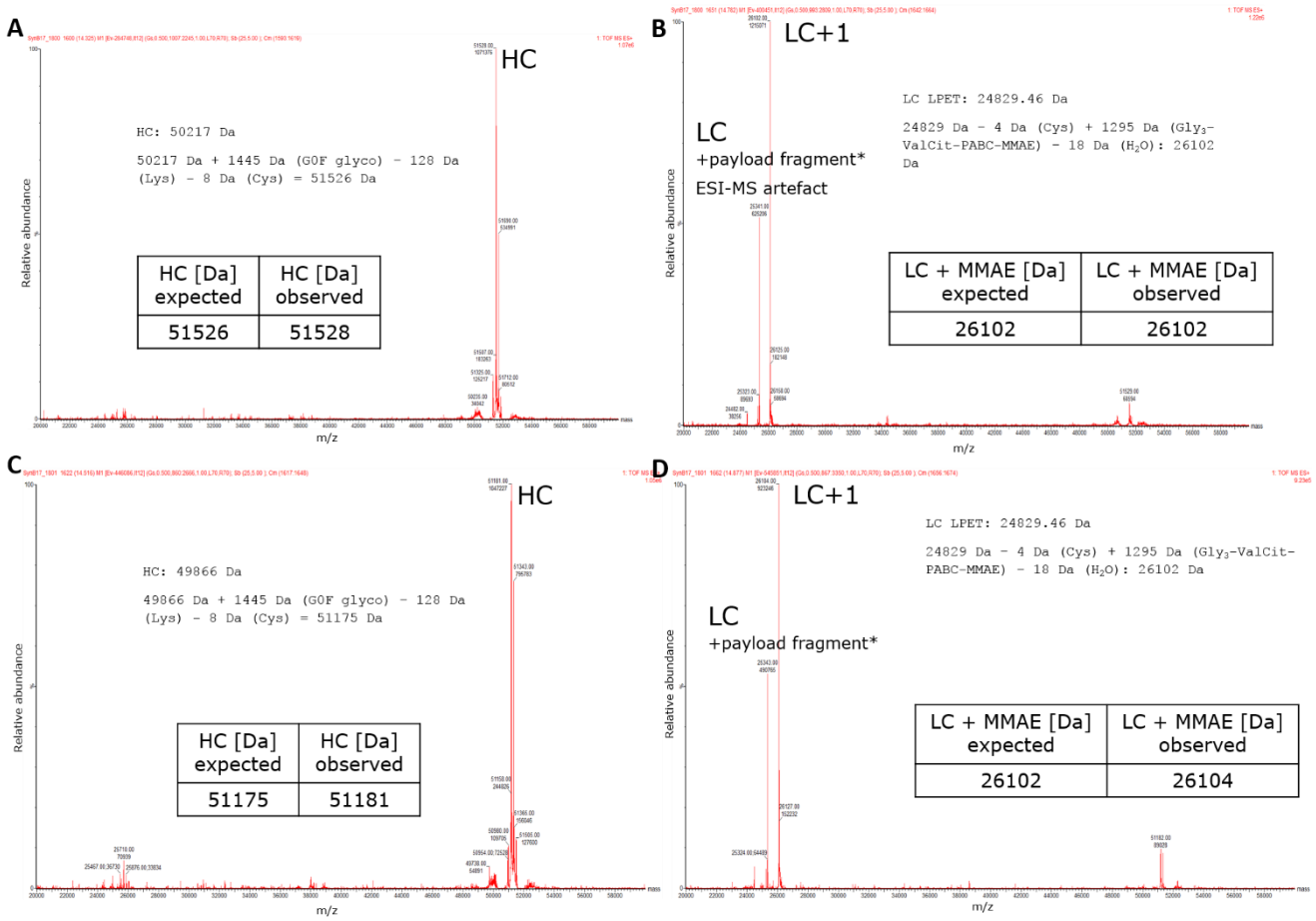

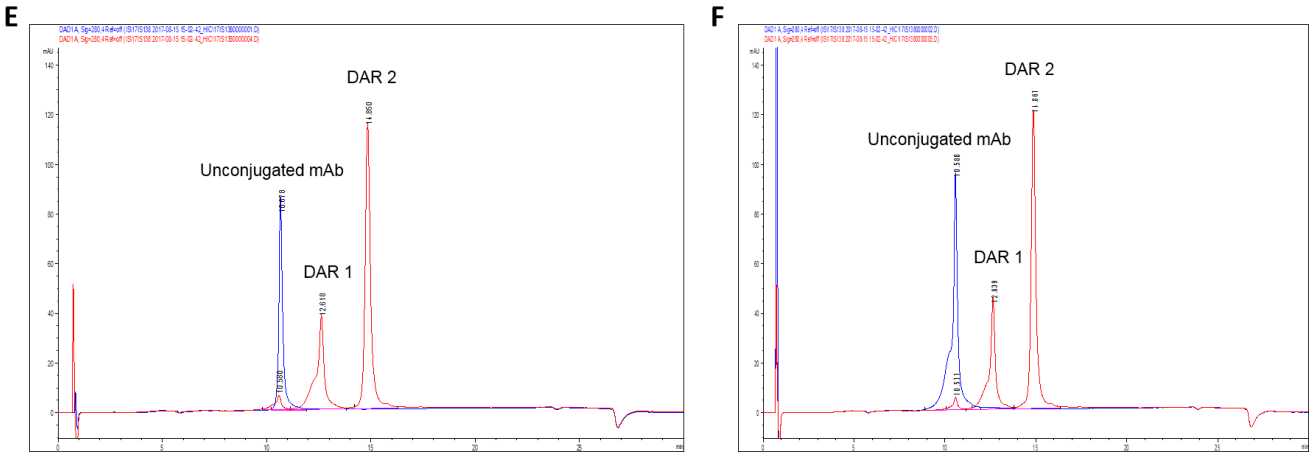

Exemplarily depicted are ESI-MS spectra of Trastuzumab CL x MMAE heavy chain (**A**) and light chain with payload (**B**) as well as overlay of HIC chromatograms (**E**) of conjugated (red line) and unconjugated (blue line) molecules. For Trastuzumab nCL x MMAE, mass confirmation of conjugated antibody with heavy chain (**C**) and light chain with payload (**D**) as well as overlay of HIC chromatograms (**F**).

Appendix 10: General ADC structure with MMAF as payload

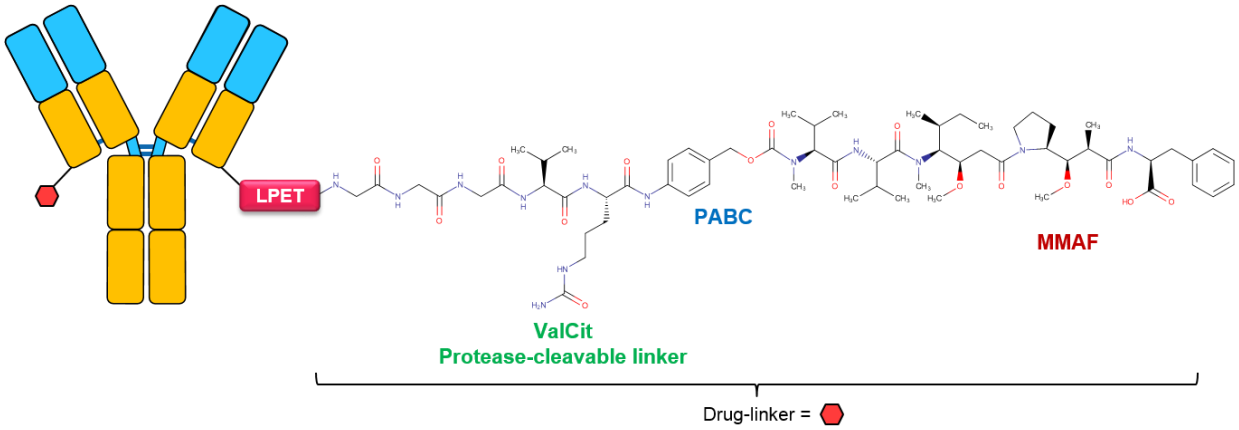

Depicted is the generic structural composition of MMAF-based ADCs (Antibody-Gly3-ValCit-PABC-MMAF). Site-specific conjugation was achieved by sortase A mediated antibody conjugation technology by attaching triple-glycine drug-linker to sortase A recognition motif LPETGS C-terminally to light chain of the antibody.

Appendix 11: Analytical SEC of selected Trastuzumab x MMAE constructs and Trastuzumab x AF488

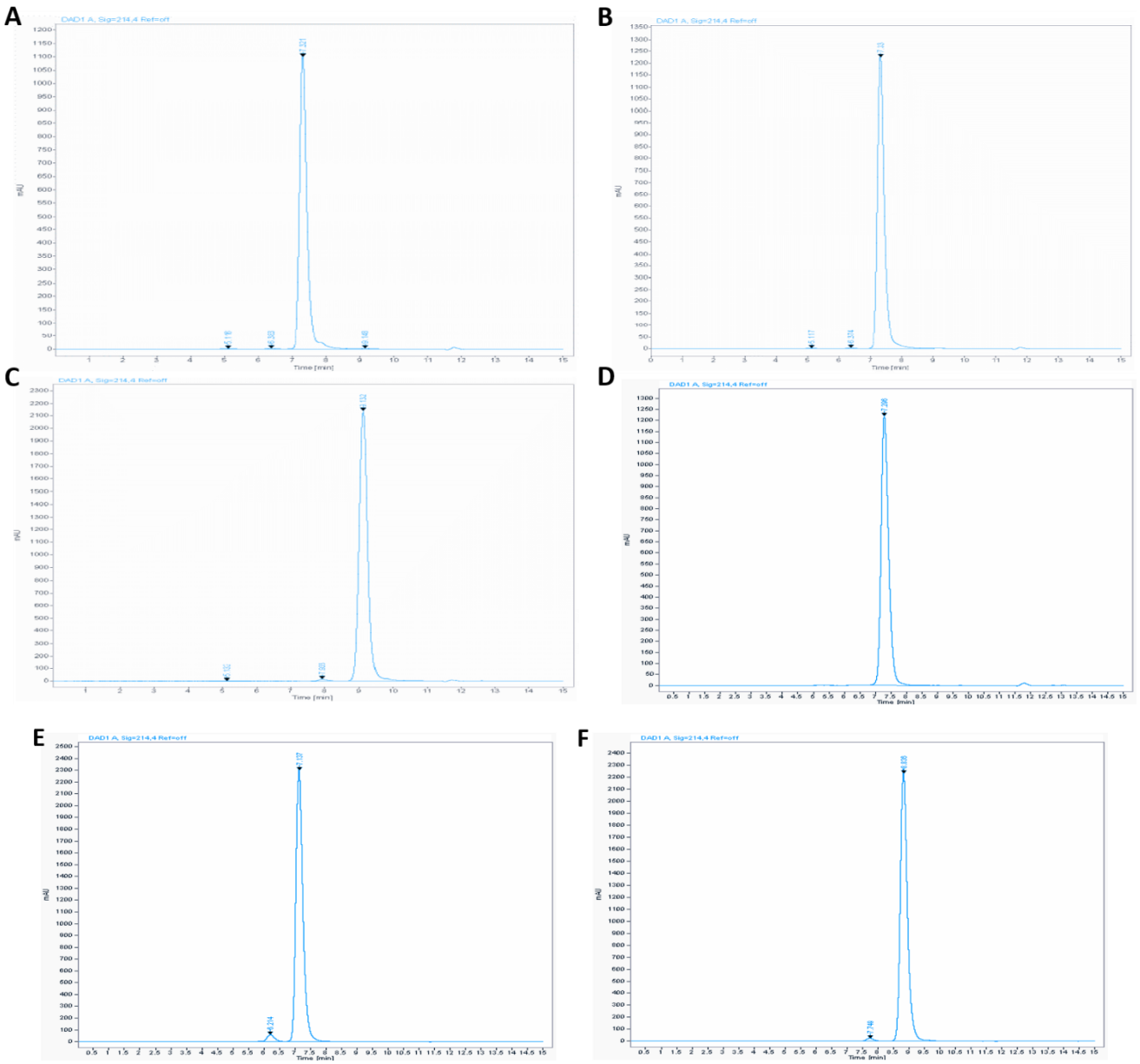

Analytical SEC of toxin-based Trastuzumab CL x MMAE (**A**), Trastuzumab nCL x MMAE (**B**), Trastuzumab Fab His x MMAE (**C**). Fluorophore-labeled Trastuzumab CL HC N297A x Alexa Fluor 488 x BHQ-10 (**D**), Trastuzumab nCL HC N297A x Alexa Fluor 488 (**E**) and Trastuzumab Fab His x Alexa Fluor 488 (**F**), exemplarily depicted. Purity was assessed with TSK Super SW3000 column and HPLC Agilent 1260. Mobile phase was PBS, pH 7.4 or 50 mM sodium phosphate (NaH_2PO_4, Na_2HPO_4), 0.4 M sodium perchlorate, pH 6.35.

Appendix 12: Protease cleavage of Trastuzumab CL x MMAF, Cetuximab CL x MMAE and Trastuzumab CL HC N297A x Alexa Fluor 488 x BHQ-10 conjugates by uPA and matriptase

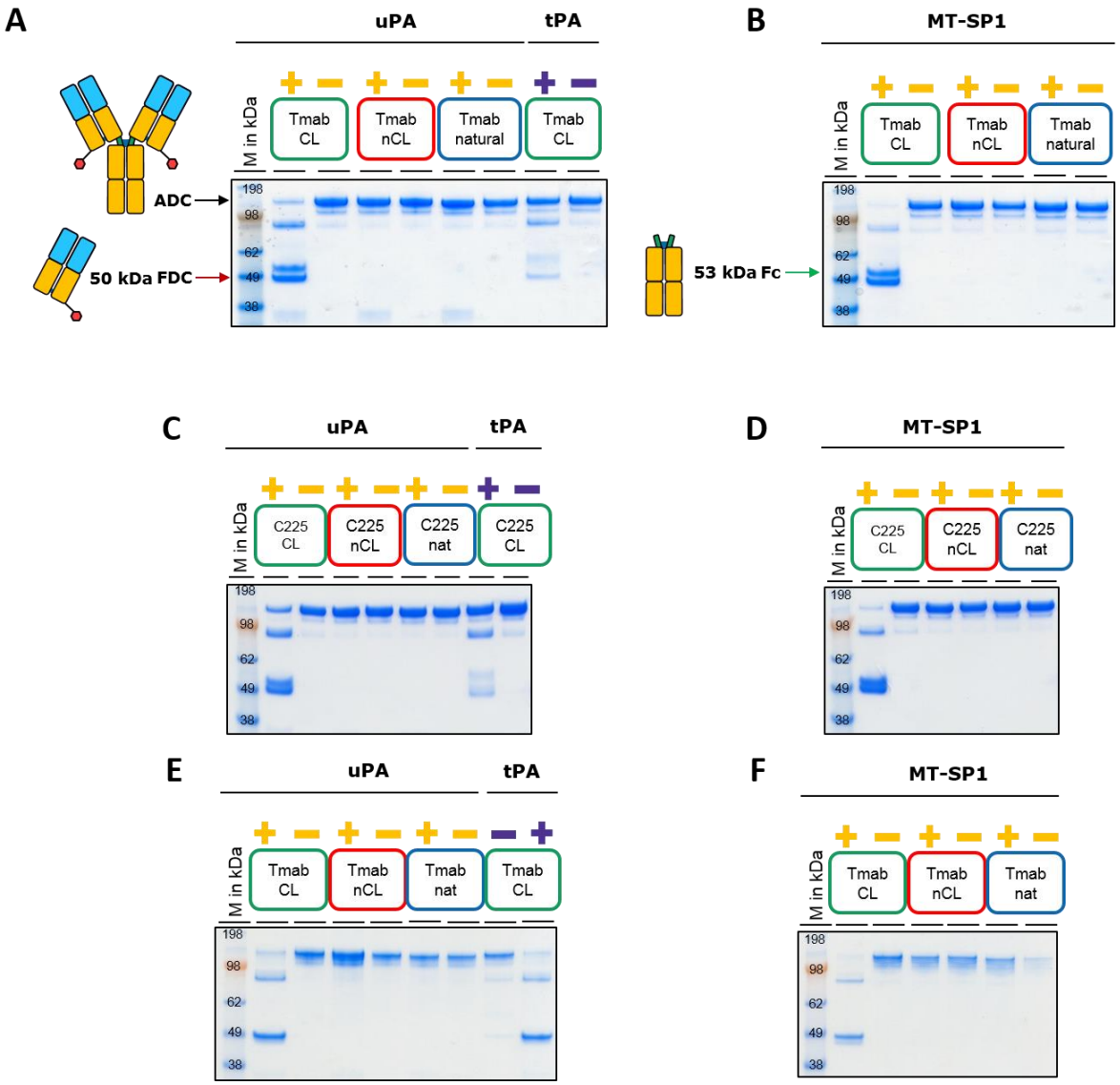

SDS-PAGE analysis of Trastuzumab x MMAF, Cetuximab x MMAE ADCs and Tmab CL HC N297A x AF488 conjugates incubated with tumor proteases uPA and matriptase. Protease cleavage of ADC variants with Trastuzumab x MMAF ADCs by uPA (**A**) and matriptase (MT-SP1) (**B**). Cetuximab x MMAE ADCs incubated with uPA (**C**) or matriptase (**D**). Protease cleavage of antibody-fluorophore conjugates with AF488 by uPA (**E**) and matriptase (MT-SP1) (**F**). Incubation of tPA, a homologous enzyme to uPA was also tested. Samples Tmab CL x MMAF, Tmab nCL x MMAF, Tmab natural x MMAF, C225 CL x MMAE, C225 nCL x MMAE and C225 nat x MMAE, Tmab CL HC N297A x AF488 x BHQ-10, Tmab nCL HC N297A x AF488 and Tmab nat HC N297A x AF488 were incubated with (+) or without (-) enzyme at 37°C for 24 h and were non-reduced. After SDS-PAGE run, InstantBlue stain was performed at least for 30 min. Tmab = Trastuzumab, C225 = Cetuximab, nat = natural, AF488 = Alexa Fluor 488, BHQ-10 = Black Hole Quechner-10, + = with enzyme, - = without enzyme

Appendix 13: Mass confirmation of FDC/Fc and verification of uPA/MT-SP1 cleavage site by ESI-MS

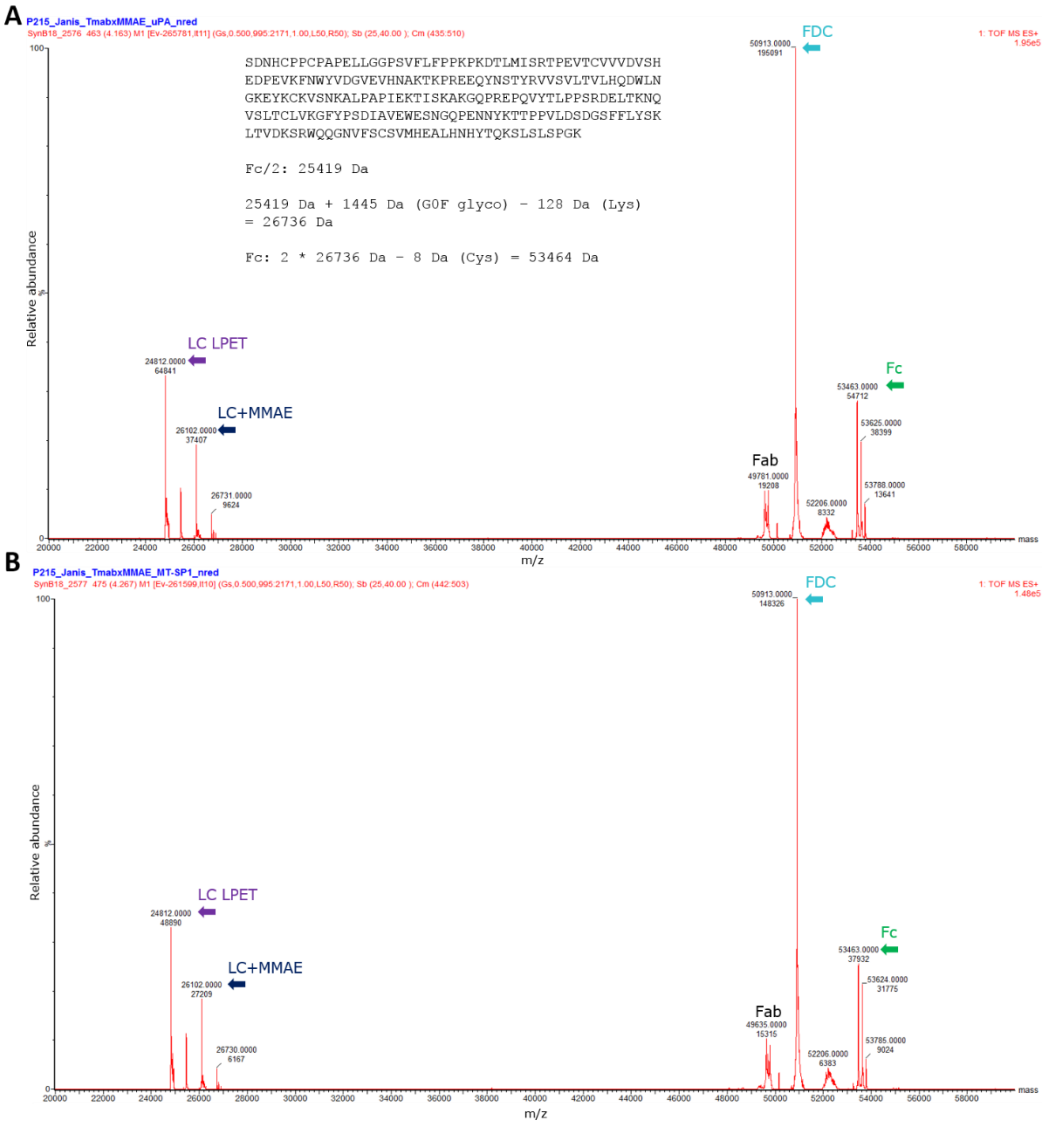

Trastuzumab CL x MMAE was incubated with uPA (**A**) and with MT-SP1 (**B**) and cleaved fragments were analyzed by ESI-MS (non-reduced). In accordance with the expected mass, hinge cleavage releases FDC fragment that correlates to observed mass.

Appendix 14: Mass confirmation of FDC/Fc (Trastuzumab CL x MMAF) and verification of uPA/MT-SP1 cleavage site by ESI-MS

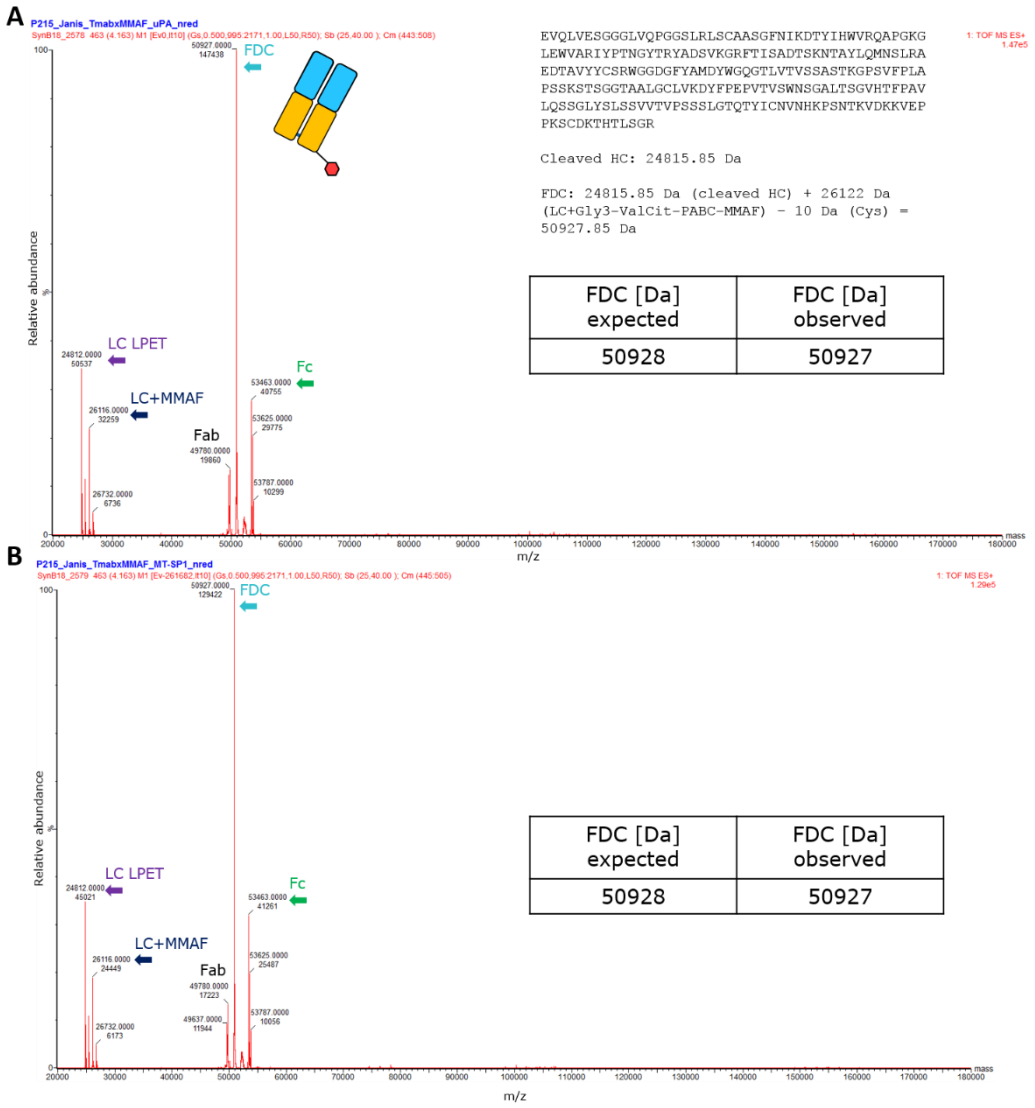

Trastuzumab CL x MMAF was incubated with uPA (**A**) and with MT-SP1 (**B**) and cleaved fragments were analyzed by ESI-MS (non-reduced). In accordance with the expected mass, hinge cleavage releases FDC fragment that correlates to observed mass.

Appendix 15: Mass confirmation of Cetuximab CL x MMAE fragments by uPA/MT-SP1 using ESI-MS

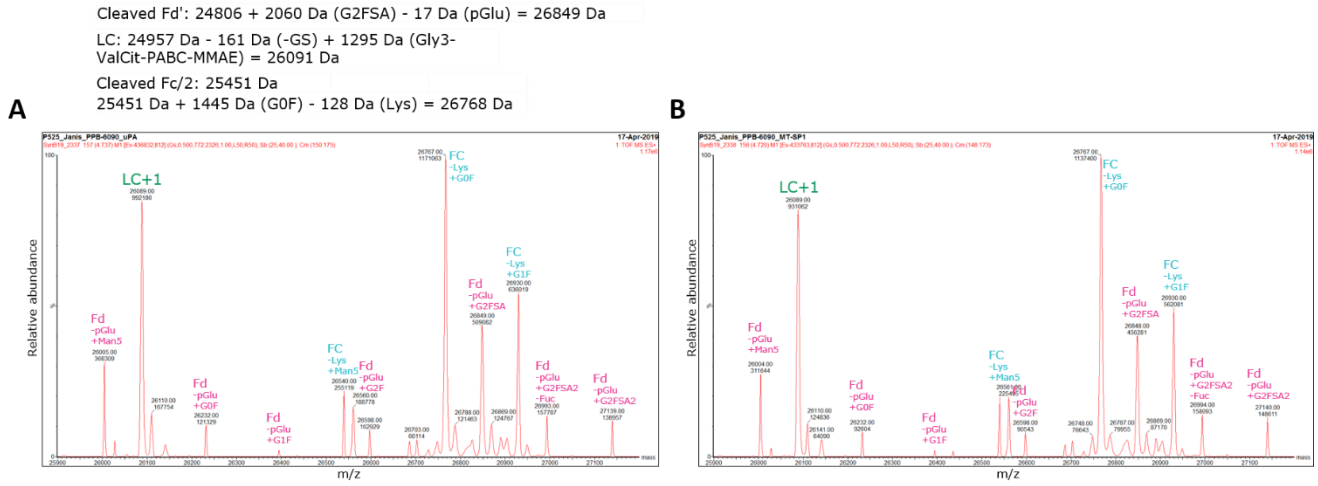

Cetuximab CL x MMAE was incubated with uPA (**A**) and MT-SP1 (**B**) and cleaved fragments were analyzed by ESI-MS (reduced).

Appendix 16: RP-MS chromatograms Trastuzumab CL x MMAE cleavage reaction with uPA and MT-SP1

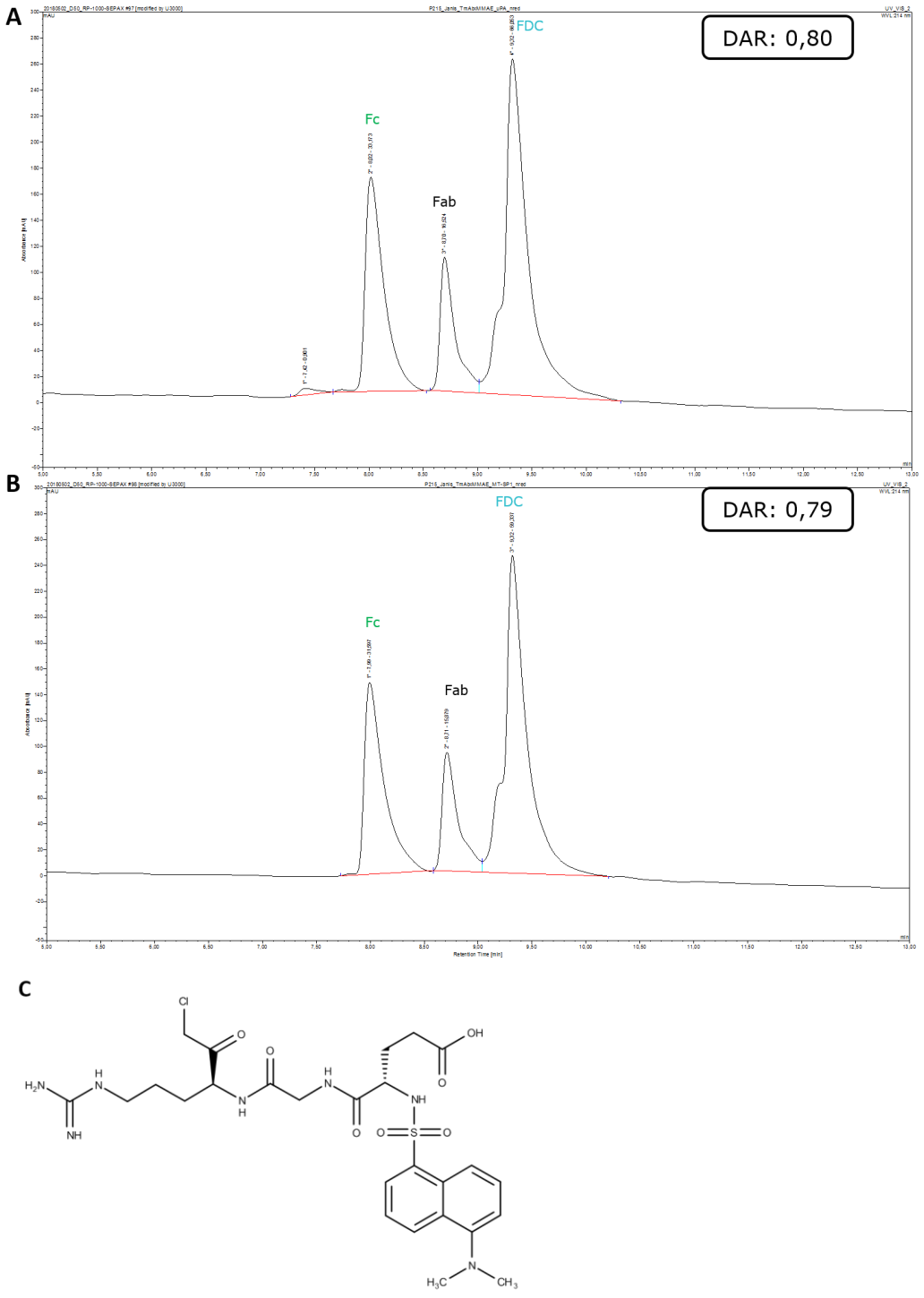

Trastuzumab CL x MMAE was incubated with MT-SP1 (**A**) and with uPA (**B**) and cleaved fragments were analyzed by RP coupled to MS. Peaks were assigned to the specific fragments according to their detected mass. Used irreversible enzyme inhibitor 1,5-Dansyl-Glu-Gly-Arg Chloromethyl Ketone (**C**) to stop the cleavage reaction of uPA and matriptase.

Appendix 17: Overlay of RP-HPLC chromatograms Trastuzumab CL x MMAE cleavage reaction with uPA and MT-SP1

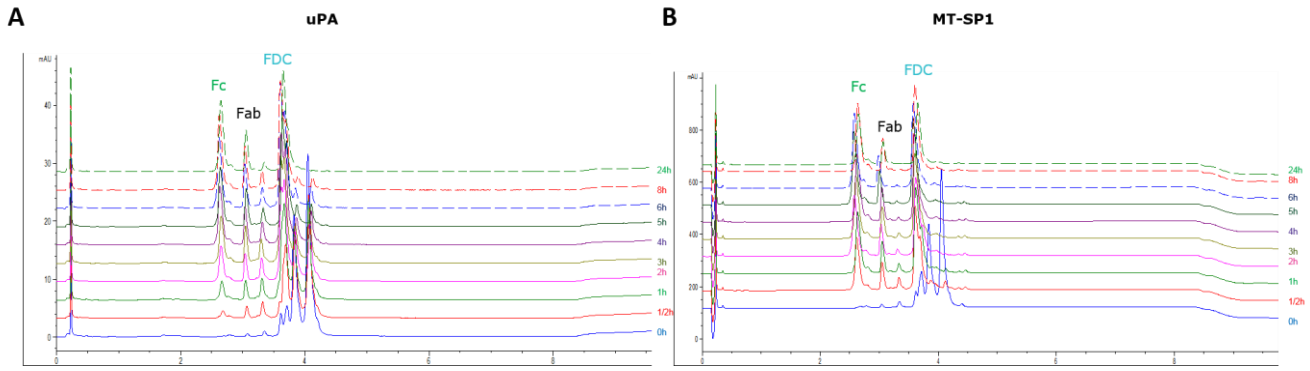

Enyzme kinetics experiments with uPA and MT-SP1. Trastuzumab CL x MMAE was incubated with uPA (**A**) and MT-SP1 (**B**) and peak assignment of cleaved fragments was achieved in a previous RP run (mobile phase: Water + 0.1% TFA) coupled to MS (see Appendix 16). Each time point was stopped by small molecule inhibitor 1,5-Dansyl-Glu-Gly-Arg Chloromethyl Ketone.

Appendix 18: Enzyme cleavage reaction of uPA and MT-SP1 with Tmab CL x MMAE at different time points

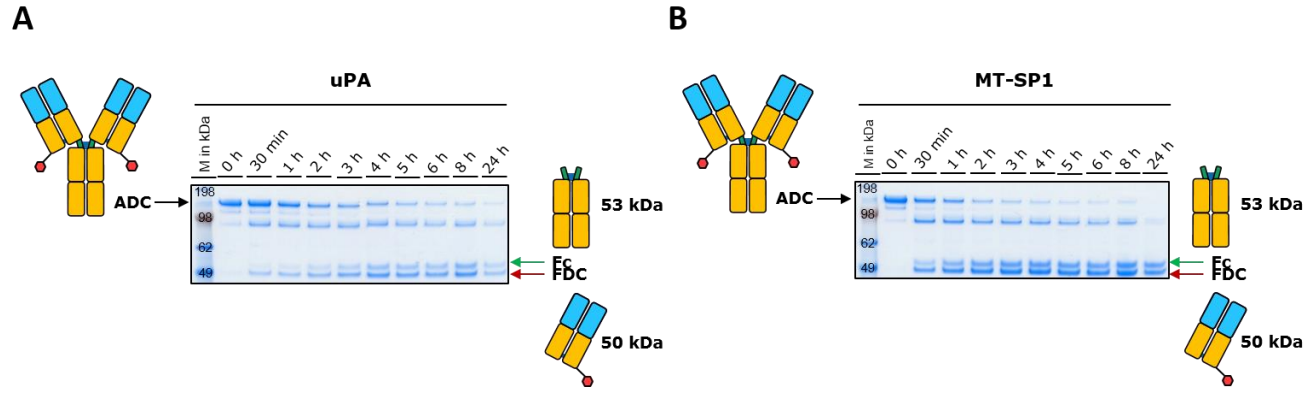

Cleaved fragments generated by uPA (**A**) and MT-SP1 (**B**) were analyzed by SDS-PAGE and each time point was stopped by small molecule inhibitor 1,5-Dansyl-Glu-Gly-Arg Chloromethyl Ketone.

Appendix 19: Affinity and kinetic analysis of commercial Herceptin and isotype control anti-HEL by BLI

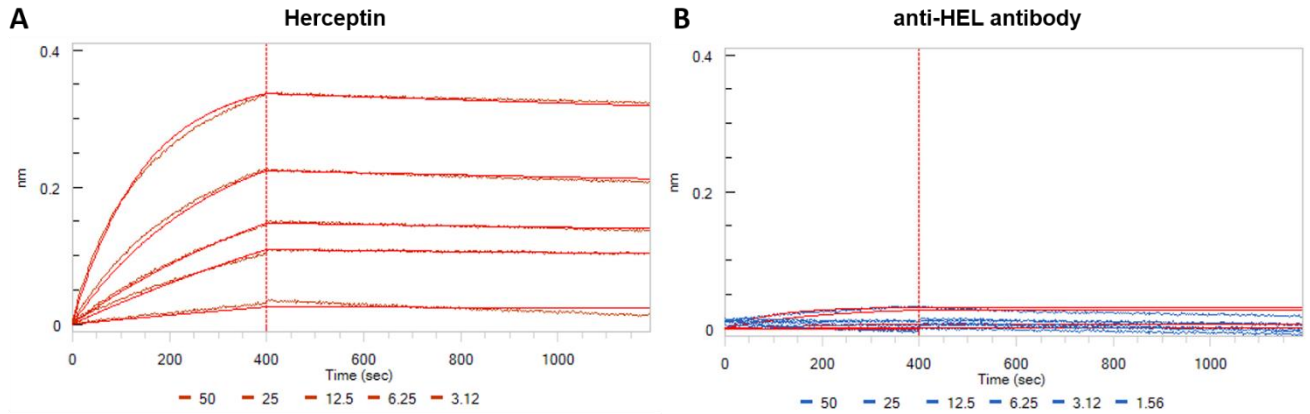

Herceptin (**A**) and anti-HEL (**B**) were analyzed with anti-human Fab-CH1 (FAB2G) biosensors. Interference pattern shift [nm] is monitored with varying concentrations of analyte over the time [sec].

Appendix 20: Cellular binding of designed Cetuximab antibodies and antibody fragments to several cancer cell lines

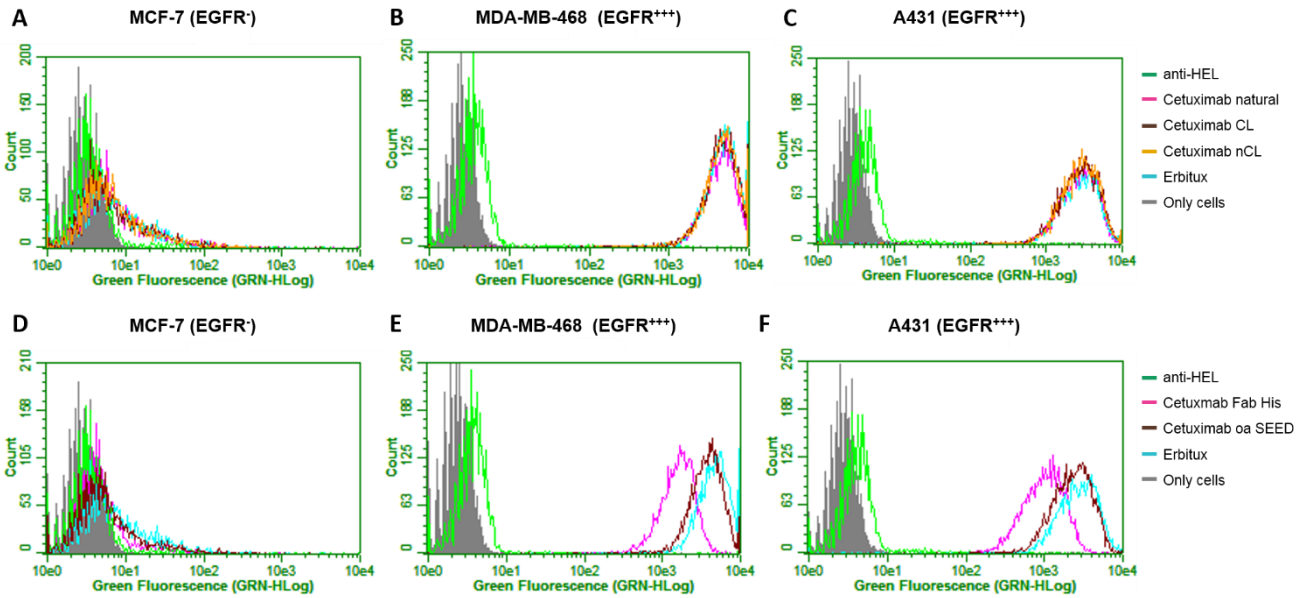

Binding assay of cetuximab antibodies and antibody fragments by flow cytometry. Constructs displayed no binding to EGFR-negative MCF-7 cells for bivalent (**A**) and monovalent antibodies (**D**). On high-expressing EGFR cell line MDA-MB-468, binding of all IgG antibodies is strongly increased (**B**), whereas monovalent Trastuzumab Fab His shows a slightly weaker binding compared to IgG antibodies (**E**). For A431 cells a strong binding effect is obtained for conventional antibody format (**C**) and antibody fragments (**F**). In all cases, binding is comparable to commercial Erbitux. Samples were measured in duplicates.

Appendix 21: Thermal stability raw data of Trastuzumab-based antibodies and ADCs by nanoDSF

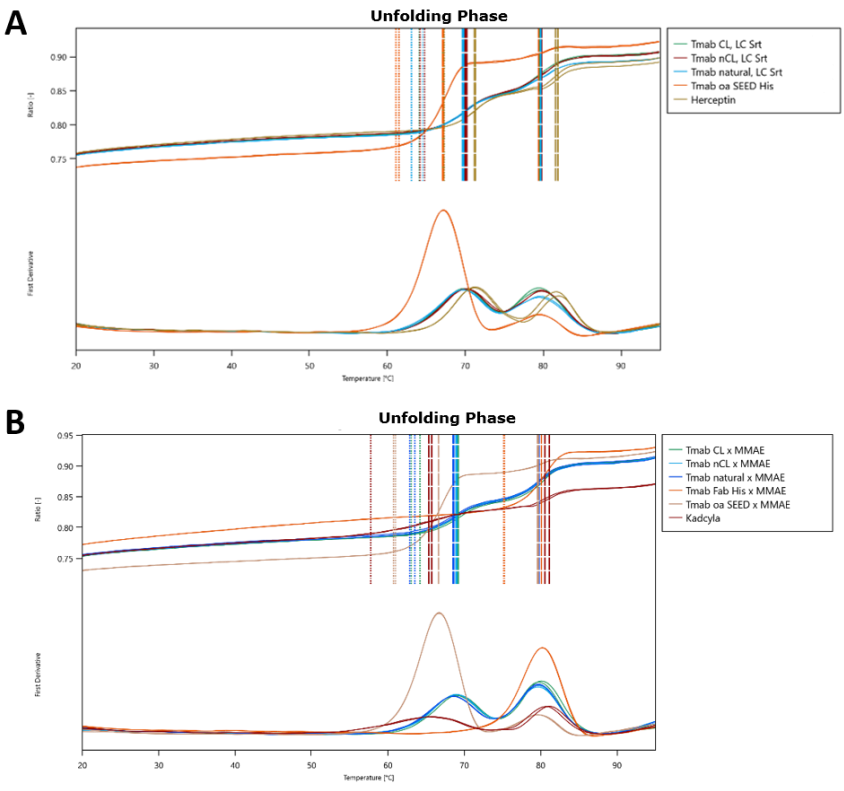

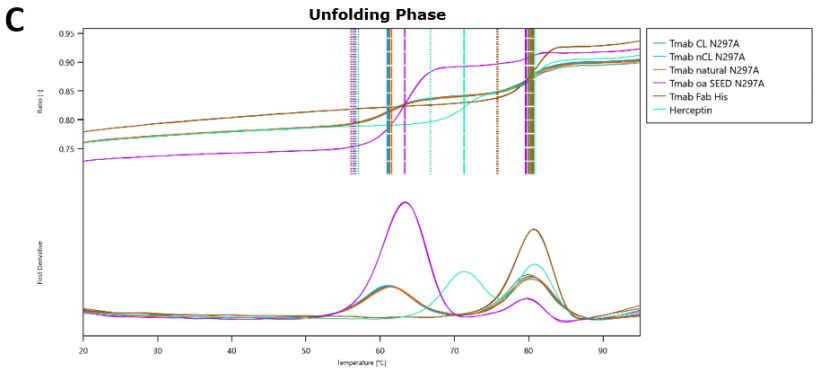

Melting points of glycosylated antibodies (**A**), ADCs (**B**) and deglycosylated antibodies (**C**) were determined by measuring the maximum of the first derivative curve of F330nm/F350nm ratios.

Appendix 22: Terminal % drug load relative to initial conjugated total MMAE for mouse and human serum

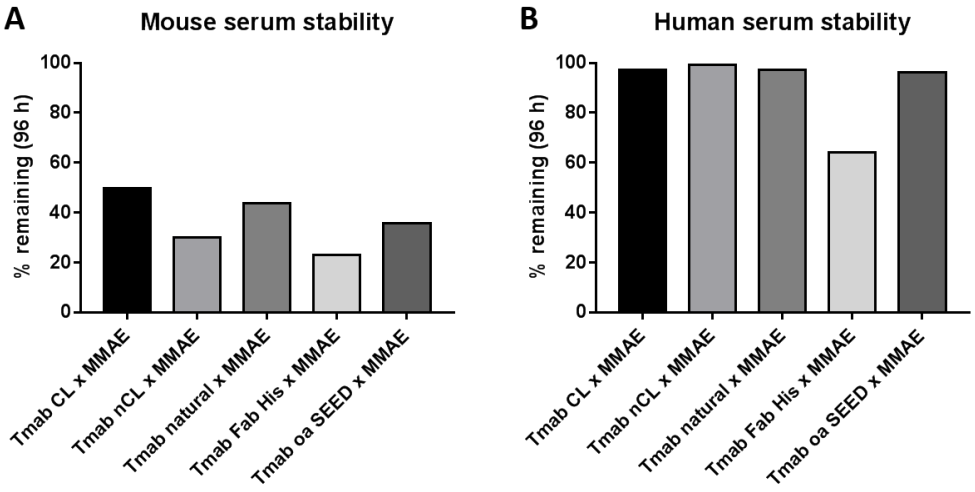

Samples were incubated in mouse serum (**A**) or human serum (**B**) at 37°C, 5% CO2 for 96 h. Samples were taken at different time points and analysis was performed by LC-MS as triplicates. As a test item MMAE was detected. Depicted are remaining % of drug load relative to initial conjugated total MMAE at time point 96 h.

Appendix 23: Drug load as percentage relative to initial conjugated total MMAE for mouse and human serum at different time points.

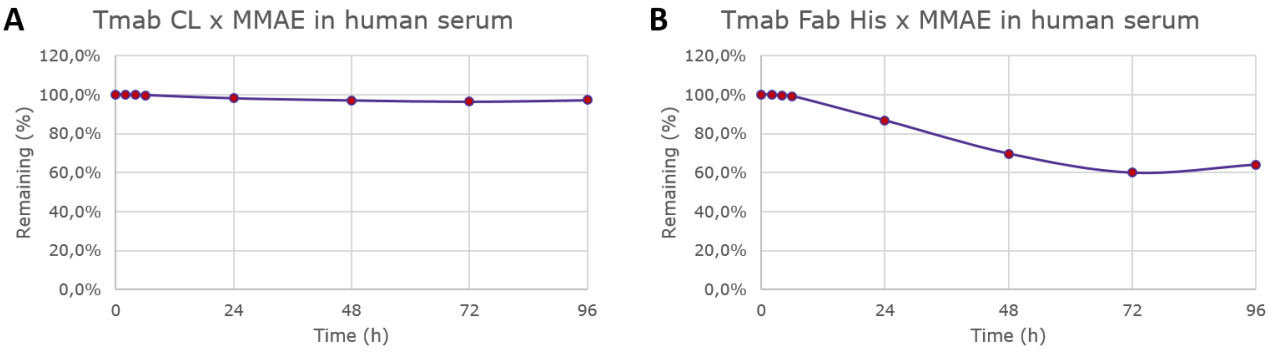

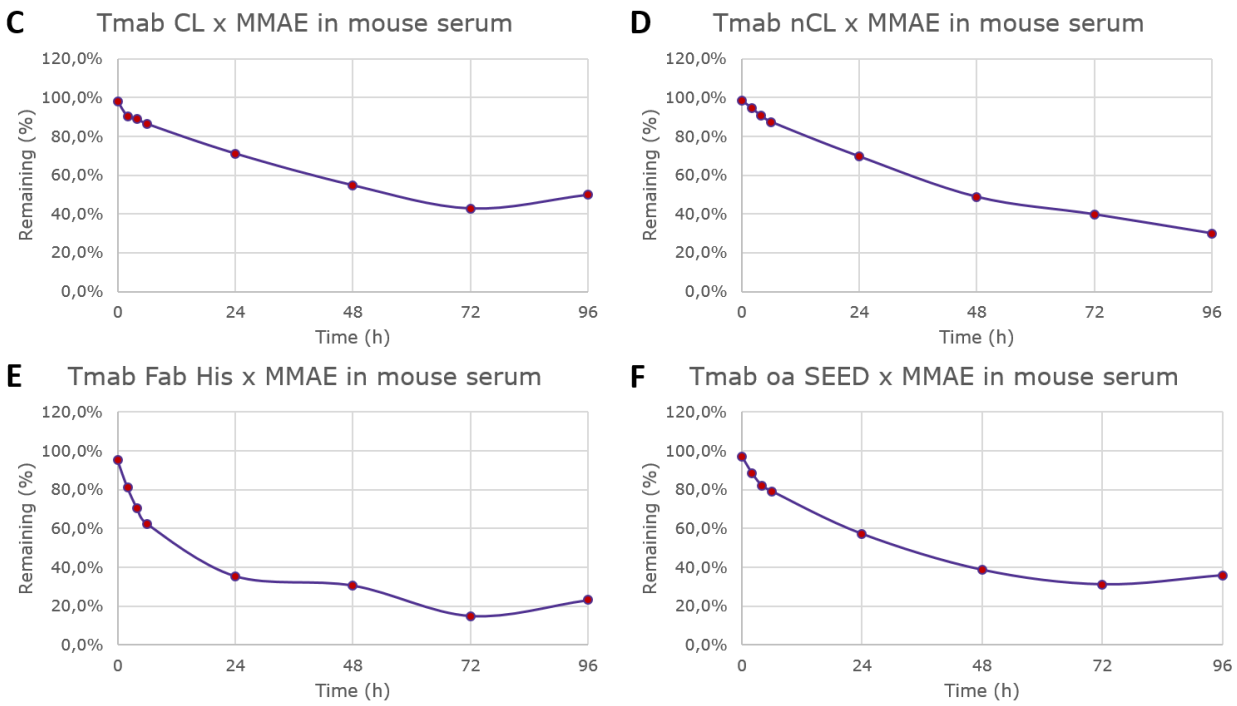

Samples were analyzed by LC-MS, using MMAE as a test item. Depicted are exemplarily remaining % of drug load relative to initial conjugated total MMAE of Trastuzumab CL x MMAE (**A**) and Trastuzumab Fab His x MMAE (**B**) in human serum as well as Trastuzumab CL x MMAE (**C**), Trastuzumab nCL x MMAE (**D**), Trastuzumab Fab His x MMAE (**E**) and Trastuzumab oa SEED x MMAE (**F**) in mouse serum.

Appendix 24: Western Blot analysis of Trastuzumab-based antibodies incubated with SKBR-3 cells

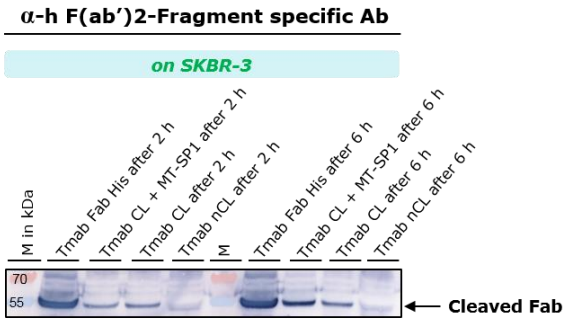

Detection of cleaved Fab fragments was carried out with goat anti-human IgG Antibody, F(ab')2 specific. Samples were Tmab Fab His, Tmab CL + MT-SP1, Tmab CL and Tmab nCL incubated with SKBR-3 cells at 37°C for 72 h. Analysis of 2 h and 6 h incubation was performed. For Immunodetection, BCIP/NBT was added. Tmab = Trastuzumab

Appendix 25: Cytotoxicity of Trastuzumab x MMAE ADCs on cancer cell lines.

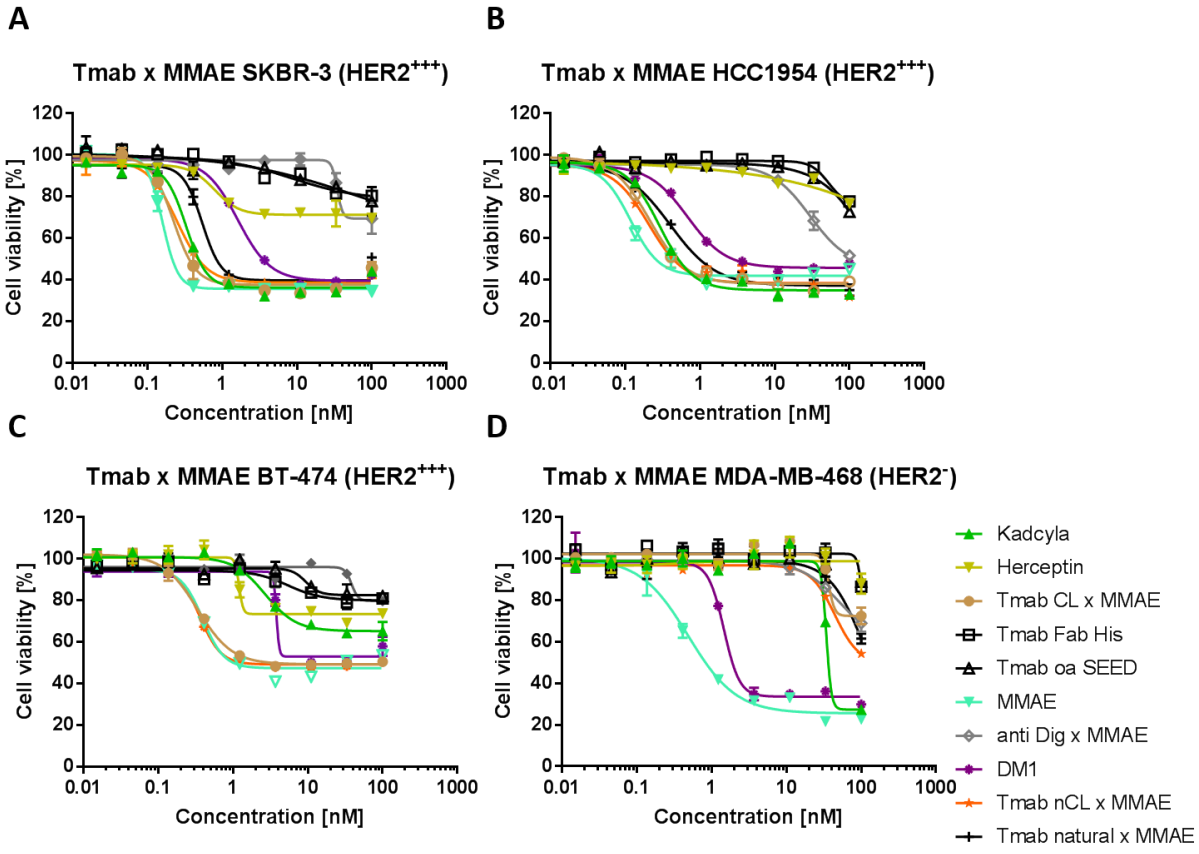

Trastuzumab ADCs generated by enzyme-assisted, site-specific conjugation of ValCit-PABC-MMAE to light chains were incubated on HER2-overexpressing SKBR-3 (**A**), HCC1954 (**B**) and BT-474 cells (**C**) as well as on HER-2 negative cells MDA-MB-468 (**D**) for 72 h. Uncojugated antibodies and antibody fragments were used as controls. Cell viability was analyzed by measuring ATP-levels using the CellTiter-Glo assay. High cytotoxic activity was observed on HER2-overexpressing cells with subnanomolar potencies (IC_{50} values), whereas no cell killing by Trastuzumab ADCs could be detected on HER2-negative cell. Illustrated are exemplary cell viability graphs from at least three independent experiments.

Appendix 26: Overview of cytotoxicity of Trastuzumab MMAE ADCs on NCI-N87

Construct	DAR	NCI-N87
Tmab CL x MMAE	1.9	0,39 ± 0,04
Tmab nCL x MMAE	1.8	0,40 ± 0,14
Tmab natural x MMAE	1.8	0,38 ± 0,07
Tmab CL x MMAE + MT-SP1	0.8	44,55 ± 44,41
Tmab Fab His x MMAE	0.9	32,72 ± 30,25
Tmab oa SEED x MMAE	0.8	11,33 ± 8,89
Kadcyla	3.5	0,15 ± 0,05
MMAE	-	0,22 ± 0,02
DM-1	-	1,22 ± 0,23

Depicted are cellular potencies of MMAE ADCs in different formats on NCI-N87 cancer cell line. Used control ADCs comprised Kadcyla and anti-Dig x MMAE. Mean IC_{50} values in nM from at least three independent experiments were used.

Appendix 27: Cytotoxicity of Trastuzumab x MMAF ADCs on cancer cell lines

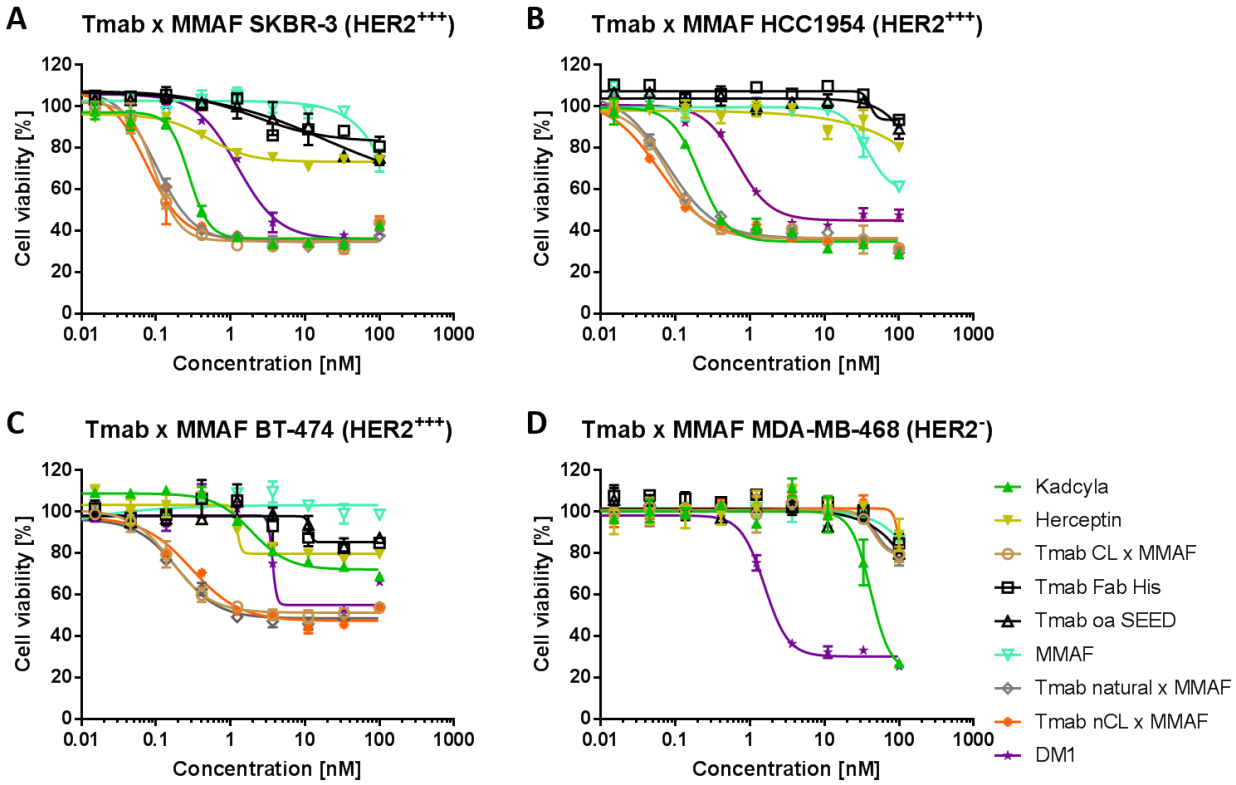

Trastuzumab ADCs with cleavable ValCit-PABC-MMAF linker drug conjugated to light chains were incubated on HER2-overexpressing SKBR-3 (**A**), HCC1954 (**B**) and BT-474 cells (**C**) as well as on HER-2 negative cells MDA-MB-468 (**D**) for 72 h. Also unconjugated antibodies were tested. Cell viability of cells was analyzed by ATP-levels using the CellTiter-Glo assay. No cell killing by Trastuzumab ADCs could be detected on HER2-negative cells. Illustrated are cell viability graphs from at least three independent experiments.

Appendix 28: Overview of cytotoxicity of Cetuximab (C225) x MMAE ADCs and FDCs on cancer cell lines

Construct	DAR	A431	MDA-MB-468	MCF-7
C225 CL x MMAE	1.1	0,54 ± 0,23	0,37 ± 0,06	> 100
C225 nCL x MMAE	1.3	0,49 ± 0,07	0,34 ± 0,13	> 100
C225 natural x MMAE	1.1	0,56 ± 0,07	0,41 ± 0,15	> 100
C225 CL x MMAE + MT-SP1	0.8	0,95 ± 0,01	0,79 ± 0,19	> 100
C225 Fab His x MMAE	0.8	0,71 ± 0,28	0,53 ± 0,22	> 100
C225 oa SEED x MMAE	0.8	1,05 ± 0,26	0,95 ± 0,44	> 100
Erbitux	-	> 100	> 100	> 100
MMAE	-	0,15 ± 0,12	0,46 ± 0,07	0,59 ± 0,10
DM-1	-	0,99 ± 0,09	0,55 ± 0,03	1,35 ± 0,27

Depicted are cellular potencies of Cetuximab x MMAE ADCs in different formats on A431, MDA-MB-468 and MCF-7 cells. Mean IC_{50} values in nM from at least three independent experiments were used.

Appendix 29: Cytotoxicity of Cetuximab x MMAE ADCs and FDCs on cancer cell lines

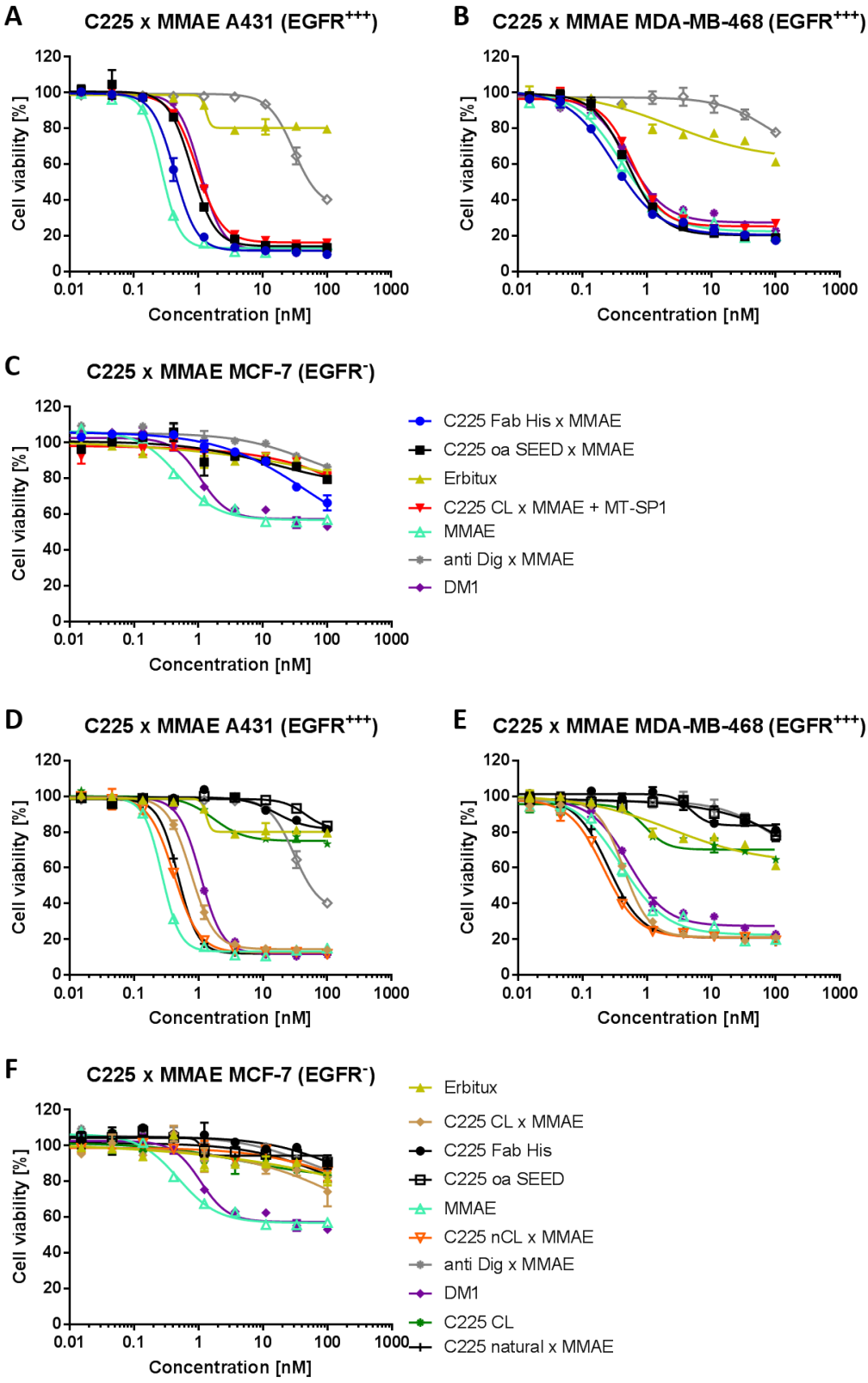

Cetuximab ADCs and FDCs generated by sortase A conjugation of ValCit-PABC-MMAE to light chains were incubated on EGFR-overexpressing A431 (**A**), MDA-MB-468 (**B**) cells as well as on EGFR-negative cells MCF-7 (**C**) for 72 h. Uncojugated antibodies and antibody fragments were used as controls and full length ADCs were also tested on A431 (**D**), MDA-MB-468 (**E**) and MCF-7 (**F**) cells. Cell viability was analyzed by measuring ATP-levels using the CellTiter-Glo assay. Illustrated are exemplary cell viability graphs from at least three independent experiments

Appendix 30: Tumor spheroid with HCC1954 cell line

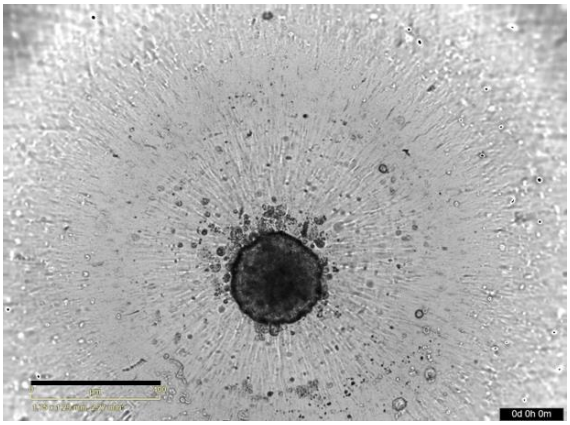

Spheroid formation was successful due to the formation of an extracellular matrix, represented by the black circle surrounding the spheroid. Scale bar = 400 µm

Appendix 31: Spheroid distribution and penetration with antibody-fluorophore conjugates using EVOS device

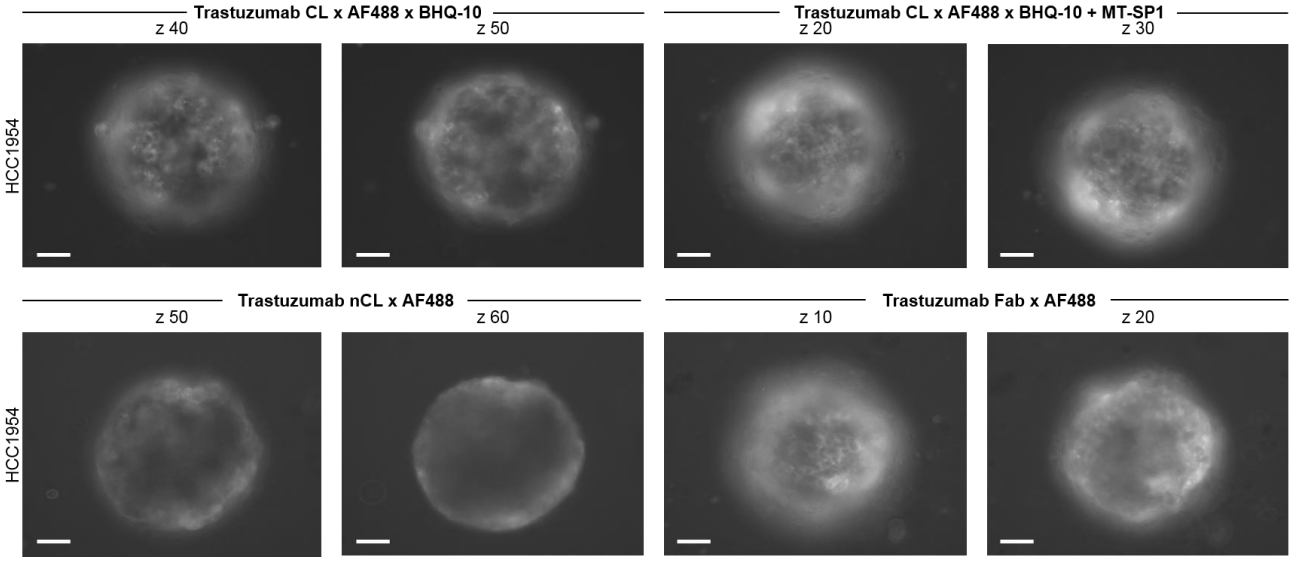

HCC1954 spheroids were treated with antibody-fluoropore conjugates with a concentration of 6.25 nM. Trastuzumab CL x AF x BHQ-10 was applied without enzyme to ensure matriptase cleavage is achieved by tumor cells. Control samples that are applied as Fab fragments attached to Alexa Fluor 488 comprised Trastuzumab CL x AF488 x BHQ-10 + MT-SP1 and Trastuzumab Fab x AF488. Prior measurement, calibration was carried out with fluorescence microscope EVOS FL 2 and the brightness and coarse (autofocus) were adjusted. Objective was used with 20x magnification, pictures were captured along Z stack at 24 h. Images are depicted in greyscale that is related to green fluorescence. Scale bar = 50 µm

8.1. Abbreviations

aa	Amino acid
ADC	Antibody-drug conjugate
ADCC	Antibody-dependent cellular cytotoxicity
ADCP	Antibody dependent cellular phagocytosis
AF488	Alexa Fluor 488
ALCL	Anaplastic large-cell lymphoma
ALL	Acute lymphoblastic leukemia
AMD	Age-related macular degeneration
AML	Acute myeloid leukemia
Amp	Ampicillin
ATP	Adenosine triphosphate
BCA	Bicinchoninic acid
BCR	B-cell receptor
BLI	Biolayer interferometry
BRCA1	Breast cancer susceptibility 1
BSA	Bovine serum albumin
C225	Cetuximab
CD	Cluster of differentiation
CDC	Complement-dependent cytotoxicity
CDR	Complementarity determining region
CH1, 2, 3	Constant domain 1, 2, 3 of the heavy chain
CL	cleavable
CLL	Chronic lymphoblastic leukemia
CML	Chronic myeloid leukemia
CTLA4	Cytotoxic T lymphocyte-associated antigen 4
CV	Column volume
Da	Dalton
DAR	Drug-to-antibody ratio
dH_20	Distilled water
DHFR	Dihydrofolate reductase
DNA	Deoxyribonucleic acid
ECD	Extracellular domain
E. coli	*Escherichia coli*
EGF(R)	Epidermal growth factor (receptor)
ELISA	Enzyme-linked immunosorbent assay
Fab	Fragment antigen binding
FACS	Fluorescence activated cell sorting

Fc	Fragment crystallizable
FcRn	Neonatal Fc receptor
FcγR	Fcγ receptor
FCS	Fetal calf serum
FDA	Food and Drug Administration
FDC	Fragment-drug conjugate / Fab-drug conjugate
FGF	Fibroblast growth factor
FITC	Fluorescein
GIST	Gastrointestinal stromal tumors
gp	Glycoprotein
h	Hour
HC	Heavy chain
HCC	Hepatocellular carcinoma
HER	Human epidermal growth factor receptor
HGF / SF	Hepatocyte growth factor, scatter factor
HGFR	Hepatocyte growth factor receptor, mesothelial epithelial transition; c-MET
HIC	Hydrophobic interaction chromatography
HIF-1a	Hypoxia inducible factor-1 alpha
His-tag	Histidine tag, usually composed of six histidines
HL	Hodgkin lymphoma
HPLC	High performance liquid chromatography
HPV	Human papillomavirus
HRP / POD	Horseradish peroxidase
hu / hs	Human / *homo sapiens*
Ig	Immunoglobulin
IGN	Indolinobenzodiazepine
IL	Interleukin
IMAC	Immobilized metal ion affinity chromatography
ITAM	Immunoreceptor tyrosine-based activating motif
ITIM	Immunoreceptor tyrosine-based inhibitory motif
k_a	Association rate constant
KB	Kinetics buffer
K_D	Equilibrium dissociation constant
k_d	Dissociation rate constant
LB medium	Luria-Bertani medium
LC	Light chain
mAb / pAb	Monoclonal antibody / polyclonal antibody
MALDI-TOF	Matrix-assisted laser desorption/ionization time of flight mass spectrometry

MAPK	Mitogen-activated protein kinase
MS	Mass spectrometry
MCS	Multiple cloning site
MES	2-(N-morpholino)ethanesulfonic acid
MFI	Mean fluorescence intensity
MMAE	Monomethyl auristatin E
MMAF	Monomethyl auristatin F
MMP	Matrix metalloproteinase
mRNA	Messenger ribonucleic acid
MSA	Multiple sequence alignment
mTG	Microbial transglutaminase
MT-SP1	Matriptase
mu	Murine, *mus musculus*
MWCO	Molecular weight cut-off
n.d.	Not determined
NC	Nitrocellulose
nCL	noncleavable
NEAA	Non-essential amino acids
NHL	Non-Hodgkin lymphoma
NHS	N-hydroxy succinimide
NK cells	Natural killer cells
NK1	N-terminal HGF fragment
NSCLC	Non-small-cell lung carcinoma
oa	One-armed
OD	Optic density
PABC	Para-aminobenzyloxycarbonyl
PAGE	Polyacrylamide gel electrophoresis
PAI	Plasminogen activator inhibitor
PAMPs	Pathogen-associated molecular patterns
PBMCs	Peripheral blood mononuclear cells
PBD	Pyrrolobenzodiazepine
PBS	Phosphate buffered saline
PCR	Polymerase chain reaction
PD-1	Programmed cell death protein 1
PD-L1	Programmed cell death protein ligand 1
PDB	Protein Data Bank
PDGF	Platelet-derived growth factor
PEG	Polyethylene glycol

PI	Propidium iodide
PI3K	Phosphatidylinositol 3-kinase
PVDF	Polyvinylidene fluoride
RCC	Renal cell carcinoma
RFU	Relative fluorescence units
RIPA buffer	Radioimmunoprecipitation assay buffer
rpm	Revolutions per minute
RT	Room temperature
RTK	Receptor tyrosine kinase
scFv	Single-chain variable fragment
SCLC	Small cell lung cancer
s.d.	Standard deviation
SDS	Sodium dodecylsulfate
SEC	Size exclusion chromatography
sec	second
SEED	Strand exchange engineered domain
SERM	Selective estrogen-receptor modulator
SHM	Somatic hypermutation
SMCC	Succinimidyl-4-(N-maleimidomethyl)-cyclohexane-1-carboxylate
SMDC	Small molecule–drug conjugate
Srt	Sortase
TCEP	Tris(2-Carboxyethyl)phosphine
TCR	T-cell receptor
T-DM1	Trastuzumab emtansine
TFF	Tangential Flow Filtration
TKI	Tyrosine kinase inhibitor
TLR	Toll-like receptor
T_m	Melting temperature
Tmab	Trastuzumab
TME	Tumor microenvironment
TNM	T (tumor) N (node) M (metastasis) Classification System for Malignant Tumors
TNF-a	Tumor necrosis factor-a
tPA	Tissue-type plasminogen activator
Tris	Tris(hydroxymethyl)aminomethane
uPA	Urokinase-type plasminogen activator
uPAR	Urokinase-type plasminogen activator receptor
US	United States
v/v	Volume per volume

ValCit	Valine-citrulline
vc	Valine-citrulline
VEGF	Vascular endothelial growth factor
VH	Variable domain of the heavy chain
VL	Variable domain of the light chain
w/v	Weight per volume
wt	Wild type

8.2. List of figures

8.3. List of tables

8.4. Curriculum Vitae

Name:	Janis Mario Roßkopf
Date of Birth:	15.08.1989
Place of Birth:	Dieburg (Darmstadt), Germany
Address:	Edith-Stein-Str. 18, 64839 Münster, Germany
E-Mail:	janis.rosskopf@gmail.com
Nationality:	German

Academic Studies and Education:

11/2016 – present	Doctoral Studies in Biochemistry, Merck KGaA, Darmstadt in collaboration with Technische Universität Darmstadt, supervision Prof. Dr. Harald Kolmar
2016	Third state examination, German Licensure as Pharmacist (Approbation)
05/2015 – 10/2015	Pharmaceutical Trainee, Public Pharmacy, Münster
11/2014 – 04/2015	Pharmaceutical Trainee, F. Hoffmann-La Roche AG, Basel
10/2014	Second state examination, Goethe-University Frankfurt am Main, Germany Major: Pharmaceutical Chemistry, Pharmaceutical Biology, Pharmacology, Pharmaceutical Technology, Clinical Pharmacy
04/2014	Elective subject: Medicinal chemistry/Pharmacology Characterizing dual modulators for the treatment of metabolic syndrome
08/2012	First state examination
10/2010 – 09/2014	Study of Pharmacy (state examination), Goethe-University Frankfurt am Main
09/2000 – 06/2009	High school diploma, Ludwig-Georgs-Gymnasium, Darmstadt

_____

(Janis Roßkopf)

8.5. Acknowledgments

Danksagung

Zuallererst möchte ich besonders Prof. Dr. Harald Kolmar für die akademische Betreuung meiner Doktorarbeit an der TU Darmstadt danken. Die bewährte Kooperation mit der industriellen Forschung hat die Promotion in vielerlei Hinsicht unterstützt. Die Seminare im Kleinwalsertal mit der Arbeitsgruppe sowie die Teilnahme an der PEGS in Lissabon waren für den wissenschaftlichen Austausch von einzigartiger Bedeutung.
Mein aufrichtiger Dank gilt auch Dr. Stefan Hecht und Dr. Jan Anderl, die mir die sehr interessante Promotion im Bereich Antikörper-Wirkstoff Konjugate in der Abteilung bei Merck ermöglicht und mein Projekt maßgeblich mit zahlreichen Anmerkungen und Anregungen jederzeit unterstützt haben.

Prof. Dr. Siegfried Neumann möchte ich für die Übernahme des Korreferats sowie den wissenschaftlichen Diskussionen danken. Prof. Dr. Alexander Löwer und Prof. Dr. Johannes Kabisch danke ich für die Bereitschaft, sich als Fachprüfer bereitzustellen.

Herzlich bedanken möchte ich mich bei Dr. Carl Deutsch für die Aufnahme in sein Team und die ständige Betreuung im Rahmen meiner Promotion. Die zahlreichen Ideen und Diskussionen, der Input für neue Ansätze sowie Mitgestaltung des Projektes haben maßgeblich diese Arbeit vorangetrieben. Für die amüsanten Teamevents abseits der Arbeit möchte ich meinen Dank an Rainer Kohl, Katrin Peschk, Marie Quillmann, Dr. Min Shan, Helene Crassier, Mirela Kunkel und Antje Schöneberg aussprechen.

Des Weiteren gilt mein Dank allen Personen aus den Abteilungen ADCs und PEAT bei Merck. Viele Personen haben direkt oder indirekt dieses Projekt enorm unterstützt, sowohl bei der Einführung neuer Methoden oder Bereitstellung von Materialien oder Instrumenten. Dr. Stanley Sweeney-Lasch möchte ich für die zahlreichen Diskussionen zu Fluorophor-Experimenten, seinen Input und das Korrekturlesen der Arbeit herzlich danken. Mein außerordentlicher Dank gilt auch Tim Hofmann und Sebastian Jäger für vielfältige Ratschläge im Labor und die hervorragende Arbeitsatmosphäre. Auch für das Korrekturlesen bedanke ich mich vielmals bei Euch. Dr. Christian Schröter danke ich für die Untersützung zu Beginn meiner Promotion bei Merck und für die konzeptionellen Diskussionen meines Projekts. Besonderer Dank gilt auch Anna Kämpffe, Dr. Doreen Könning, Gernot Musch, Anja Lamack und Vanessa Lautenbach für viele Ideen und Anregungen rund um diverse Laborversuche.
Dr. Roland Kellner, Dr. Jason Tonillo, Jennifer Schanz, Amanda Vanselow und Claudia Kubis möchte ich für Ihren hervorragenden Support bei der LC-MS Analytik und der Quantifizierung der Enzym Kinetik danken.
Dr. Marcel Rieker gilt mein besonderer Dank für die unzähligen Einführungen bei diversen Geräten, Experimenten und Hilfestellungen im Labor. Bei Marie Quillmann möchte ich mich für die Synthese und Bereitstellung der Fluorophor Moleküle bedanken. Für viele Tipps im Bereich Antibody Engineering möchte ich mich bei Dr. Simon Krah und Dr. Carolin Sellmann bedanken.

Für die außerordentliche Unterstützung bei der Antikörper-Aufreinigung und Analytik danke ich besonders Dirk Müller-Pompalla, Stephan Keller, Alexander Müller und Sigrid Auth. Es hat mir stets große Freude bereitet an Euren Anlagen arbeiten zu dürfen.
Das Team um Dr. Stefan Becker mit Deniz Demir, Iris Willenbücher und Kerstin Hallstein (ehemaliges Eck-Labor) danke ich für zahlreiche Tipps bei Zellexperimenten und Geräteeinführungen.
Für Input bei unterschiedlichen Experimenten und die Hilfsbereitschaft danke ich besonders Christina Bauer, Dominik Reitz, Denise Berghäuser und Ramona Gaa.
Ebenso geht mein großer Dank an Dr. Birgit Piater, Kirsten Leidinger, Konstanze Waurisch, Dr. Dmitry Zabezhinsky, Dr. Jean Wakim für den hilfreichen Austausch und die Unterstützung bei diversen Zellassays sowie Imaging Experimenten.
Dem Konjugationslabor von Dr. Nicolas Rasche mit Dr. Stephan Dickgießer, Jens Hannewald und Ingrid Schmidt danke ich für die Unterstützung und Bereitstellung der Konjugate.
Für die Ideen und den wissenschaftlichen Austausch, sowie die Durchführung von Small Molecule Analysen möchte ich besonders Dr. Sebastian Fuchs und Dr. Sven Pötzsch von SM-AH danken.
Dr. Daniel Kuhn und Dr. Tim Knehans danke ich für die vielen Hilfestellungen bezüglich Modell-Analysen von Molekülparametern.

Mein außerordentlicher Dank geht auch an die Innospire-Gruppe Dr. Min Shan, Dr. Marco Passafaro, Dr. Christian Schröter, Dr. Stefan Becker, Dr. Jan Gajewski und Dr. Carl Deutsch für die zahlreichen Meetings und Vorbereitungen im Rahmen von Innospire.
Besonderer Dank gilt auch dem Innospire-Team vom Merck Innovation Center mit Dr. Carsten Vogt, Kai Wambach und Jennifer Paysen (und auch Prof. Dr. Stefan Stremersch) für die tolle Betreuung während des Bootcamps. Über mehrere Wochen und Monate habt ihr es verstanden, das Projekt mit unterschiedlichen Aspekten zu durchleuchten und für die finale Präsentation vor der GL vorzubereiten.

Allen derzeitigen (und auch ehemaligen) AK Kolmar Mitgliedern möchte ich für den wissenschaftlichen Austausch, Seminare und diversen Veranstaltungen danken. Insbesondere Arturo Macarron, Ataurehman Ali (Ata), Steffen Hinz, Hendrik Schneider und Simon Englert. Des Weiteren gilt ein besonderer Dank den Merck-Doktoranden(innen) Sandra Müller, Lukas Pekar (Roth), Markus Lubda, Martina Zimmermann, Gregory Som und Janina Klemm.

Zum Schluss möchte ich insbesondere meiner Familie (sowohl hier als auch in Griechenland) und meinen Eltern für die kontinuierliche Unterstützung während meines Studiums aufrichtig danken.

9. Affirmations

Janis Mario Roßkopf
Edith-Stein-Str. 18
D-64839 Münster

_____
(Datum)

Erklärung

Ich erkläre hiermit, dass ich meine Dissertation selbstständig und nur mit den angegebenen Hilfsmitteln angefertigt habe.

_____
(Janis Roßkopf)

Janis Mario Roßkopf
Edith-Stein-Str. 18
D-64839 Münster

_____
(Datum)

Erklärung

Ich erkläre hiermit, noch keinen Promotionsversuch unternommen zu haben.

_____
(Janis Roßkopf)

Janis Mario Roßkopf
Edith-Stein-Str. 18
D-64839 Münster

_____
(Datum)

Erklärung

Ich erkläre hiermit, dass die elektronische Version der Doktorarbeit mit der schriftlichen Version übereinstimmt. Die elektronische Version liegt dem Prüfungssekretariat vor.

_____
(Janis Roßkopf)